Chemie

Dissertation

Liquid-Delivery Metal-Organic Chemical Vapour Deposition of Perovskites and Perovskite-Like Compounds

zur Erlangung des akademischen Grades
doctor rerum naturalium
(Dr. rer. nat.)

Mathematisch-Naturwissenschaftlichen Fakultät I
der Humboldt-Universität zu Berlin

Frau M. Sc. Rasuole Lukose

Dekan: Prof. Dr. Andreas Herrmann

Gutachter: 1. Prof. Dr. Erhard Kemnitz
2. Prof. Dr. Roberto Fornari
3. Prof. Dr. Anjana Devi

eingereicht: 26.07.2010

Datum der Promotion: 09.09.2010

Selbstständigkeitserklärung

Hiermit erkläre ich, das ich die vorliegende Dissertation selbständig angefertigt habe und nur die angegebenen Quellen und Hilfsmittel verwendet habe.

(Datum, Ort) Rasuole Lukose

Acknowledgments

I wish to express my sincere gratitude to my research supervisor Prof. Dr. Roberto Fornari, for providing me the opportunity to make my PhD at the Leibniz-Institute for Crystal Growth, for his support throughout this work and his helpful suggestions in reviewing this thesis.

My special thanks go to Prof. Dr. Erhard Kemnitz at Humboldt University for accepting my candidature as a PhD student and for the assistance at the University.

I equally express my gratitude to the leader of the oxide layers group, Dr. Jutta Schwarzkopf, who directly supervised this work. I am thankful for the support in every aspect of the experimental work, comprehensive and useful discussions.

I am also very grateful to my colleague Dr. Günter Wagner not only for the helpful conversations in scientific field but as well as for his help in daily life. I would like to express my gratitude to group colleagues, Sebastian Markschies and Dr. Saud Bin Anooz for the nice working atmosphere and for the fact that I could always rely on their assistance.

I would like to express my gratitude to Jr. Prof. Dr. Anjana Devi for the effective collaboration in the field of metal-organic precursors that were applied in this particular work. In this context, I would like to thank also all the PhD students of her group, especially Daniela Beckerman and Ke Xu, for the thermoanalytic measurements of metal-organic precursors.

I would like to thank sincerely to my colleagues at IKZ, especially PD Dr. habil. Martin Schmidbauer for his help and advices concerning High Resolution X-ray Diffraction measurements and Albert Kwasniewski for performing these measurements. I am grateful to Dr. Klaus Irmscher for the discussions on electrical results, Mike Pietsch for performing these measurements and Dr. Martin Albrecht for the support in characterization with Scanning Electron Microscopy and Transmission Electron Microscopy. In this context, I would like to thank Dr. habil. Detlef Klimm and Steffen Ganschow for their help performing some measurements of the metal-organic precursors. My special thanks go to Dr. Reinhard Uecker for the supply of the substrates and useful discussions about oxide materials.

I also want to thank the colleagues from the Department of Physics in Humboldt University, namely Jens Lienemann, Dr. Marco Busch and Prof. Dr. Helmut Winter for the fruitful collaboration and AES measurements.

Additionally, I would like to thank Dr. Andrea Harrer, Carsten Hartmann, Dr. Tobias Schulz, Dr. Daniela Gogova for the friendly and encouraging atmosphere at work and also outside the Institute.

My specials thanks go to my colleagues at Faculty of Chemistry in Vilnius University, especially Dr. Valentina Plausinaitiene for the scientific discussions and support.

Last but not the least; I express huge thanks to my family: my husband, my mother and my sister for their support, encouragement and trust in me during all these study years.

Abstract

Perovskites and perovskite-like materials are actually of great interest since they offer a wide range of structural and physical properties giving the opportunity to employ these materials for different applications.

Liquid-Delivery Metal Organic Chemical Vapour deposition (LD-MOCVD) was chosen due to the easy composition control for ternary oxides, high uniformity and good conformal step coverage. Additionally, it allows growing the films, containing elements, for which only solid or low vapour pressure precursors, having mainly thermal stability problems over long heating periods, are available.

The purpose of this work was to grow $SrRuO_3$, $Bi_4Ti_3O_{12}$ and $(Na, Bi)_4Ti_3O_{12}$ films by LD-MOCVD and to investigate the influence of the deposition conditions on the properties of the films. Additionally, the effect of the strain due to the lattice mismatch between substrates and films on the physical properties of the films was also investigated.

$SrRuO_3$ films were grown on stepped $SrTiO_3(001)$, $NdGaO_3(110)$ and $DyScO_3(110)$ substrates, which were prepared under different conditions by changing the annealing time and atmosphere. The termination of the substrates was measured by surface sensitive proton-induced Auger Electron Spectroscopy (p-AES) technique.

Another systematic study of the relation between epitaxial strain and Curie temperature of thin $SrRuO_3(100)$ films was performed by using substrates with different lattice constants. The observed Curie temperature decreased with compressive and increased with tensile strain.

Thin films of $Bi_4Ti_3O_{12}$ as well as $(Na, Bi)_4Ti_3O_{12}$ were successfully deposited. In order to grow stoichiometric and epitaxial $Bi_4Ti_3O_{12}(001)$ films, Bi excess in the precursor solution was necessary, due to the volatility of Bi. Substitution of Bi with Na in $Bi_4Ti_3O_{12}$ was achieved for the first time for the films deposited by LD-MOCVD.

Perovskites, LD-MOCVD, oxide substrates, thin films, strain.

Zusammenfassung

Perowskite und Perowskit-artige Materialien sind von großem Interesse, da sie eine Vielzahl von strukturellen und physikalischen Eigenschaften haben, welche die Möglichkeit bieten, sie für unterschiedliche Anwendungen einzusetzen.

Die Methode der Liquid-Delivery Metal Organic Chemical Vapour Deposition (LD-MOCVD) wurde gewählt, da sie eine gute Kontrolle über die Zusammensetzung ternärer Oxide und eine hohe Homogenität der Filme ermöglicht. Darüber hinaus können mit dieser Methode Filme hergestellt werden, die aus Elementen bestehen, für welche nur feste Precursor oder welche mit niedrigem Dampfdruck zur Verfügung stehen.

Ziel dieser Arbeit war es, mit Hilfe der LD-MOCVD Filme aus $SrRuO_3$, $Bi_4Ti_3O_{12}$ und $(Na,Bi)_4Ti_3O_{12}$ abzuscheiden und den Einfluss der Wachstumsbedingungen auf die Eigenschaften der Filme zu untersuchen. Zusätzlich wurde die Wirkung der Verspannung, die durch die Gitterfehlanpassung zwischen Substrat und Film entsteht, auf die physikalischen Eigenschaften der Schichten untersucht.

$SrRuO_3$ Filme wurden auf gestuften $SrTiO_3$(001), $NdGaO_3$(110) und $DyScO_3$(110) Substraten gewachsen, deren Oberflächenterminierung durch oberflächensensitive Proton-induzierte Auger-Elektronen-Spektroskopie (AES) bestimmt wurde. Die Substrate wurden unter verschiedenen Bedingungen durch Änderung der Temperdauer und -atmosphäre präpariert.

Die systematische Untersuchung der Beziehung zwischen Verspannung und Curie-Temperatur von dünnen $SrRuO_3$(100) Filmen erfolgte unter Verwendung von Substraten mit unterschiedlichen Gitterkonstanten. Die beobachtete Curie-Temperatur sank mit erhöhter kompressiver Verspannung und nahm mit erhöhter tensiler Verspannung zu.

Um stöchiometrische und epitaktische $Bi_4Ti_3O_{12}$(001) Filme zu wachsen, war aufgrund der Flüchtigkeit des Bismuts ein Bi Überschuss in der Precursor-Lösung notwendig. Die Substitution von Bi durch Na in $Bi_4Ti_3O_{12}$ wurde zum ersten Mal in LD-MOCVD-Filmen erreicht.

Perowskite, LD-MOCVD, oxidische Substrate, dünne Filme, Verspannung.

Table of contents

List of Abbreviations

AES – Auger Electron Spectroscopy

AFM – Atomic Force Microscopy

CVD – Chemical Vapour Deposition

DSC – Differential Scanning Calorimetry

DTA – Differential Thermal Analysis

$\varepsilon_{\perp}$ – epitaxial strain

e-AES – electron-induced Auger Electron Spectroscopy

EI-MS – Electron Impact Mass Spectrometry

FWHM – Full Width of Half Maximum

XRF – X-ray Fluorescence Analysis

HRXRD – High Resolution X-ray Diffraction

LD-MOCVD – Liquid-Delivery Metal-Organic Chemical Vapour Deposition

LSAT – $(LaAlO_3)_{0.3} – (Sr_2AlTaO_6)_{0.7}$

MBE – Molecular Beam Epitaxy

ML – Monolayer

O^iPr - isopropoxide

p-AES – proton-induced Auger electron Spectroscopy

PLD – Physical Layer Deposition

R_a – average roughness

RHEED – Reflexion High Energy Electron Diffraction

RMS – Root mean square

SEM – Scanning Electron Microscopy

θ_B – Bragg angle

T_c – Curie temperature

TEM – Transmission Electron Microscopy

TG – Thermogravimetry

thd – 2,2,6,6-tetramethyl-3,5-heptanedione

UHV – Ultra High Vacuum

XPS – X-ray Photoelectron Spectroscopy

Introduction

Perovskites and perovskite-like materials are very interesting materials because they offer a wide range of structural and physical properties. They are very well known for their common structural instabilities which can be caused by temperature, pressure, strain or partial substitution by different cations. These instabilities cause not only changes in structure, but also in physical properties like Curie temperature, spontaneous polarization, dielectric constant, fatigue, which are important for the application of such materials in non-volatile random access memories, high dielectric constant capacitors and optical waveguides.

In order to measure the electrical properties of the ferroelectric thin layers, one possibility is to sandwich the ferroelectric between two electrodes to form a capacitor. The properties of these capacitors depend on stoichiometry, phase composition, morphology and microstructure of both the electrode and ferroelectric film, as well as on the structural and electronic character of the electrode-ferroelectric interfaces. Two main groups of the electrodes are used to form metal-ferroelectric-metal capacitors: single metals (Pt, Au, Ru) and metallic oxides (RuO_2, IrO_2, $SrRuO_3$).

In addition, the properties of the heterostructure also depend strongly on the interface between substrate and electrode. The initial growth of electrode films actually depends on the surface morphology and termination layer of the substrate. Therefore, in the present work vicinal $SrTiO_3$, $NdGaO_3$ and $DyScO_3$ substrates were prepared under different preparation conditions before the deposition of thin epitaxial $SrRuO_3$ films. The terminating surface layer of the substrates was determined by proton-induced Auger electron spectroscopy in order to investigate the status of the interface between the substrate and epitaxial layer.

In the present study metallic-ferromagnetic $SrRuO_3$ was chosen as a model system for possible bottom electrode, which was grown on perovskite substrates, therefore it may serve as an epitaxial template with a proper crystallographic orientation for the epitaxial growth of ferroelectric films. $SrRuO_3$ was selected because it is chemically stable and has a structural similarity to most perovskite substrates and thin films and has a good electrical conductivity. Additionally, strained thin $SrRuO_3$ films showed a clear behaviour of the Curie temperature depending on the strain caused by using different oxide substrates which is interesting for fundamental and practical studies and only marginally studied so far.

However, growth conditions like deposition temperature and pressure, supersaturation, gas phase composition, post annealing conditions etc. determines the growth mode of thin

films as well. The liquid-delivery MOCVD was used for the growth of epitaxial perovskite and perovskite-like layers because it offers excellent film uniformity, and good conformal step coverage. Additionally, it allows growing the films, containing elements, for which only solid or low vapour pressure precursors, having thermal stability problems during transportation, are available. In LD-MOCVD these problems are solved by dissolving precursors in a liquid solvent and transporting them as a liquid to a flash evaporator with the help of carrier gas. In addition, by using this method, the stoichiometry of the films can be easily controlled.

The main goal of this thesis was to grow ferromagnetic-metallic $SrRuO_3$ and ferroelectric $Bi_4Ti_3O_{12}$, $(Na, Bi)_4Ti_3O_{12}$ thin films in order to get single phase epitaxial layers and to investigate the fundamental properties of the films depending on deposition conditions. To this extent, the structural and physical properties of the films depending on different oxide substrates ($SrTiO_3$, $NdGaO_3$, $DyScO_3$) inducing epitaxial strain in thin layers were investigated and used as feedback for the definition of optimized growth parameters.

The thesis is organized as follows: **Chapter 1** describes the general structural and physical properties of the investigated perovskite and perovskite-related materials. The mismatch between the film and substrate and its effect on the properties of the epitaxial thin film is also presented in this chapter.

The growth method and characterization techniques used to investigate the properties of $SrRuO_3$, $Bi_4Ti_3O_{12}$ and $(Na, Bi)_4Ti_3O_{12}$ films are summarized in **Chapter 2**.

The detailed discussion of the experimental results can be found in **Chapter 3**. In **Section 3.1** the preparation process and conditions of atomically flat $SrTiO_3(001)$, $DyScO_3(110)$ and $NdGaO_3(110)$ surfaces and the measurement of the termination layer of the surfaces are described in detail. In **Section 3.2** special attention has been paid to the physical and chemical properties of metal-organic precursors used for deposition of the layers with liquid-delivery MOCVD. A study of $SrRuO_3$ layers in terms of the surface morphology, phase composition, epitaxial strain and Curie temperature is presented in **Section 3.3**. The deposition results of layered $Bi_4Ti_3O_{12}$ films are summarized in **Section 3.4**. **Section 3.5** deals with the deposition results and structural properties of A-site substituted $(Na, Bi)_4Ti_3O_{12}$ layers. In the last chapter (**Chapter 4**) general conclusions of the work are summarized.

1. Fundamentals

1.1 Perovskites and their structural properties

Perovskite and perovskite-like materials are interesting due to diverse physical and chemical properties in a wide range of temperature. For example, perovskites are known for their superconducting properties ($(K,Ba)BiO_3$) [1], piezoelectric properties ($Pb(Zr,Ti)O_3$) [2] relaxor ferroelectric properties ($Pb(Nb,Mg)O_3$) [3], ($(Na,Bi)TiO_3$) [4], dielectric properties ($BaTiO_3$ [5], $SrTiO_3$ [6]), conductive-ferroelectric ($SrRuO_3$) [7], electro-optic properties ($(Pb,La)(Zr,Ti)O_3$) [8], magneto-resistive properties ($(La, Ca)MnO_3$) [9] and catalytic properties ($LaCrO_3$) [10].

The ideal perovskite structure ABO_3 belongs to the cubic crystal structure and consists of a three-dimensional framework of corner sharing BO_6 octahedron, where big A cations are coordinated with 12 equidistant oxygen anions and relatively small B cations are in the middle of these octahedral (Fig. 1.1 a).

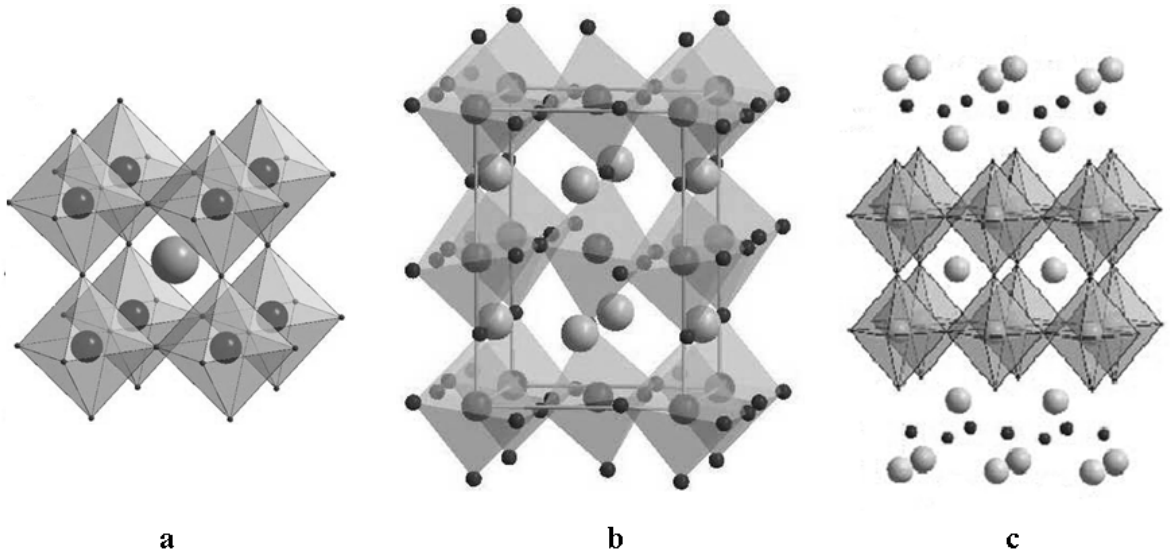

Fig. 1.1 Perovskite-type structures: a) ideal cubic perovskite, b) perovskite with tilted BO_6 octahedra, c) layered-perovskite structure with two perovskite blocks.

According to Lufaso and Woodward [11], most perovskite structures are distorted and do not have an ideal cubic symmetry. Common distortions such as cation displacements within the

BO_6 octahedra and tilting of the octahedra are related to the properties of the A and B substituted atoms. Factors that contribute to distortion in the structure include radius size effect and bond length between the cations and oxygen. Such octahedral tilting distortions (Fig. 1.1. b), present in many perovskites, is related to the stability of the perovskite structure and is described by the so called 'tolerance factor' *t* which was introduced by Goldschmidt in early 1920s [12]:

$$t \equiv \frac{(A-O)}{\sqrt{2}(B-O)} \equiv \frac{r_A + r_O}{\sqrt{2}(r_B + r_O)}, \qquad \text{Eq. 1.1}$$

where r_A, r_B and r_O are the ionic radii of cation A, B and anion O, (A-O) and (B-O) the bond length between the cations and oxygen, respectively. Geometrically, for an ideal perovskite, if the bond length is roughly assumed to be the sum of the two ionic radii, the t-value of the ideal perovskite should be equal to 1. When the value of t is 0.81 or less and the radius of the A site ion is smaller than ideal, the BO_6 octahedra will tilt in order to fill the space. Stable perovskite structures have values approximately in the $0.78 < t < 1.05$ range. The distortions result in bending of the B–O–B bridges which reduces the strength of B–B interactions (e.g. magnetic exchange coupling, transfer or hopping integral, width of the energy bands) so that the critical temperatures for ordering phenomena (e.g. magnetic, superconducting and ferroelectric) usually decrease as t falls. Even a small structural distortions which can be driven by parameters like temperature, pressure, strain, external electric and magnetic fields, etc., may change significantly the physical properties of the perovskites.

Another class of perovskite-related compounds is provided by the so-called layered perovskites (Fig. 1.1 c), where the perovskite blocks $(A_{m-1}B_mO_{3m+1})^{2-}$ are separated by A-site cation oxide $(Bi_2O_2)^{2+}$ in the case of Bi-layered compounds. The Bi – layered perovskite compounds are one of the best candidates for the lead-free non-volatile ferroelectric memories due to their promising ferroelectric properties, where the cation substitution at A and B sites helps to improve the ferroelectric properties necessary for memory applications [13,14]. There is a big interest in these materials, from an environmental point of view also, because there is a need for the preparation of a new generation of efficient lead-free ferroelectrics.

1.2 Epitaxial growth

Epitaxy is commonly defined as the oriented growth of a crystalline material on a single crystal surface. Epitaxial growth is classified in: a) homoepitaxy - when film and substrate

consist of the same material, and b) heteroepitaxy - when they are different. The present work will concern only heteroepitaxial growth. In the ideal case, epitaxy proceeds as so-called pseudomorphic growth with the substrate lattice continuing in the thin film. It is evident that the continuation of the substrate crystal lattice will be associated with the incorporation of strain into the layer when the layer and substrate unit cells are different [15] up to the critical thickness of the film.

1.2.1 Misfit strain

Enormous strains can exist in thin films when one material is deposited onto another [16], resulting from differences in crystal lattice parameters and thermal expansion behaviour between the film and the underlying substrate or arising from defects formed during film deposition [17,18]. As a result, the properties of thin films can be evidently different than the intrinsic properties of the corresponding unstrained bulk materials [7,19,20,21]. Right selection of substrates, growth parameters and strain, offers the opportunity to enhance particular properties of a chosen material in thin film form, which is called strain engineering. It was observed that the resulting strain induces large shifts in the ferroelectric-to-paraelectric transition temperature (T_c) and remnant polarization for ferroelectric materials [22,23,24].

The difference of lattice parameters between substrate and layer plays a very important role for film stress and defect density. The driving force for film relaxation increases with strain and film thickness. When films are grown to thicknesses greatly exceeding their critical values, relaxation toward a zero strain state by the introduction of dislocations begins. Thus, for strain engineering to be effective, it is important to grow films below, or at least close to, their critical thickness for relaxation. If the mismatch between the film and substrate is large, the critical thickness can be only few atomic layers, while for a small mismatch in may reach hundreds of nanometers. To avoid dislocations in the thin films it is necessary to select a small mismatch ($\Delta a/a$) between thin film and substrate, which is defined by (Eq. 1.2):

$$\frac{\Delta a}{a} = \frac{a_f - a_s}{a_s} \times 100\% \qquad \text{Eq. 1.2}$$

where a_f and a_s are the bulk lattice constants of the film and the substrate, respectively [21].

Depending on the choice of substrate, films may be grown under compressive or tensile strain. When the lattice constant of the substrate is smaller than the one of the layer, the layer will be compressively strained (the cell is elongated in the out-of-plane direction and

compressed in-plane). Whereas a larger lattice of the substrate leads to the tensile strain in the layer (the cell is compressed in out-of-plane direction and elongated in-plane) (Fig. 1.2). Strain energy accumulates rapidly with film thickness resulting in misfit dislocation generation or morphological transformation from 2D layer-by-layer to 3D island growth. Which of these mechanisms is operative depends on the quality and termination of the substrate surface (see Section 3.1) and on the kinetics of the film growth, depending on the deposition conditions.

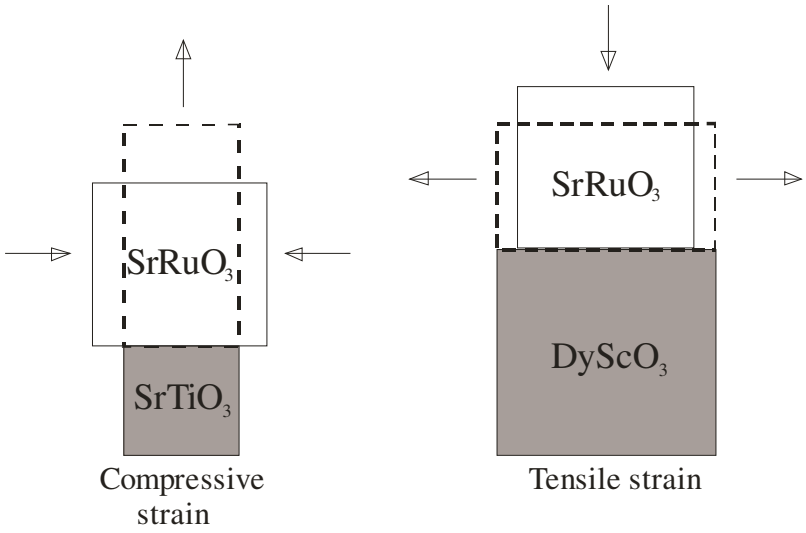

Fig. 1.2 Schematic drawings of the lattice cell distortion of strained epitaxial $SrRuO_3$.

1.2.2 Growth modes

For heteroepitaxy in general, three growth modes are observed depending on three main parameters: the supply of the material to the reaction zone, the deposition temperature and mismatch between the film and the substrate, resulting in different film morphologies [25]. In this section, for the description of the growth modes the effect of mismatch will be taken into account. These main growth modes are a) the layer-by-layer (Frank-van der Merwe) growth, e.g., in the case of a very thin layer, or in the case of almost perfectly lattice-matched materials; b) the layer-then-island (Stranski-Krastanov) growth, an intermediate growth mode, where a layer grows below a critical thickness and subsequently 3D island growth occurs, and c) the island (Volmer-Weber) growth, mainly for (highly) lattice-mismatched materials (Fig. 1.3).

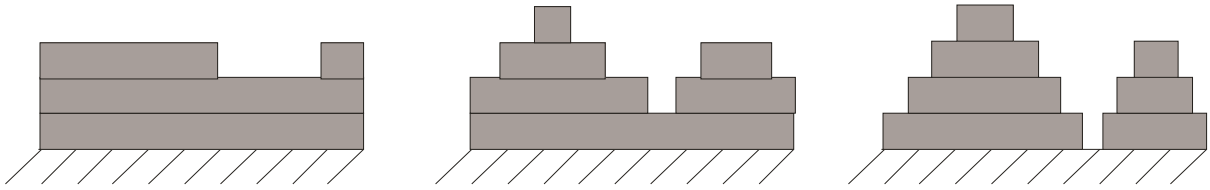

Fig. 1.3 The main heteroepitaxial growth modes.

The interface between the substrate and the film is very important especially at the beginning of the growth. The structure of the interface, and its properties, depend essentially on four parameters: a) the misfit between the substrate and the layer, b) the thickness of the film, c) the strength of the interaction between the substrate surface and the first atomic layers of the deposited film, d) the surface quality of the substrate.

The strain resulting from lattice mismatch contributes to the interface energy, a key parameter in determining the growth mode. However, the surface free energies of the substrate and film materials also influence the mode of growth. Bauer and van der Merwe [26] have cast the energetics of film growth into a particularly simple form under the assumption of equilibrium between the film components in the gas phase and those at the film surface. In this formalism, layer-by-layer growth requires that:

$$\Delta\gamma = \gamma_{film} + \gamma_i - \gamma_{subs} \leq 0 \qquad \text{Eq. 1.3}$$

where γ_{film} and γ_{subs} are the surface free energies of film and substrate, respectively, and γ_i the free energy of the interface. The latter quantity depends on the strain and the strength of chemical interactions between atoms of the film and substrate at the interface. The equation says that the sum of the film surface energy and the interface energy must be less than the surface energy of the substrate ($\gamma_{subs} > \gamma_{film} + \gamma_i$) in order layer-by-layer growth to occur, which becomes easier as the surface energy of the substrate increases. However, the strain energy (γ_i), increases linearly with the number of strained layers. At some thickness, $\gamma_{film} + \gamma_i$ exceed γ_{subs} and the growth mode transforms from layer-by-layer to island growth resulting in 3D islands on the 2D layer (layer-then-island growth). Alternatively, γ_{film} may be sufficiently in excess of γ_{subs} that the equation is never fulfilled even for a strong attractive interaction between the atoms of the layer and substrate and little strain ($\gamma_i < 0$). In this case, 3D island nucleation occurs [27].

Additionally, the growth mode of the films depends largely on the surface morphology, termination and lattice mismatch of the substrate. Therefore, controlling the surface morphology and chemistry of the substrates is very important for the reproducibility of the grown layers. The control the surface morphology and chemistry of the substrate is possible by applying surface treatments such as annealing or chemical etching of the substrate. It has been found that single crystal $SrTiO_3$ substrate cutted at a vicinal angle and annealed in oxygen [28] produce a periodic step-and-terrace pattern with mixed SrO and TiO_2 termination layers on the substrate surface. Chemical etching and following high temperature annealing of the $SrTiO_3$ substrates produces uniform steps of single unit cell height with a purely TiO_2 terminated surface [29,30]. The terraced surface, which results from these surface treatments, offers a reproducible surface template to reduce the number of domains in the grown films.

The substrate surface step density, overall substrate morphology, and surface adatom diffusivity also effect the growth on stepped surfaces. If the diffusion length of adatom is longer compared to the mean terrace width on the surface, adatom condensation will occur preferentially at steps rather than on terraces. Step-flow growth is a specialized case in which there is preferential adatom attachment from lower terraces adjacent to steps (Fig. 1.4). Step-flow leads to step-step annihilation and a gradual reduction in step density if the step-flow is disturbed. At lower temperatures, adatom diffusivities are lower leading to enhanced condensation on terraces. If the distribution of adatoms on the terraces is 2D, a periodic change in step density occurs as growth proceeds if the temperature is high enough, otherwise 3D growth can occur. Also if the step density is too low (i.e. width of the terraces is too large), then 2D island nucleation is more likely on terraces and not at the step edges.

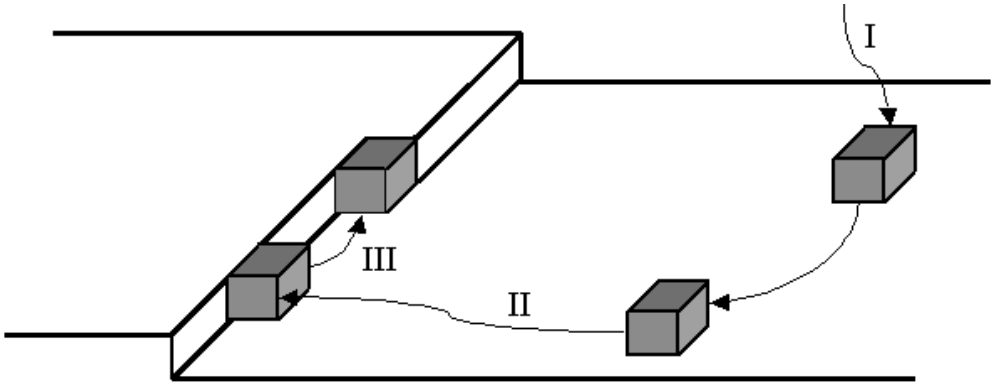

Fig. 1.4 Sequence of incorporation of atoms on the stepped substrate surfaces [31]. I) adsorption of adatom on the surface, II) surface diffusion, III) migration of adatom to a kink site on the terrace.

1.3 Ferroelectrics and ferromagnets

In this section the general similarities and differences between the ferroelectric and ferromagnetic materials and the reasons causing these processes will be shortly described, because this thesis will focus mainly on two different materials: ferromagnetic $SrRuO_3$ and ferroelectric $Bi_4Ti_3O_{12}$.

There are indeed many similarities between the ferroelectrics and ferromagnets. The ferroelectrics can be defined as materials with spontaneous permanent electrical polarization switchable by the external electric field. Likewise, a ferromagnet has a spontaneous permanent magnetic polarization which changes the orientation with application of an external magnetic field. Usually the switching process between two equivalent states is associated with the hysteresis, which has a very similar form in both cases (Fig. 1.5 and Fig. 1.6).

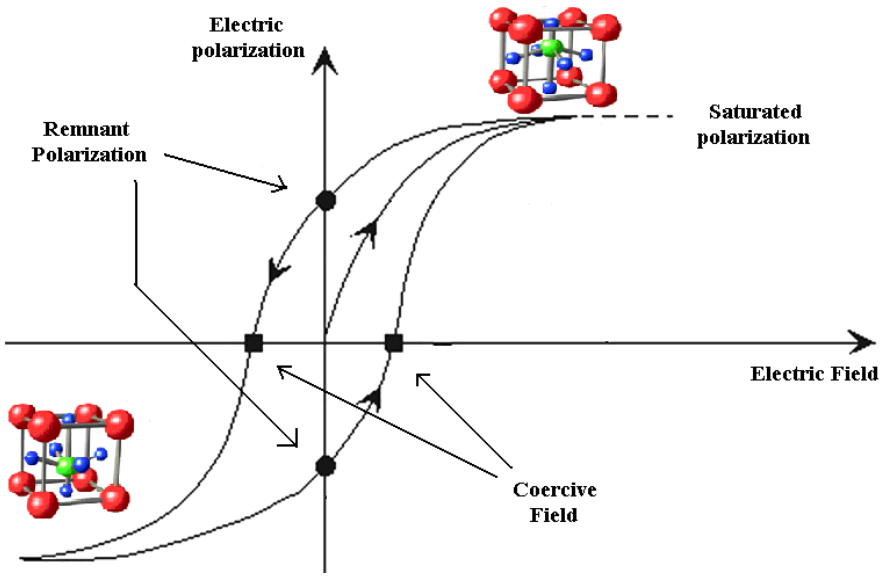

Fig. 1.5 Switching between two equivalent ferroelectric states under applied electric field and resulting polarization hysteresis. Coercive field is the electric field required for bringing the internal polarization to 0.

For both material classes the hysteresis is characterized by the three quantities: remnant polarization (residual magnetization) is the measured polarization (magnetization) in absence of an external electric (magnetic) filed, saturated polarization (magnetization) is the state reached when an increase in applied external electric (magnetic) field can not increase the polarization (magnetization) of the material further, and the coercive filed is defined as

electric (magnetic) field, which is required to reduce the polarization (magnetization) to zero after the polarization (magnetization) of the sample has been driven to saturation.

Of course, the reasons of ferromagnetism and ferroelectricity are quite distinct; ferroelectrics have an asymmetry in charge, whereas ferromagnets have an asymmetry in electronic spin. A ferroelectric material exhibits a spontaneous electrical polarization[1] if a non-centrosymmetric arrangement of the constituent ions and their corresponding electrons occur. Off symmetry is not sufficient for ferroelectricity, the electrical polarization must in addition be switchable and a transition between two stable states of opposite polarization must be accessible. The non-centrosymmetric structure is reached by shifting either the A or B cations (or both) from the center relative to the oxygen anions, and the spontaneous polarization derives largely from the electric dipole moment created by this shift. This property is exploited for non-volatile ferroelectric random accesses memories [32].

Ferromagnetism occurs due to completely different reasons: while a ferroelectric requires off center displacements of the cations, in a ferromagnet the constituent electrons must have a net angular magnetic momentum.

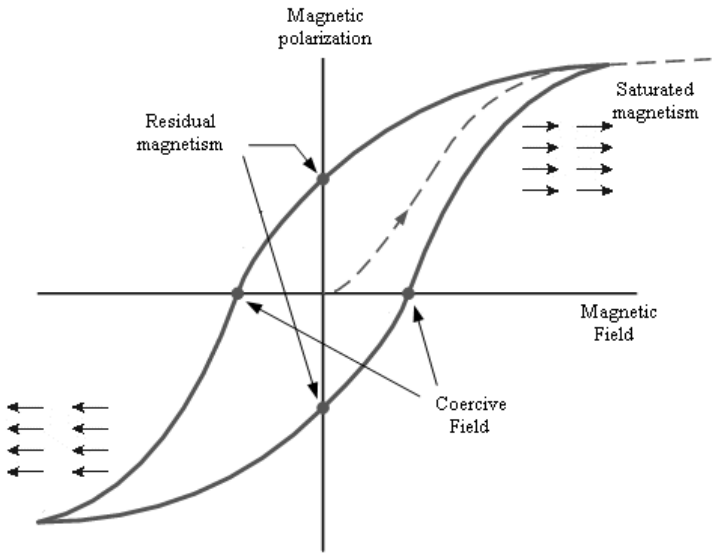

Fig. 1.6 Switching between two equivalent ferromagnetic states under applied magnetic field and resulting polarization hysteresis.

[1] Electric polarization that a ferroelectric possesses in the absence of an external electric field. The maximum value of remnant polarization is a spontaneous polarization, having specific value for the material at the given temperature.

This can arise from either the orbital component of the angular momentum or the spin component (if there are unequal numbers of the up- and down-spin electrons) or both. By applying a magnetic field the random orientated magnetic domains are ordered in the direction of the magnetic field. Potential applications of ferromagnetic films are magnetic memory devices [33].

Both the ferromagnetic and ferroelectric polarization decreases with increasing temperature, with a transition to an unpolarized (paramagnetic or paraelectric) state occurring at Curie temperature. Above Curie temperature for ferromagnets there are equal numbers of up- and down-spin electrons, and hence no magnetic moment. Below Curie temperature the up- and down-spins are unequally populated by electrons, leading to a net magnetic moment. Here the analogy with ferroelectricity can be found, where Curie temperature is coincident with off-centring of the ions, causing the net polarization below Curie temperature.

1.4 Magnetic and electric properties of perovskites and perovskite-like materials

1.4.1 Ferromagnetic – metallic $SrRuO_3$

$SrRuO_3$ is a metallic conductive oxide that crystallizes in an orthorhombic perovskite-type structure with the lattice parameters of a = 5.538 Å, b = 5.573 Å, and c = 7.856 Å at room temperature [34] (Fig. 1.1 b). Because of the small structural distortions (rotations and tilts) in the RuO_6 octahedron, the crystal structure of $SrRuO_3$ can be regarded as a pseudo-cubic structure (Fig. 1.7) with a lattice parameter of a_c = 3.93 Å.

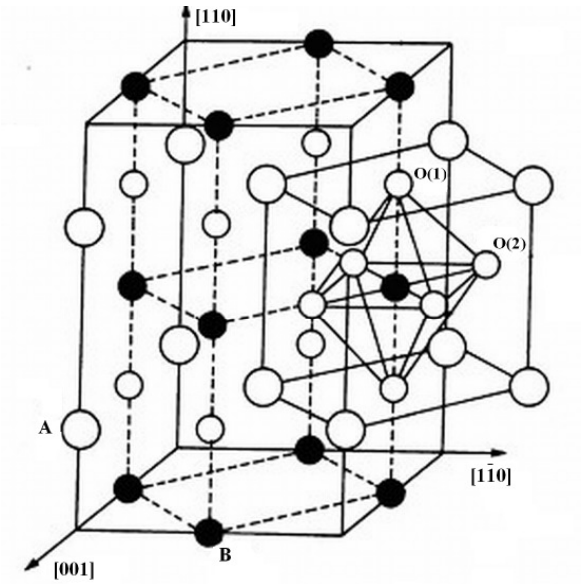

Fig. 1.7 The general view of the orthorhombic elementary cell and selection of pseudo-cubic ABO_3 structure (structure with octahedral inside). Big open circles represent A-site atoms, filled circles represent B-site atoms and small open circles represent oxygen atoms. O(1) stands for the apical oxygens in the BO_6 octahedra along the [110] crystallographic direction and O(2) represents the oxygens in the (110) plane.

Thin films of $SrRuO_3$ have attracted considerable interest due to their low room temperature resistivity of about 280 μΩ·cm (bulk) [35] and a small lattice mismatch with a range of functional oxide materials such as $Bi_{4-x}La_xTi_4O_{12}$ [36], $SrBi_2Ta_2O_9$ [37], $BiFeO_3$ [20], $Pb(Zr_xTi_{1-x})O_3$ [38]. Furthermore, ferroelectric capacitors fabricated from epitaxial $SrRuO_3/Pb(Zr_xTi_{1-x})O_3/SrRuO_3$ heterostructures grown on miscut $SrTiO_3$ substrates have demonstrated significantly improved fatigue[2] behaviours when the oxide/oxide interface has replaced the traditional oxide/platinum interface [39,40,41]. This improvement in fatigue behaviour is partly attributed to improved electrode-ferroelectric interfaces, due to similarities in crystal structure of the electrode and ferroelectric layer. Therefore $SrRuO_3$ is one of the most suitable conductive oxides used as a bottom electrode in a thin film form for a variety of ferroelectric and multiferroic thin film heterostructures.

[2] Decrease of remnant polarization with repeated switching of polarization.

1.4.2 Curie temperature dependence on different effects of $SrRuO_3$

$SrRuO_3$ is the only known ferromagnetic oxide of 4d transition metals with a Curie temperature of about 160 K [42]. In $SrRuO_3$ the interaction between two transition metal (Ru) cations is through the oxygen atom (Ru-O-Ru), where p orbitals of the oxygen hybridize with d orbitals of Ru, leading to p-d orbital hybridization. The magnetic state of $SrRuO_3$ is very fragile and depends critically on the overlapping of Ru 4d and O 2p orbitals, which is the main reason of ferromagnetism in this compound. Since the ferromagnetic interaction in $SrRuO_3$ appear when α is close to 180° (163° [43] for orthorombically distorted $SrRuO_3$), where α stands for Ru-O-Ru bonding angle. Therefore structural changes are known to lead to a shift of the Curie temperature (T_c). There are three main effects resulting in a structural change of $SrRuO_3$; a) substitution of Sr with cations of different atomic radius, b) non-stoichiometry of Ru, c) induced strain in the layers, when mismatched substrates are used. In all these cases the change of Curie temperature can be explained by the structural changes in the films involving Ru-O-Ru bonding angle in RuO_6 octahedron.

Concerning (a) case Jin et al. [43] published the structural differences in three ruthenium oxides ($ARuO_3$, A = Ca^{2+}, Sr^{2+}, Ba^{2+}). The ferromagnetic properties in these oxides are different mainly due to the different Ru-O-Ru bending angles and origin of the A-site cation. Replacement of Sr^{2+} with Ba^{2+} leads to lower T_c (60 K), however as $BaRuO_3$ is a cubic perovskite the maximal interaction between neighbouring Ru^{4+} ions appear and it should lead to higher T_c as for $SrRuO_3$ (Table 1.1). In the case of $CaRuO_3$ the highest structural distortions occur, therefore the interaction between neighbouring Ru ions is suppressed and $CaRuO_3$ is paramagnetic. The changes in the Curie temperature depend not only on the structural changes in $ARuO_3$ crystal structure, but also on the ionic nature of the cation substituted in A-site, therefore such big differences in the ferromagnetic properties in $CaRuO_3$, $SrRuO_3$, $BaRuO_3$ appear.

Table 1.1 Structural and ferromagnetic differences of $ARuO_3$ perovskites.

	Ionic radius $<r_A>$, Å	Ru-O-Ru angle, °	Structure	Curie temperature, K
$CaRuO_3$	Ca^{2+} = 1.34	148.6	orthorhombic	paramagnetic
$SrRuO_3$	Sr^{2+} = 1.44	163.1	orthorhombic	ferromagnetic (160)
$BaRuO_3$	Ba^{2+} = 1.61	180	cubic	ferromagnetic (60)

(b) Ru deficiency: Dabrowski et al. [44] showed that at certain preparation conditions Ru deficient compounds $SrRu_{1-\upsilon}O_3$ can be formed with randomly distributed vacancies at Ru sites. The bond angle between the Ru ions connected via apical oxygen increases with the increase of Ru vacancies leading to the increase of lattice volume (Table 1.2) and decrease of Curie temperature. Similar results are expected if oxygen vacancies are present in the structure.

Table 1.2 Structural and magnetic properties of $SrRu_{1-\upsilon}O_3$ compounds [45].

Ru deficiency, υ	Lattice volume, V [Å^3]	Ru–O $_{apical}$-Ru angle, °	Curie Temperature, T_c [K]
0	240.85	162.94	163
0.02	241.05	163.49	135
0.09	241.53	164.60	82

(c) Thin films epitaxially grown on the mismatched substrates, thinner than the critical film thickness will be strained to match the lattice of the substrate. However, when the film thickness exceeds the critical thickness value, the layer relaxes by introducing misfit dislocations [46]. With the relaxation of the structure, an increase of the electrical resistivity (Fig. 1.8. b) and a shift of the Curie temperature from 160 K for a strain-free to 150 K for a compressively strained $SrRuO_3$ film grown on $SrTiO_3$ by off-axis sputtering was noticed [7] (Fig. 1.8 a and b).

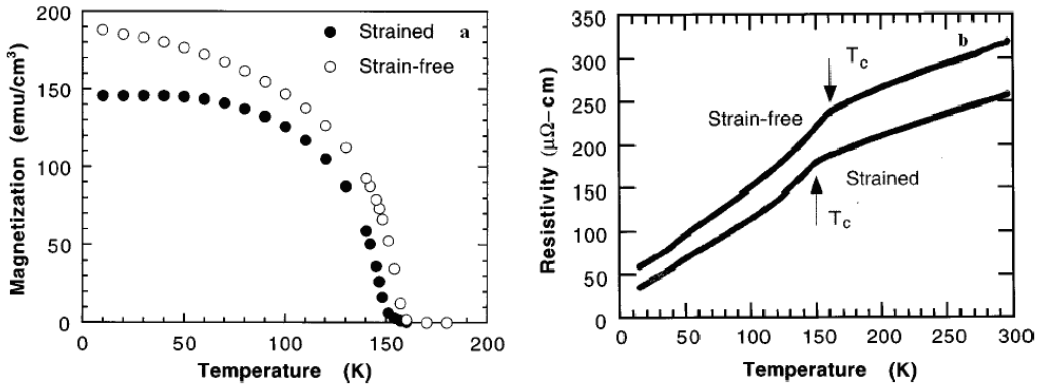

Fig. 1.8 a) Magnetization, **b)** and resistivity dependence on temperature of strained and strain-free $SrRuO_3$ films [7].

Terai et al. [47] also noticed a change of the Curie temperature in the 160 K to 164 K range for $SrRuO_3$ films grown by PLD on $SrTiO_3$ substrates, where films under tensile strain exhibited higher Curie temperature than compressively strained or relaxed films. The tensile

strain was changed by modifying the composition of the $Ba_{1-x}Sr_xTiO_3/BaTiO_3$ buffer layer, deposited on $SrTiO_3$.

1.4.3 Electrical resistivity of thin $SrRuO_3$ films

The Ru amount in the layers is directly related to the Ru supply and to the oxygen pressure during the deposition process [48]. In particular, it turns out that Ru off-stoichiometry can be varied in $SrRuO_3$ thin films by using different deposition techniques (PLD, MBE). It seems that until know no reports about Ru deficient films deposited by chemical vapour deposition technique were published. The deficiency of ruthenium, as well as deficiency of oxygen changes the electrical properties of the $SrRuO_3$. In both cases the Ru and oxygen vacancies increase the volume of the crystal lattice and alter the average Ru-O-Ru bond angle. Thus, electron correlation in $SrRuO_3$ can be reduced or even completely suppressed [49]. Semiconductor behaviour with higher resistivity compared with stoichiometric $SrRuO_3$ occur when the oxygen pressure during the deposition process is reduced below a certain limit [50] (Fig. 1.9) resulting in oxygen vacancies, whereas high oxygen pressures leads to Ru deficiency due to probable Ru removal in form of volatile RuO_4 [51].

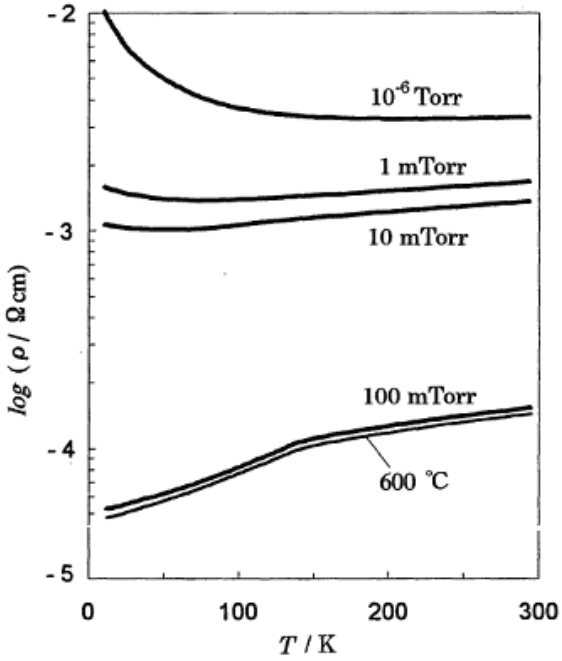

Fig. 1.9 Resistivity-temperature dependence on oxygen pressure of $SrRuO_3$ thin films grown by PLD on $SrTiO_3$ substrates at 640 °C. The kink in the curve is coincident with ferromagnetic transition [50].

The electronic and magnetic properties of oxides are very sensitive also to film thickness [52] and the structure of the interface [53] between the layer and substrate. In thin films, higher resistivity in conducting oxides is commonly found when the film thickness is decreased from 320 nm to 8 nm, influenced by the interface with the substrates, resulting in different morphology of the films [54,55]. According to Toyota et al. [56] the critical film thickness at which metal-insulator transition occurs is 4–6 monolayers (ML), where resistivity decreases with the film thickness (Fig. 1.10).

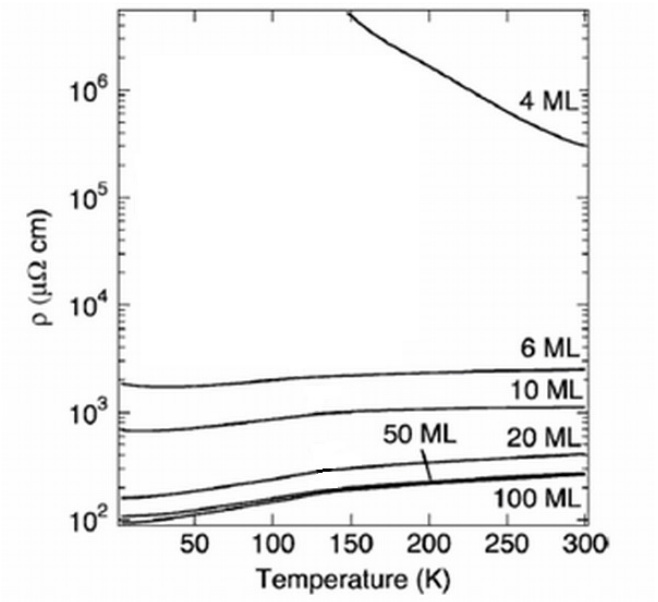

Fig. 1.10 Temperature dependence of resistivity for ultrathin $SrRuO_3$ films with various nominal film thicknesses [56].

This behaviour can be affected by the microstructural disorder caused by the 3D island formation at the initial growth stage of ultrathin $SrRuO_3$ films. Electrical resistivity decreases with the increase of the smooth area of the 3D islands and finally saturates when the atomically flat surface appear at 50 ML thickness (Fig. 1.11).

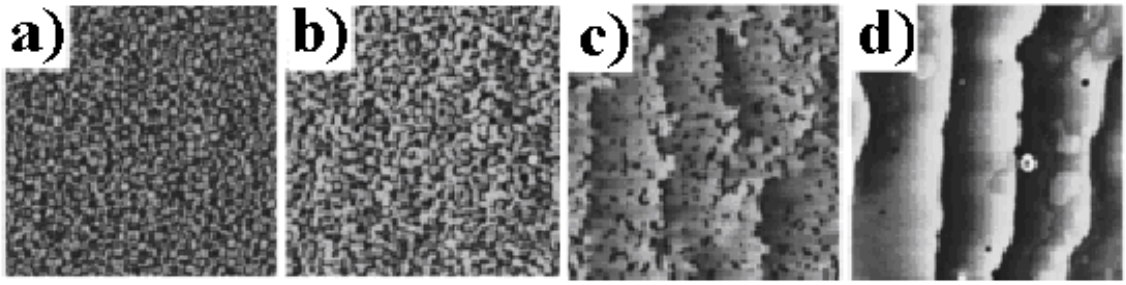

Fig. 1.11 AFM images (scan area 2×2 μm^2) of ultrathin $SrRuO_3$ films with nominal film thicknesses of a) 6 b) 10; c) 20; d) 50 ML [56].

Higher resistivities were observed for the ultrathin $SrRuO_3$ films (5 nm) compared with the thicker films (100 nm) grown on different oxide substrates by PLD method, where the mismatch between the substrate and film results in different surface microstructure of the layers [57]. The morphology of films on $LaAlO_3$, LSAT and $BaTiO_3$ substrates indicated that the large lattice parameter mismatch promoted 3D island growth, whereas $SrRuO_3$ grow under step-flow-mode on substrates with similar lattice constants ($SrTiO_3$, $DyScO_3$). As a result, semiconductor behaviour from 2 to 380 K was observed for 5 nm $SrRuO_3$ films on $LaAlO_3$, $BaTiO_3$ and LSAT, while thicker (10 – 20 nm) films had metallic behaviour like 5 nm films on $GdScO_3$, $DyScO_3$ and $SrTiO_3$ substrates (Fig. 1.12). These results show that lattice mismatch between the substrate and the film, the resulting morphology of the film and also thickness of the layers have a large impact on the resistivity values and electrical behaviour of $SrRuO_3$ films.

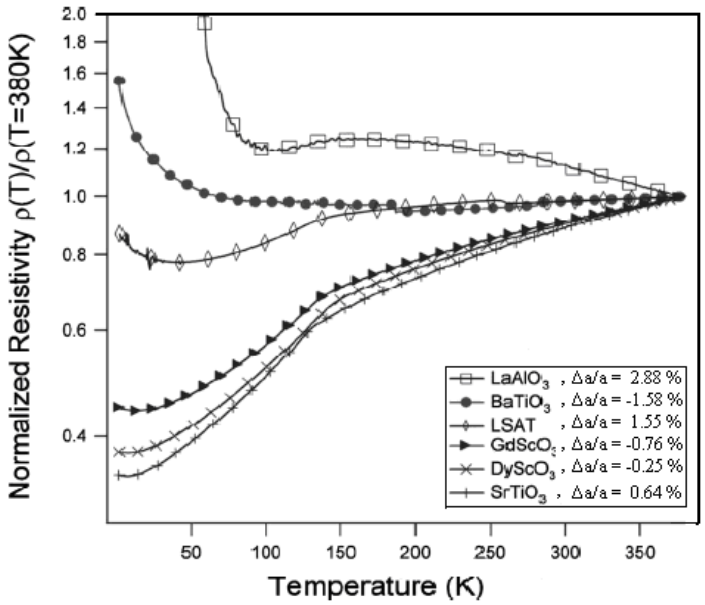

Fig. 1.12 Normalized resistivity versus temperature for 5 nm thick $SrRuO_3$ films with 5 % FeO_x impurity on various substrates [57].

1.4.4 Ferroelectric - dielectric $Bi_4Ti_3O_{12}$

Bismuth titanate $Bi_4Ti_3O_{12}$ is a member of the Aurivillius family of layered perovskites, which consist of three perovskite-like units $(Bi_2Ti_3O_{10})^{2-}$, sandwiched between bismuth oxide $(Bi_2O_2)^{2+}$ layers along the c-axis with a lattice parameters of a = 5.450 Å, b = 5.406 Å, c = 32.832 Å [58]. Bismuth titanate is a lead-free material and one of the promising

candidates for the non-volatile ferroelectric memories due to its large spontaneous polarization along the *a* axis, and the high Curie temperature (980 K) which makes it useful over a wide range of temperature.

For application in a NvFRAM (non-volatile ferroelectric random access memory) device, ferroelectric materials should have a low coercive field[3], a high remnant polarization, a poor fatigue, and a low leakage current[4]. However, pure $Bi_4Ti_3O_{12}$ in the form of ceramic or film unfortunately suffers from serious degradation problems such as large leakage current and low remnant polarization. To solve these problems, the proper element substitutions in $Bi_4Ti_3O_{12}$, such as Sm^{3+} [59], La^{3+} [60] and Nd^{3+} [61] in A-site position and Zr^{4+} [62], V^{5+} [63], Ta^{5+} [64], Nb^{5+} [65], W^{6+} [66] in B-site position were applied in the last decade, which helps to improve the ferroelectric properties necessary for memory applications.

The selective cation substitution, also known as site engineering technique [67], is an effective method for improving the ferroelectric properties of $Bi_4Ti_3O_{12}$. Substitution at Bi-site shows an increase in spontaneous polarization and fatigue free behaviour [13]. The large ferroelectricity as well as low leakage current can be explained by the enhanced rotation of the TiO_6 octahedron in the *a*-*b* plane accompanied with a shift of the octahedron along the *a*-axis by the cation substitution at Bi-site in the pseudo-perovskite layer [68]. As is generally known, the oxygen vacancies alter the fatigue property in ferroelectrics. The vacancies in the $Bi_4Ti_3O_{12}$ normally are formed at high processing temperatures, where volatile Bi is removed from the perovskite component, proceeding Bi vacancies [69]. The formation of Bi vacancies ($V_{Bi}^{'''}$) is accompanied by oxygen vacancy ($V_O^{\cdot\cdot}$) adjacent to the Bi due to fragility of Bi-O bonds. This reaction of vacancy formation (Eq. 1.4) has been reported to occur above 1000 °C in air [70].

$$2Bi_{Bi}^{*} + 3O_O^{*} \rightarrow 2V_{Bi}^{'''} + 3V_O^{\cdot\cdot} + 2Bi_{(g)} + 3/2O_{2(g)} \qquad \text{Eq. 1.4}$$

The substitution with isovalent cation on A-site can improve the ferroelectric properties of $Bi_4Ti_3O_{12}$, because oxygen is stabilized in perovskite due to isotropic chemical bonding Bi/Ln-O through less volatile Ln cations [71].

The substitution at Ti-site with higher valency (larger) cations helps to reduce the amount of oxygen vacancies, by compensating charge difference to keep charge neutrality

[3] The electric field needed for switching between two equivalent polarization states.
[4] A gradual loss of electrical current from the charged capacitor.

[72] in the structure. The occurring additional distortion in the lattice suppresses the movement of still present oxygen vacancies therefore remnant polarization increases [73].

Raman spectroscopy is sensitive to the coordination of local sites caused by the distortions of BO_6 octahedron or the atomic substitution because its spectrum is originated from the lattice vibrational modes depending on the atomic masses of constituent atoms. Therefore atomic substitution can be monitored through the variations in frequency and intensity of Raman active modes. Higher frequencies of characteristic Raman modes are obtained if $Bi_4Ti_3O_{12}$ is substituted with lighter and smaller cations [74].

The ferroelectric-to-paraelectric transition in the case of substituted $Bi_4Ti_3O_{12}$ changes with the composition variation. By the increase of the cation amount the energy required for this transition is reduced and therefore the Curie temperature decreases with the increase of the amount of cation (Fig. 1.13). Indeed, the Curie temperature is proportional to the structural distortions of the material substituted by La^{3+}, Nd^{3+} for Bi^{3+} leading to the enhanced rotation of TiO_6 octahedral in the *a-b* plane accompanied with a shift of the octahedron in a-axis responsible for a reduced Curie temperature [61].

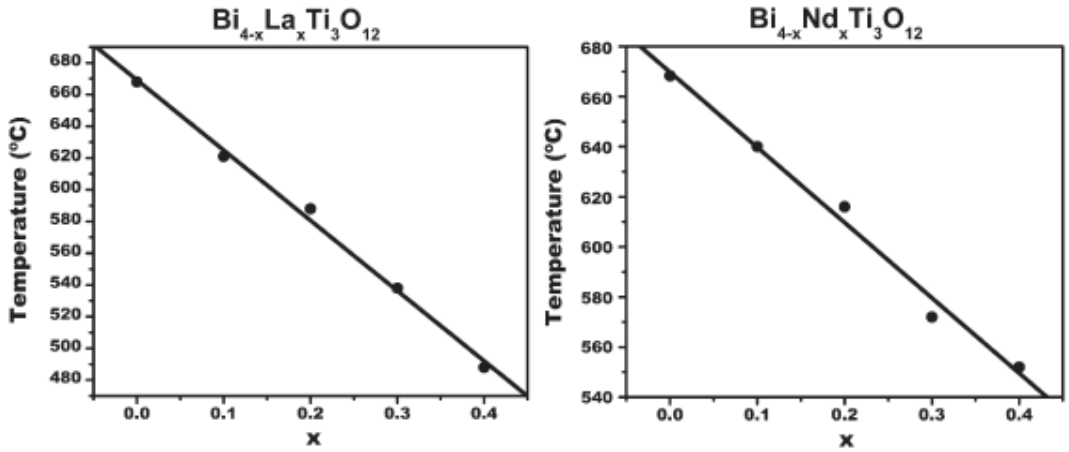

Fig. 1.13 Curie temperature dependence on composition variation in A-site substituted $Bi_4Ti_3O_{12}$ compounds [61].

2. Experimental techniques

In this chapter the main principles of the deposition method applied for the growth of the perovskite ($SrRuO_3$) and layered-perovskite ($Bi_4Ti_3O_{12}$, $(Na, Bi)_4Ti_3O_{12}$) films will be described. Furthermore, all characterisation techniques employed to characterize the surface of oxide substrates, the oxide layers as well as the metal-organic precursors will be introduced.

2.1. Vertical liquid-delivery metal-organic chemical vapour deposition technique

2.1.1 Principle of the method

Metal-organic chemical vapour deposition is an attractive deposition technique for the growth of thin epitaxial thin films since it has some advantages compared to techniques, like PLD, MBE or sputtering. This method provides uniform deposition over large areas, good conformal step coverage, easy and reproducible control of stoichiometry of deposited films, and direct growth of epitaxial films without any post-annealing [75,76,77,78]. However, the most crucial requirement for MOCVD deposition technique is to find high-purity precursors which should have sufficient volatility for evaporation at moderate temperatures. The difficulties of transporting low volatility metal precursors in MOCVD for obtaining oxide films required a further development in MOCVD. Therefore, LD-MOCVD was developed, where metal-organic precursors are used for the depositions of oxide layers. The precursors are dissolved in liquid solvent and delivered through the stainless steel lines first to the flash evaporator and then to the reaction zone. With the help of LD-MOCVD the problems of insufficient thermal stability of solid precursors to withstand heating for long periods, leading to decomposition of the precursor, poor film uniformity, irreproducible process conditions and reactor blockages were solved.

Description of different classes of precursors, as well as their chemical and physical properties will be described and summarized in Section 3.2.

To avoid any reactions of the precursor with moisture, the precursor is first dissolved in a suitable organic solvent under inert atmosphere in a glove box. The liquid source containing the precursor is then transferred from the glove box and is connected with the liquid transfer system of the MOCVD reactor.

During deposition micro-amounts of the precursor solution are pumped by micro-pumps into a flash evaporator held at moderate temperatures, depending on the evaporation temperature of the used precursor solution. In the evaporator the solution is immediately evaporated. The vapour is transferred through the heated pipes and valves with the help of the carrier gas up to the substrate where the deposition reaction takes place. The occurring reaction is heterogeneous because a change of state is involved, from gaseous (precursor vapour) to solid (thin film). The evaporator temperature is chosen to be below the temperature at which the thermal cracking of precursor molecules can occur but above the temperature at which condensation of the precursor will occur. To prevent condensation of the precursor additional heating of the pathway from evaporator and to the deposition zone has to be used. Usually the lines are kept at the same temperature of the evaporator.

A more detailed picture of the basic physicochemical steps in the reactions happening in MOCVD system is illustrated in Figure 2.1, which indicates several key steps [79]:

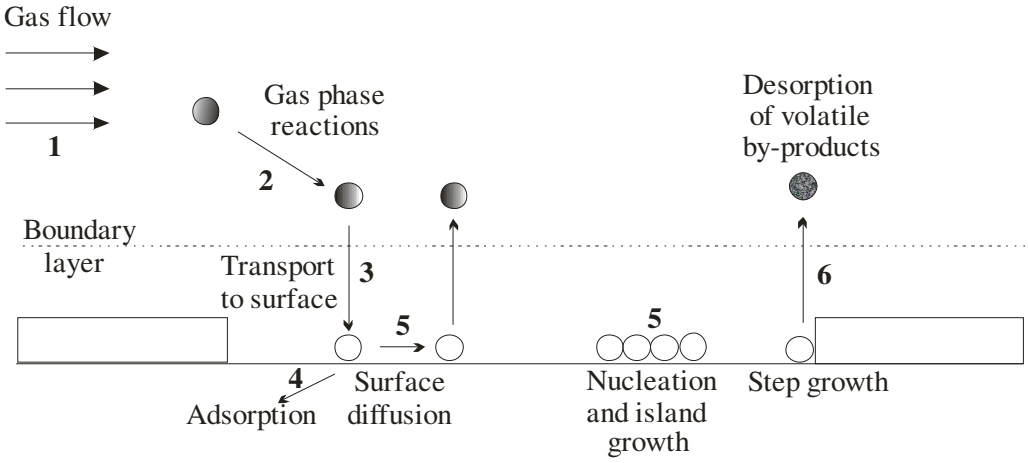

Fig. 2.1 Schematic representation of the transport and reaction processes in MOCVD.

1. Evaporation and transport of reagents with help of carrier gas into the reactor;

2. Gas phase reactions of the precursors in the reaction zone to produce reactive intermediates and gaseous by-products;

3. Diffusion of the reactants to the substrate surface via boundary layer;

4. Adsorption of the reactants on the substrate surface;

5. Surface diffusion to the growth sites, nucleation and surface chemical reactions leading to film formation;

6. Desorption and mass transport of remaining fragments of the deposition away from the reaction zone.

The properties of the deposited oxide film depend on the selected precursor material, deposition temperature, and deposition pressure and on partial pressure of precursor, reactive and carrier gas. The deposition temperatures for oxide materials with MOCVD vary in 400 - 850 ºC temperature range [77]. The precursors usually contain oxygen but to deposit high-purity films an additional source of oxygen is required. For this oxygen or oxygen-containing gases have to be used. Indeed, high amount of oxidant species can be important for the reduction of C level in the deposited film coming from the precursor solution, but it can also drastically affect the properties of the films. Oxide films with MOCVD technique normally are deposited under reduced pressure ranging from a few tens to a few hundreds mbar.

In MOCVD the growth rate is determined by several parameters. The most important ones are concentration and composition of the gas-phase, temperature of the substrate, and the operating pressure of the reactor. The general dependence of CVD growth rate on substrate temperature is shown in Fig. 2.2, where logarithm of the growth rate versus inverse of deposition temperature is plotted.

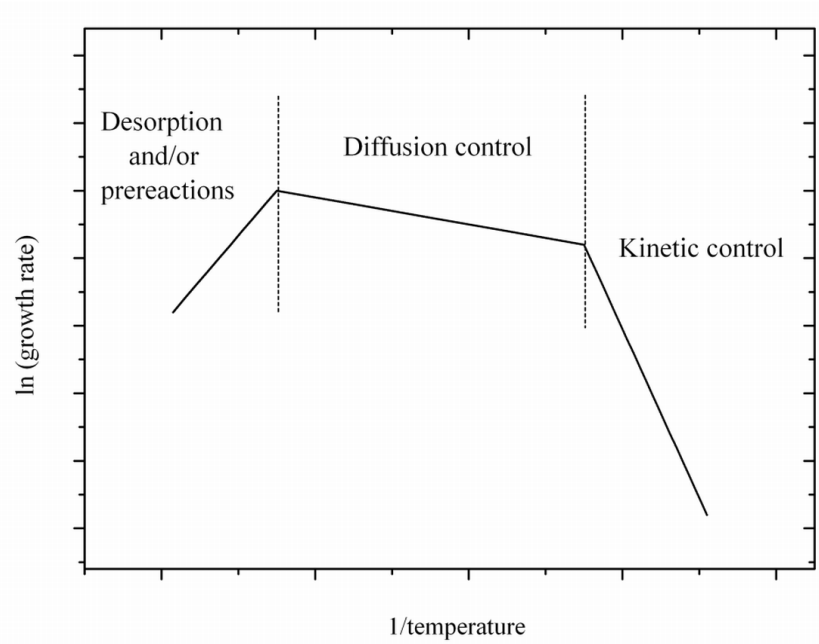

Fig. 2.2 Plot of MOCVD growth rate as a function of 1/growth temperature.

Three different regions appear in this plot. The rate limiting step during the film growth is generally determined by either the surface reaction kinetics or by the mass transport. At lower growth temperatures the growth rate is controlled by kinetics of chemical reactions occurring either in the gas-phase or on the substrate surface. This region is generally defined as kinetically-limited. The film growth rate increases exponentially with substrate temperature according to the Arrhenius equation:

$$\text{Growth rate} \sim \exp(E_A/RT) \qquad \text{Eq. 2.1}$$

where E_A is the apparent activation energy, R is the gas constant and T is the temperature. As the film growth rate is controlled by kinetics, uniform film thickness can be achieved by minimizing temperature variations over the substrate surface.

As the temperature increases, the growth rate becomes nearly independent of temperature and is controlled by mass transport of reagents through the boundary layer to the growth surface and back-diffusion through this layer of the gaseous by-products. This region is called mass transport or diffusion-controlled growth region.

At even higher deposition temperatures the growth rate tends to decrease, due to increased rate of desorption of film precursors or desorption of the molecules or other by-products from the growth surface.

To summarize, the surface kinetics is the limiting step at lower temperature and diffusion is the rate limiting factor at higher deposition temperatures. As it was mentioned before it is possible to switch from one rate-limiting step to the other by changing the temperature regime.

Another crucial factor for the growth rate of the film is the pressure of the MOCVD reactor. From atmospheric pressure (1013 mbar) to intermediate pressures (e.g. 13 mbar) gas phase reactions are important and, in addition, a significant boundary layer is present on the substrate surfaces. As the pressure falls gas phase reactions tend to become less important, and particularly at pressures below 1.3 mbar layer growth is controlled by surface reactions.

The boundary layer thickness can additionally be controlled by the rotation of the substrate carrier. Higher rotations reduce the thickness of the boundary layer, whereas slow rotation increases the thickness of the boundary layer and can cause thickness inhomogeneities in the layers.

2.1.2 Experimental setup

Liquid-delivery MOCVD refers to a special MOCVD technique where solid precursors, with very low vapour pressures are solved in the solvent and solution is transferred to the system in order to get a thin film of the required composition. In Fig. 2.3 the real view of key components of the MOCVD deposition system used in this work is shown.

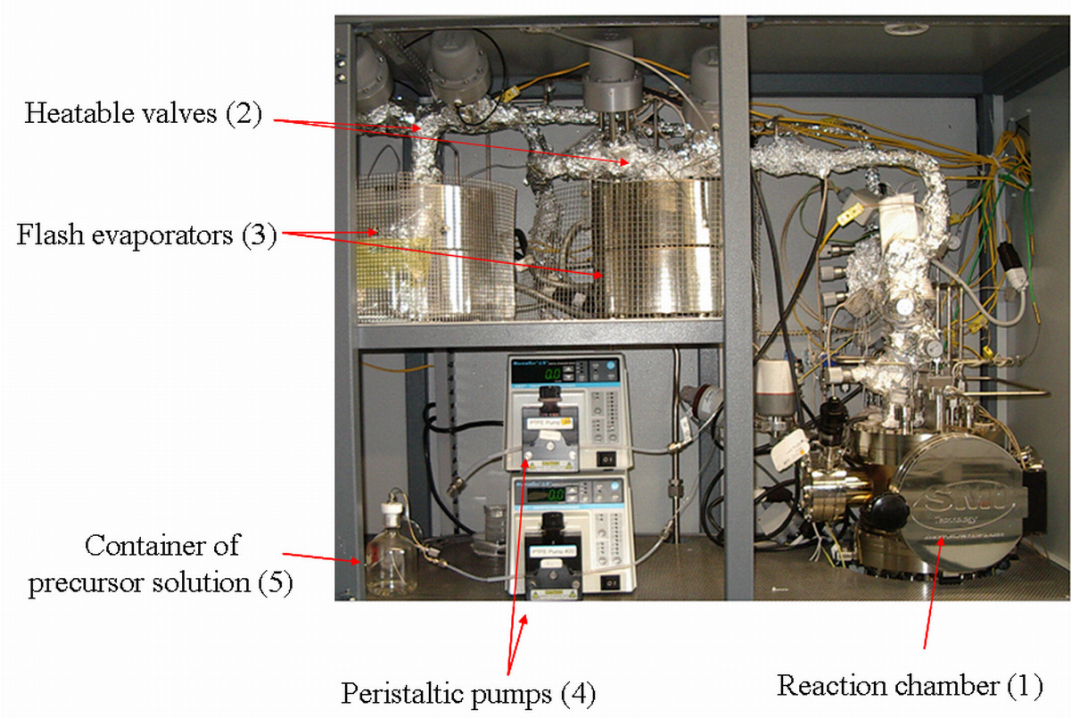

Fig. 2.3 MOCVD reactor used for the deposition of oxide layers during this thesis.

Small quantities of the precursor solution/solutions are transferred with the help of peristaltic pumps into the hot flash evaporator/s, where the precursor solution is evaporated simultaneously. A large temperature gradient is created in this step of the process to avoid reactor blockages due to the polymerization or decomposition of the precursors in the near hot zone region. The approximate temperature of the flash evaporator can be set according to the chemical and physical properties of the used precursor (see Section 3.2). More than one flash evaporator was used to avoid any interaction between vapours of different precursors or to combine different evaporation temperatures of metal-organic compounds. Argon was used as carrier gas to deliver the precursor vapours through the heatable valves to the reaction zone. Oxygen ambient was used as reactive gas and was delivered directly to the reaction chamber. The main/general deposition parameters are listed in Table 2.1.

In order to get intermixing of the gases and to influence the boundary layer above the substrates, the substrate carrier was rotated at 300 - 1250 rpm. Aditionally, the substrates were glued with silver paste to improve the heat contact.

Table 2.1 Typical deposition parameters for deposition of oxide layers in the present work.

Deposition temperature, °C	600 - 750
Temperature of flash evaporator, °C	230 - 240
Deposition pressure, mbar	26
Oxygen gas flow, sccm	1500 - 5000
Argon gas flow, sccm	1500 - 5000
Carrier rotation, rpm	300 - 1250
Precursor solution supply, ml/min	0.4 – 0.65

2.2 High resolution X-ray diffraction

X-ray diffraction is a non destructive technique that provides detailed information about the strain, film composition and layer thicknesses [15]. A crystal lattice is a periodic three-dimensional distribution of atoms in space. They are arranged such that they form a periodic array of parallel net-planes with an interplanar spacing d. These spacings depend on the Miller indices (hkl) and the lattice parameter of the material (Fig. 2.4). The incident x-rays can be reflected by each net-plane. Constructive interference of the waves reflected from these periodic arranged planes is described by Bragg's law which is given by:

$$\sin\theta_B = \frac{\lambda}{2d_{hkl}} \qquad \text{Eq. 2.2}$$

where θ_B is the glancing angle of the x-ray beam to the net-plane, λ is the x-ray wavelength and d_{hkl} is the net-plane spacing.

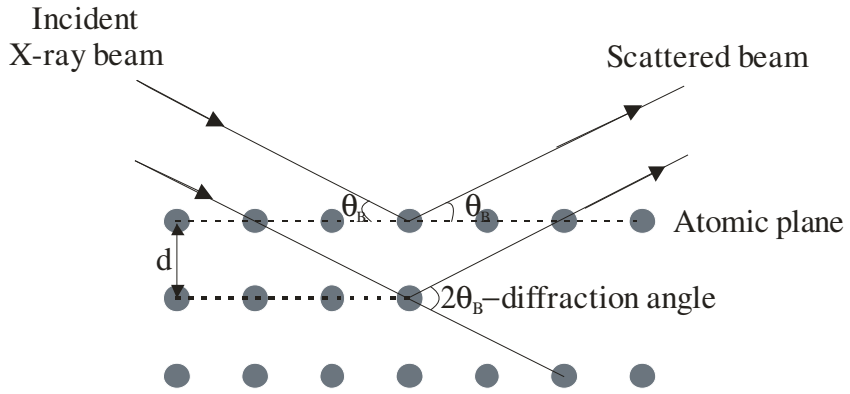

Fig. 2.4 Illustration of Brag reflection.

The used high resolution X-ray diffraction such properties as: a) good collimation of incident beam ($\Delta\theta \approx 11$ arc sec (or 0.0036 °)), b) incident beam is monochromatic ($\lambda = 1.5405$ Å) Cu $K\alpha_1$. Both, collimation and monochromatozation, can be achieved by using 4-bounce Ge 220 Bartels-Monochromator [80].

In epitaxial layers the crystal lattice of underlying single-crystal substrate is like a template for the deposited thin film which repeats the crystal structure of the substrate until the critical thickness after which relaxations occurs. When the films are grown under the critical film thickness it is said that they are pseudomorphic (the lattice of the film is adapted to the substrate), as was already illustrated in Fig. 1.2 (drown by broken lines). For the pseudomorphic growth the total vertical strain is described as follows:

$$\varepsilon_{\perp} = \left(\frac{\Delta d}{d}\right)_{\perp} = \frac{1}{p}\cdot\frac{\Delta a}{a} = -\frac{\Delta\theta}{\tan\theta_B} \qquad \text{Eq. 2.3}$$

where $\varepsilon_{\perp}$ is total vertical strain, d is net-plane spacing, a is the in-plane lattice parameter, Δa is the difference between the in-plane lattice parameter of the film and the substrate, and p is a factor dependent on elastic constants. θ_B is the Bragg angle of the substrate and $\Delta\theta$ is the difference between the Bragg angles of the film and the substrate. The total vertical strain $\varepsilon_{\perp}$ can, thus, be calculated from the measured HRXRD pattern from the difference between the teoretical and experimental position of the film Bragg peak. $\Delta a/a$ is the (in-plane) lattice mismatch between the film and the substrate. The in-plane total strain in pseudomorphic growth is equal to zero.

In the case of compressive strain, in-plane lattice parameter of the film is larger than of the substrate, therefore to mach the lattice of the substrate the unit cell of the film lattice has to be compressed. This compression leads to reduced in-plane lattice parameter and to

increased out-of-plane lattice parameter of the film. Therefore the shift of the film peak to lower 2θ values compared to the bulk position (dashed line in Fig. 2.5 a) occur. For the films grown under tensile strain the opposite effect is noticed, higher 2θ values of the film compared with the bulk position and extended unit cell of the film to mach the lattice of the substrate.

If film surface and interface to the substrate are smooth, constructive and destructive superposition of the x-rays scattered at the front and the back side of the film leads to thickness oscillations (see Fig. 2.5b). The thickness of the well ordered epitaxial films can be determined from these thickness fringes.

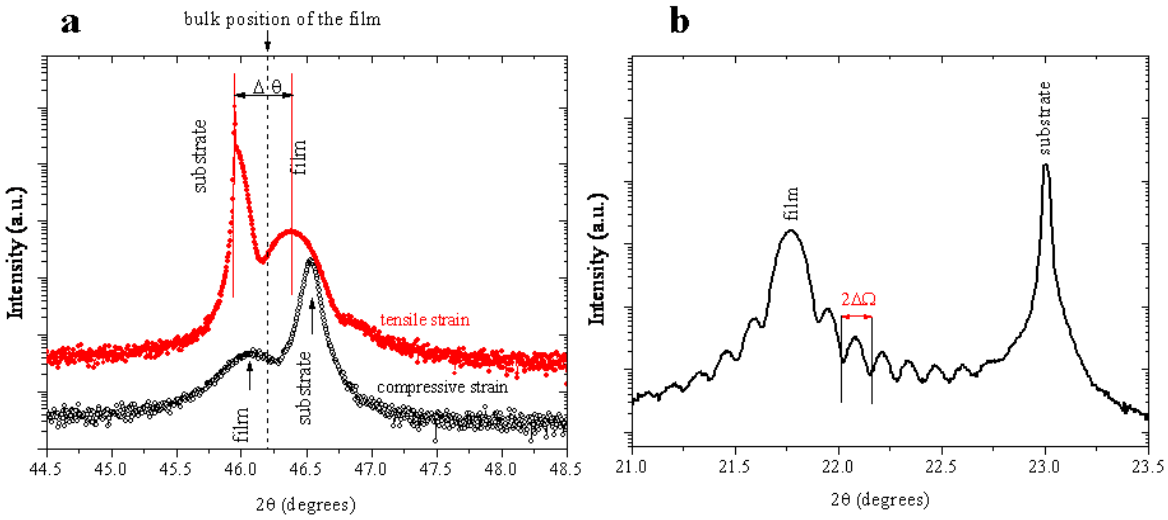

Fig. 2.5 a) Illustration of the Bragg reflections position in the case of compressive and tensile strain, **b)** illustration of the thickness oscillations.

They are equidistantly located at both sides of the Bragg peak of the film. From the difference ΔΩ between adjacent minima, the thickness of the film can be calculated by:

$$t = \frac{\lambda}{2\cos(\Delta\Omega)} \qquad \text{Eq. 2.4}$$

where t is the film thickness.

2.3 Auger electron spectroscopy

Auger Electron spectroscopy (AES) was used to study the termination of the topmost layer of $SrTiO_3$(001), $NdGaO_3$(110), $DyScO_3$(110) substrates, prepared in different ways.

2.3.1 Principle of the method

Auger electron spectroscopy is a surface analytical technique which allows the determination of the chemical composition of the surface and near surface regions (0.5 nm - 2 nm) in solid materials. The Auger process is initiated by creation of a core hole - this is typically carried out by exposing the sample to a beam of high energy electrons, typically having a primary energy in the range 2 - 10 keV [81].

The basic Auger process starts with removal of an inner shell atomic electron to form a core hole by the incident electron beam. These electrons with sufficient primary energy (E_o) remove an electron from a the core level, such as the K level. The produced vacancy is immediately filled by another electron from L_1 (see Fig. 2.6).

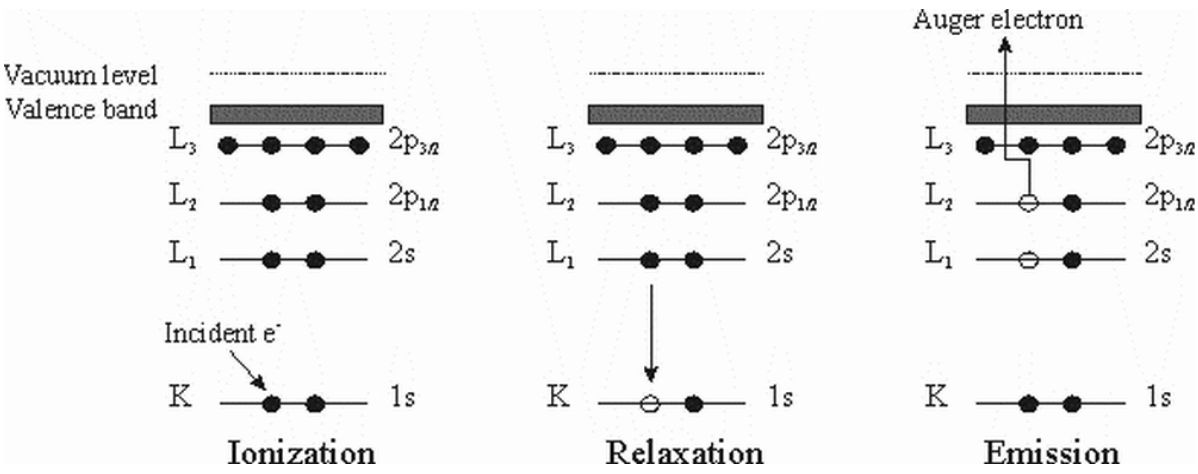

Fig. 2.6 Schematic representation of the Auger process in three steps. The KL_1L_2 Auger transition is illustrated. The open circles symbolize absence of electrons.

The energy (E_K-E_{L1}) released from this transition can be transferred to another electron, as in the L_2 or L_3 level. There the excess of energy is simultaneously released as the emission

of x-ray photons (radiative process - EDX method) or an Auger electron (nonradiative process). The Auger electron will have energy equal to:

$$E = E_K - (E_{L1} + E_{L2,3}) \qquad \text{Eq. 2.5}$$

This excitation process is denoted as a KL_1L_2 Auger transition. It is obvious that at least two energy states and three electrons must take part in an Auger process. Therefore, H and He atoms cannot give rise to Auger electrons. Several transitions (KL_1L_1, KL_1L_2, LM_1M_2, etc.) can occur with various transition probabilities. For low atomic number elements, the most probable transitions occur when a K-level electron is ejected by the primary beam, L-level electron drops into the vacancy, and another L-level electron is ejected. Higher atomic number elements have LMM and MNN transitions that are more probable than KLL.

The kinetic energy of the Auger electron, specific and characteristic to the atom from which it originated, is measured and the quantity of Auger electrons is proportional to the concentration of the atoms on the surface or surface near region independently of the incident beam energy. Each element in a sample being studied give rise to a characteristic spectrum of peaks at various kinetic energies.

Instead of an incident electron beam also a collimated proton beam under grazing incidence conditions can be used to remove electrons from inner shells (p-AES). Due to the small angle between the proton beam and the surface and the larger size of protons compared to electrons the interaction is restricted exclusively to the surface atoms.

2.3.2 Experimental setup for AES experiments

The AES measurements were performed at room temperature in an ultrahigh vacuum (UHV) chamber attached via two differential pumping stages to the beam line of an electrostatic ion accelerator with energies up to 350 kV for p-AES. The collimated proton beam (angular divergence ±0.02°) was incident upon the crystal at a grazing angle of incidence (measured with respect to the surface plane) of $\Phi_{in} \approx 1°$ (for $NdGaO_3$ substrates) and 1.5° (for $DyScO_3$ substrates) with target currents of about 450 nA. The AES measurements were performed at constant pass energy of 80 eV with an energy resolution of 3 eV (FWHM of the peak of elastic scattered electrons). Under these conditions, inner shell holes in target atoms are excited only in the topmost layer and contribute to the proton-induced AES (p-AES) spectra. The elemental composition of the near-surface layers was

additionally investigated with electron-induced AES using an electron gun with a primary electron energy of 3 keV.

2.4 X-ray photoelectron spectroscopy

X-ray photoelectron spectroscopy (XPS) is an electron spectroscopic method that uses x-rays to eject electrons from inner shell orbitals [82] (Fig. 2.7).

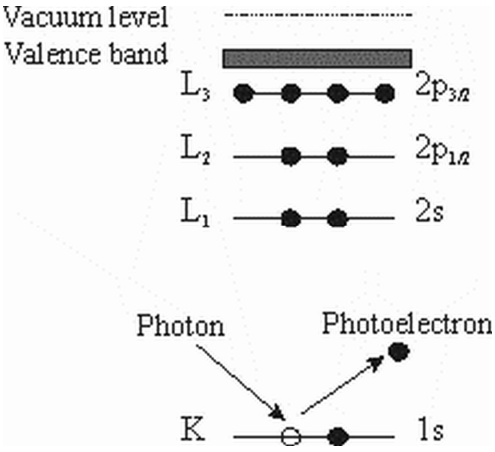

Fig. 2.7 Schematic representation of the XPS process.

The kinetic energy (E_k), of these photoelectrons is determined by the energy of the x-ray radiation ($h\nu$), and the electron binding energy (E_b) as given by:

$$E_k = h\nu - E_b \qquad \text{Eq. 2.6}$$

A XPS spectrum is a plot of the number of detected electrons versus the binding energy of the detected electrons. Each element produces a characteristic set of XPS peaks at characteristic binding energy values that directly identify each element that exist in the material being analyzed. These characteristic peaks correspond to the electron configuration of the electrons within the atoms, e.g., 1s, 2s, 2p, 3s, etc. The number of detected electrons in each of the characteristic peaks is directly related to the amount of element within the area (volume) irradiated. To generate atomic percentage values, each raw XPS signal must be corrected by dividing its signal intensity (number of electrons detected) by a "atomic sensitivity factor" (ASF) and normalized over all of the elements detected.

With XPS only occupied core levels can be investigated. The photo-emitted electrons that have escaped into the vacuum of the instrument are those that originated from a surface

region of about 2 to 4 nm thickness. XPS is used to identify the elements and the quantity of those elements that are present in the sample and the binding energy (BE) of one or more electronic states of the existing elements.

In this study a Mg Kα (1253.5 eV) was used as x-rays source to analyze the energy of the detected electrons which leaved the analyzed layers. Energetic resolution was in the range of 0.8 eV.

2.5 Atomic force microscopy

Contact mode atomic force microscopy (AFM) is one of the widely used scanning probe modes, and operates by linear scanning a sharp tip across the sample. A sharp tip usually about 2 μm long is located at the free end of the cantilever 100 - 200 μm long (Fig. 2.8).

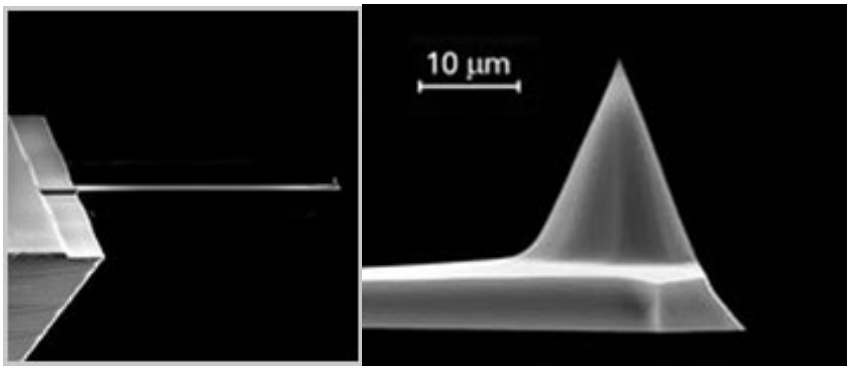

Fig.2.8 SEM image of Si cantilever and tip (left) and detail of the tip (right).

There are two working regimes due to the interaction between the tip and the investigated sample surface: attractive or repulsing regime (Fig. 2.9). In the contact mode AFM, the surface is scanned with the tip at constant distance, either in attractive or repulsive regime. Due to the surface topography changes the scanner has to go up or down in order to keep the distance to the surface constant.

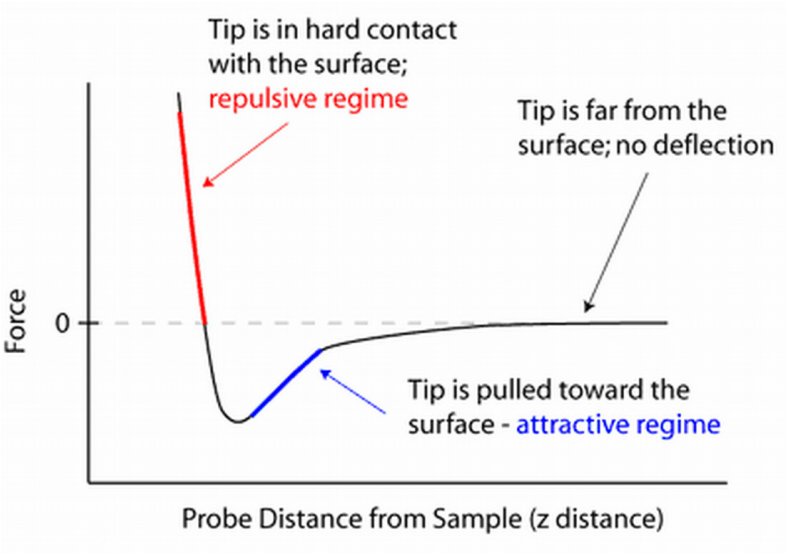

Fig. 2.9 Tip-sample interactions.

The AFM tip is first brought (manually) close to the sample surface, and then the scanner makes a final adjustment in tip–sample distance based on a set point determined by the user. The tip, now in contact with the sample surface is then scanned across the sample under the action of a piezoelectric actuator, either by moving the sample or the tip relative to the other. The cantilever deflection due to tip-surface interactions is monitored by a photodiode sensitive to laser light reflected at the cantilever backside (Fig. 2.10).

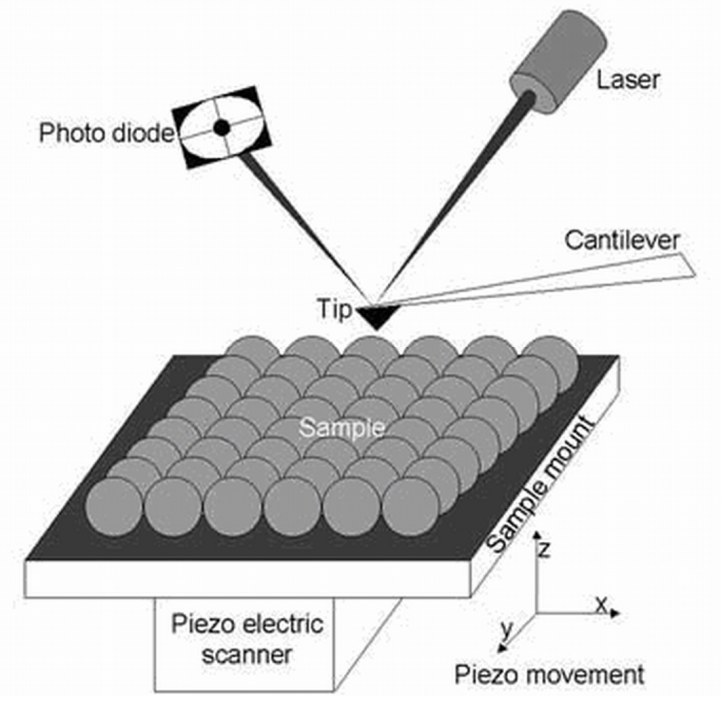

Fig. 2.10 Principal operational scheme of AFM.

The force between the tip and the surface is kept constant during scanning by maintaining a constant deflection. Without this feedback loop, the tip would "crash" into a sample with even small topographic features. By maintaining a constant tip-sample separation and using Hooke's Law:

$$F = -kx, \qquad \text{Eq. 2.7}$$

where F is force, k is the spring constant, and x is the cantilever deflection, the force between the tip and the sample is calculated. Finally, the distance the scanner moves in the z direction is stored in the computer relative to spatial variation in the x-y plane to generate the topographic image of the sample surface.

The AFM has several advantages over the electron microscope. Unlike the electron microscope which provides a two-dimensional projection or a three-dimensional image of a sample, the AFM provides a three-dimensional surface profile. Additionally, AFMs require neither a vacuum environment nor any special sample preparation, and they can be used in either an ambient or liquid environment.

The main disadvantage of the AFM compared to the electron microscope is the image size. The electron microscope can show an area on the order of millimeters by millimeters and a depth of field on the order of millimeters. The AFM can only show a maximum height on the order of micrometers and a maximum area of around $100 \times 100\ \mu m^2$.

All AFM measurements were performed using Autoprobe CP-Research device with 5 μm piezoelectric scanner. The CSC17/Ti-Pt type cantilevers were used for surface investigation of the substrates and the films. It is a silicon etched probe tips with Ti-Pt coating consisting of a 10 nm Pt layer on a 20 nm Ti sub-layer, which increases adhesion and electromigration firmness of Pt. The Ti-Pt coating is formed on both tip and reflective side of the cantilever.

2.6 Scanning electron microscopy

The scanning electron microscope (SEM) is one of the most widely used techniques for microstructural analysis [83]. FEI Nova 600 Nanolab apparatus was used in this work to investigate the topographical changes in the grown perovskite ($SrRuO_3$) and perovskite-like ($Bi_4Ti_3O_{12}$, $(Na, Bi)_4Ti_3O_{12}$) oxide films.

The principle of scanning electron microscopy is shown in Fig. 2.11. The sample under investigation is bombarded by a focused beam of high energy electrons, where the electrons are accelerated by a voltage of 1 - 50 kV between cathode (electron gun) and anode [84]. With the help of the lens system the electron beam is demagnified, so that an electron probe of diameter 1 - 10 nm carrying an electron probe current of 10^{-10} – 10^{-12} A is formed at the specimen surface. A deflection (scanning) coil system, in front of the last lens, scans the electron probe across the specimen.

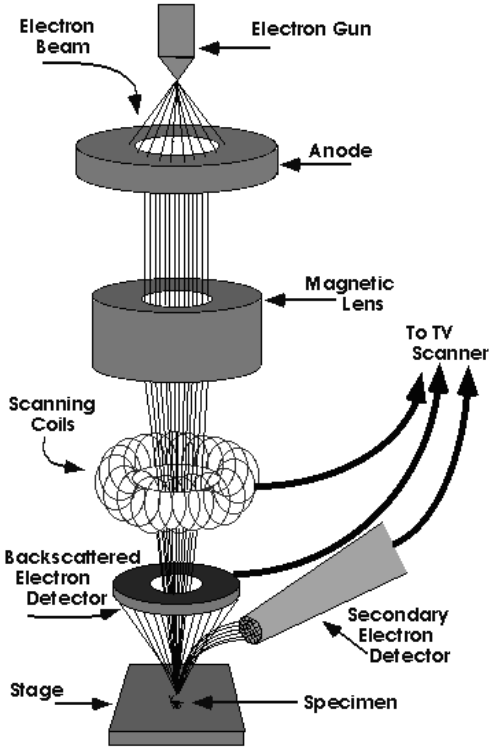

Fig. 2.11 The principle of the scanning electron microscopy.

The electron-probe aperture[5] is small – of the order of a few tens of milliradians – with the result that depth of focus is much larger than in light microscopy, therefore sharp images of the specimens can be observed even if low magnifications are used (20 - 50 times).

Another advantage of SEM is the wide variety of the electron-specimen interactions that can be used to form an image or to collect additional qualitative and quantitative information.

Elastic and inelastic scattering are elementary atomic interaction processes of the specimen with the incident electron beam. The final signal used for formation of the image is not a result of single scattering process but the complete electron diffusion caused by gradual

[5] opening through which rays travel that come to a focus in the image plane.

loss of the electron energy and by lateral spreading. The information depth and the lateral extension of the information volume that contributes to each of the possible signals depend on where the corresponding interaction takes place. The information and interaction volumes are not sharply limited and in some cases, decrease exponentially with increasing depth.

Fig. 2.12 shows schematically the most important interaction processes and their information volumes.

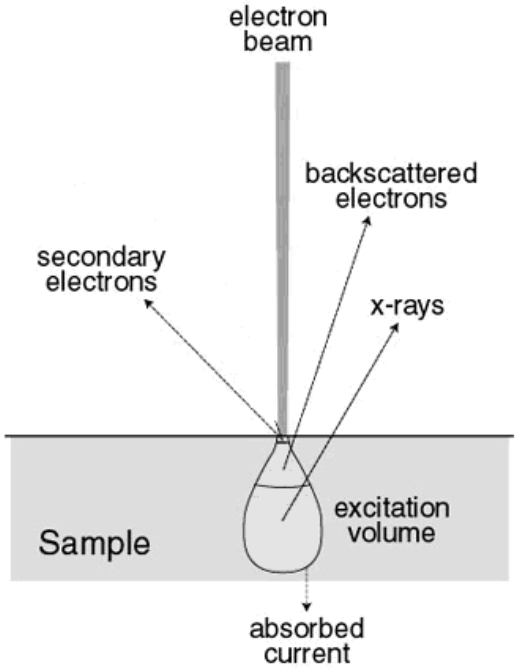

Fig. 2.12 Schematic representation of several signals generated by beam-specimen interaction in the SEM and the information volumes of the interaction processes.

Secondary and backscattered electrons as well as X-rays are generated after interaction of the sample with the incident electron beam. Conventionally defined limit between secondary and backscattered electron drawn at 50 eV. Secondary electrons are highly susceptible to elastic and inelastic scattering and can leave the specimen only from a very thin surface layer of the order of few nanometres. Due to the higher energy of backscattering electrons the information depth is larger as in the case of secondary electrons.

The secondary electrons are the most important because they can be collected easily due to their low exit energy of 2 - 5 eV and they are used to detect the surface topography. The low exit depth, of the order of few nanometres, allows a resolution of 5 - 20 nm to be reached. The backscattered electron contrast is used to detect different materials because it is highly dependent on the atomic number of the investigated material.

2.7 Raman spectroscopy

Raman spectroscopy is a powerful technique providing a range of information, including chemical and phase composition, bonding strength, mechanical strain, degree of crystallinity, and the effects of pressure and temperature on phase transformations.

The films grown during this thesis were measured by using a LabRAM HR-UV spectrometer with external lasers which provided wavelengths of 325, 488, 633, 785 nm.

Raman spectroscopy is based on the inelastic scattering of light by matter and is capable to investigate the structure of gases, liquids and solids. First of all, the sample is irradiated with monochromatic radiation [85]. For the transparent samples, most of the light is transmitted. When a photon interacts with the specimen, the photon can be absorbed or scattered. The photon polarizes the electronic cloud of the specimen and this interaction is said to form a virtual excited state, as shown in the energy level diagram below (Fig. 2.13).

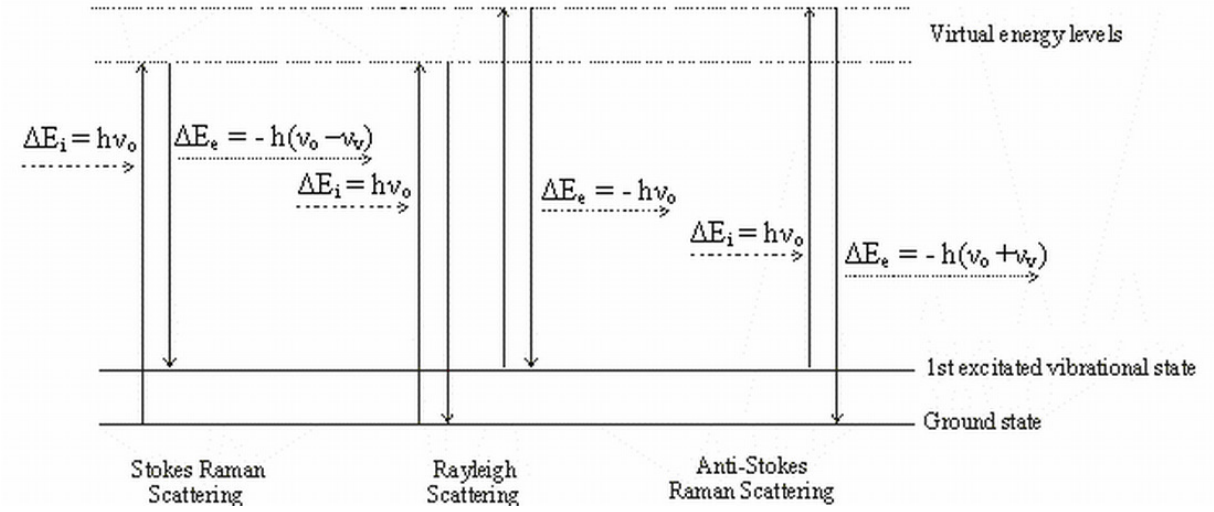

Fig.2.13 Rayleigh and Raman scattering. Where ΔE_i represents the energy of the initial phonon, ΔE_e represents the energy of the emitted (scattered) phonon, ν_o represents the frequency of the initial photon and ν_v is the frequency of the emitted photon.

The virtual excited state has very short lifetime and decays quickly with re-emission of a photon. When the re-emitted photon has the same energy of the incident photon is said to be elastically scattered (Rayleigh scattering). However, when nuclear, i.e. vibrational, motion occurs during the lifetime of the virtual state, a quantum of vibrational energy is transferred between the specimen and the incident photon and the energy of the emitted photon is different from the original one. In this case the scattering mechanism is inelastic. This

phenomenon is known as Raman scattering. If the transfer of energy in the virtual state is from the photon to the specimen, the scattered photon has a lower energy than the incident photon and this effect is referred to as Stokes Raman scattering ($\Delta E_e = -h(\nu_o - \nu_v)$. Conversely, if the transfer of energy in the virtual state is from the specimen to the photon, the scattered photon has a higher energy than the incident photon and the effect is referred to as anti-Stokes Raman scattering ($\Delta E_e = -h(\nu_o + \nu_v)$). The intensity of anti-Stokes scattering relative to Stokes scattering will increase with temperature. The inelastically scattered light is collected and dispersed and resulted Raman spectrum is plotted as a function of the shift of wavenumber of the radiation. Peaks in the Raman spectrum obtained using exiting radiation are generally associated with vibrational modes of the investigated specimen (Fig. 2.14).

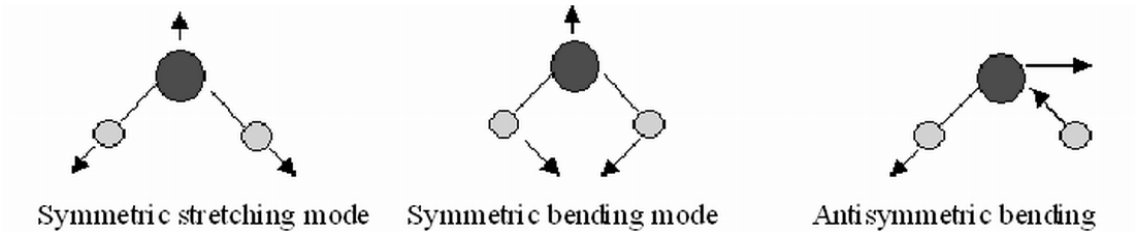

Fig. 2.14 The three vibrational modes.

To obtain the peaks in Raman spectrum due to vibrations in the specimen (lattice vibration modes for the films and substrates) the Raman transition has to be symmetrically allowed, because only molecules with center of symmetry are Raman active.

2.8 Electrical measurements

In the present work the dependence of electrical resistivity (ρ) on temperature (T) was measured for $SrRuO_3$ films.

Resistivity of materials shows how strongly a material opposes the flow of electrical current. In general, electrical resistivity of metals increases with temperature (more scattering by the lattice); while the resistivity of semiconductors decreases with increasing temperature (more carriers are generated). In crystals, crystal type and orientation and in polycrystalline materials the size of the grains affects the electronic structure of material as well as the value of resistivity.

Theoretically foundations of the electrical resistivity measurements on irregular shaped samples is based on conformal mapping developed by van der Pauw [86,87]. To get the correct measurement values without knowing the exact shape of the specimen the following conditions has to be fulfilled: a) the contacts have to be positioned at the very periphery of the sample, b) the contacts have to be small compared to sample size, c) the thickness of the sample has to be uniform, d) the surface of the sample has to be connected, without any holes.

For a flat sample of conducting material of arbitrary shape, with the contacts 1, 2, 3, and 4 along the periphery which satisfy the conditions above, the resistance $R_{12,\,34}$ is defined as [88]:

$$R_{12,34} = \frac{V_{34}}{I_{12}} \qquad \text{Eq. 2.8}$$

where the current I_{12} enter the sample at contact 1 and through contact 2 and $V_{34} = V_3 - V_4$ is the voltage difference between the contacts 3 and 4. $R_{23,\,41}$ is defined similarly. The resistivity is given by:

$$\rho = \frac{\pi t}{\ln(2)} \cdot \frac{(R_{12,34} + R_{23,41})}{2} \cdot F \qquad \text{Eq. 2.9}$$

where F is a function of $R_r = R_{12,34}/R_{23,41}$ ratio, and t is the thickness of film.

For a square uniform sample $R_{12,34} = R_{23,41}$ and F is equal to 1, therefore Eq. 2.9 can be simplified:

$$\rho = \frac{\pi t}{\ln(2)} \cdot \frac{V}{I} \qquad \text{Eq. 2.10}$$

As it was mentioned above the transport properties of $SrRuO_3$ thin films were measured as a function of temperature in the range of 50 - 300 K, whereas a kink in resistivity-temperature dependence coincides with the Curie temperature of the paramagnetic-ferromagnetic phase transition. The reason for this coincidence is that the resistivity of a ferromagnetic metal contains a significant temperature dependent magnetic contribution (Eq. 2.11):

$$\rho = \rho_o + \rho_{ph} + \rho_m \qquad \text{Eq. 2.11}$$

where ρ_o is the residual resistivity[6], ρ_{ph} is the resistivity due to electron-phonon scattering, and ρ_m is the magnetic resistivity due to spin scattering of electrons.

In the ferromagnetic state this contribution is caused by electron-magnon scattering with quadratic temperature dependence [89], whereas in the paramagnetic state (above T_c) the resistivity of $SrRuO_3$ increases linearly with temperature as predicted by the Bloch-Grüneisen (BG) law for electron-phonon scattering at elevated temperatures. BG model predicts an initial T^5 increase of resistivity at lower temperatures and a linear dependence at higher temperatures (T^1) for metals. Therefore the slope of the resistivity curves changes step-like at T_c.

Electrical resistivity of $SrRuO_3$ samples was measured in cryostat where the samples were cooled down to 50 K by using liquid He. Contacts were prepared by silver glue at the corners of 5×5 mm^2 samples.

2.9 Electron impact mass spectrometry

Mass spectrometry (MS) is an analytical technique for the determination of the elemental composition of a sample or molecule. It also gives information about the decomposition properties of different metal-organic compounds.

The principle of MS is that chemical compounds are ionized to generate charged molecules or molecule fragments and measurement of their mass-to-charge ratios. Electron Impact (EI) is the original ionization method of mass spectrometry. In the EI process, the sample of interest is vaporized into the mass spectrometer ion source, where it is impacted by the beam of electrons with energy of 70 eV sufficient to ionize the molecule.

Therefore a typical MS instrument consists of three modules: a) an ion source, which converts the molecules of a gaseous sample into ions; b) a mass analyzer, which sorts the ions by their masses by applying electromagnetic fields; and c) a detector, which provides data for calculating the abundances of the present ion species.

The ionization process can be summarized by the equation:

[6] The value to which the electrical resistivity of a metal drops as the temperature is lowered to near absolute zero, caused by imperfections and impurities in the metal.

$$M_{(g)} + e^- \Rightarrow M^+_{(g)} + 2e^- \qquad \text{Eq. 2.12}$$

where M^+ is corresponding molecular ion, which has the same weight like molecule M. The molecular ion will undergo fragmentation under the further impact with electrons:

$$M_1^+ \Rightarrow M_2^+ + M_n \qquad \text{Eq. 2.13}$$

where M_1^+ is molecular ion, M_2^+ is fragment ion, M_n is the neutral fragment.

Every electron in organic molecule is paired with an electron of opposite spin. Therefore if a molecular ion is generated by removing one electron, an unpaired electron must be somewhere in the molecule. Species with unpaired electrons are radicals, so the molecular ion is a radical. Radicals are not very stable species and tend to fragment.

A mass spectrum is usually presented as a vertical bar graph, in which each bar represents an ion having a specific mass-to-charge ratio (m/z) and the length of the bar indicates the relative abundance of the existing ion. The most intense ion is assigned to an abundance of 100, and it is referred to as the base peak. Most of the ions formed in a mass spectrometer have a single charge (z = 1), so the m/z value is equivalent to mass itself. The highest-mass ion in a spectrum is normally considered to be the molecular ion, and lower-mass ions are fragments from the molecular ion, assuming the sample is a single pure compound.

Electron Impact ionization mass spectra (EI-MS, 70 eV), both at low and high resolution, were recorded using a VG Instruments Autospec instrument. Output spectra were given as specific masses (m/z) based on the most abundant isotopes.

2.10 Thermoanalytic methods

2.10.1 Principle of TG-DTA and TG-DSC analysis methods

The thermal analysis [90] (TA), involves the measurements of certain physical and chemical properties as a function of temperature. One of the main TA techniques is thermogravimetry (TG), where the mass change of the sample as a function of temperature or time is recorded. In this thesis TA was used to investigate thermal stability of the metal-organic precursors used for MOCVD process.

The measurement technique of TG usually consists of a high-precision balance with a crucible loaded with the sample on one side of the balance and an inert reference (empty Al crucible) on the other. The balance is placed in a small electrically heated oven with a thermocouple to accurately measure the temperature. The investigated material and reference undergo identical thermal cycles were the difference in weight is registered. Thermal analysis for metal-organic precursors was carried out by raising the temperature gradually (5 °/min). The atmosphere in the oven was purged with a N_2 gas to prevent oxidation or other undesired reactions. A computer was used for the control of the instrument. TG data also provide information on precursor stability, there the presence of large amounts of residue indicate decomposition during evaporation. Since, the temperatures of different processes like melting, evaporation and decomposition can overlap in TG curves, for detection of exact transition temperatures the differential thermal analysis (DTA) was made simultaneously. In DTA the temperature difference between a sample and an inert reference material is registered as a function of temperature. Exothermic or endothermic changes in heat content due to phase changes or transformations are revealed as positive or negative peaks in the spectra. The key features are of two thermocouples connected to a voltmeter. One thermocouple is placed in the inert material, while the other is placed in a sample of the material under study. As the temperature is increased, a brief deflection of the voltmeter is observed when the sample is undergoing a phase transition.

In order to confirm the reliability of the TG-DTA results simultaneous TG-DSC (differential scanning calorimetry) measurements were made additionally to TG-DTA measurements, because both methods provide similar information. Due to different power applications in the methods endothermic peak points upward in DSC and downward in DTA. In DSC occurring enthalpy (quantity of heat energy) changes between the reference and investigated sample are detected.

TG-DTA analyses of the metal-organic precursors developed in the course of this work were performed using a “Seiko TG/DTA6200/SII” instrument. All metal organic-samples were prepared in a glove box and transferred to the instrument under argon. The TGA-DTA measurements were carried out in aluminium crucibles with approximately 10 mg of the sample. The employed heating rate was 5 K/min and nitrogen flow (99.9999 %) of 300 ml/min was used to protect the sample from oxidation. The TG-DSC measurements were made at the same conditions.

2.10.2 Isothermal TG studies

Detailed isothermal TG studies were carried out to determine the evaporation rates and analyse the long term thermal stability of the individual solid metal-organic complexes, maintained at two different temperatures 120 °C and 150 °C for long periods of time (up to 4 h) in N_2 flow at atmospheric pressure. For the isothermal studies the crucibles were closed with an Al lid that had a hole with an area of 1.5 mm^2.

These temperatures were chosen because normally at 120 °C no decomposition/evaporation of the compound occurs or evaporation rate is very slow (at least for the precursors used in this study), whereas, at 150 °C for some precursors the evaporation starts which is evident from the increased evaporation rate of the compound, which nevertheless always increases with the increase of temperature.

2.10.3 Heating stage microscope

The heating stage microscope was used for a visual investigation of the melting properties of metal-organic compounds. Heating stage cell was placed under a microscope, where the samples were heated up under N_2 atmosphere and the changes in the sample were documented by video recording. By varying the temperature and heating rate the melting points of each metal-organic precursor used for the deposition of perovskite and perovskite-like oxide thin films were investigated. The melting temperatures were compared with the results obtained from thermal analysis measurements.

3. Experimental results and discussion

3.1 Vicinal surfaces of cubic and orthorhombic substrates

3.1.1 General remarks

Perovskite type (ABO_3) oxides such as $SrTiO_3$ are widely used as substrates for the epitaxial growth of complex oxide films, like high temperature superconductors [91], ferroelectrics [92], dielectrics [93] or colossal magneto-resistive materials [94], due to the small lattice mismatch and similar thermal expansion coefficients.

Surface morphology and termination of the substrate have an important influence on the early growth stages of the film. Rough surfaces can cause a variety of structural defects and thus alter the functional properties of the oxide layer [95]. Furthermore, uncontrolled surface morphology results in poor reproducibility of film growth and properties, even if the same kind of substrate is used. Since the crystal structure of ABO_3 perovskites with (001) surface orientation (for orthorhombic symmetry: (110) orientation) consist of alternating AO (A-site) and BO_2 (B-site) planes, theoretically both surface terminations are possible and the growth mode on different terminated surfaces can differ significantly. For example, it was reported that the growth of $YBa_2Cu_3O_{7-x}$ films on the TiO_2 (B-site) terminated surface results in segregation of CuO_x precipitates, while, layer-by-layer growth without any precipitate formation was observed on SrO terminated $SrTiO_3$ [96]. On the other hand, epitaxial $SrRuO_3$ films with atomically smooth surfaces can be grown by step-flow mode on TiO_2 terminated $SrTiO_3$ substrates [97].

Epitaxial growth of thin oxide films is often performed on a substrate, which is cut at a vicinal angle[7] resulting in steps of height equal to the lattice parameter of the substrate. Growth on vicinal surfaces, in step-flow growth mode, enhances the possibility of avoiding twins and getting single domain thin oxide films in comparison to exactly oriented substrates [98]. By using vicinal substrates island growth on nominal substrates can be transformed to step-flow growth [99,100] resulting in high quality films suitable for the fabrication of

[7] The term vicinal defines a crystal plane whose position varies very little from that of the nearest low-index surface plane.

different heterostructures. Well prepared vicinal surfaces exhibit regular terraces separated by unit cell steps, indicating a single layer termination of the surface.

It is known that depending on the termination of the surface the electrical properties at the interface of the heterostructures can differ [101,102]. Therefore for the oxide-electronic device applications as well as for general understanding, surfaces exhibiting both possible surface terminations obtained at different preparation conditions are of the great interest.

A large number of studies have been performed to prepare and to examine the surface of $SrTiO_3$(001) [103,104,105,106,107,108]. However, less is known about the surface termination of other oxide substrates like $NdGaO_3$, $SrLaAlO_4$, $LaAlO_3$, $KTaO_3$, $DyScO_3$. Few papers have been published describing the preparation and analysis of the surface termination of $NdGaO_3$(110), showing either an A-site (NdO) [109,110,111,112] or B-site (GaO_2) [113] termination. However, there are no published studies concerning surface termination of the rare-earth scandate substrates, even if they are used for the epitaxial growth of thin oxide films [24,114,115].

Therefore, in this section the preparation conditions of $SrTiO_3$(001), $NdGaO_3$(110) and $DyScO_3$(110) substrates, which are then employed for the growth of epitaxial $SrRuO_3$ films, were investigated in detail. Preparation conditions were varied with the aim to obtain atomically smooth surfaces with single surface termination. Surface morphology and roughness was investigated by means of Atomic Force Microscopy (AFM). The termination of the topmost layer was investigated by means of Auger Electron Spectroscopy (AES) induced by grazing scattered protons (p-AES) and composition of near-surface layer by impact of electrons (e-AES). Surfaces prepared under optimised conditions were used for the epitaxial growth of thin $SrRuO_3$ films.

3.1.2 Preparation and properties of vicinal substrate surfaces

Commercially available $SrTiO_3$(001), $NdGaO_3$(110), $DyScO_3$(110) single crystal substrates (CrysTec, Berlin) with 0.1° miscut angle toward [100], [$1\bar{1}0$] and [$1\bar{1}0$] directions were used for the stepped surface preparation and investigation of the topmost layer termination. In the case of $SrTiO_3$, the substrate preparation procedure and termination is often investigated in literature, therefore only slight modifications were introduced in this work, since different groups have achieved similar results by using different preparation

conditions. On the contrary, the preparation of $NdGaO_3$ substrates is rarely mentioned in literature, and for $DyScO_3$ have not been reported up to now. In these cases it was necessary to develop entirely new processes in order to get the desired surface termination and condition.

The as-received substrates were rinsed in acetone and *2*-propanol in ultrasonic bath for 10 min to remove the impurities residual from mechanical polishing procedure.

In order to obtain a regular step-and-terrace structure, annealing temperatures higher than 950 °C and at least 30 minutes are required for the final recrystallization process of the surface. Under optimal preparation conditions the surfaces consist of single unit cell height steps (~ 0.4 nm) and 200 nm width terraces corresponding to a miscut angle of 0.1°. The average surface roughness determined from the contact AFM of such surfaces varied in the 0.12 – 0.19 nm range. Resolution limit of AFM is 0.09 nm.

The high temperature annealing procedures of the cleaned or chemically etched substrates were performed in a tube-oven. The substrates were placed inside the quartz tube and annealed at atmospheric pressure under flowing gasses (~ 1 L/min). The temperatures were ramped up with 24 K/min, and were kept constant at the set point. After the annealing time they were cooled down with a rate of 4 K/min.

The annealing parameters and the corresponding results and termination of the substrates are described in the following sections separately for each substrate type.

3.1.2.1 $SrTiO_3$(001)

In contrast to $NdGaO_3$ and $DyScO_3$, the thermal treatment is not sufficient for $SrTiO_3$ substrates to obtain single terminated and atomically ordered surfaces, because the surface of the as-received substrate simply re-grow with the regularly spaced steps separated by terraces with irregular edges and mixed surface termination [105]. Therefore, a chemical treatment has to be applied to $SrTiO_3$ before the final thermal procedure.

The principal of the chemical etching is that more basic oxide (SrO) in the perovskite structure is selectively etched and after following high temperature annealing single TiO_2-terminated surface is obtained. The first work in this direction was made by Kawasaki et al. [103], who treated $SrTiO_3$ substrates with a NH_4F-HF (BHF) solution. However, reproducing single terminated surfaces using this method depends strongly on the pH value of the solution. Koster et al. [30] later reported a modified chemical treatment

procedure, where an additional hydrolysis step, before etching, was applied. During this thesis both methods were combined for preparation of stepped $SrTiO_3$ substrates. This means that $SrTiO_3$ substrates were soaked in deionised water for 10 min in ultrasonic bath before the etching step. In this way the basic Sr-oxide reacts with the water and Sr-hydroxide complex is formed:

$$SrO_{(s)} + H_2O_{(l)} \rightarrow Sr(OH)_{2\ (s)} \qquad \text{Eq. 3.1.1}$$

Since, $Sr(OH)_2$ is more reactive with acidic solutions than SrO, it was etched for a short time (30 s) in BHF solution (pH = 4.6, T = 30 °C):

$$Sr(OH)_{2\ (s)} + 2\ HF_{(aq)} \rightarrow SrF_{2\ (aq)} + 2\ H_2O_{(aq)} \qquad \text{Eq. 3.1.2}$$

After etching procedure the samples were rinsed in deionised water for 3 min to remove any possible precipitates and dried in a nitrogen stream.

After the etching procedure, an annealing temperature series (850 – 1100 °C) were done in order to find the optimal annealing temperature to obtain step-and-terrace structure with the steps of one unit cell of 0.4 nm height, showing a single surface termination. The smoothest surface with a pronounced step-and-terrace structure was observed at an annealing temperature of 1100 °C for 60 min.

The surface of as-received, etched and annealed at 850 °C, 950 °C and 1100 °C temperatures in oxygen atmosphere are shown in Fig. 3.1.1. The as-received and etched surfaces consist of hardly visible terraces, with disordered step edges. The following $SrTiO_3$ sample was annealed at 850 °C, but no terraces or steps were observed, because this temperature is below the threshold for recrystallization of the surface, additionally the surface is relatively rough (R_a = 0.74 nm) (Fig. 3.1.2). The increase of annealing temperature lead to the smoothening of the surface and appearance of some terraces with still not straight step edges at 950 °C. The substrate annealed at 1000 °C shows a very smooth surface (R_a = 0.14 nm) with a regular arrangement of terraces with a step height of ~ 0.4 nm, which corresponds to one lattice constant of $SrTiO_3$. That means that only one surface termination is provided, in agreement with literature data for these preparation conditions. According to literature data it is assumed that the surface has TiO_2 termination [106,116].

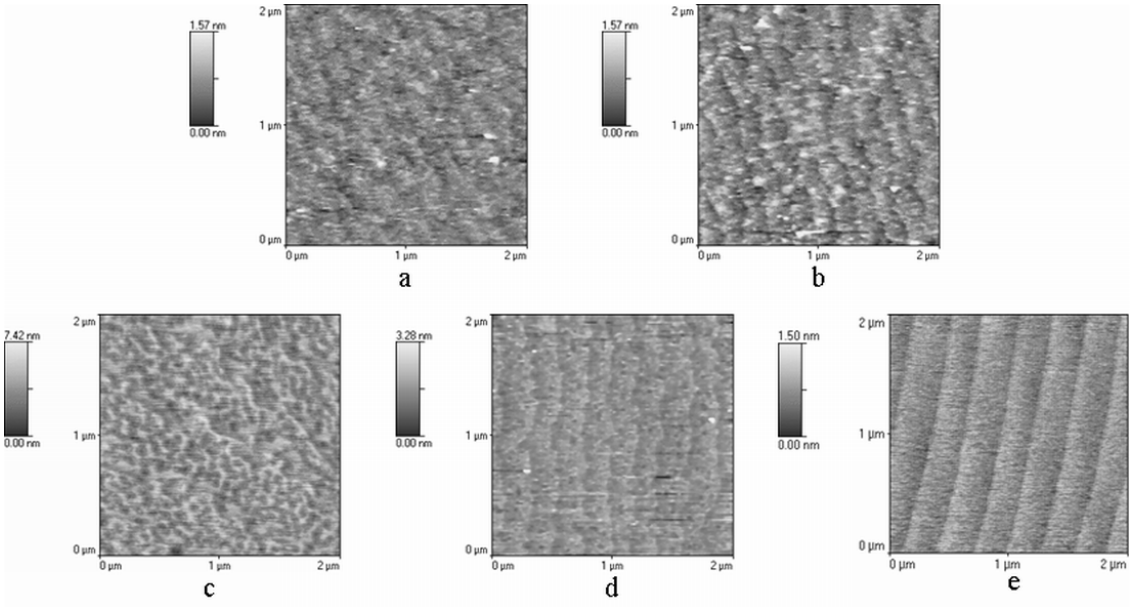

Fig. 3.1.1 Topographic AFM micrographs of $SrTiO_3$(001): a) as-received, b) etched in BHF for 30 s, c) annealed at 850 °C, d) annealed at 950 °C, e) annealed at 1100 °C for 60 min in O_2 atmosphere.

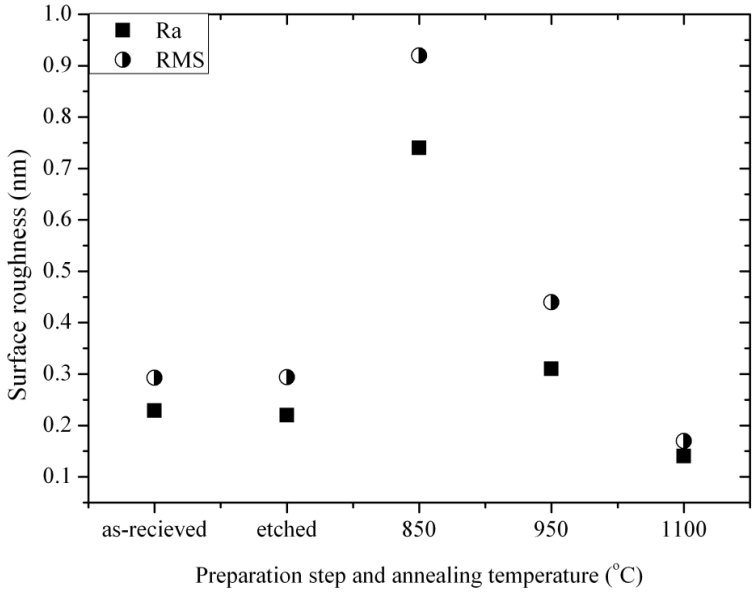

Fig. 3.1.2 Surface roughness of the as-received, etched and annealed $SrTiO_3$ substrates at different temperatures in O_2 atmosphere for 60 min.

3.1.2.2 $NdGaO_3$(110)

In contrast to the $SrTiO_3$ surface, the stepped $NdGaO_3$ surfaces can be obtained even without any use of chemical etching and a high temperature annealing step is sufficient. Therefore only high temperature treatment was selected in this work to obtain stepped $NdGaO_3$ surfaces in order to avoid any surface deterioration by chemical etching.

Annealing temperatures (950 – 1050 °C) and time (30 – 90 min), as well as the atmosphere (O_2, Ar, and Ar + 5 % H_2) were varied to investigate their influence on the surface properties and to check if both surface terminations are possible to obtain, because little has been known about this surface [109,110,111,112,113].

The topographic AFM images of as-received $NdGaO_3$(110) and annealed at different temperatures in oxygen atmosphere are shown in Fig. 3.1.3.

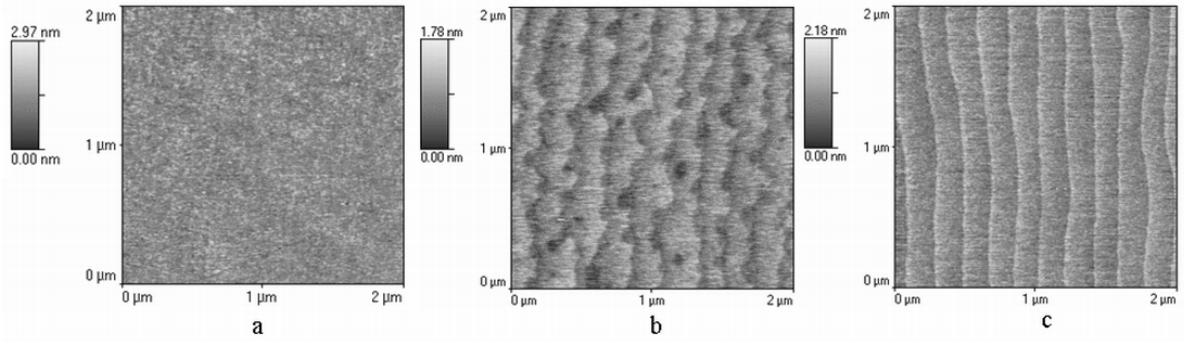

Fig. 3.1.3 Topographic AFM micrographs of $NdGaO_3$(110): a) as-received, b) annealed at 950 °C, c) annealed at 1050 °C in O_2 atmosphere for 60 min.

Like in the case of $SrTiO_3$ substrates, the terraces and steps starts to appear at 950 °C and the straight terraces with the regular step height (~ 0.4 nm) are observed after annealing at 1050 °C. The $NdGaO_3$ substrates were annealed at slightly lower temperature compared to $SrTiO_3$, because of the different chemical nature of the chemical elements in $NdGaO_3$ and their behaviour at high annealing temperatures (will be explained later in this section).

The annealing time and annealing temperature are very important parameters for the formation of step-and-terrace structure and depend on each other. If the annealing temperature is increased the annealing time should be reduced in order to get the desired surface morphology.

In order to find optimal preparation conditions the annealing temperature was fixed at 1050 °C and annealing time was varied. $NdGaO_3$ sample annealed for 30 min (Fig. 3.1.4 a)

had a rougher surface as after annealing it for 60 min (Fig. 3.1.4 b), which exhibits a nearly perfect surface with straight terraces and single unit cell steps. Roughening of the surface increased when the annealing time was increased up to 90 min, probably due to the increased defect density on the substrate surface.

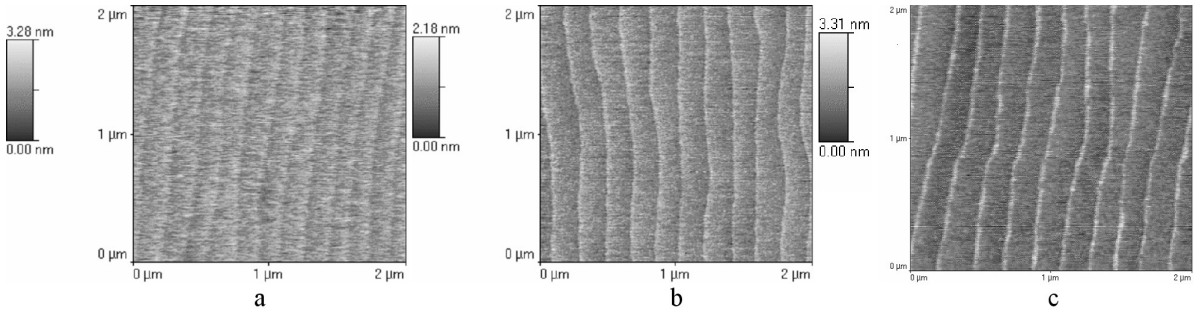

Fig. 3.1.4 Topographic AFM micrographs of $NdGaO_3$(110): a) annealed for 30 min (R_a = 0.26 nm), b) annealed for 60 min (R_a = 0.17 nm), c) annealed for 90 min (R_a = 0.28 nm) at 1050 °C in O_2 atmosphere.

The annealing of $NdGaO_3$ samples in different gas atmospheres showed some differences in the surface morphologies of the substrates as can be seen from the Fig. 3.1.5. The samples were annealed in reducing (Ar + 5 % H_2), inert (Ar), and oxidative (O_2) atmospheres in order to observe firstly the evolution of surface morphology and afterwards the termination of the surface. Surface of the $NdGaO_3$ annealed in forming gas (Fig. 3.1.5 a) is completely distorted and has a very high average surface roughness of 6.1 nm, because no supply of oxygen during annealing process is available. No difference in surface morphology was observed for the samples annealed in Ar and O_2 atmospheres (Fig. 3.1.5 b and c). Therefore, for the surface termination studies these samples were investigated, as they provide regular step-and-terrace structures. The appearance of regular step-and-terrace structure after annealing in Ar atmosphere can be explained by the low partial pressure of oxygen of about 10^{-3} mbar, which is sufficient for the formation of stepped surface. The terrace widths differ in these two samples due to the small changes in the miscut angle, where narrower terraces appear for slightly higher miscut.

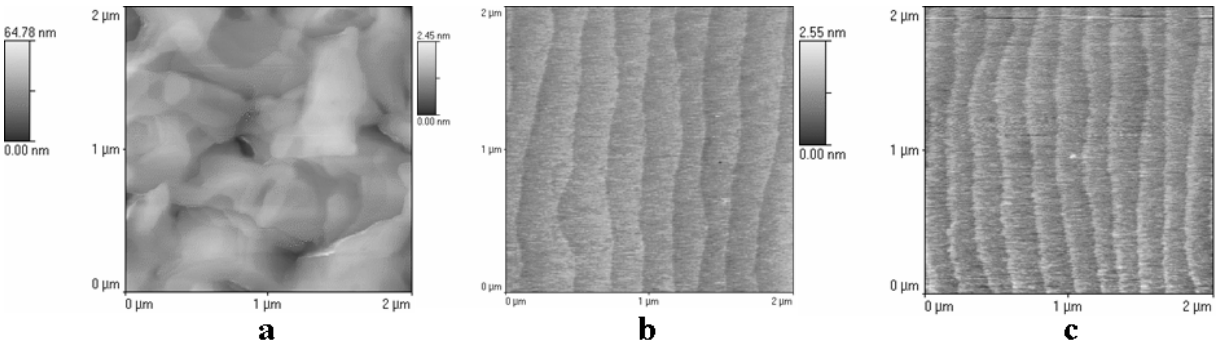

Fig. 3.1.5 Topographic AFM micrographs of $NdGaO_3$(110): a) annealed in Ar +5 % H_2, b) annealed in Ar, c) annealed in O_2 for 60 min at 1050 °C.

The termination of the topmost layer of the surface presented in Fig. 3.1.5 c is investigated by AES induced by grazingly scattered 200 keV protons at room temperature. Fig. 3.1.6 shows a differential AES spectrum of secondary electrons. In this spectrum one can relate Auger signals from O with a pronounced peak at electron energy of 515 eV (KLL transition), Nd with a peak at 734 eV (MNN transition) and from Ga with a peak at 1064 eV (LMM transition). Due to different magnitudes of the ionization cross sections and relative Auger sensitivities S_X of the elements X, the measured signals which correspond to the Nd and Ga Auger transitions are significantly smaller than the O Auger signal.

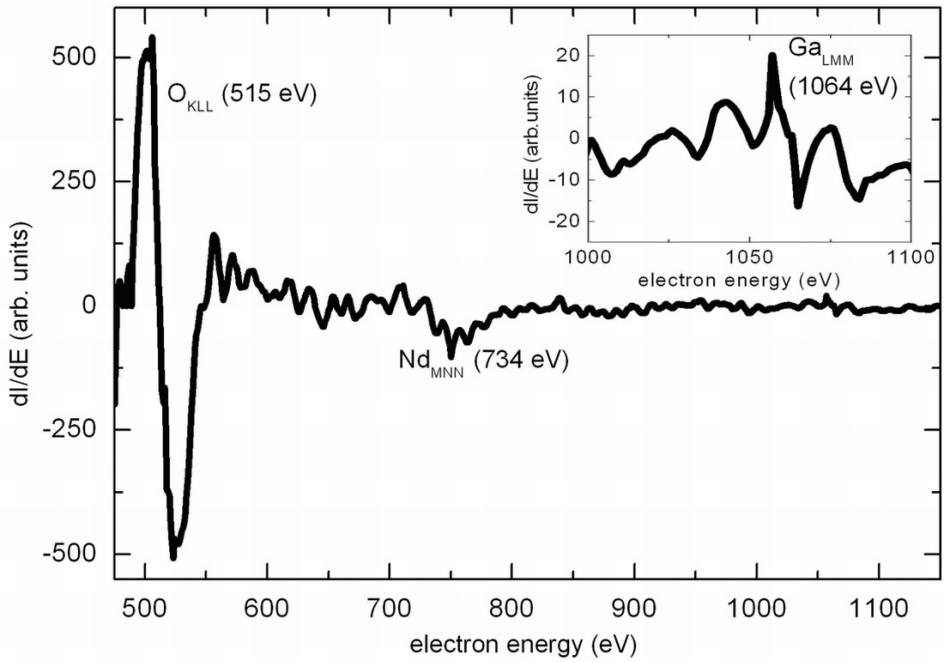

Fig. 3.1.6 Differential intensity spectrum of secondary electrons emitted from $NdGaO_3$ surface annealed in O_2 atmosphere for 60 min at 1050 °C, excited by grazingly scattered 200 keV protons under $\Phi_{in} = 1°$. Inset shows the energy range of Ga LMM Auger transitions.

The relative Auger sensitivities S_X^p for the excitation with protons were calculated by the estimation

$$S_X^p \propto S_X^e / (\sigma_X^e E_X^B), \qquad \text{Eq. 3.1.3}$$

where S_X^e is the relative Auger sensitivity for the excitation with electrons ($S_O^e = 0.52$, $S_{Nd}^e = 0.04$ and $S_{Ga}^e = 0.13$ for a primary electron energy of 3 keV [117]), σ_X^e the ionization cross section for the impact with electrons, and E_X^B the electronic binding energy [118]. For the calculation of the concentrations $c_{X,n=0}$ of the elements O, Nd and Ga in the topmost layer (n = 0) the ratios of the relative Auger sensitivities S_X^p are essential. In terms of the ionization cross sections σ_X^e taken from Ref. [119] and the electronic binding energies E_X^B taken from Ref. [120] the following ratios: $S_O^p / S_{Nd}^p = 5.9$, $S_O^p / S_{Ga}^p = 0.8$ and $S_{Ga}^p / S_{Nd}^p = 7.5$ were calculated. From the peak-to-peak intensities in the p-AES spectrum in Fig. 3.16, together with the sensitivity ratios, the atomic concentrations in the topmost layer were evaluated to:

$$c_O = (55 \pm 10)\%,\ c_{Nd} = (43 \pm 9)\% \text{ and } c_{Ga} = (2 \pm 4)\%.$$

These concentrations are consistent with a perfect NdO (A-site) termination, where 50 % of O and 50 % of Nd would be provided. In contrast, for a perfect GaO_2 termination (B-site), one would expect a concentration ratio of 66 % and 33 % for O and Ga, respectively. Therefore, a GaO_2 termination for the investigated $NdGaO_3$ surface is excluded. The small amount of gallium (2 at. %) was attributed to the excitation of Ga atoms at step edges of the imperfect surface as well as to segregated Ga atoms from deeper layers to the topmost layer during the annealing procedure.

Electron-induced AES of the same $NdGaO_3$ substrate suggests a deficiency of gallium and oxygen in a near-surface region. This result was confirmed by Rutherford-Backscattering measurements, whereby the thickness of the deficiency layer was estimated by 4 nm.

NdO termination layer was always observed for other annealing time and temperature combinations as well as for an annealing in pure Ar (Fig. 3.1.5 b), as long as a clear step-and-terrace structure could be generated. This observation substantially agrees with the results of Ohnishi et al. [107] who reported that after the annealing process the $NdGaO_3$(001) surface shows a NdO termination of 100 %. In contrast to their work, a small amount of Ga (2 - 4 %)

atoms on the topmost layer was found here and attributed to the defects on the step edges or segregated Ga atoms.

The result of NdO termination can be explained according to a model of Yamaji et al. [121], developed for $LaGaO_3$ crystals (which exhibit a lower chemical reactivity at elevated temperatures due to the higher melting point [122]). Ga is evaporated as gaseous Ga-oxide already above 800 °C [123]. Due to a lack of Ga and O on the surface and in the subsurface layer a concentration gradient between the surface and near-surface layers forms. This gives the driving force for the diffusion of Ga (O) from deeper layers to the surface and results in a depletion layer with thickness of several nm below the surface, as proved by e-AES results. Similar results were observed by Talik et al. [110] who reported about the escape of Ga not only from the surface, but also from the bulk of $NdGaO_3$ after thermal treatment at 850 – 1200 °C.

Diffusion of Ga atoms from the bulk $NdGaO_3$ to the surface is also supported by the observation of several authors who detected Ga accumulation at the interface or in the films grown on $NdGaO_3$ substrates [124,125].

The exclusive observation of a NdO termination is in contrast to the results of Leca et al. [111] and Gunnarsson et al. [113]. Leca et al. [111] described that a change of the surface termination (NdO or GaO_2) is possible by adjusting the preparation conditions. The authors observed that an increase of the O_2 partial pressure changes surface termination from single NdO to a mixed one (NdO and GaO_2). However, they determined the surface termination indirectly by means of ex-situ AFM and in-situ reflection high energy electron diffraction (RHEED), which do not allow a direct identification of the elemental composition of the surface. Also Gunnarsson et al. [113] argued that by annealing $NdGaO_3$ at 950 °C for 30 min in oxygen atmosphere GaO_2 termination was observed by means of XPS.

3.1.2.3 $DyScO_3$(110)

The investigation of the surface morphology and termination of $DyScO_3$ substrates is even more crucial and important, because no published studies concerning surface preparation and termination of the rare-earth scandates are available. The $DyScO_3$ samples were annealed at the same temperatures as for the previous oxides, and showed similar behavior to the case of $NdGaO_3$ regarding the surface morphology in Fig. 3.1.3. Therefore an annealing

temperature of 1050 °C was selected and the subsequent investigation was limited to the effects of annealing time (30 – 600 min) and atmosphere (Ar and O_2).

In the case of $NdGaO_3$ roughening or degradation of the surface appeared when annealing time was increased to 90 min. However, for $DyScO_3$ no significant difference was noticed in the morphology and surface roughness of the samples annealed in oxygen atmosphere for different annealing times (Fig. 3.1.7).

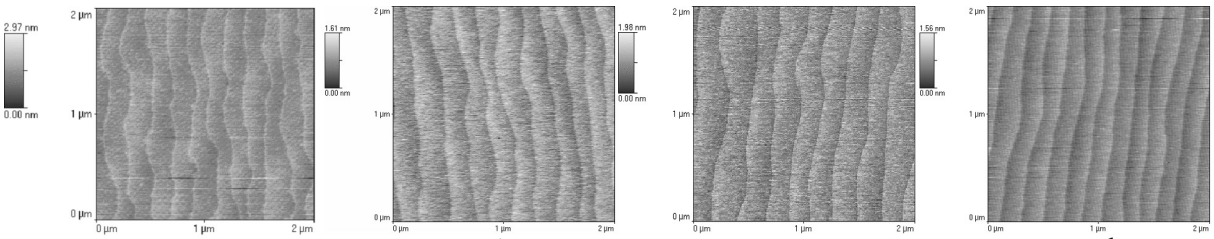

Fig. 3.1.7 Topographic AFM micrographs of $DyScO_3$(110): a) annealed for 30 min (R_a = 0.17 nm), b) annealed for 60 min (R_a = 0.14 nm), c) annealed for 90 min (R_a = 0.19 nm), d) annealed for 600 min (R_a = 0.12 nm) at 1050 °C in O_2 atmosphere.

The same result was observed for $DyScO_3$ samples annealed in Ar atmosphere for annealing times between 30 and 600 min. It seems that the gas atmosphere does not have any influence on the surface morphology

The differential p-AES spectrum of emitted secondary electrons of the $DyScO_3$ sample, which was annealed for 60 min in O_2 atmosphere, is reported in Fig. 3.1.8. A pronounced peak at electron energy of 515 eV is visible in the AES spectrum for the sample annealed in oxygen gas ambient for 60 minutes. This peak can be attributed to KLL transition of oxygen (Fig. 3.1.8). The characteristic peak at 1123 eV is assigned to the MNN transition of dysprosium, while LMM transition of scandium has electron energy of 340 eV.

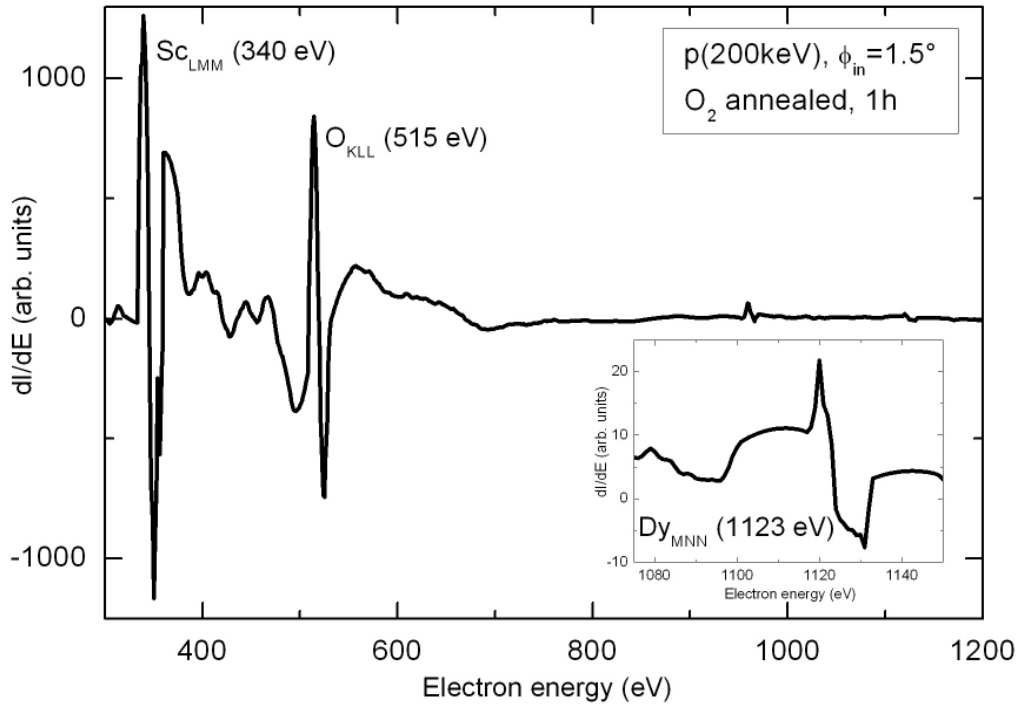

Fig. 3.1.8 Differential intensity spectrum of secondary electrons emitted from the $DyScO_3$ surface annealed in O_2 flow for 60 min at 1050 ˚C, excited by grazingly scattered 200 keV protons under Φ_{in}=1.5°. The inset shows the energy range of the Dy MNN Auger transitions.

Analogue to the AES analysis of the $NdGaO_3$ surfaces the relative AES sensitivities for excitation with electrons of $S_O^e = 0.52$, $S_{Sc}^e = 0.35$ and $S_{Dy}^e = 0.024$ for oxygen, scandium, and dysprosium were used. The rations of these elements for proton excitation were calculated by equation 3.1.3: $S_O^p / S_{Sc}^p = 0.42$, $S_O^p / S_{Dy}^p = 21.51$ and $S_{Sc}^p / S_{Dy}^p = 50.68$. Due to different magnitudes of the ionization cross sections and relative Auger sensitivities (S_X) of the elements X, the signals which correspond to the Dy and O Auger transitions are weaker than Auger signal of the Sc.

Considering the calculated ratios, from the peak-to-peak intensities in the proton-induced AES spectrum the atomic concentrations in the topmost layer for the $DyScO_3$ surface annealed in oxygen atmosphere for 60 min were deduced (Table 3.1.1).

Table 3.1.1 Concentrations of the surface elements after annealing at 1050 °C for 60 min in O_2 and Ar atmospheres.

	60 min, O_2	**60 min, Ar**
Dy	(36 ± 8) %	(8 ± 5) %
Sc	(9 ± 4) %	(43 ± 9) %
O	(55 ± 8) %	(49 ± 8) %
c_{Dy}/c_{Sc}	4	0.19

From these concentrations determined from p-AES measurements on several $DyScO_3$ samples, it is evident that annealing of $DyScO_3$ substrates in oxygen ambient for 60 min leads to a DyO termination with only small residual amount of Sc (an ideal DyO termination would result in 50 at.% Dy and 50 at.% O).

$DyScO_3$ substrates were also annealed in argon atmosphere for 60 min in order to investigate the influence of the gas atmosphere on the surface termination. The calculated concentrations of the elements (Dy, Sc, O) in the topmost layer of the $DyScO_3$ substrates annealed in argon flow for 60 min are also listed in Table 3.1.1. This results indicate that the surface is mainly covered by scandium oxide (a perfectly ScO_2 termination would contain 33 at. % Sc and 66 at. % O). The small amounts of Sc and Dy after annealing in oxygen and argon atmospheres, respectively, are attributed to the excitation of Sc and Dy atoms at step edges and surface imperfections. Since the surface termination of the as-received $DyScO_3$ substrates results also in predominant ScO_x coverage, it can be concluded that annealing in Ar atmosphere 60 min does not change the surface termination.

It has to be noted, that in contrast to the results of $NdGaO_3$ no depletion layer in the near-surface region was detected for the $DyScO_3$ samples annealed for 60 min.

By increasing the annealing time to 90 – 120 min in both gas atmospheres, the Dy to Sc concentration ratio c_{Dy}/c_{Sc}, calculated from the p-AES data, which was taken as a surface termination indicator, is equal to 1 in argon and 0.6 - 1.8 in oxygen atmosphere. This clearly shows an intermixing of topmost layer of the surface (Fig. 3.1.9).

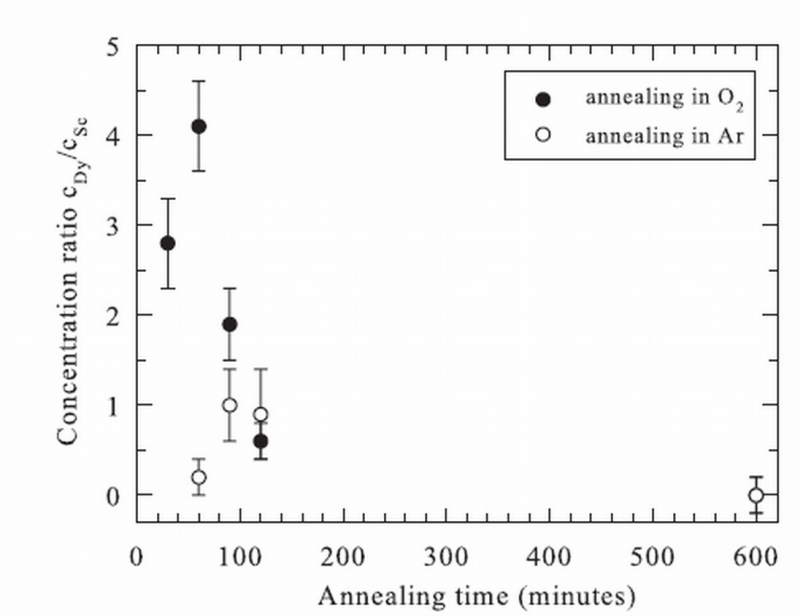

Fig. 3.1.9 Concentration ratio c_{Dy}/c_{Sc} as a function of time for annealing in oxygen (full circles) and in argon (open circles) atmospheres at 1050 °C calculated from p-AES spectra. Note: $c_{Dy}/c_{Sc} = 0$ for annealing in oxygen and argon for 600 min.

But a significant prolongation of the annealing time to 600 min, led to a drastic change of the surface composition. Only a single ScO_x ($x \leq 2$) surface termination without any Dy at the surface (inset of Fig. 3.1.10) for both annealing atmospheres was observed.

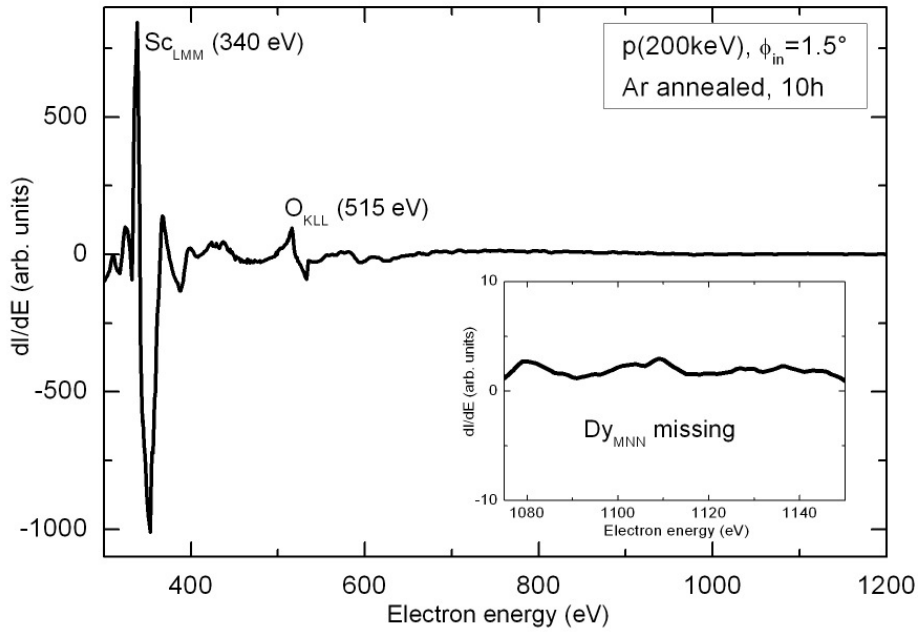

Fig. 3.1.10 Differential intensity spectrum of secondary electrons emitted from the $DyScO_3$ surface annealed in Ar flow for 600 min at 1050 ˚C, excited by grazingly scattered 200 keV protons under $\Phi_{in} = 1.5°$. The inset shows the energy range of the Dy MNN Auger transitions.

The corresponding concentrations of Dy, Sc and O calculated from p-AES spectra, for the samples annealed at 1050 °C for 600 min in O_2 and Ar atmospheres, are listed in Table 3.1.2.

Table 3.1.2 Concentrations of the surface elements after annealing at 1050 °C for 600 min in O_2 and Ar atmospheres.

	600 min, O_2	**600 min, Ar**
Dy	0	0
Sc	(38 ± 8) %	(37 ± 8) %
O	(62 ± 8) %	(63 ± 8) %
c_{Dy}/c_{Sc}	0	0
ScO_x	$ScO_{1.63}$	$ScO_{1.70}$

Electron-induced AES measurements of the substrates annealed for 600 min in O_2 and Ar gas ambient showed a deficiency of Dy and O in a near-surface region within a thickness of about 4 nm, which gives rise to non-stoichiometry of the elements in the near-surface region. To summarize the results the concentration ratio of Dy and Sc for both gas atmospheres are presented in Fig. 3.1.9 in dependence of the annealing time. The data can be explained in terms of a three step process: a) diffusion of oxygen from the gas ambient into the bulk, b) oxidation of dysprosium, c) diffusion and evaporation of dysprosium and oxygen.

It is assumed that oxygen is diffusing initially from the gas ambient into the bulk of $DyScO_3$ due to a concentration gradient of oxygen. In such a way Dy with the oxidation state of 3+ can be oxidized to 4+, which is supported by the observation of the substrate colour change from yellow to brown [126]. The oxidation of Dy is followed by the evaporation of Dy probably as dysprosium oxide (DyO_x). The resulting lack of Dy and O on the surface induces a concentration gradient between the surface and the bulk of the $DyScO_3$ substrate, leading to the diffusion of Dy and O from the bulk towards the near-surface layers. Thus, after a short time annealing for 30 – 60 min in oxygen atmosphere, the DyO termination is caused by the high concentration of Dy in the near surface layers. However, with the increase of annealing time the diffusion length of the Dy atoms increases. Furthermore, oxygen atoms from gas ambient diffuse a longer path into the bulk to oxidise Dy^{3+} and oxidised Dy^{4+} has to move to the surface layer as well. Therefore, the annealing of the $DyScO_3$ substrates for 600 min results in a single ScO_x termination, where depletion of Dy(O) occur due to the evaporation of Dy and O from the surface.

In a similar manner one can explain the surface termination after annealing in Ar atmosphere. However, the oxidation process in argon atmosphere is considerably reduced due to the low background pressure of residual oxygen of about 10^{-3} mbar. Thus, after annealing for 60 min in argon atmosphere, no change in surface termination compared to the as-received substrates was observed. The oxidation of Dy^{3+} to Dy^{4+} and evaporation of Dy(O) from the surface occurred initially after an annealing for 90 – 120 minutes and resulted in a mixed surface termination. However, annealing for 600 min in argon gas ambient resulted in single ScO_x surface termination, because sufficient amount of oxygen was supplied to oxidize Dy on the surface and a sub-surface region, leading to the depletion layer of Dy(O) due to evaporation process. The depletion of Dy(O) can be explained by different strength of Dy-O and Sc-O bonds in the $DyScO_3$. Delugas et al. [127] published an average value of 2.33 Å for the Dy-O bond length, whereas Sc-O bond length is 2.11 - 2.12 Å. A shorter bond length of Sc-O was also reported by Velickov et al. [128]. In general, the longer chemical bonds are weaker, therefore, a depletion layer of Dy(O) after long time annealing was observed due to the weaker bonding of dysprosium with oxygen in $DyScO_3$ crystal structure.

3.2 Chemistry of metal-organic precursors

Liquid-delivery metal-organic chemical vapour deposition (LD-MOCVD) is a specific type of CVD, where solid metal-organic compounds are dissolved in solvent and transferred to flash evaporator, where immediate evaporation takes place. The decomposition of evaporated precursor occurs at the elevated temperatures resulting in thin film deposition.

In this section, general requirements for the precursors, available precursors and characterization of physical and chemical properties of the used precursors by mass spectrometry and thermoanalytic methods will be described.

3.2.1 Precursor requirements for MOCVD

Precursors for MOCVD of thin films can be broadly classified into three types: inorganic–metal precursors, metal-organic precursors, which contain organic ligands but do not contain any carbon-metal bonds, and organo-metallic precursors which contain organic ligands with carbon-metal bonds (e.g. metal alkyls, metal carbonyls) [129]. However, the definition of MOCVD include also precursors containing metal-oxygen bonds (e.g. metal-alkoxides, metal-aryloxides, metal-β-diketonates) or metal-nitrogen bonds (e.g. metal alkylamides), the precursors with mixed ligands are also used in order to tune the properties of used precursors.

General requirements for 'ideal' MOCVD precursor can be summarised as follows [79]:

- Adequate volatility to achieve sufficient mass transport to the film deposition zone.
- Stability of the chemical compound so that its decomposition does not occur before reaching the deposition zone.
- A sufficiently large temperature 'window' between the evaporation and decomposition for film deposition.
- High chemical purity.
- Clean decomposition without incorporation of residual impurities.
- Good compatibility with co-precursors during the growth of complex materials.
- Long shelf-life with indefinite stability under ambient conditions, i.e. unaffected by air or moisture.
- Non-hazardous or with a low hazard risk.

- Manufactured in high yield at low cost.

Normally not all of these requirements can be fulfilled simultaneously; therefore the precursor chemistry has to be well understood, as far as possible, taking into account the match of thermal properties and reasonable vapour pressures of the precursors for the successful deposition of complex multi-component oxides with uniform properties. Ideal combination of these properties and optimization of deposition parameters allows vaporization of the precursor without decomposition or condensation and clean decomposition on the substrates without incorporation of carbon into the films from the ligands or solvent.

Solid precursors suffer from disadvantages like low volatility, low thermal stability and instability in air. Therefore, the liquid-delivery MOCVD was established. By this method even precursors possessing low vapour pressures can be used efficiently if they are stable in common organic solvents which can be then volatized at high temperature. The most commonly used precursors for the deposition of oxides thin films in MOCVD include metal alkoxides, metal carboxylates, β-diketonates. Oxygen gas is usually used as an oxidant. Different classes of the precursors are listed in the Table 3.2.1.

Table 3.2.1 Different classes of the precursors, where, M represents the metal atom and R, R^1, R^2, R^3 are different alkyl, aryl substituents.

<table>
<tr><th colspan="2">Monodentate</th><th colspan="2">Bidentate/Chelating ligands</th></tr>
<tr><td>Alkyls
 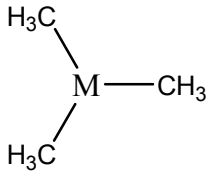 </td><td>Alkoxides
 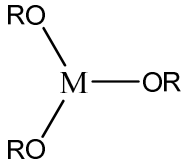 </td><td>β-diketonates
 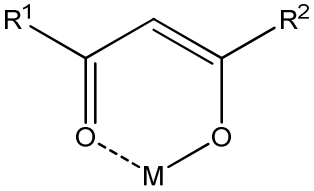 </td><td>Ketoimines
 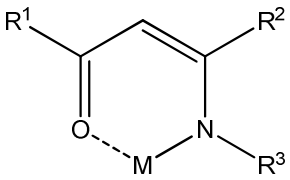 </td></tr>
<tr><td colspan="2">Cyclic ligands
 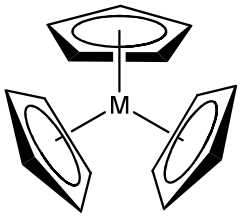 </td><td>Amidines
 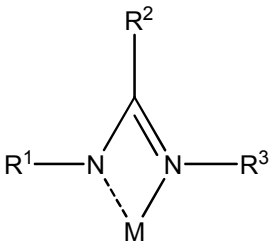 </td><td>Amides
 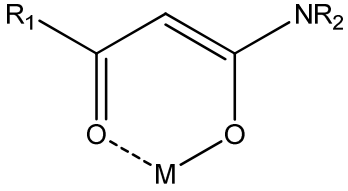 </td></tr>
</table>

In the liquid-delivery MOCVD used for the deposition of thin oxide films, the precursor is dissolved in relatively inert solvent, such as toluene and delivered as liquid to a flash evaporator, where immediate evaporation occurs and precursors in the gas form are transported by carrier gas to reactor chamber and deposition zone. In this way the premature decomposition of the precursor during mass transport can be avoided, especially when the temperature window between vaporization and decomposition is very narrow. Liquid-delivery MOCVD has a requirement that precursors must be soluble and stable for long periods in the chosen solvent and must not react with other precursors in the same solution. If this happens separate sources and injection lines have to be used for each precursor. In addition, for the deposition of complex oxides selected precursors should evaporate in similar temperature 'window'. Otherwise two flash evaporators with different temperatures have to be used to control the mass transport of the elements and thus the stoichiometry of complex oxides films. For optimization of compositional uniformity of the film it is also important that the various precursors deposit oxide within similar temperature regime.

A crucial requirement for the precursor is adequate volatility for sufficient evaporation and transport in the vapour phase without decomposition during evaporation step. In general, volatility is achieved by reduction of intermolecular forces (preventing the formation of dimers, oligomers or polymers). In ideal case, a precursor should be monomeric, with the filled coordination sphere of the metal. However, many alkaline earth metal alkoxides or β-diketonates show a tendency to decompose or oligomerize, since it is challenging to fulfil the coordination sphere of the large ionic radius of such metals like Sr^{2+} = 132 pm [130], Ba^{2+} = 149 pm [130]. Normally, simple monodentate alkoxide act as a terminal, doubly or triply bridging ligand and so oligomeric species can be formed until coordinative saturation of the metal is achieved. The formation of oligomers lowers the solubility as well as volatility of the precursor and makes them less useful as precursors in MOCVD, therefore usually neutral donor ligands as triglyme, tetraglyme or other chelating donors (Table 3.2.2) are used to synthesize a monomeric compound containing alkaline earth metal. The use of bulky and chelating ligands in the precursor is often advantageous, as this can also increase the vapour pressure of the precursor and lower sensitivity towards air/moisture due to steric hindrance of the central metal atom. On the other hand, it has to be noted that a very high thermal stability will cause very high deposition temperatures, which is not suitable in the case of dielectric oxides used in microelectronics (HfO_2, ZrO_2). Furthermore, for microelectronic applications the precursors with fluorinated ligands are also not suitable, because of fluorine contamination which can alter the properties of the films.

Table 3.2.2 Structures and abbreviations of different chelating donor ligands [131,132].

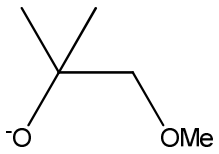 1-Methoxy-methyl-2-propanolate (mmp)	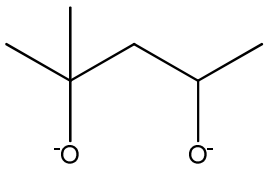 2-Methylpentane-2,4-bis(olate) (mpd)	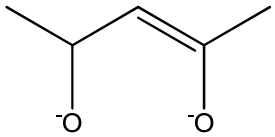 2-pentene-2,4-bis(olate) (acac)
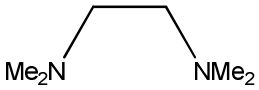 Tetramethylethylene-diamine (TMEDA)	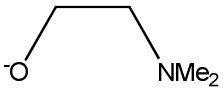 2-Dimethylamino-ethanolate (dmae)	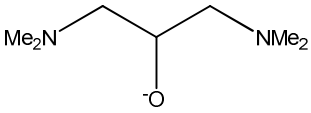 1,3-Bis(dimethylamin)-propan-2-olate (bis-dmap)
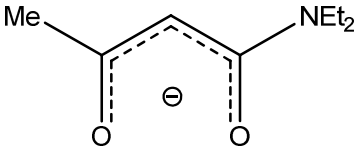 N,N-Diethylacetoacetamide (deacam)	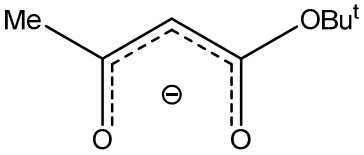 *t*-Butyl acetoacetate (tbaoac)	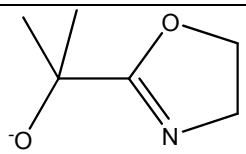 2-(4,4-Dimethyl-4,5-dihydrooxazol-2-yl)propan-2-olate (dmop)

Often alkoxides which possess sufficient volatility are used for the deposition of the films containing transition metals. For the II group (alkaline earth) ions, the β-diketonates are widely used as far as volatility and stability are concerned. In order to increase the volatility of β-diketonates, the alkoxide ligand can be added, therefore the precursor could have the volatility associated to alkoxides and the stability associated to β-diketonates.

In general, the alkoxides have higher vapour pressures than β-diketonates but are less stable, which may lead to lower deposition temperatures. Therefore the combination of ligands with different physical and chemical properties allows getting a good match between the different metal precursors especially if just one flash evaporator is used.

After evaporation of the precursor/precursors in the flash evaporator, the corresponding gaseous mixture is transferred with the help of a carrier gas to the reaction zone, where

decomposition of the molecules takes place at high temperature. The general decomposition sequence of β-diketonate is shown in (Fig. 3.2.1) and consists of three main steps [133]:

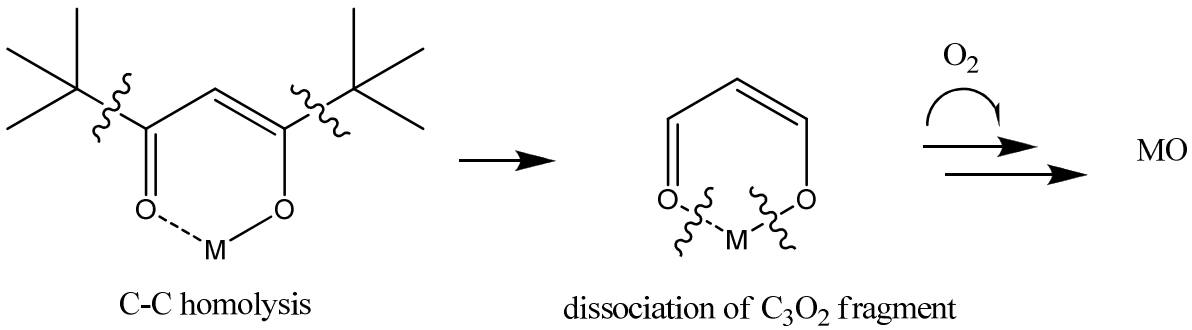

Fig. 3.2.1 General decomposition sequence of β-diketonates.

1 step: homolysis[8] of C-C bond, where tert-butyl groups are removed,

2 step: dissociation of C_3O_2 fragments,

3 step: reaction with oxygen and formation of metal-oxide film.

β-diketonate precursors have many attractive features: relatively easy to synthesize, easy to handle and to modify for tuning their properties, and generally have good volatility. However, due to their high thermal stability high deposition temperatures are required which turn out in C contamination. Carbon can be incorporated in the films because after C-C bond homolysis, $C(CH_3)_3$ groups are removed from the molecule and the resulting radical can react with the M-O bonds in the growing film leading to C incorporation in the layer. With a high oxygen partial pressure in the gas phase, these fragments of the molecule can be further broken or passivated and a high carbon level in the films may be prevented.

3.2.2 Available precursors for metal oxides

The following paragraphs present a literature survey of the available precursors for the deposition of different oxides containing Na, Bi, Ti, Sr, Ru metals with MOCVD.

[8] Chemical bond dissociation of a neutral molecule generating two free radicals.

3.2.2.1 Sodium precursors

The availability of sodium precursors is very limited. Only few papers describe the use of sodium β-diketonate [Na(thd)] and fluorinated sodium [$NaPr(tfa)_3$] (tfa = 1,1,1-trifluoro-2,4-pentadionate) complexes for the deposition of thin films by atomic layer epitaxy method [134] or doping of manganites with sodium by using the [Na(thd)] precursor [135]. For solution depositions normally sodium acetate is used (CH_3COONa) [136].

3.2.2.2 Bismuth precursors

Various Bi precursors, including aryl [137], alkyl [138], β-diketonates [139,140], and alkoxides [141] have been proposed and used for MOCVD applications. Among them, triphenyl bismuth [$Bi(C_6H_5)_3$] represents one of the most commonly used precursors because of its thermal stability upon evaporation and during storage. On the other hand, [$Bi(thd)_3$] is often used as the precursor for the deposition of ferroelectric ($SrBi_2Ta_2O_9$ [142]) or multiferroic ($BiFeO_3$ [143]) layers.

3.2.2.3 Titanium precursors

The most widely used precursors for deposition of Ti-containing thin films by MOCVD are alkoxides of the type [$Ti(OR)_4$], where R = Et, ^{i}Pr, ^{t}Bu, which are volatile and easily prepared [144,145,146,147]. Such type precursors have a tendency to oligomerize due to unsaturated metal center. Therefore more stable compounds are often used. One of the favoured strategies for inhibiting oligomerization in metal alkoxides, as well as increasing the coordination number of highly positively charged central metal atoms is to incorporate bidentate ligands into the complex (Table 3.2.2). Mainly β-diketonates were used as stabilizing ligands. The combination of O^{i}Pr and thd ligands coordinated with Ti yielded the precursors, which are relatively stable and volatile. Due to relatively high volatility associated to alkoxide groups (O^{i}Pr) and stability associated with diketonate (thd) groups, in recent years the [$Ti(O^{i}Pr)_2(thd)_2$] precursor was used for deposition of Ti-containing films [148,149,150].

3.2.2.4 Strontium precursors

Strontium β-diketonate [$Sr(thd)_2$] is commonly used as a precursor for the deposition of strontium-containing films deposited by liquid-delivery MOCVD technique. As described earlier, alkaline-earth metal β-diketonates have some drawbacks such as low volatility, decomposition during evaporation and high sensitivity to water and carbon dioxide, due to large radius of alkaline earth metal. To fulfil the coordination sphere of the metal and to screen the strong polarization of the Sr atom, mono- or oligo-ethers may be used. Precursors containing stabilising triglyme, tetraglyme molecule vaporizes at temperatures lower than for non-stabilised $Sr(thd)_2$ [151] and, furthermore, sensitivity to water and carbon dioxide of such compound is suppressed.

3.2.2.5 Ruthenium precursors

Several Ru metal-containing complexes have been examined as potential MOCVD precursors for the deposition of Ru-containing thin films, including a) ruthenocene [152] and its alkyl substituted derivatives such as [$Ru(C_5H_4Et)_2$] [153], b) metal carbonyl complexes, [$Ru(CO)_3(C_6H_8)$] [154], [$Ru_3(CO)_{12}$] [155], c) and tris-β-diketonate complexes, such as [$Ru(acac)_3$] [156,157], [$Ru(tfa)_3$] [158], [$Ru(thd)_3$] [159,160,161,162], d) organo-metallic alkenyl and alkene complexes of bis(2,4-dimethylpentadienyl)ruthenium [163], and arene complexes as [$Ru(C_3H_5)_2(COD)$] (COD = 1,4-cyclooctadiene) [164]. As mentioned earlier, highly volatile precursors, which do not decompose during evaporation, and are relatively stable in the dissolved solvent are necessary for the growth of thin films with MOCVD. Metal β-diketonates meet these criteria; therefore this class of compounds is widely used for deposition of Ru-containing films in MOCVD process.

3.2.3 Thermal and mass spectrometry analysis of precursors used for the deposition of $SrRuO_3$, $Bi_4Ti_3O_{12}$ and $(Na, Bi)Ti_4O_{12}$ films

The main chemical and physical properties of the precursors used for the deposition of epitaxial perovskite and perovskite-like oxide thin films ($SrRuO_3$, $Bi_4Ti_3O_{12}$, $(Na, Bi)_4Ti_3O_{12}$) (Table 3.2.3) will be discussed in this section. The thermogravimetric (TG) and differential thermal analysis (DTA) were carried out in inert gas atmosphere (N_2) for each precursor.

Scope of these investigations was to determine the evaporation and decomposition temperatures of the precursors at ambient pressure and to check to compatibility between different precursors used for the deposition of the films. The vaporization studies were done also at two different temperatures in order to determine the evaporation rate of the solid precursors, where weight loss (has to be constant over long periods of time) of each complex as a function of time was registered.

Furthermore, the EI-MS (electron impact mass spectrometry) results of each precursor will be presented. However, the EI-MS results obtained in this study do not reflect the actual processes in MOCVD, because the latter is carried out at high temperatures and under pressure, while decomposition of molecules in mass spectrometry is induced by electron beam not by temperature. Nevertheless, the results are still useful for studying the decomposition and oligomerization of the metal-organic precursors.

Table 3.2.3 Precursors used for the deposition of perovskite and perovskite-like films.

Structure	Name/ Abbreviations
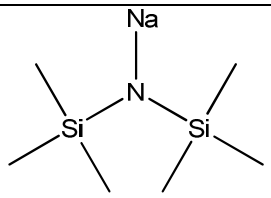	Sodium bis(trimethylsilyl)amide [NaTMSA] or [$NaN(Si(CH_3)_3)_2$]
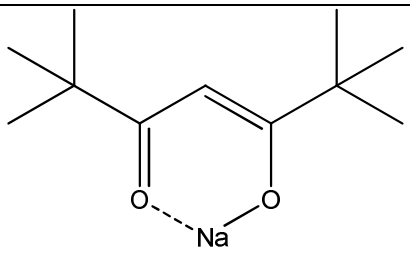	2,2,6,6-tetramethyl-3,5-heptandionato-sodium [Na(thd)]
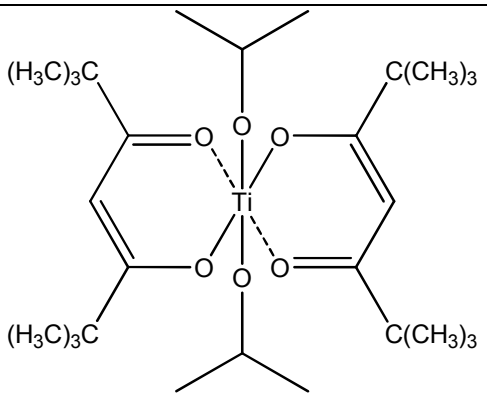	Bis(isopropoxy)bis(2,2,6,6-tetramethyl-3,5-heptandionato)titanium [$Ti(O^iPr)_2(thd)_2$]

Table 3.2.3 Precursors used for the deposition of perovskite and perovskite-like films (continued).

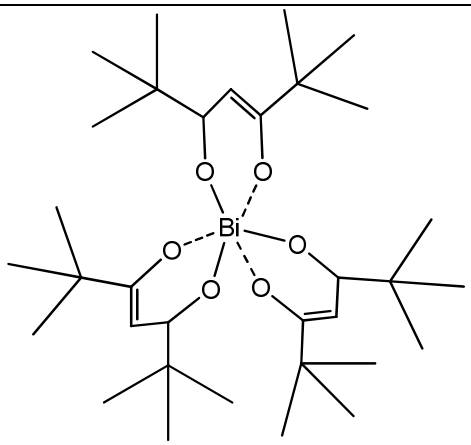	Tris(2,2,6,6-tetramethyl-3,5-heptandionato)bismuth [$Bi(thd)_3$]
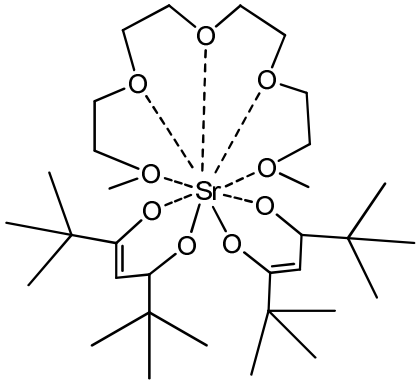	Tris(2,2,6,6-tetramethyl-3,5-heptandionato)strontium tetraglyme complex [$Sr(thd)_2$tetraglyme]
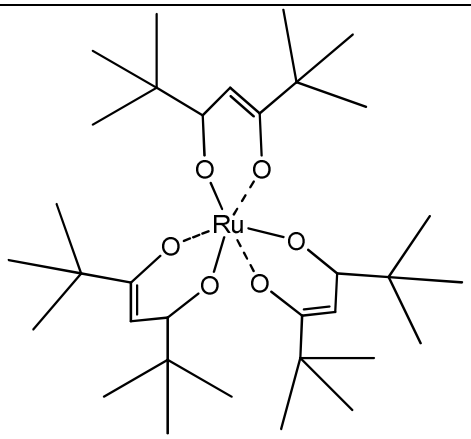	Tris(2,2,6,6-tetramethyl-3,5-heptandionato)ruthenium [$Ru(thd)_3$]

3.2.3.1 [Na(thd)]

The measured TG-DTA curves of [Na(thd)] are shown in Fig. 3.2.2. The loss of weight of [Na(thd)] precursor occurs in two steps, starting at about 52 °C and finishing at a temperature of 305 °C. From DTA curve one can see two endothermic and one exothermic peak. First indistinct endothermic peak is associated with the first weight loss at 76 °C, where 9.2 % of mass was lost which can be related to evaporation of coordinated solvent or free

ligand left after the synthesis of the compound [165]. The endothermic peak at 214 °C is assigned to the melting temperature of the compound, which agrees with the melting point of 217 °C reported in the literature [134]. The exothermic peak shows the decomposition of [Na(thd)] compound which occurs at 305 °C. The compound decomposes without any residuals, showing that no decomposition of the precursor happened during the evaporation.

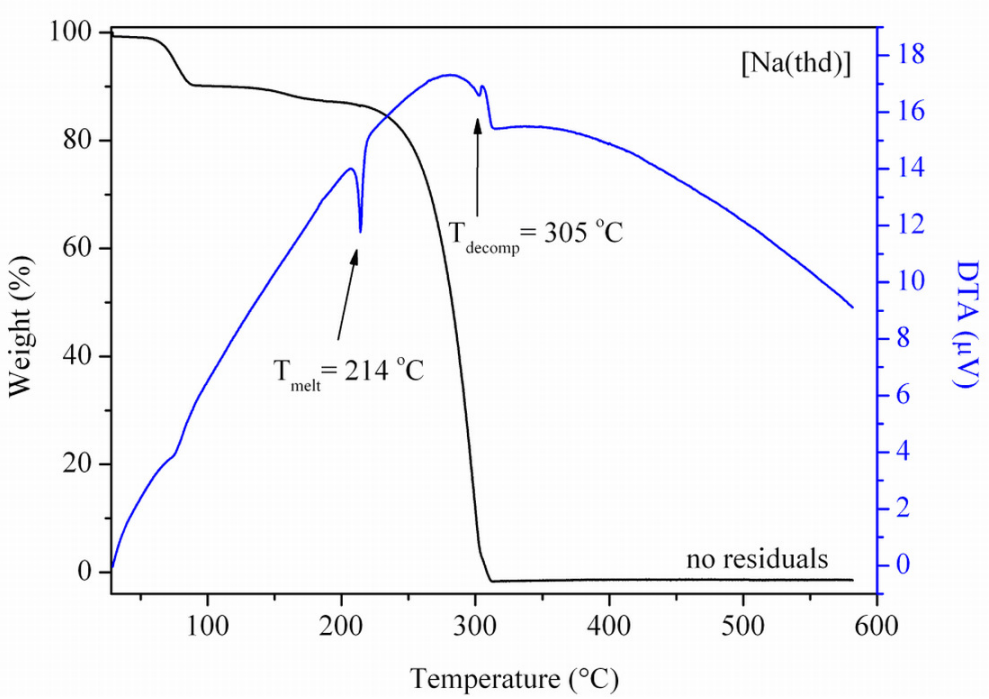

Fig. 3.2.2 Simultaneous TG-DTA curves of [Na(thd)] precursor.

The characteristic TG isotherms of [Na(thd)] are shown in Fig. 3.2.3. Surprisingly, evaporation at lower temperature (120 °C) is five times faster compared to the one at higher temperature (150 °C). This very atypical behaviour can be attributed to the oligomerization of the compound. Oligomerization always lowers the evaporation rate of the compound. Additionally, oligomerization may render the formed compound completely non-volatile.

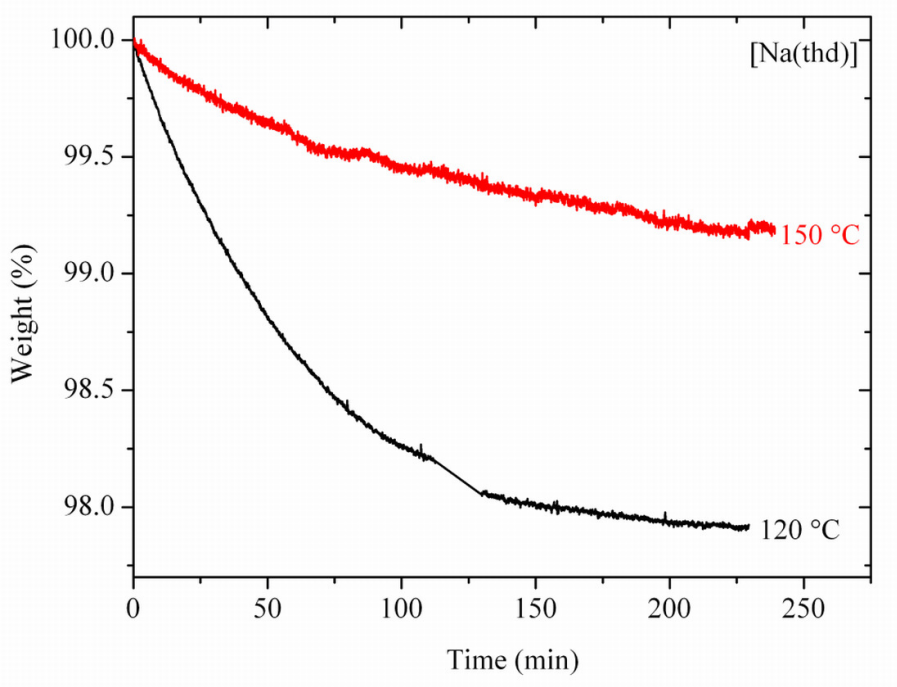

Fig. 3.2.3 Mass loss as a function of time at two different temperatures of [Na(thd)] precursor.

The evaporation rates of [Na(thd)] compound at two different temperatures is also not compatible with evaporation rates of other precursors used for the deposition of (Na, Bi)$_4$Ti$_3$O$_{12}$ films (Table 3.2.4). Therefore use of such compound can lead to difficulties in incorporation of the Na metal in the films and poor reproducibility in properties of deposited thin films if the same evaporation temperatures as for Bi and Ti precursors are used.

Table 3.2.4 Average evaporation rates (mg/min) of the precursors used for the deposition of (Na, Bi)$_4$Ti$_3$O$_{12}$ films.

Temperature, °C	[Na(thd)]	[NaTMSA]	[Bi(thd)$_3$]	[Ti(O^{i}Pr)$_2$(thd)$_2$]
120	0.2×10^{-3}	0.7×10^{-3}	1.1×10^{-3}	0.68×10^{-3}
150	0.04×10^{-3}	1.9×10^{-3}	1.3×10^{-3}	5×10^{-3}

As it was mentioned above, mass spectrometry helps to detect the weakest bonds in metal-organic compounds and therefore the possible decomposition ways. The prevailing mass signals of [Na(thd)] precursor are shown in Fig. 3.2.4. The most intensive mass signals occur at lower mass to charge ratios (< 200). The peaks at m/z = 43, 57, 127, 184 represent fragments of the thd ligand corresponding to $[HC(CH_3)_2]^+$, $[C(CH_3)_3]^+$, $[OCCH_2COC(CH_3)_3]^+$ and the ligand itself $[(CH_3)_3CCOCH_2COC(CH_3)_3]^+$. The intermediate values at m/z = 85, 100,

156 are also attributed to the fragments of the thd ligand. The small molecular peak at 207 corresponds to [Na(thd)]. Additional peaks with mass-to-charge ratios higher than 207 are also observed, whereas the peak at mass number of 414 corresponded to the dimer of $[Na_2(thd)_2]$. Additional peaks at 349 and 473 were not identified so far. Formation of the dimer leads to the very low evaporation rates observed from TG isothermal studies.

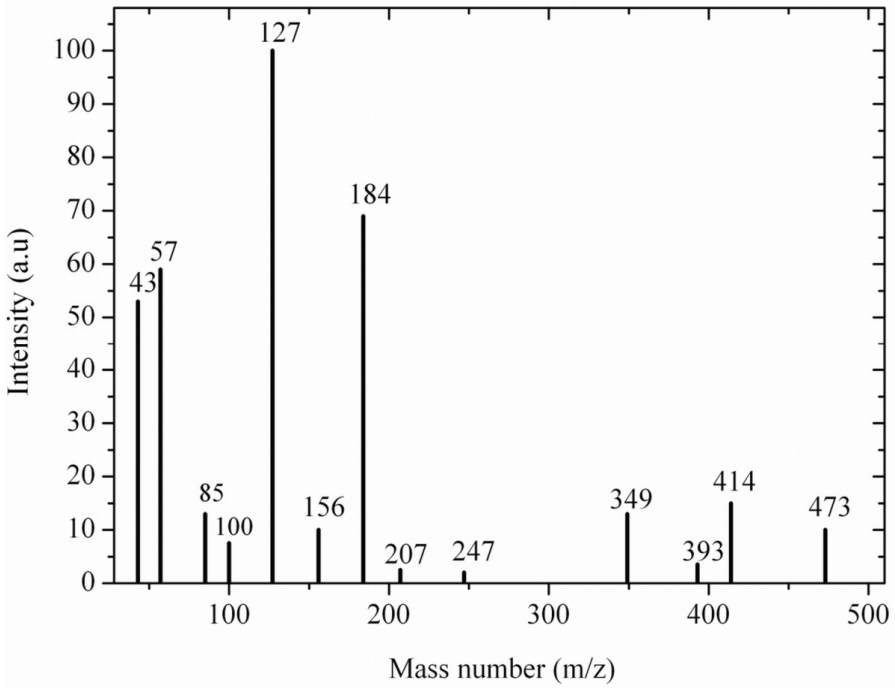

Fig. 3.2.4 Mass spectra of [Na(thd)] precursor. The signals represent individual mass fragments.

3.2.3.2 [NaTMSA]

As alternative to the [Na(thd)] which tends to oligomerize a novel sodium bis(trimethylsilyl)amide ([NaTMSA]) precursor was synthesized in the course of this work. Simultaneous TG-DTA measurements were made in order to examine the thermal behaviour of the newly developed precursor. TG curve (Fig. 3.2.5) showed that this precursor evaporated in one step starting at 152 °C and finishing at 277 °C with 4.56 % residuals left after it, showing a partial decomposition of the precursor during the evaporation step. The DTA curve showed two endothermic peaks at 152 °C and at 174 °C. It was not possible to detect exactly the melting temperature, because it was melting in the 159 – 169 °C range, therefore the second endothermic peak at 174 °C was attributed to some phase transitions of the compound. The exothermic peak at 277 °C confirms the decomposition of the precursor.

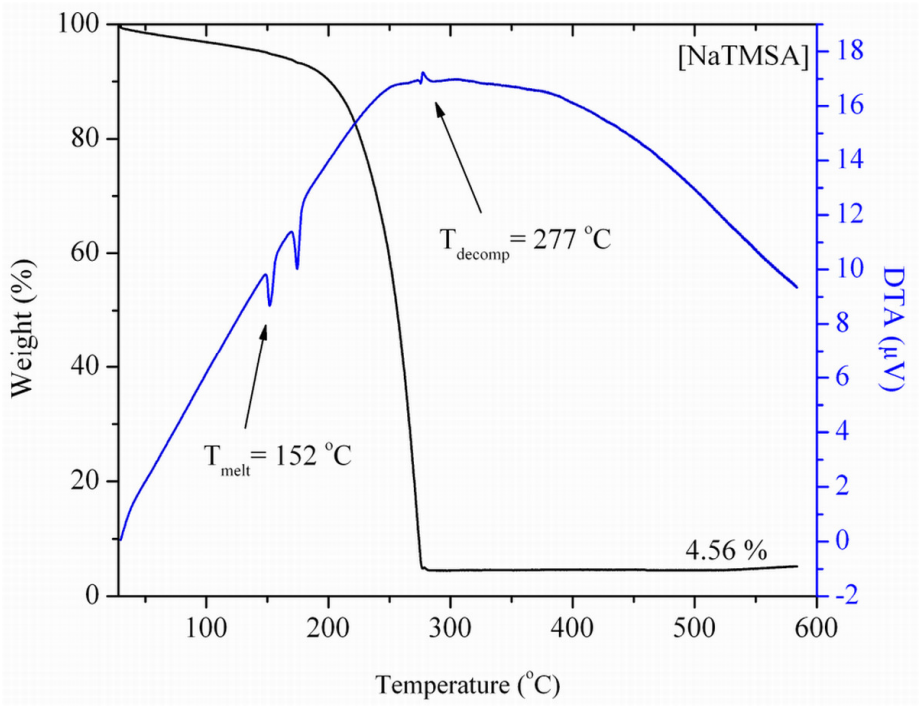

Fig. 3.2.5 Simultaneous TG-DTA curves of [NaTMSA] precursor.

The mass loss as a function of time for the [NaTMSA] precursor at two different temperatures is shown in Fig. 3.2.6. It is generally known that evaporation rate increases as a function of temperature and it is evident in the case of [NaTMSA] as well. It can be seen that at both temperatures (120° C and 150 °C) the mass loss slightly deviates. The evaporation is faster up to 50 min (2.8×10^{-3} mg/min) in both temperatures and afterwards is constant. The evaporation rate in the time period of 50 - 230 min is equal to 0.7×10^{-3} mg/min and 1.9×10^{-3} mg/min at 120 °C and 150 °C, respectively. The evaporation rates of this Na compound is compatible with evaporation rates of $[Bi(thd)_3]$ (see Table 3.2.4), therefore by using solid precursors the same supply of Na and Bi to the reaction chamber can be achieved if the same evaporation temperatures are used.

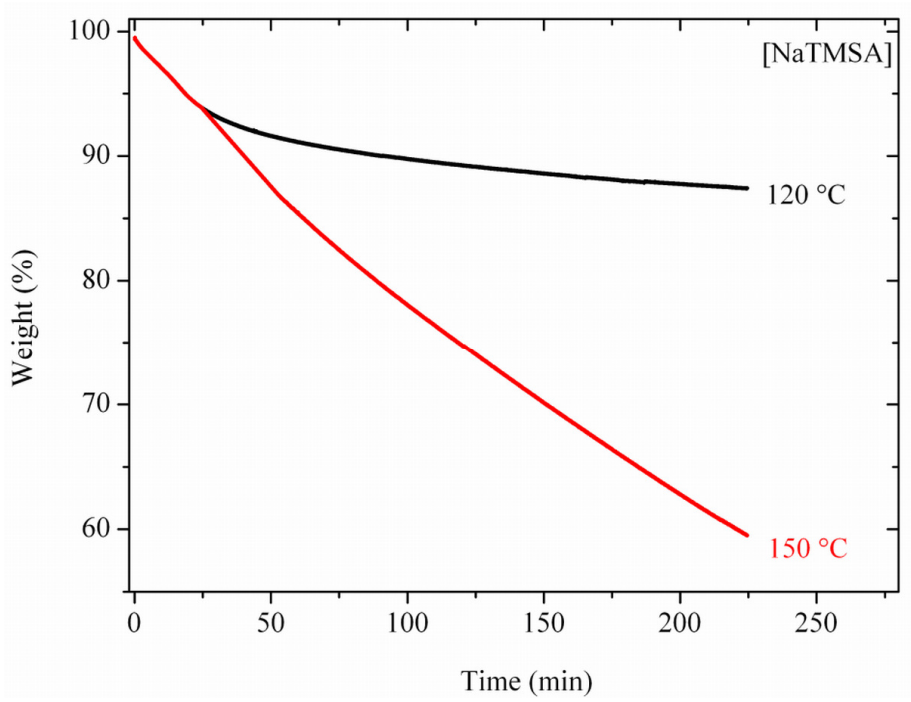

Fig. 3.2.6 Mass loss as a function of time at two different temperatures of [NaTMSA] precursor.

A small molecular peak at m/z = 183 was observed in the mass spectra of the $[NaN(Si(CH_3)_3)_2]$ compound (Fig. 3.2.7). The peak at the m/z = 221 has a higher ratio than the molecular peak of the precursor and can be attributed to different combinations of the ligand $HNSi(CH_3)_2$ or other fragments resulted after ionization of the compound. The peaks at lower m/z = 39, 73, 130, 147, 169 positions, than the molecular peak (m/z = 183), can be attributed to the following fragments: $[NaCH_3]$, $[Si(CH_3)_3^+]$, $[NSi_2(CH_3)_4]^+$, $[HNSi_2(CH_3)_5]^+$, $[NaNSi_2(CH_3)_5]^+$. No oligomerization of the compound was observed which is also in agreement with TG isothermal studies where evaporation of the compound is faster at higher temperatures.

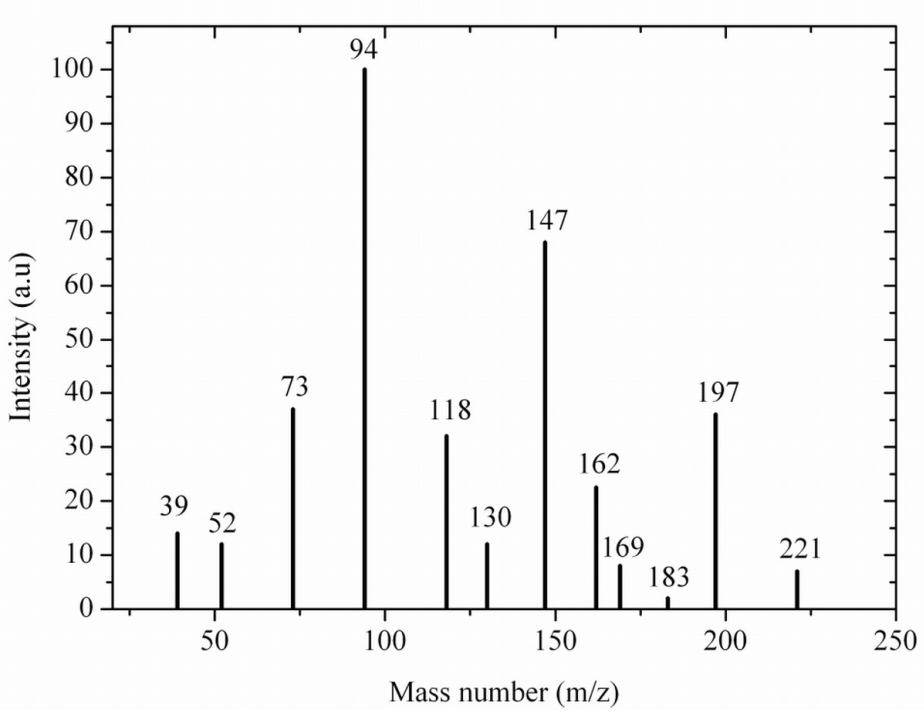

Fig. 3.2.7 Mass spectra of [NaTMSA] precursor. The signals represent individual mass fragments.

3.2.3.3 [Bi(thd)$_3$]

TG-DTA data in Fig. 3.2.8 shows that evaporation and partial decomposition occurs simultaneously in the case of [Bi(thd)$_3$] precursor. First endothermic peak at 116 °C in DTA curve can be assigned to some phase transitions or probably to the partial decomposition of the compound, because a slight weight loss is observed also in the TG curve for the same temperature range. This slight weight loss can be also assigned to the evaporation of coordinated solvent, free ligand or water [165]. The second endothermic peak at 129 °C is assigned to the melting point of the compound, which is in a slight contradiction with the melting point reported in the literature. Bedoya et al. [166] reported that melting temperature of [Bi(thd)$_3$] is equal to 117.6 °C and the second endothermic peak at 135.1 °C was assigned to the partial decomposition of the precursor. Kang et al. [139] observed only one endothermic peak at 120 °C and assigned it to the melting temperature of the precursor, because no weight loss in this temperature range was observed. The weight loss starting from 190 °C shows a clean evaporation process, even if the small fraction of the precursor decompose, which is evident from the amount of the residuals 3.13 %. The endothermic peak at 277 °C is associated with the complete evaporation of the Bi precursor.

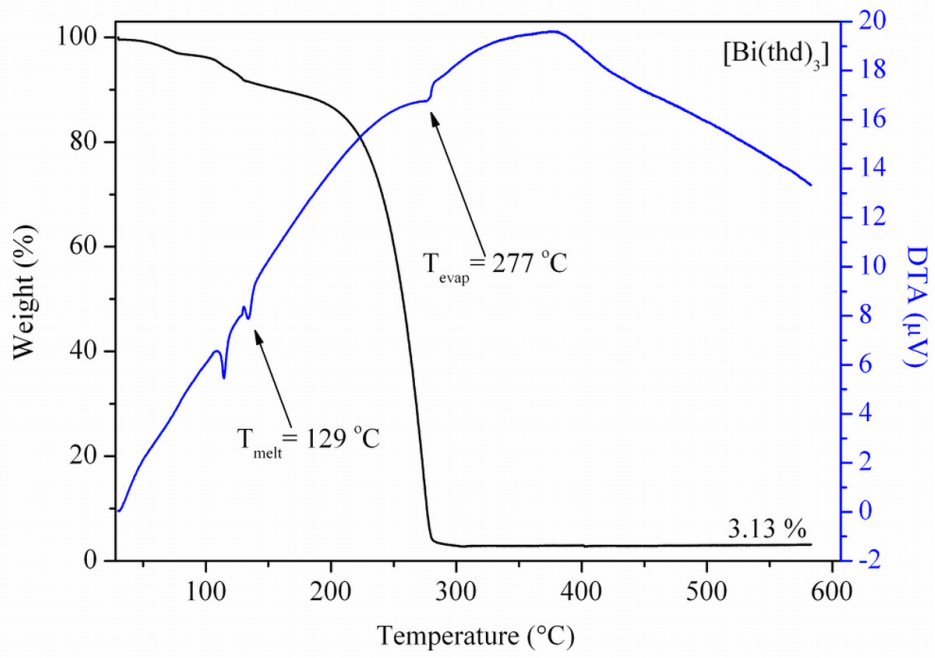

Fig. 3.2.8 Simultaneous TG-DTA curves of $[Bi(thd)_3]$ precursor.

The vaporization/sublimation studies (Fig. 3.2.9) of $[Bi(thd)_3]$ showed a constant mass transport over long periods of time at 120 °C with an evaporation rate of 1.1×10^{-3} mg/min. A slight increase in sublimation rate was observed at 150 °C, above which the average evaporation rate is 1.3×10^{-3} mg/min. Nevertheless, the mass supply of the material is constant over long periods of time and almost no difference in evaporation rate occurs at both temperatures.

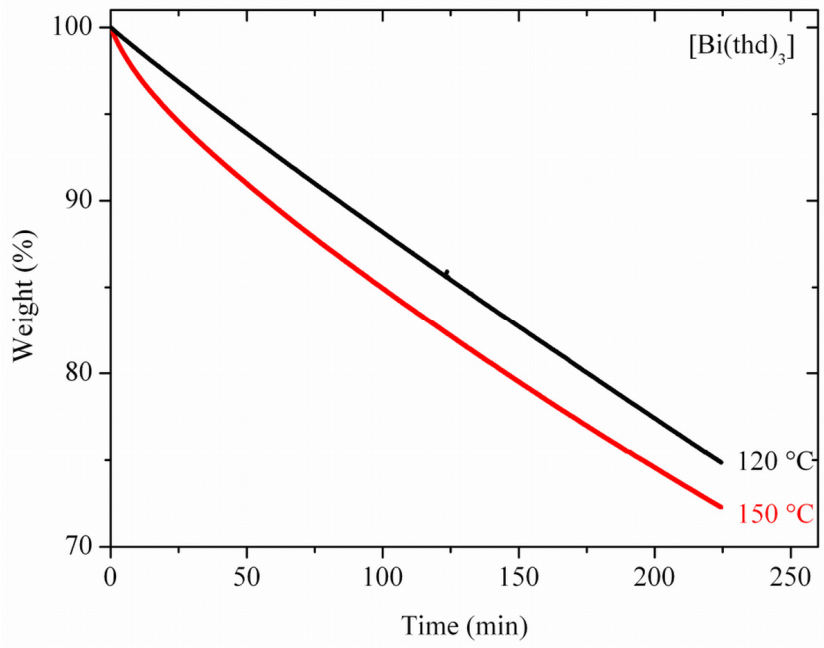

Fig. 3.2.9 Mass loss as a function of time at two different temperatures of $[Bi(thd)_3]$ precursor.

In the mass spectra (Fig. 3.2.10) the molecular $[Bi(thd)_3]^+$ peak occurs at mass-to-charge ratio of 758. The sequential liberation of the thd ligands is evident from the m/z = 575 and 392 peaks assigned respectively to $[Bi(thd)_2]^+$ and $[Bi(thd)]^+$ fragments. Relatively intensive peaks at m/z = 57 and 127 are attributed to the fragments $[C(CH_3)_3]^+$ and $[OCCH_2COC(CH_3)_3]^+$ of thd ligand. The dissociation of one of the Bi-O between the Bi atom and the thd ligand in such a way that ligand chain remains bonded to the Bi atom at one end is evident from the m/z peak at 335. No oligomerization of the compound was observed which is also in agreement with TG-DTA and TG isothermal studies.

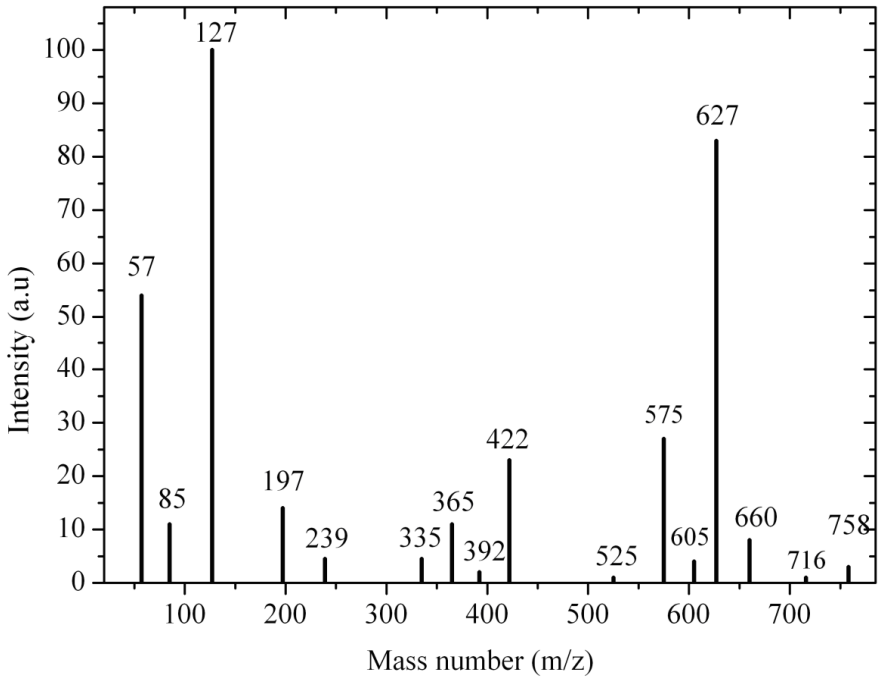

Fig. 3.2.10 Mass spectra of $[Bi(thd)_3]$ precursor. The signals represent individual mass fragments.

3.2.3.4 $[Ti(O^iPr)_2(thd)_2]$

The $[Ti(O^iPr)_2(thd)_2]$ precursor looses mass in one single step starting from 103 °C and finishing at 224 °C as can be seen from the simultaneous TG-DTA curves shown in Fig. 3.2.11. A small kink in the TG curve at about 103 °C may be assigned to the loss of water traces in the precursor, due to short exposure to the air during transfer of the material to TG-DTA measurement technique. Three clear endothermic peaks at 59.7 °C, 162.5 °C and 224 °C and one exothermic at about 257 °C appear in TG-DTA curves. The first two endothermic

peaks may be assigned to phase transitions, whereas the peak at 224 °C corresponds to the evaporation temperature of titanium precursor. The melting of the complex appeared at 201 °C. The only endothermic peak at about 257 °C shows the decomposition process of the precursor, nevertheless after evaporation process no residuals were left.

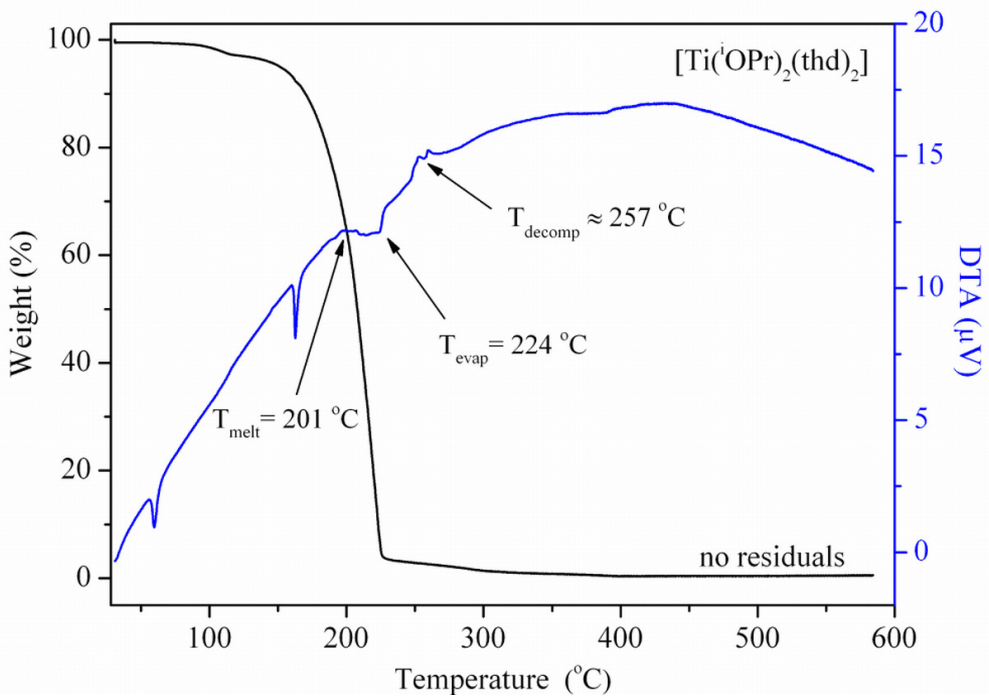

Fig. 3.2.11 Simultaneous TG-DTA curves of $[Ti(O^iPr)_2(thd)_2]$ precursor.

The mass loss as a function of time of the $[Ti(O^iPr)_2(thd)_2]$ is shown in Fig. 3.2.12. The corresponding evaporation rates are 0.68×10^{-3} mg/min for 120 °C and $\sim 5.0 \times 10^{-3}$ mg/min for 150 °C temperatures, respectively. It is evident that the mass loss of the precursors is constant over long periods of time in the used temperature range. However, evaporation at 150 °C is five times higher than at 120 °C and in comparison to [NaTMSA] and $[Bi(thd)_3]$ precursors used for the growth of epitaxial $Bi_4Ti_3O_{12}$ and $(Na, Bi)_4Ti_3O_{12}$ films (Table 3.2.4). Therefore, for the CVD process the evaporation temperature of $[Ti(O^iPr)_2(thd)_2]$ should be between 120 °C and 150 °C in order to have similar evaporation rates and mass supply of the $[Ti(O^iPr)_2(thd)_2]$ and already mentioned precursors to the reaction chamber.

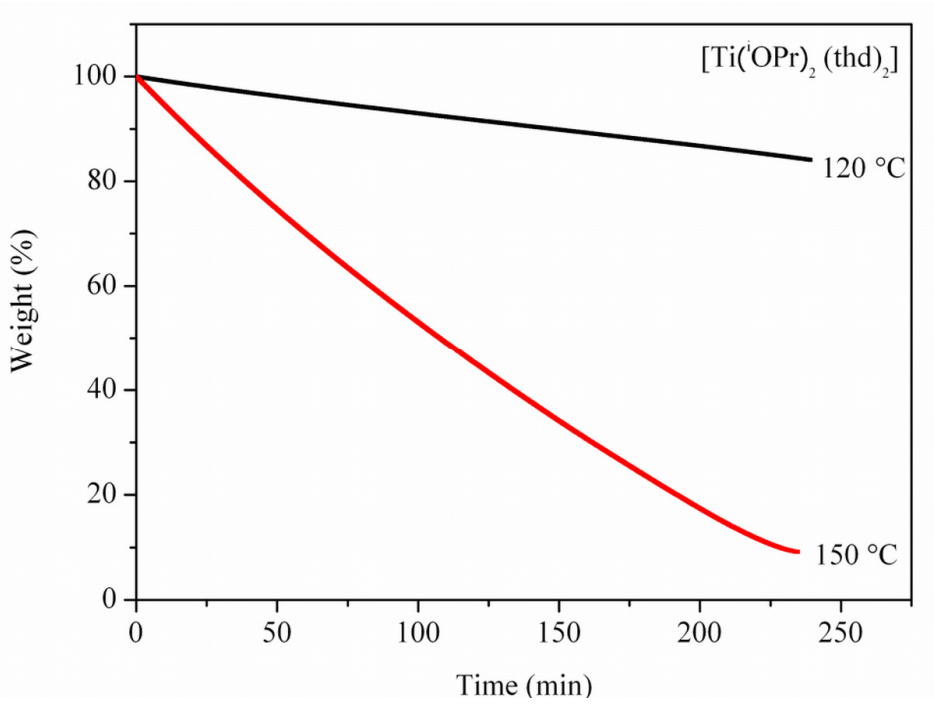

Fig. 3.2.12 Mass loss as a function of time at two different temperatures of $[Ti(O^iPr)_2(thd)_2]$ precursor.

The molecular peak at m/z = 532 of the $[Ti(O^iPr)_2(thd)_2]$ compound was not observed in the mass spectra (Fig. 3.2.13). The peak at the m/z = 597 has a higher ratio than the molecular peak of the precursor and according to Turgambaeva et al. [167] can be attributed to $[Ti(thd)_3]^+$, still showing monomeric composition, therefore TG isotherms show normal behaviour, where evaporation of the compound is faster at higher temperatures. The peaks at lower m/z = 57, 265, 349, 414, 473, 517 positions, than the molecular peak (m/z = 532), can be attributed to the following fragments: $[C(CH_3)_3]^+$, $[Ti(OH)_2(thd)]$, $[Ti(thd)(O^iPr)_2]^+$, $[Ti(thd)_2]^+$, $[Ti(thd)_2(O^iPr)]^+$, $[Ti\ (thd)_2(O^iPr)(OC_2H_4)]^+$. First of all, the tert-butyl ($-C(CH_3)_3$) groups from thd ligand, or methyl ($-CH_3$) groups from (O^iPr) dissociate leading to the subsequent fragmentations of the compound.

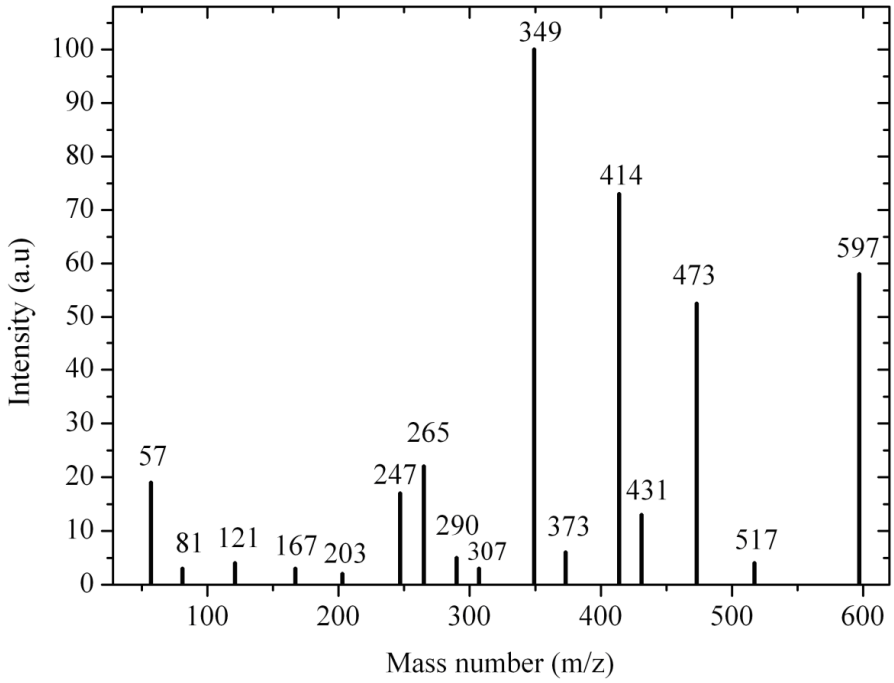

Fig. 3.2.13 Mass spectra of $[Ti(O^iPr)_2(thd)_2]$ precursor. The signals represent individual mass fragments.

3.2.3.5 [Sr(thd)$_2$tetraglyme]

The endothermic peak at 77 °C (Fig. 3.2.14) is assigned to the melting temperature of the precursor, whereas DSC and melting temperature measurements showed that the compound melts at 71 °C. The difference may be probably explained considering the different amounts of used precursor during DTA and DSC measurements.

The used Sr complex loses weight in two distinct temperature regions. The first weight loss occurs between 123 °C and 230 °C, and amounts to about 30 % of initial weight. Considering the fact that the weight fraction of tetraglyme adduct included in Sr complex is 33 %, it is assumed that the first weight loss is due dissociation of tetraglyme adduct from the precursor complex [139]. The second weight loss was observed in the 220 – 350 °C temperature interval and corresponds to the evaporation of the compound. At 350 °C the compound completely evaporates with only 1.3 % residuals of the initial weight, which is also confirmed by the endothermic peak in the DTA spectrum. The exact evaporation temperatures of each precursor have to be always optimized for the MOCVD process in order to have the highest incorporation efficiency of the metal in the film. Especially in this case the decomposition of the tetraglyme molecule can influence the volatility of the Sr precursor.

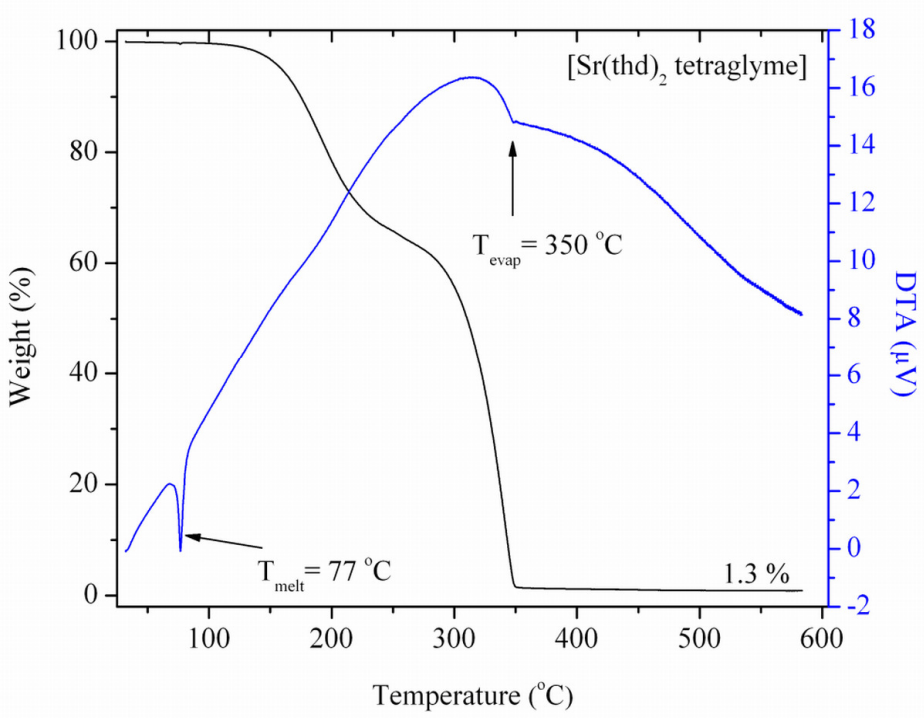

Fig. 3.2.14 Simultaneous TG-DTA curves of [Sr(thd)$_2$tetraglyme] precursor.

An interesting behaviour in the TG isotherms of [Sr(thd)$_2$tetraglyme] compound was observed (Fig. 3.2.15). At both temperatures different evaporation rates were detected. However, the evaporation rate at 120 °C differs not so much from 1.9×10^{-3} mg/min to 1.0×10^{-3} mg/min (in all measurement range) leading to almost constant mass loss over a long periods of time. On the contrary, a strong deviation of mass loss of [Sr(thd)$_2$tetraglyme] occurs at 150 °C. The material is evaporated faster in the first 50 minutes, with evaporation rate of 4×10^{-3} mg/min, and more slowly beyond this time (1.5×10^{-3} mg/min). Therefore, the TG isotherms show a cross point at 200 minutes. Beyond this time the mass loss rate is higher for the lower temperature. This effect can be explained by the dissociation of tetraglyme adduct starting from 123 °C (TG curve), which leads to a reduced volatility of the compound [139] and therefore a lower material supply (of solid precursor) at higher evaporation temperature after a certain period of time.

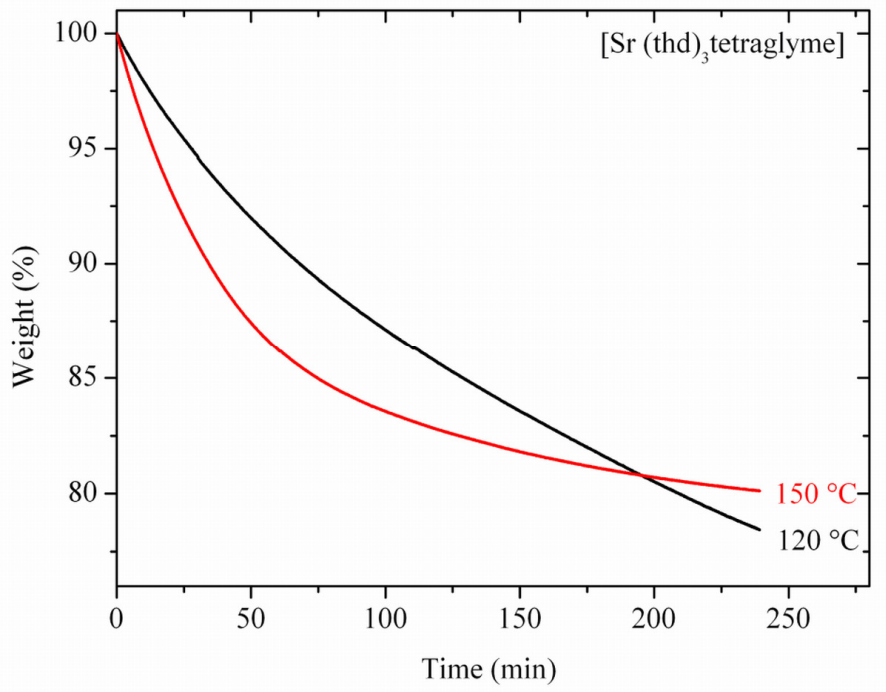

Fig. 3.2.15 Mass loss as a function of time at two different temperatures of [Sr(thd)$_2$tetraglyme] precursor.

Sr precursor was further investigated with electron impact mass spectrometry in order to study the decomposition properties: the weakest bondings in the compound. In Fig. 3.2.16 the main mass signals are reported. The first weight loss starting from 123 °C in TG curve was assigned to the liberation of tetraglyme adduct from the molecule of the [Sr(thd)$_2$tetraglyme] compound. The characteristic peaks representing fragments of tetraglyme are clearly visible in the mass spectra at m/z = 59 and 103 and are assigned to $[CH_3OC_2H_4]^+$ and $[CH_3OC_2H_4OC_2H_4]^+$, which are stronger in intensity than peak at m/z = 127 corresponding to the fragment of thd ligand $[OCCH_2COC(CH_3)_3]^+$. Therefore, tetraglyme adduct is easier liberated as thd ligand from the complex. The dissociation of the tert-butyl group from the thd ligand is evident from the peak at m/z = 397 $[Sr(thd)(CH_3)_3OCCHCOC(CH_3)_3]^+$. The peaks at m/z = 271 and 454 are assigned to the $[Sr(thd)]^+$ and $[Sr(thd)_2]^+$ fragments. No characteristic peak related to [Sr(thd)$_2$tetraglyme] was observed at 677. According to the literature [151] peak at m/z = 725 can be attributed to the oligomerized fragment $[Sr_2(thd)_3]^+$ due to easy liberation of the tetraglyme adduct, leading to unsaturated metal ion. The oligomerization can cause lower evaporation rates at higher temperatures as has been seen in Fig. 3.2.15.

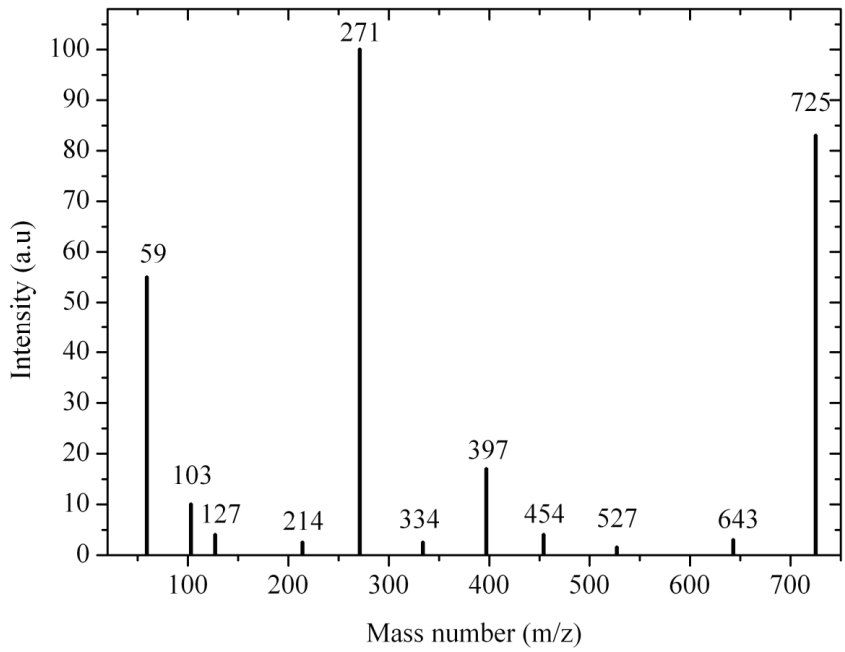

Fig. 3.2.16 Mass spectra of [Sr(thd)$_2$tetraglyme] precursor. The signals represent individual mass fragments.

3.2.3.6 [Ru(thd)$_3$]

The measured TG-DTA curves of [Ru(thd)$_3$] are shown in Fig. 3.2.17. The [Ru(thd)$_3$] precursor evaporated in one step starting at 140 °C and finishing at the temperature of 250 °C. The compound vaporizes completely without any residuals, which proves that no dissociation occurred during evaporation of the precursor. From DTA curve six endothermic peaks can be seen, whereas DSC showed only three of them. The first three occur probably due to phase changes while the fourth at 212 °C is the melting temperature of Ru β-diketonate. It agrees quite well with the published melting temperatures of 216 °C [168] and 218 °C [161] of [Ru(thd)$_3$].

The most important thing is that the temperature window of evaporation of this Ru compound and co-precursor [Sr(thd)$_2$tetraglyme] is in the similar temperature window, therefore both precursors were used for the growth of $SrRuO_3$ films by using the same flash evaporator in MOCVD process. In order to avoid any possible pre-reactions of [Ru(thd)$_3$] and [Sr(thd)$_2$tetraglyme] precursors, two separate bottles with precursor solutions were used.

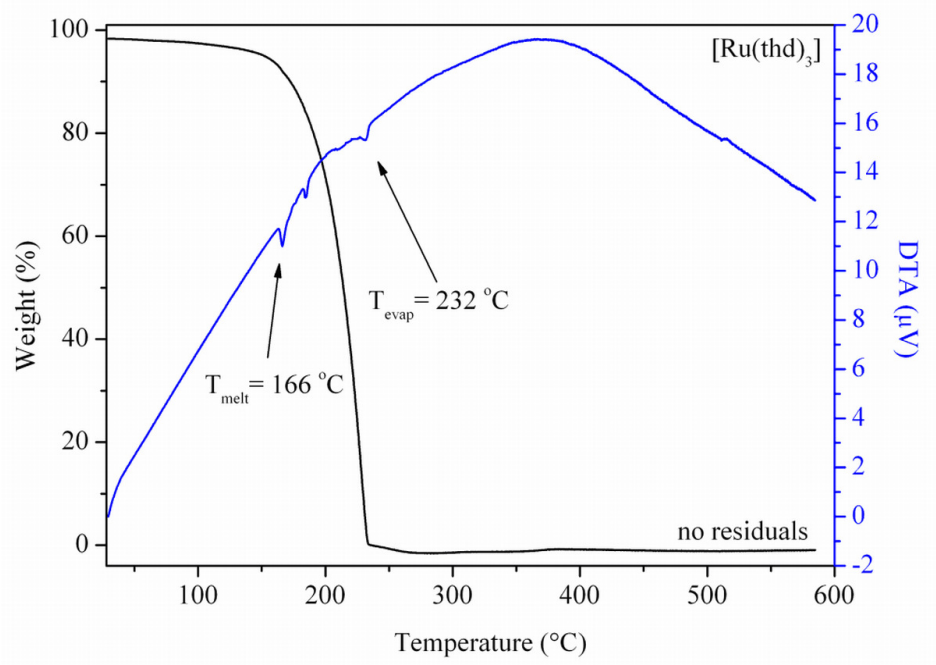

Fig. 3.2.17 Simultaneous TG-DTA curves of [Ru(thd)$_3$] precursor.

The characteristic TG isotherms of [Ru(thd)$_3$] are shown in Fig. 3.2.18. It is evident that the mass loss of the precursor is constant over long periods of time at 120 °C temperature and only slightly deviates at 150 °C in the range of evaporation rates from 4.1×10^{-3} to 3×10^{-3} mg/min. However, evaporation at 150 °C is ten times faster than at 120 °C.

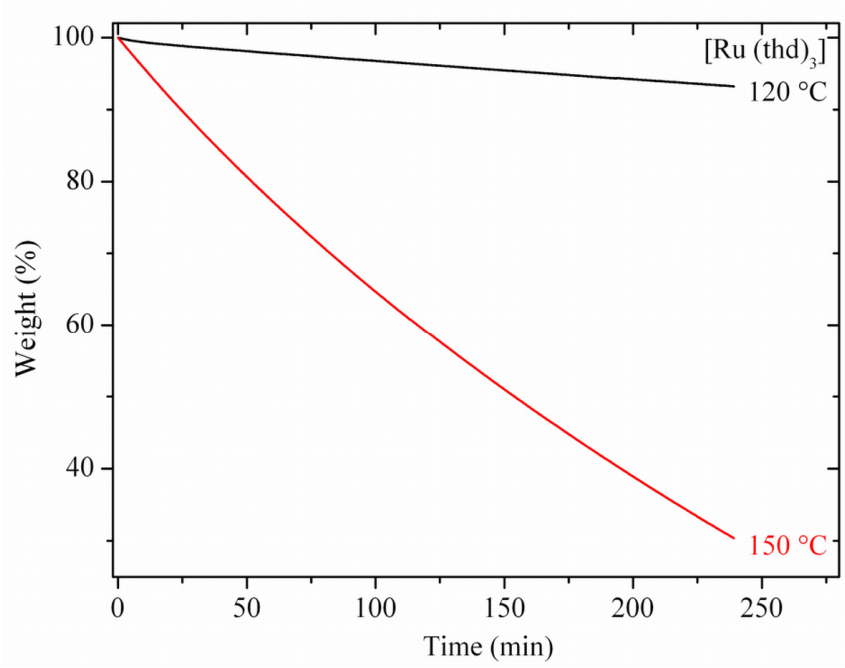

Fig. 3.2.18 Mass loss as a function of time at two different temperatures of [Ru(thd)$_3$] precursor.

In comparison to [Sr(thd)$_2$tetraglyme] precursor, used for the growth of epitaxial $SrRuO_3$ films, [Ru(thd)$_3$] evaporates at least three times slower at 120 °C and two times faster at 150 °C (see Table 3.2.5). Due to the differences in the rates of evaporation, [Sr(thd)$_2$tetraglyme] and [Ru(thd)$_3$] precursors are not compatible at the investigated evaporation temperatures. Therefore, for the depositions of $SrRuO_3$ films, either the ratio of the elements in the precursor solution or evaporation temperatures should be adjusted in order to get stoichiometric films.

Table 3.2.5 Average evaporation rates (mg/min) of the precursors used for the deposition of $SrRuO_3$

Temperature, °C	[Sr(thd)$_2$tetraglyme]	[Ru(thd)$_3$]
120	1.1×10^{-3}	0.3×10^{-3}
150	1.5×10^{-3}	3.3×10^{-3}

The fragmentation of [Ru(thd)$_3$] compound is shown in Fig. 3.2.19 and can be described as follows. The first step is dissociation of one of the thd ligands. The molecular $[Ru(thd)_3]^+$ peak occurs at m/z = 651, while peak at m/z = 468 shows that only two thd ligands are bonded to Ru atom $[Ru(thd)_2]^+$. The relatively intense peaks at 127 and 57 are assigned to the corresponding fragments of $[OCCH_2COC(CH_3)_3]^+$, $[C(CH_3)_3]^+$, related to dissociation of thd ligand.

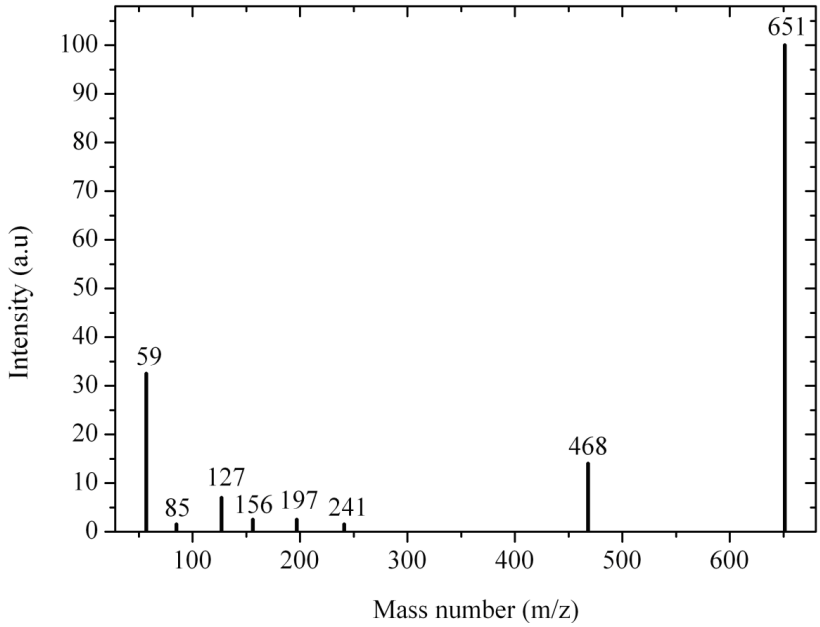

Fig. 3.2.19 Mass spectra of [Ru(thd)$_3$] precursor. The signals represent individual mass fragments.

3.3 Deposition of epitaxial $SrRuO_3$ films

No systematic and detailed investigations of the influence of the growth conditions on the structural and electronic properties of thin $SrRuO_3$ films epitaxially grown by the MOCVD method has been performed yet. Since MOCVD has some advantages like uniform film thickness, easy control of film composition and higher throughput, it is a method which is much more interesting for industrial and technological applications. However, most studies on $SrRuO_3$ have been done with PLD technique. This can be traced back to the fact that the availability of adequate MOCVD precursors is remarkably worse compared to PLD targets. Furthermore, the gas phase chemistry in a MOCVD is often not understood so far.

This section is focused on the optimization and investigation of the deposition conditions, in order to obtain thin epitaxial $SrRuO_3$ films. First of all, Ru/Sr ratio in the precursor solution and ratio between Ar/O_2 gas flows during heating up, deposition process and cooling down step were changed to control the composition of the layers and to obtain single phase $SrRuO_3$ films. Second, the effect of the substrate temperature and supersaturation as well as the lattice mismatch on the surface morphology and the growth mode are investigated. So far just one paper has described step-flow growth mode of $SrRuO_3$ on $SrTiO_3$ achieved by MOCVD [169], while for the films produced by PLD, step-flow growth has been often observed [97,170,171]. For this purpose $SrRuO_3$ was deposited on 0.1° off-oriented $SrTiO_3$(001), $NdGaO_3$(110) and $DyScO_3$(110) substrates with the stepped surfaces with a terrace length of about 200 nm (for preparation conditions see Section 3.1). And finally, a fundamental systematic study on the impact of epitaxial compressive ($SrRuO_3/SrTiO_3$, $SrRuO_3/NdGaO_3$) and tensile ($SrRuO_3/DyScO_3$) strain on the structural and electrical properties of $SrRuO_3$ thin layers is carried out. Since, $SrRuO_3$ is often considered as a model system, it is important to investigate this material fundamentally. Up to know it has not been performed for the films deposited by MOCVD.

3.3.1 Control of $SrRuO_3$ film composition

If MOCVD is used, the stoichiometry of the films can be directly controlled by varying the concentration of different precursor sources in the solution. Nevertheless, the ratio in the

solution is not equivalent to the ratio of the elements in the films, since other parameters like temperature of the flash evaporator, the ratio of the gas flows during deposition and cooling down process, deposition and evaporation temperatures, and pressure in the chamber also influence the final film composition.

In the following section two main deposition parameters, the Ru/Sr ratio in the precursor solution and the Ar/O_2 ratio during deposition and cooling down process will be described, since they have the highest influence on the composition of the films. Non-stoichiometry of the films often leads to the formation of extra phases and changes the structural and electrical properties of the layers limiting the application of $SrRuO_3$ as bottom electrode.

3.3.1.1 Ruthenium-strontium ratio in the precursor solution

Since Ru/Sr ratio in the precursor solution influences directly the composition of the films, this ratio was varied from 0.5 to 1. For the initial investigations, $SrRuO_3$ films were deposited at 600 °C on $SrTiO_3$ from two separate Ru and Sr sources with liquid solutions which were evaporated at 230 °C. For the depositions of epitaxial oxide films, the typical deposition temperature range is 500 – 850 °C. As Ru is rather volatile element, the deposition temperature of 600 °C was chosen.

The Raman spectra, measured at room temperature in backscattering configuration using the 488 nm laser line of an Ar^+ laser for the films deposited from the different precursor ratio in the solution, are shown in Fig 3.3.1. The spectra were measured in the range of 100 – 900 cm^{-1} within the accuracy of 0.1 cm^{-1}. As it can be seen in part a), no RuO_2 phase was found when the ratio of Ru/Sr in the precursor solution was 0.5. If this ratio was increased to 0.7, the characteristic peaks of RuO_2, appearing at 522, 641 and 714 cm^{-1} (corresponding E_g, E_{1g} and E_{2g} modes), are clearly visible. The peaks of this additional RuO_2 are becoming more intensive if the ratio of Ru/Sr is increased to 1 (Fig. 3.3.1 c). Three main characteristic peaks of $SrRuO_3$ appear in the 350 - 410 cm^{-1} range and are located at 353, 374 and 397 cm^{-1} for bulk $SrRuO_3$ (black vertical lines in Fig. 3.3.1), which are assigned to the B_{2g}, A_g, B_{2g} modes, respectively [172,173]. These modes are related to the apical oxygen vibrations, related to the changes in the Ru-O-Ru bond angle. From these results it is concluded, that on the one hand $SrRuO_3$ is deposited on the $SrTiO_3$ substrate and on the other hand, Raman spectroscopy gives additional information about existing of RuO_2 as an extra phase in the film, which is also indicated by HRXRD (Fig. 3.3.2).

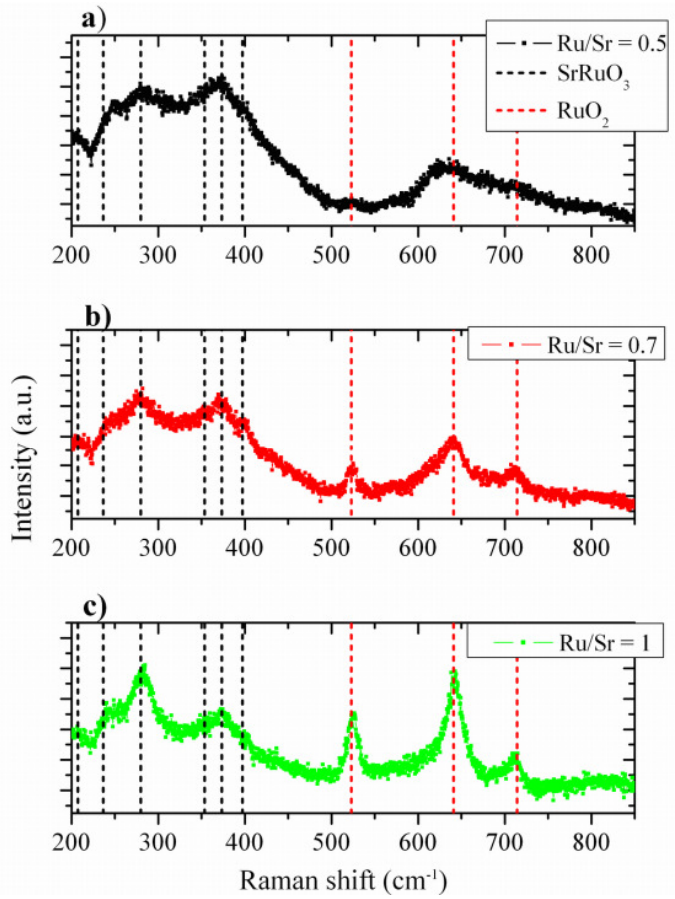

Fig. 3.3.1 Raman spectra of $SrRuO_3$ layers deposited at 600 °C at 26 mbar pressure with: a) Ru/Sr = 0.5, b) Ru/Sr = 0.7, c) Ru/Sr = 1. The dashed lines indicate the characteristic lines of $SrRuO_3$ (black) and extra RuO_2 (red) phase.

The HRXRD patterns of the films in 2θ interval between 39° and 48° represent the (200) diffraction peaks of $SrRuO_3$ (pseudo-cubic notation) at 2θ ~ 46.22° and the $SrTiO_3$(200) substrate peak (Fig. 3.3.2). Additionally, an (*l*00)-oriented RuO_2 phase is observed at 2θ = 40°, when the Ru/Sr ratio is 1. A small peak of RuO_2 can be also observed if the Ru/Sr is equal to 0.7. The position of the (200) diffraction peak of $SrRuO_3$, for the samples deposited from different solution compositions, slightly differs due to a modified out-of-plane lattice parameter, influenced by some elemental deficiencies or incorporation of extra elements in the film.

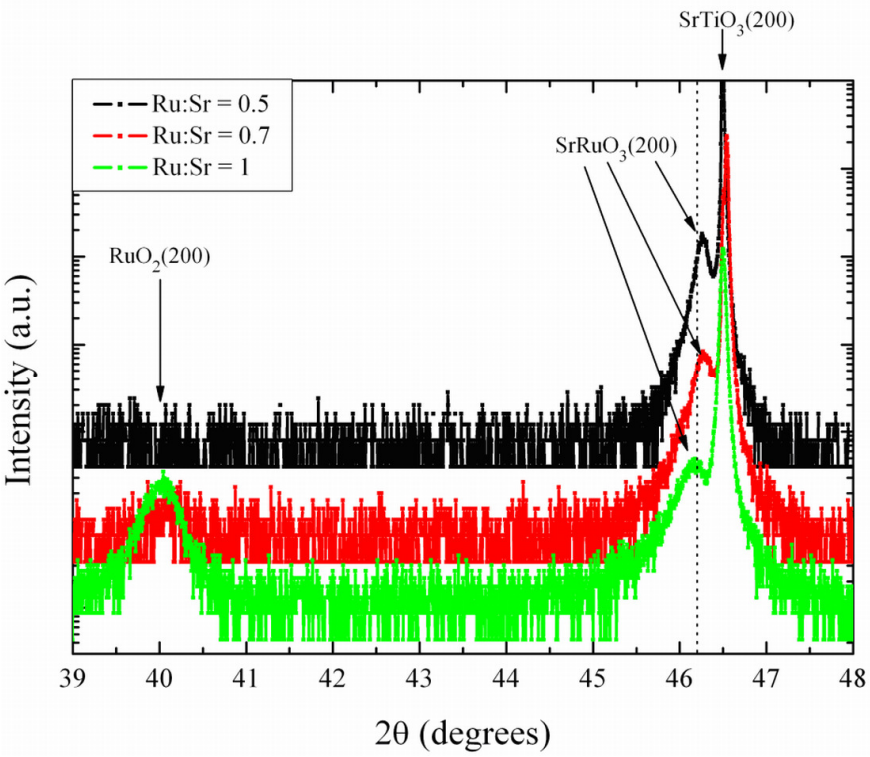

Fig. 3.3.2 HRXRD patterns of the (200) reflection peak of RuO_2 and (200) reflection peaks of $SrRuO_3$ deposited on $SrTiO_3$ substrates at 600 °C deposition temperature. The arrows indicate the position of the respective Bragg reflections. Vertical dotted line indicates the bulk position of $SrRuO_3$.

A secondary RuO_2 phase was also observed by Dabrowski et al. [44], but only in polycrystalline $SrRuO_3$ samples, obtained by pressing $SrCO_3$ and RuO_2 powders into pellets and annealing them in different atmospheres at different temperatures. Thus, RuO_2 phase was observed because of incomplete reaction of RuO_2 with $SrCO_3$ under certain preparation conditions. Here, the formation an additional RuO_2 phase in the epitaxial $SrRuO_3$ films can be explained by limited solubility of the B-site ions in ABO_3 perovskite structure [174]. Therefore an excess of B-site ions (Ru) is accommodated by precipitating of a second phase in $SrRuO_3$ film matrix [175].

In order to get stoichiometric $SrRuO_3$ films, the Sr/Ru ratio has to be adjusted in the gas phase, due to the different evaporation efficiencies at a fixed evaporation temperature of [$Sr(thd)_2$tetraglyme] and [$Ru(thd)_3$] precursors (see Table 3.2.5).

The values of full-widths at half-maximum (FWHM) of the (200) reflection peak of $SrRuO_3$ increases if the amount of Ru increases in the layers as well (Fig. 3.3.3). This indicates a reduction of structural perfection in the films. Furthermore, with the increase of Ru

amount in the films not only structural ordering is reduced, but also the roughness of the surfaces increases (Fig.3.3.3 and Fig. 3.3.4), due to the presence of RuO_2 phase probably as precipitates in $SrRuO_3$ films.

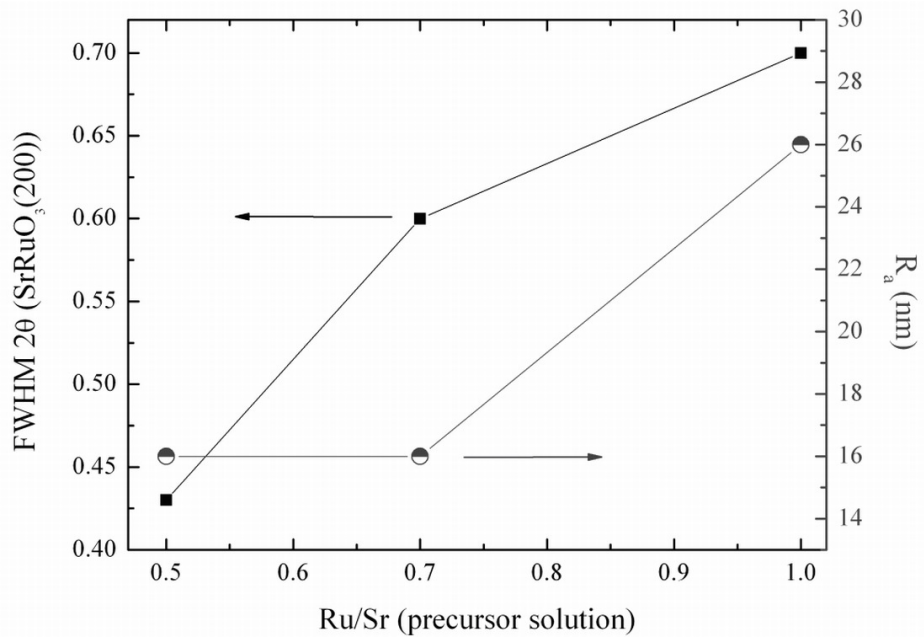

Fig. 3.3.3 Dependence of FWHM of (200) reflection and average roughness (R_a) on the Ru/Sr ratio in the precursor solution.

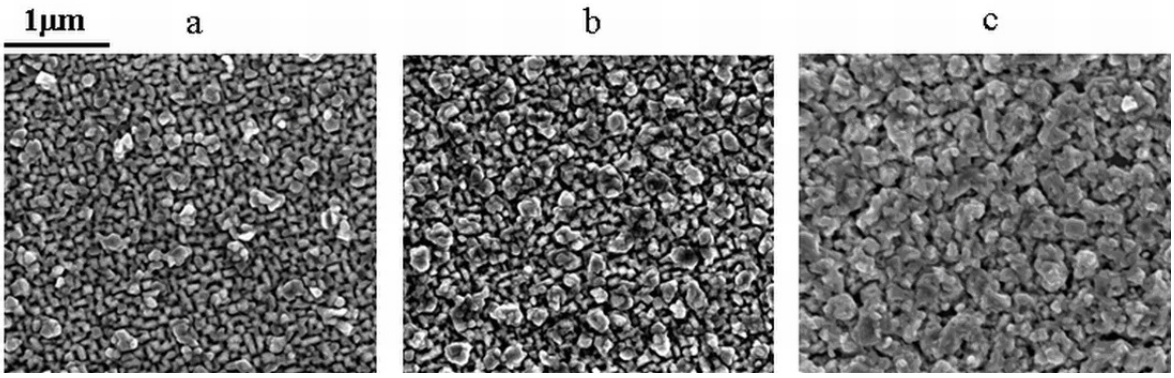

Fig. 3.3.4 SEM images of the same $SrRuO_3$ films like in Figs. 3.3.1 and 3.3.2. a) Ru/Sr = 0.5, b) Ru/Sr = 0.7, c) Ru/Sr = 1.

Systematic *ex-situ* post-growth annealing procedures, in the temperature range from 400 to 700 °C of a $SrRuO_3$ film, which contains RuO_2 as an extra phase, were made in oxygen atmosphere at atmospheric pressure for 1h in order to observe if the excess of RuO_2 can be removed from the $SrRuO_3$ layer [176]. Raman spectra of the as deposited (600 °C and Ru/Sr = 1) and *ex-situ* annealed $SrRuO_3$ sample at 700 °C are shown in Fig. 3.3.5.

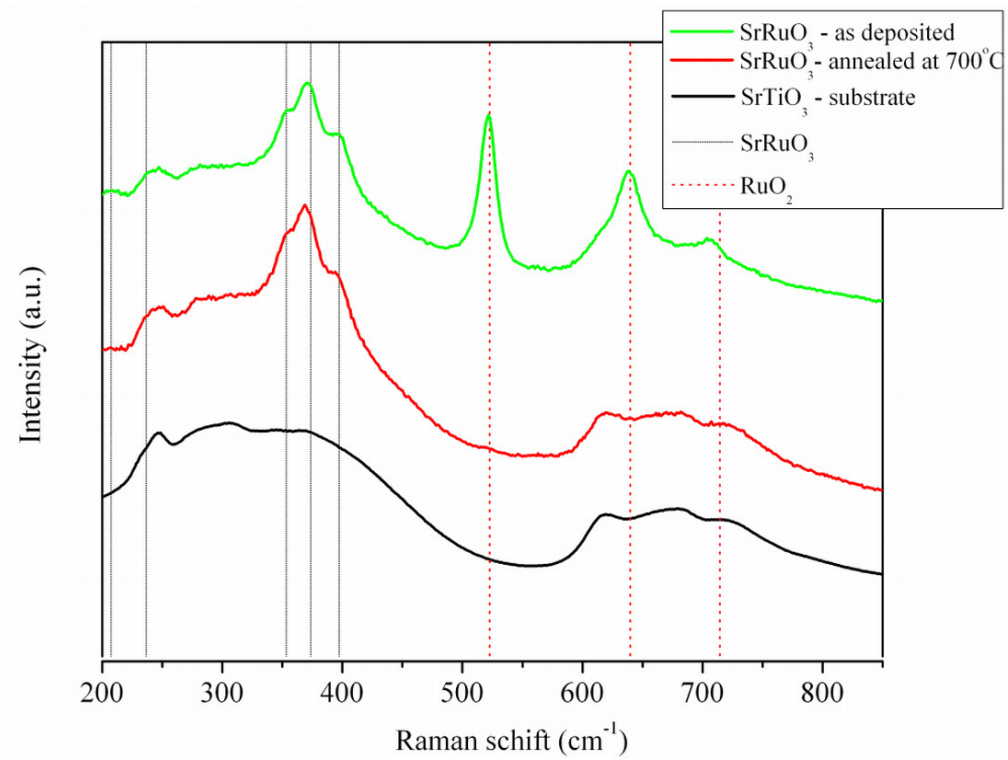

Fig. 3.3.5 Raman spectra of the $SrRuO_3$ layer deposited at 600 °C with Ru/Sr = 1 ratio in the precursor solution, as well as the spectrum of the same film ex-situ annealed in oxygen atmosphere at 700 °C in atmospheric pressure. The vertical lines indicate the characteristic peaks of $SrRuO_3$ and extra RuO_2 phase. The spectrum of $SrTiO_3$ substrate is shown for comparison.

The intensity of the peaks at 522, 641 and 714 cm^{-1} which are related to the RuO_2 phase, fully disappear after the annealing at 700 °C temperature, indicating the complete evaporation of secondary RuO_2 phase which coincides with HRXRD observation (Fig. 3.3.6).

This observation of the removal of extra RuO_2 phase agrees well with the work of Dabrowski et al. [44], who noticed weight losses and a change of the $SrRuO_3$ and RuO_2 fractions ratio due to evaporation of ruthenium oxide at temperatures above 700 °C by TG measurements. In fact, Shin et al. [51] reported that $SrRuO_3$ films, deposited by PLD technique under high pressure oxidizing conditions, can decompose and Ru can be lost in a volatile RuO_4 form.

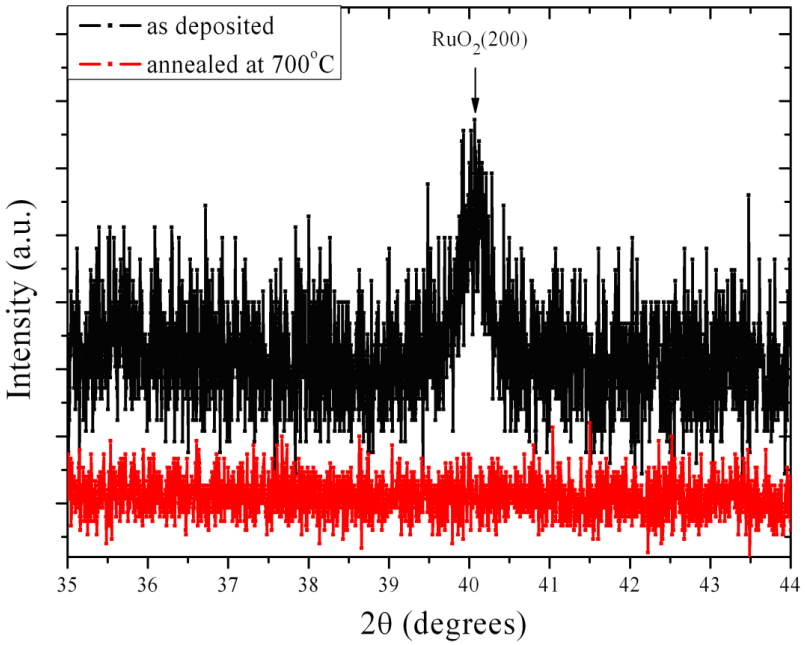

Fig. 3.3.6 HRXRD patterns of the $SrRuO_3$ layer containing extra RuO_2 phase as deposited at 600 °C in Ar/O_2 flow at 26 mbar with Ru/Sr = 1 and ex-situ annealed at 700 °C in oxygen flow at atmospheric pressure. The arrow indicates the position of the respective Bragg reflection.

These results show that, with an adjustment of the Ru/Sr precursor ratio in the solution, stoichiometric $SrRuO_3$ films can be obtained. However, the temperature also plays a crucial role. At higher temperatures, more Ru is re-evaporated as RuO_4 and this may help to remove excess of RuO_2 if the ratio is not optimized. On the other hand, higher temperatures may indicate that a higher Ru/Sr is necessary to prevent Ru deficiency in the films.

3.3.1.2 Influence of argon to oxygen ratio for $SrRuO_3$ composition

The content of oxygen in the carrier gas can be easily varied in MOCVD technique, since it is also influences the Sr/Ru ratio in the films. In this section the change in the film composition and structure of the $SrRuO_3$ films depending on argon to oxygen ratio during the pre-heating, deposition and cooling processes will be described.

It was observed that the ratio between the carrier/dilution gas (Ar) and oxidizing gas (O_2) is important not only during the growth of the oxide films, but also for maintaining a good surface of the oxide substrates before the deposition process. To preserve the steps on the chemically and thermally prepared $SrTiO_3$ substrates, it is necessary to add a small amount

of oxygen (2 %) to the Ar atmosphere during heating up stage ((Ar)/(O_2) = 50). A high amount of oxygen in the gas mixture leads to an increased Sr (O) diffusion from the bulk to the surface due to the higher chemical potential of O_2 above the surface, leading to the formation of Ruddlesden-Popper (RP) $SrO(SrTiO_3)_n$ phases [177]. Whereas heating up in pure Ar atmosphere causes damage to the step-and-terrace structure due to decomposition of the surface, similar to observations of $SrRuO_3$ surfaces [51], where reducing conditions lead to the formation of small amount of SrO, Ru and O_2.

It was observed that a certain ratio between Ar and O_2 gas flows is required during deposition in order to get single phase of well ordered $SrRuO_3$ films. If the Ar to O_2 ratio during deposition process is above a certain limit ($Ar/O_2 \geq 3.3$, i.e. oxygen partial pressure is low), only metallic Ru phase was observed from HRXRD patterns without any evidence of $SrRuO_3$ phase. However, too high supply of oxygen ($Ar/O_2 \leq 1$) leads to the formation of an extra RuO_2 phase (Fig. 3.3.7).

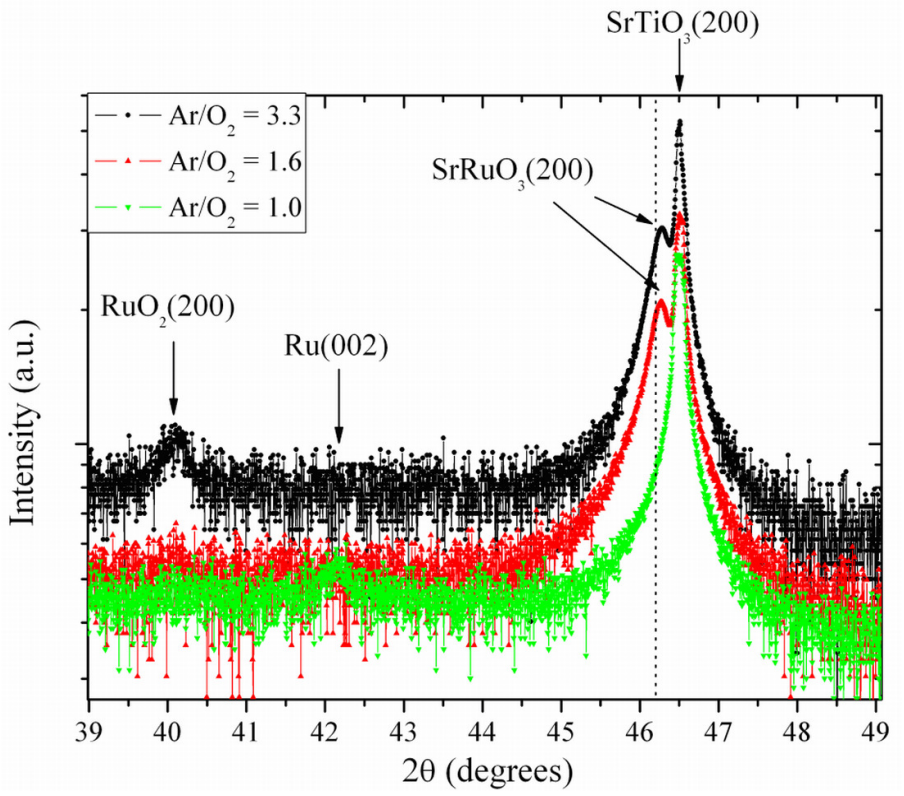

Fig. 3.3.7 HRXRD patterns of the (200) reflection peaks of $SrRuO_3$ and other reflection peaks of films deposited at different Ar/O_2 flows at 600 °C. The arrows indicate the position of the respective Bragg reflections. Vertical dotted line indicates the bulk position of $SrRuO_3$.

These results are in agreement with the observations of Hartmann et al. [178], who investigated $SrRuO_3$ films by photoelectron spectroscopy and noticed a coexistence of Ru^{4+} and Ru° in the polycrystalline $SrRuO_3$ films after annealing them in ultra high vacuum. The metallic Ru° appeared due to the reduction of ruthenium from Ru^{4+} to Ru° in oxygen deficient atmosphere, while sufficient amount of oxygen leads to complete oxidation to Ru^{4+} existing in $SrRuO_3$.

The phase composition and structure of $SrRuO_3$ films do not only depend on the conditions during film growth, but also on the atmosphere in which the films are cooled (Fig. 3.3.8). If the film is cooled in pure Ar atmosphere a broad reflection at 43.7° emerges (instead of 46.22° for a stoichiometric $SrRuO_3$), which is attributed to the Ruddlesden-Popper phase $Sr_3Ru_2O_7$ (layered ruthenate structure). Shin et al. [51] observed the same transformation of $SrRuO_3$ in reducing atmosphere and assumed that $SrRuO_3$ is converted to metallic Ru and SrO or to a Sr rich R-P structure (Sr_2RuO_4 and $Sr_3Ru_2O_7$).

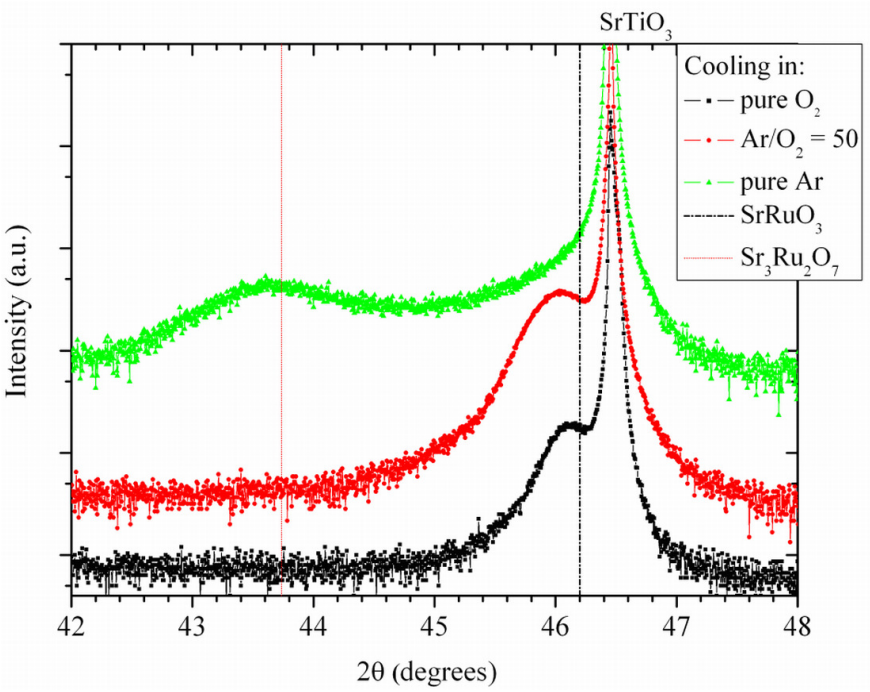

Fig. 3.3.8 HRXRD patterns of the (200) reflection peaks of $SrRuO_3$ and $Sr_3Ru_2O_7$ phase for the samples cooled to room temperature in different Ar/O_2 gas flows. The vertical lines indicate the position of the respective Bragg reflections.

A shift of the $SrRuO_3$ film reflection in Fig. 3.3.8 to higher 2θ values ($SrRuO_3$ bulk value) was observed for the film deposited in pure O_2, which is ascribed to a reduced compressive lattice strain caused by a degraded structural ordering of the $SrRuO_3$ films, due

to loss of volatile RuO_4. However, if a cooling is performed in an atmosphere with a certain amount of oxygen $Ar/O_2 = 50$ well ordered stoichiometric $SrRuO_3$ structure can be preserved.

3.3.2 Surface morphology of $SrRuO_3$ films in dependence of deposition temperature, time and supersaturation

Growth mechanism of the films critically depends on main deposition parameters like deposition temperature, deposition time and supersaturation. Additionally, the surface morphology, termination of the surface layer, and lattice mismatch of the substrate determines the growth mode of thin films. The following section deals with the systematic investigation of the influence of the mentioned growth parameters on the structural properties and growth mode of thin $SrRuO_3$ films. With the knowledge of the results of the previous section, the deposition temperature here was increased from 600 °C to 750 °C. To investigate these effects $SrRuO_3$ films were grown on vicinal $SrTiO_3(001)$, $NdGaO_3(110)$ and $DyScO_3(110)$ substrates. The pressure in the chamber was set to 26 mbar and the temperature of flash evaporator to 230 °C. The ratio of $Ar/O_2 = 1.6$ and ratio of $Ru/Sr = 0.5$ in the precursor solution was used for the depositions.

The corresponding (200) reflection peaks of $SrRuO_3$ films in HRXRD 2θ patterns occur in the 44 - 47.5° range (Fig. 3.3.9). As it can be seen, the films grown at 600 °C and 650 °C had a broad (200) reflection, whereas with the increase of deposition temperature to 720 °C structural ordering of the $SrRuO_3$ layer is improved (lower FWHM value). This can be explained by the significant enhancement of the kinetic energy of the atoms due to the energy supplied by the higher substrate temperatures, which enables the atoms to move to more energetically favourable places on the surface, leading to a better atomic alignment [179]. Nevertheless, the structural ordering of the film is worse, at the highest deposition temperature (750 °C) than for the film deposited at 720 °C. This could be related to desorption of the Ru at higher deposition temperatures [51].

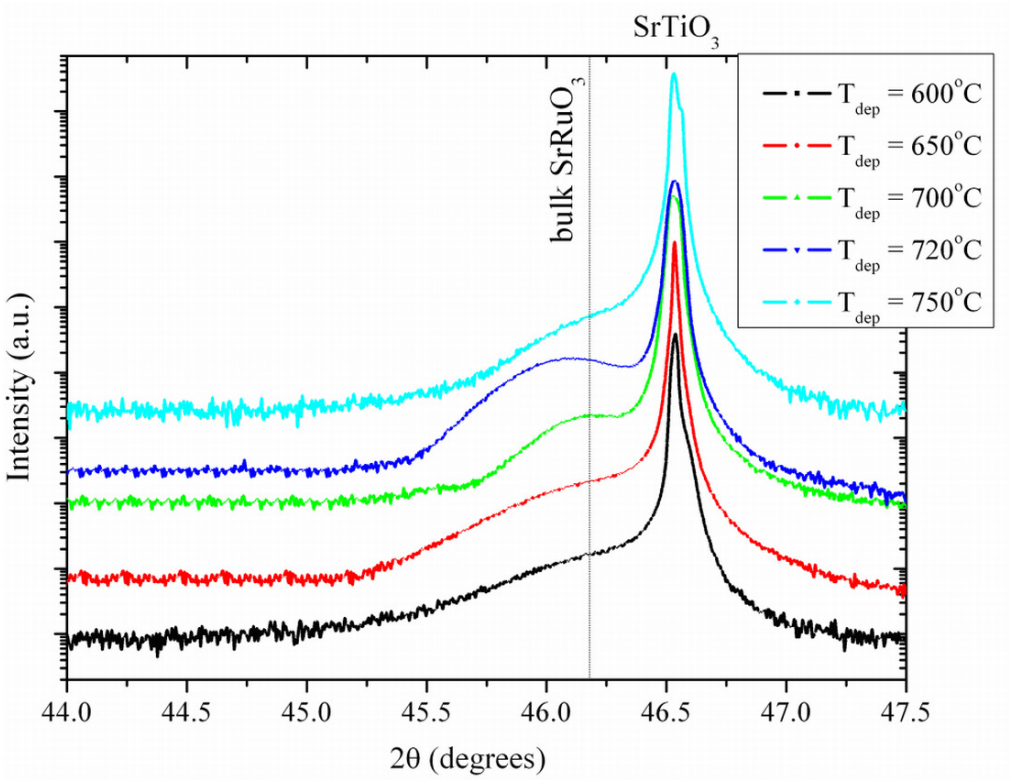

Fig. 3.3.9 HRXRD patterns of the (200) reflection peak of $SrRuO_3$ deposited on $SrTiO_3$ substrates at different deposition temperatures at 26 mbar.

If the deposition temperature is increseased to 750 °C, the growth rate decreases from ~ 0.225 nm/min to ~ 0.075 nm/min (Fig. 3.3.10). This effect could be attributed to the desorption of Ru from the surface.

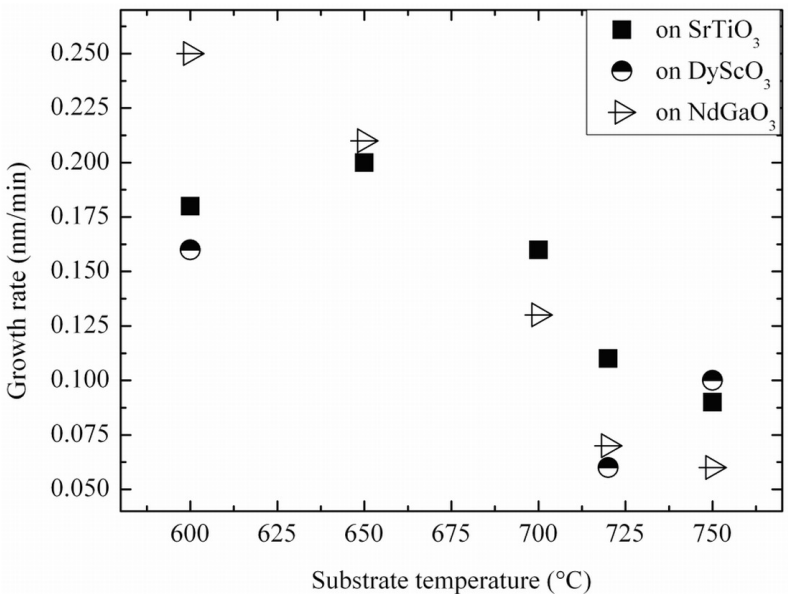

Fig. 3.3.10 Growth rate vs. substrate temperature of $SrRuO_3$ films grown on vicinal oxide substrates $SrTiO_3$(001), $NdGaO_3$(110), $DyScO_3$(110).

The surface morphology of the films, deposited at 600 °C, 720 °C and 750 °C are represented in Fig. 3.3.11. Film thickness was evaluated by ellipsometry and was in the range between 14 and 17 nm. From the AFM pictures, one can see the improved surface quality (bigger grains) of the film deposited at 720 °C compared with the one deposited at 600 °C. Enhanced surface diffusion [179] is the reason for the bigger grains at higher deposition temperature.

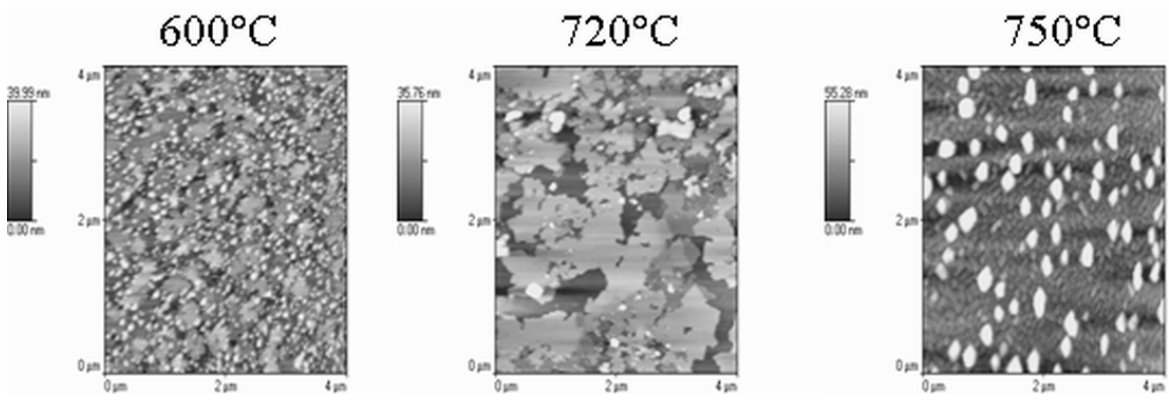

Fig. 3.3.11 AFM images of $SrRuO_3$ films grown on vicinal $SrTiO_3$ substrates at different deposition temperatures at 26 mbar pressure.

However, the further increase of deposition temperature to 750 °C resulted again in surface with small grains. This can be attributed to a reduced growth rate (Fig. 3.3.10) with the increase of deposition temperature and desorption of Ru from the film as RuO_4 [51], leading to enhanced incorporation of impurities (will be discussed later in more detail).

The film morphology depends not only on the growth temperature but also on the thickness of the films. Therefore films with different thicknesses were deposited on $SrTiO_3$, $NdGaO_3$ and $DyScO_3$ substrates. This was achieved by changing the deposition time between 50 and 400 min with a growth rate of ≤ 0.1 nm/min. The corresponding changes in surface morphology were observed by AFM (Fig. 3.3.12). The investigation revealed that already in the early stages of the growth (50 min), where steps are still visible, islands with a height of ~ 4 nm were formed, either directly on the terraces of the stepped surfaces or on a wetting layer (i.e. 3D island growth or layer-then-island growth).

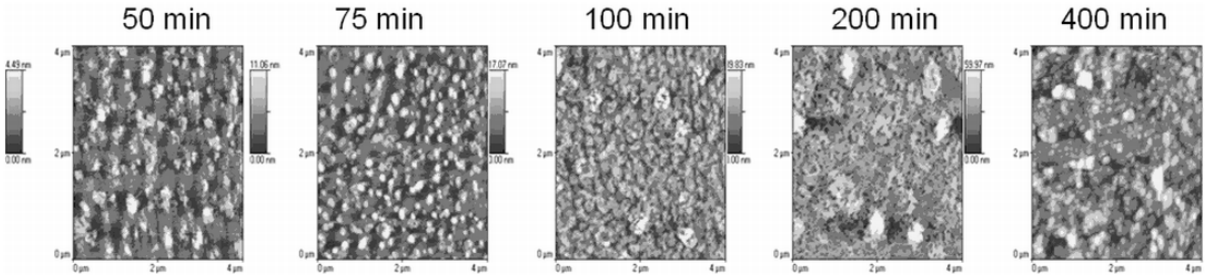

Fig. 3.3.12 $SrRuO_3$ films deposited on $SrTiO_3$ substrates at 720 °C in an optimal Ar/O_2 = 50 flow for a different deposition time.

With increasing film thickness, the island density increased while the step-and-terrace structure of the bare surfaces disappeared. When the density of islands was high enough, coalescence of the islands was observed. For the films deposited for 300 – 400 min the measured thicknesses were about 30 – 40 nm. The lattice strain of these $SrRuO_3$ films decreased with the thickness (observed from HRXRD results, which are not shown here) due to the formation of defects, which is more evident on $NdGaO_3$ substrates due to the higher mismatch between the substrate and the film.

In order to identify whether $SrRuO_3$ grows by island or layer-then-island mode, HRTEM measurements were performed. This analysis suggests that MOCVD-grown $SrRuO_3$ films grow in layer-then-island growth mode on vicinal $SrTiO_3$ substrates (Fig. 3.3.13). This assumption can be done because a wetting layer of about 4 nm was observed followed by island growth. It is evident that $SrRuO_3$ on $SrTiO_3$ substrate grows epitaxially, and no defects occur at the interface, where islands are partially or completely relaxed.

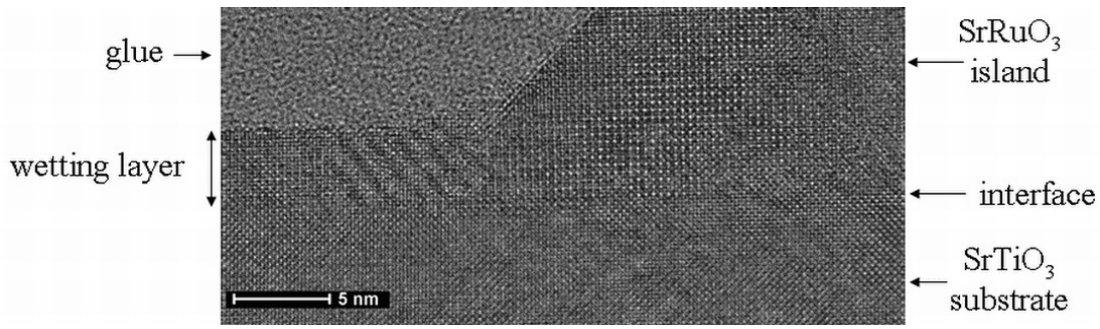

Fig. 3.3.13 HRTEM image of $SrRuO_3$ films deposited on $SrTiO_3$ substrate showing the layer-then-island growth at 720 °C for 160 min.

Nevertheless, the film is not homogenous over the full scan range, because islands of different size was observed (Fig. 3.3.14).

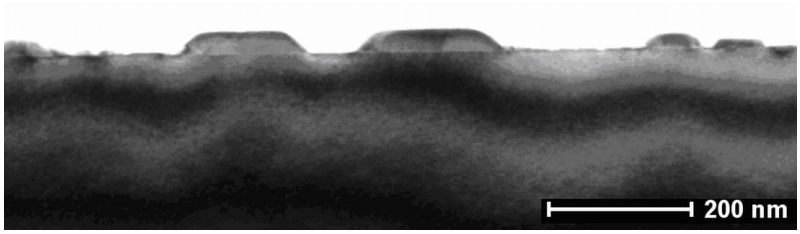

Fig. 3.3.14 HRTEM image of $SrRuO_3$ films deposited on $SrTiO_3$ substrate showing they distribution and size of the islands.

The observed results lead to the assumption that $SrRuO_3$ grow on vicinal $SrTiO_3$ in layer-then-island growth mode by MOCVD technique (Fig. 3.3.13). The islands are formed shortly after the beginning of the growth process (50 min Fig. 3.3.12) without any transition to step-flow growth mode. 3D island growth mode is typical for $SrRuO_3$ films grown by MOCVD, while for the films, grown by PLD, often step-flow growth is reported. This fact can be attributed to the main difference between these two methods: the gas phase composition and higher kinetic energy of the particles in PLD process. In MOCVD a solvent (C, O, H) containing the organic precursor (here: Sr, Ru, C, O, H) is used, whereas in PLD the targets contain only the required elements in a certain ratio (however, some carbon could be also incorporated in the films from the targets, but in a remarkably low amount). Therefore, in the MOCVD case, there is a carbon incorporation which changes not only the growth mode but also the composition of the film. The carbon incorporation during the MOCVD process is well known from literature [180,181,182] and is assumed to suppress the diffusion of the atoms on the surface, leading to the layer-then-island or 3D island growth of $SrRuO_3$ deposited by MOCVD technique. Step-flow growth mode of thin $SrRuO_3$ films on $SrTiO_3$ substrates by MOCVD technique has been described so far only in one paper [169]. Sumi et al. [169] indeed prepared atomically flat $SrRuO_3$ films with $[Ru(C_7H_{11})(C_7H_9)]$ as Ru source material. In the present work, the $[Ru(thd)_3]$ precursor was used, which is known to exhibit strong bonds to the metal atom, probably leading to a higher carbon contamination in the films compared to other metal-organic precursors [183].

By the reduction of the precursor solution concentration, it was expected to suppress the island formation on the surface and to achieve the transition to step-flow growth mode of $SrRuO_3$. If high concentration of the precursor solution is used for the deposition of the films, a high number of the species reach the substrate surface, leading to the formation of islands on the surface, due to a high mass transport through a boundary layer and suppressed diffusion on the surface. If higher dilution of the precursor solution is used lower number of species

arrive to the surface, therefore they have enough time to diffuse on the surface in order to reach the step edges of vicinal substrates due to the lower growth rate.

To observe if supersaturation influence the growth mode of the $SrRuO_3$ films, the concentration of the precursor solution was reduced from 0.05 M (as used up to now) till 0.0125 M (Fig. 3.3.15). If the concentration of precursor solution was reduced the supersaturation and the growth rate decreased as well.

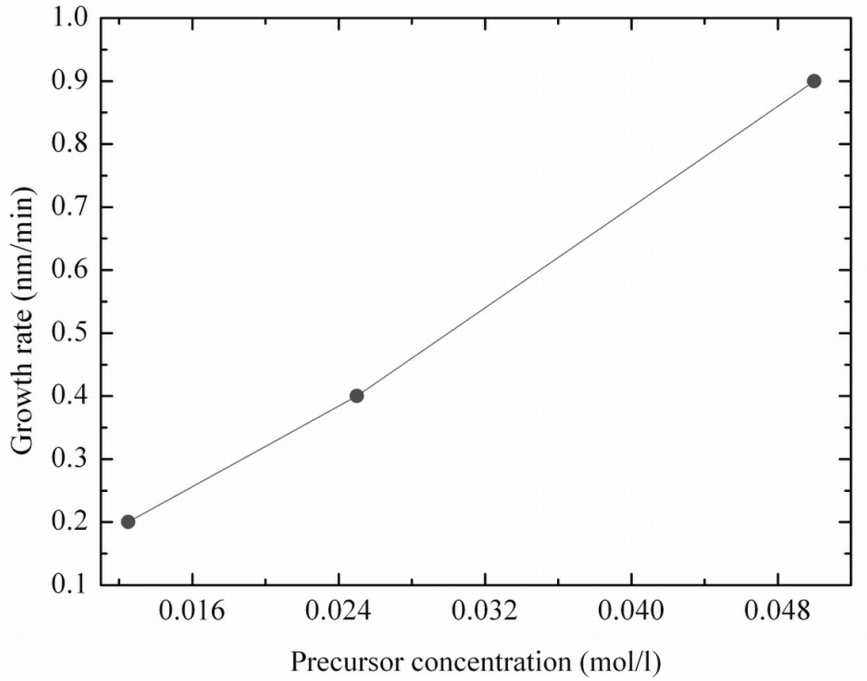

Fig. 3.3.15 Growth rate vs. precursor solution concentration for $SrRuO_3$ films grown on vicinal $NdGaO_3$(110).

$SrRuO_3$ films became slightly strained on vicinal $NdGaO_3$ substrates (Fig. 3.3.16) as long as the growth rate was higher than 0.1 nm/min. Similar results were obtained for the films grown on $SrTiO_3$ and $DyScO_3$ substrates. From the relative position of the film and substrate peaks in HRXRD patterns the total strain $\varepsilon_\perp = (\Delta d/d)_\perp$ was calculated by Equation 2.3.

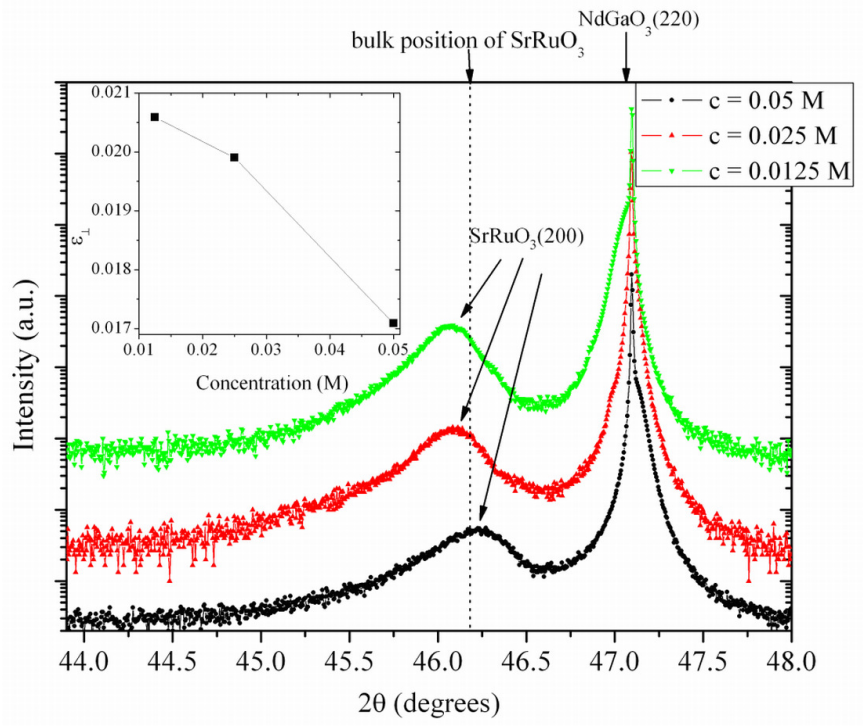

Fig. 3.3.16 HRXRD patterns of the (200) reflection peak of $SrRuO_3$ films deposited at 720 °C on $NdGaO_3$ substrates in dependence of the precursor concentration. Inset – dependence of epitaxial total strain on concentration of the precursor solution.

Increase of the strain state (film peak shifts toward lower 2θ angles compared to the 2θ position of the bulk $SrRuO_3$) (see also inset of Fig. 3.3.16) can be related to the morphology changes of the films (Fig. 3.3.17). Highest supersaturation (Fig. 3.3.17 a) results in many isolated islands with a lot of open areas around. Reduction of supersaturation increases the island density on the surface (Fig. 3.3.17 b) until the whole surface is completely covered by a connected network of islands (Fig. 3.3.17 c), leading to more strained $SrRuO_3$ films (Fig. 3.3.16).

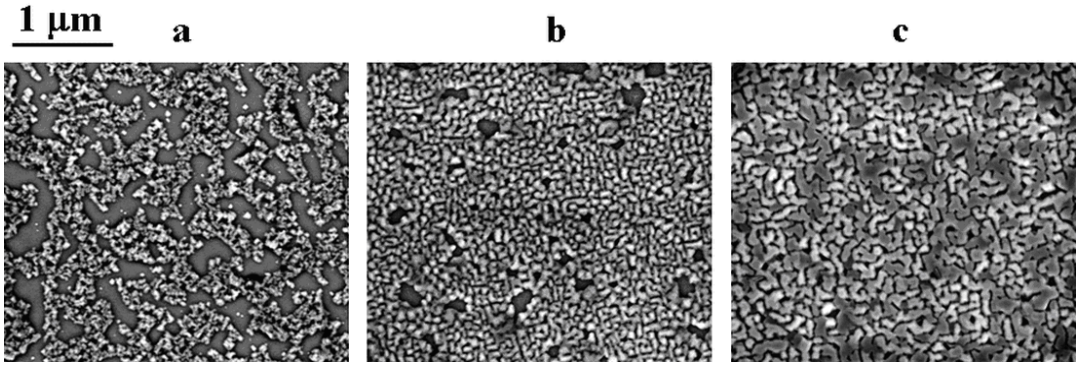

Fig. 3.3.17 SEM images of $SrRuO_3$ films deposited at 720 °C on $NdGaO_3$ substrates by using different concentrations of the precursor solution: **a)** 0.05 M, **b)** 0.025 M, **c)** 0.0125 M.

However, when the growth rate was lower than ~0.1 nm/min, the structural ordering and strain state in the films decreased again (determined from HRXRD, not shown here) [184]. Therefore, $SrRuO_3$ has to be grown above a minimum growth rate in order to achieve well ordered films. Nevertheless, by reducing the supersaturation, the aim to obtain step-flow growth of $SrRuO_3$ films was not achieved, presumably due to higher incorporation of carbon which is assumed to be higher at low growth rates.

3.3.3 Strain engineering of $SrRuO_3$ electrical properties

It is known that properties of the films can be drastically changed if strain is introduced into the films by choosing substrates with different crystal lattice parameter and thermal expansion behaviour. In this section, the influence of the epitaxial strain on the magnetic/electrical properties of $SrRuO_3$ films, is investigated. Considering the lattice mismatch between $SrRuO_3$ films and the different oxide substrates, it is expected that $SrRuO_3$ films grow under compressive strain on $SrTiO_3$ and $NdGaO_3$ substrates, whereas tensile strain may be developed for growth on $DyScO_3$ (Table 3.3.1).

Table 3.3.1. Bulk lattice constants of different substrate materials. $(\Delta a/a)_c$ describes the pseudo-cubic lattice mismatch between film (index f) and substrate (index s) with $(\Delta a/a)_c = (a_{c(f)} - a_{c(s)})/a_{c(s)}$ and a_c the pseudo-cubic lattice constants, which are calculated by $a_c = 0.5\sqrt{a^2 + b^2}$.

	Lattice structure	Lattice constants (Å)	$(\Delta a/a)_c$ (%)
$SrTiO_3$(001)	Cubic, perovskite type	a = 3.905	0.64
$DyScO_3$(110)	Orthorhombic, $GdFeO_3$ type (pseudo-perovskite)	a = 5.44; b = 5.72; c = 7.90 [185] (a_c = 3.94)	-0.25
$NdGaO_3$(110)	Orthorhombic, $GdFeO_3$ type (pseudo-perovskite)	a = 5.43; b = 5.50; c = 7.71 [186] (a_c = 3.86)	1.81

For this purpose $SrRuO_3$ films were deposited at optimized growth temperatures in the range of 700 – 730 °C with the solution concentrations of 0.0033 - 0.004 M. The temperature of flash evaporator was kept constant at 230 °C and the process pressure during deposition was 26 mbar. The film thicknesses were measured by ellipsometry and were about 25 nm, smaller than the critical thickness for the onset of misfit dislocations.

HRXRD scans between 10 and 90° exhibit only the (*l*00) diffraction peaks of $SrRuO_3$ films and the corresponding peaks of the substrates (not shown). This indicates the epitaxial growth of pure $SrRuO_3$ on oxide substrates without any foreign phase. The (200) Bragg reflection peaks of two $SrRuO_3$ thin films grown on $SrTiO_3$ and $DyScO_3$ substrates are shown in Fig. 3.3.18.

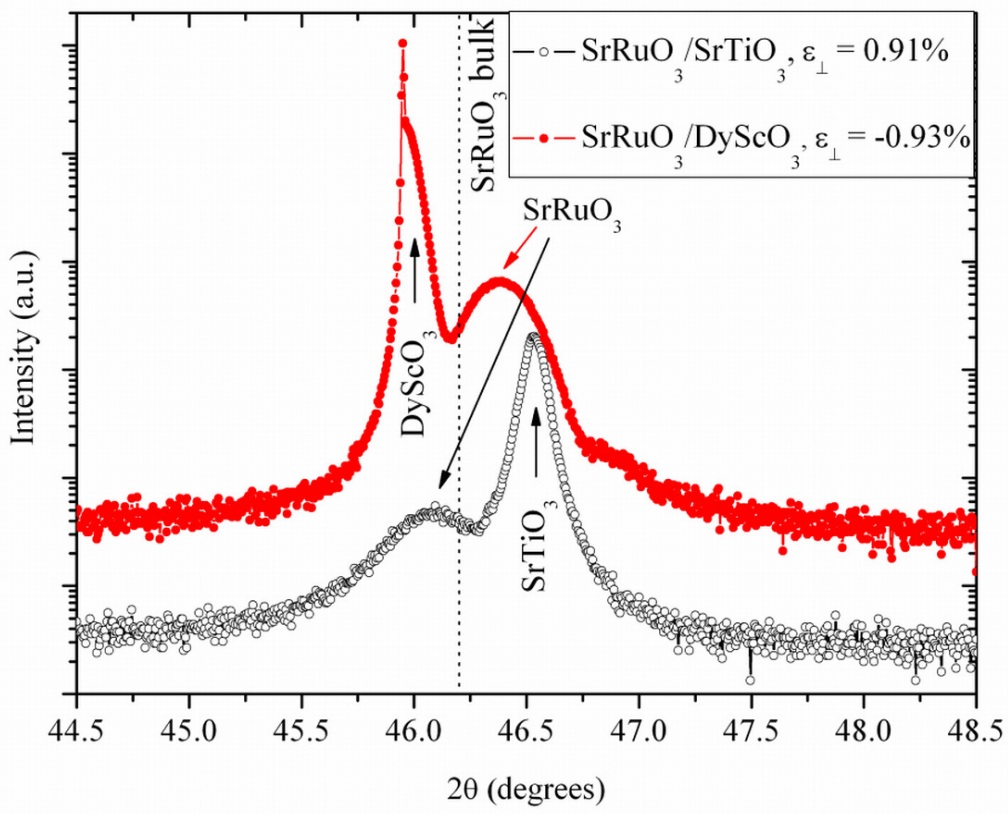

Fig. 3.3.18 HRXRD patterns of the (200) reflection peaks of epitaxially strained $SrRuO_3$ films on $SrTiO_3$ and $DyScO_3$ substrates. The vertical line indicates the position of bulk $SrRuO_3$ (200) Bragg reflection.

It is obvious that the peak position of the $SrRuO_3$ film in Fig. 3.3.18, deposited on $SrTiO_3$ shifts towards lower 2θ angles compared to the 2θ position of bulk $SrRuO_3$ (indicated by the vertical broken line in Fig. 3.3.18). This shift is correlated with an increased out-of-plane lattice constant. In contrast, for the growth on $DyScO_3$ the position of the film

peak shifts to higher 2θ angles indicating a decrease of the out-of-plane lattice constant. From these observations it is concluded that the films are grown under compressive and tensile strain on $SrTiO_3$ and $DyScO_3$, respectively. The experimentally calculated epitaxial total strain is equal to $\varepsilon_\perp$ = 0.91 % for $SrRuO_3$ grown on $SrTiO_3$ and $\varepsilon_\perp$ = -0.93 % for the film grown on $DyScO_3$.

Fig. 3.3.19 a) shows the temperature dependence of the electrical resistivity ρ(T) between 75 K and 300 K of two highly strained $SrRuO_3$ films on $SrTiO_3$ ($\varepsilon_\perp$ = 1.6 %) and $DyScO_3$ ($\varepsilon_\perp$ = - 0.93 %) substrates. The resistivity decreases with the decrease of the temperature, showing the characteristic metallic behaviour of $SrRuO_3$ films [187]. The kinks in the resistivity curves between 145 K and 165 K coincide with the Curie temperature of the paramagnetic-ferromagnetic phase transition [7,46,188]. The reason for this coincidence is that the resistivity of a ferromagnetic metal contains a significant temperature dependent magnetic contribution, which is described in more detain in Section 2.8. The shape of the curves and the magnitude of the resistivity values are in good agreement with literature data for $SrRuO_3$ thin films [35] as well as for bulk crystals [189]. However, it has to be mentioned that since in previous section the layer-then-island growth for the $SrRuO_3$ films was observed, the absolute electrical resistivity values can be slightly influenced by the morphology of the films. The larger resistivity values can be attributed to the increased scattering of the carriers at grain boundaries [190].

T_c was determined from the temperature derivative of the resistivity (dρ/dT) (Fig. 3.3.19 b) by the following procedure: a polynomial fit was applied between 100 K and the temperature position, which is indicated as T_{min} in Fig. 3.3.19 b, followed by two linear fits with different slopes for the intermediate region (between T_{min} and T_{max}) and the high temperature region ($T > T_{max}$). T_{min} and T_{max} are defined as the intersection points of two adjacent fit curves, where the average value $(T_{min} + T_{max})/2$ considered being T_c.

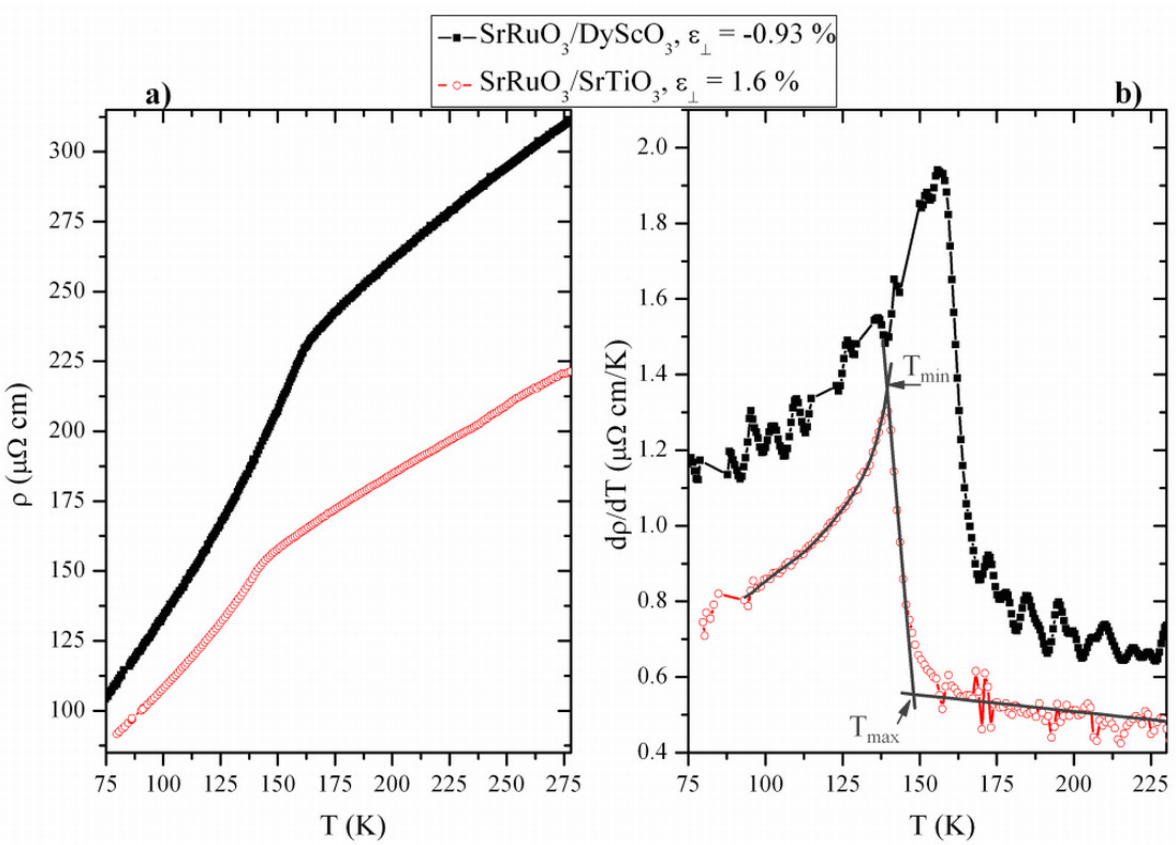

Fig. 3.3.19 a) ρ(T) for two $SrRuO_3$ thin films deposited on $DyScO_3$ and $SrTiO_3$, **b)** dρ/dT of the respective $SrRuO_3$ layers. For the definitions of T_{min} and T_{max} see text.

The systematic investigation of the strain influence on T_c was carried out following two experimental approaches: on one hand, by choosing three different substrates $SrTiO_3$, $DyScO_3$, and $NdGaO_3$. On the other hand, by changing the concentration of the precursor solutions and the substrate temperature, the growth rate of the films could be changed leading to different strain states in the $SrRuO_3$ films. Higher growth rates were observed at lower deposition temperature or higher precursor concentration, due to the reduced desorption from the surface and higher supersaturation during the growth. Since the films were deposited with a growth rate lower than 0.1 nm/min, a high amount of impurities (especially C) was incorporated in the films (see previous section, where it was discussed in detail), and it is assumed that surface diffusion is low. The incorporation of many defects releases lattice strain caused by the differences in lattice constant.

Since the epitaxial strain is related to the out-of-plane lattice constant of the films a set of $SrRuO_3$ films with various out-of-plane lattice constants were obtained. Out-of-plane lattice constants of these films, calculated from HRXRD data, varied from 3.907 Å up to 3.988 Å. The correlation between the out-of-plane lattice constant *c* and the Curie temperature

T_c is shown in Fig. 3.3.20. A significant decrease of the Curie temperature from 163 K to 144 K is observed in the above specified out-of-plane lattice constant range.

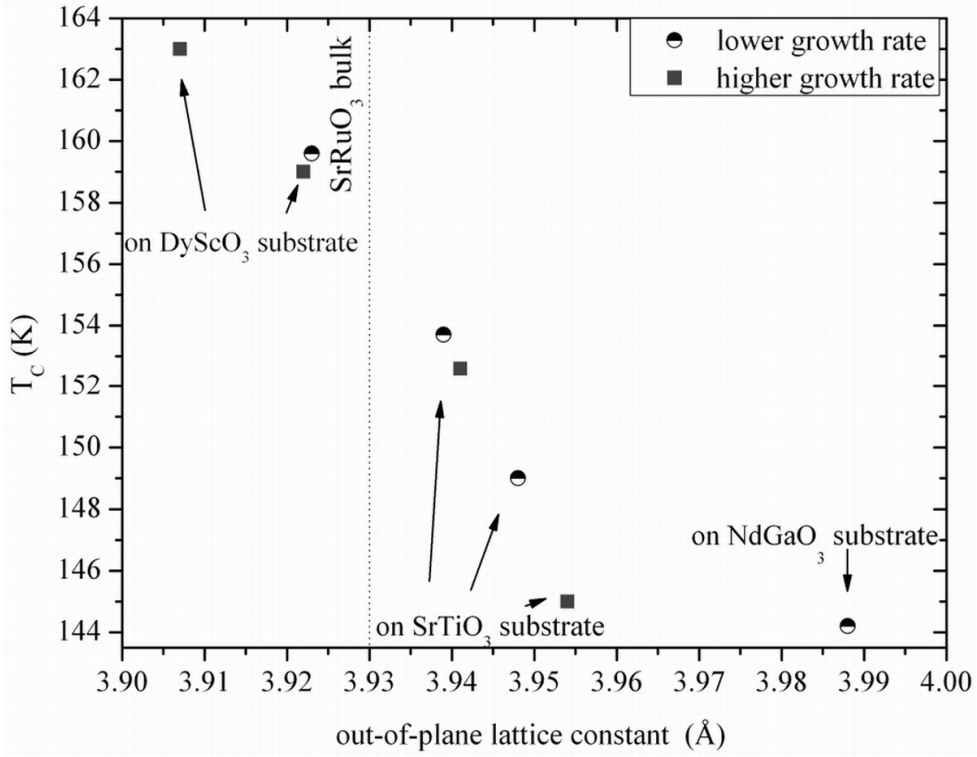

Fig. 3.3.20 Curie temperature T_c versus out-of-plane lattice parameter *c*. Squares and circles represent samples grown at different growth rates. Substrates are indicated by arrows.

Regardless of the differences in growth rate, the relation between the Curie temperature and the out-of-plane lattice constant is the same, within the accuracy of the measurements, for the films deposited at different deposition temperature or by using different concentration of the precursor solution.

$SrRuO_3$ films were grown on different oxide substrates in the same run and since the Sr/Ru and the Ar/O_2 ratio were always kept constant it is assumed that the film composition was constant for all samples. Therefore it was excluded that Ru and/or O deficiency are responsible (see Section 1.4.2) for the shift of Curie temperature. Based on the results obtained from the depositions of the films on different oxide substrates, the dependence of the Curie temperature on the out-of-plane lattice parameter is explained by the changes in structure induced by incorporated lattice strain. From the literature it is known that relaxed (bulk) $SrRuO_3$ exhibits a distorted perovskite structure, where the O atoms are slightly displaced from the Ru planes [191,192]. Hence the Ru-O-Ru bond angle is equal to 164°

instead of 180° expected for an ideal cubic structure. By epitaxial deposition of thin $SrRuO_3$ films on lattice mismatched oxide substrates, an elongation or a contraction of the lattice in the out-of-plane direction is obtained, caused by the compressive or tensile in-plane strain, respectively. A change of the out-of-plane lattice constant is connected with the deviation of the Ru-O-Ru bond angle in the xy plane. For cubic perovskites it is known that a deviation from 180° results in reduced ferromagnetism, since the electron hopping interaction strength between the B site atoms in a perovskite structure ABO_3 via oxygen atom is stronger for larger B-O-B bond angles [54]. According to the results in Fig. 3.3.20 it is concluded that the strength of the ferromagnetic interaction for $SrRuO_3$ thin films and therefore the paramagnetic-ferromagnetic transition is correlated with the Ru-O-Ru angle, similar to observations reported in other perovskites [193,194]. In $SrRuO_3$ films with compressive (tensile) strain the Ru-O-Ru angle becomes smaller (larger), resulting in a reduced (stronger) electron hopping interaction between the Ru sites via the oxygen atom and thus in a decreased (increased) Curie temperature.

Corresponding strain behaviour of the Curie temperature was observed for $La_{1-x}Ba_xMnO_3$ layers. Zhang et al. [194] reported a T_c increase under tensile strain and Yuan [193] correlated the Curie temperature shifts to the changes of the lattice constants and to a bending of the B-O-B bonds in epitaxially strained $La_{1-x}Ba_xMnO_3$ films. Some additional relations between epitaxial strain and Curie temperature for $SrRuO_3$ films grown by PLD or sputtering technique are described in Section 1.4.2.

In the present work it was shown that $SrRuO_3$ can be grown under different epitaxial strain (compressive and tensile) without using any buffer layer simply by choosing the substrates with different lattice constants. This was seen to markedly influence the structural and electrical properties of the films. Furthermore, the systematic investigations of the strain influence on the Curie temperature of $SrRuO_3$ films shows that MOCVD can be applied for the epitaxial growth of highly strained oxide films, so far reported only for the physical (PLD, sputtering) deposition techniques.

3.4 Deposition of epitaxial $Bi_4Ti_3O_{12}$ films

In this section, the effect of the deposition conditions on the stoichiometry, structure, the growth rate, the composition, and the strain of epitaxial $Bi_4Ti_3O_{12}$ films, deposited by liquid-delivery MOCVD will be described. $Bi_4Ti_3O_{12}$ system was chosen for the further investigations, since it is promising system for non-volatile ferroelectric memory applications due to their ferroelectric properties. Therefore, the understanding of the initial growth of these films is a crucial issue. In this work, a systematic investigation of the influence of deposition parameters on the properties of the $Bi_4Ti_3O_{12}$ films was performed. It has to be mentioned that such detailed investigation of the growth of $Bi_4Ti_3O_{12}$ by MOCVD is shown for the first time.

For getting single phase epitaxial $Bi_4Ti_3O_{12}$ films the Bi/Ti ratio in the precursor solution, deposition temperature and rotation were changed. The films have been also deposited on the different substrates $SrTiO_3(001)$, $NdGaO_3(110)$ and $DyScO_3(110)$ to investigate the effect of the lattice mismatch on the film properties.

For the present investigations, films were deposited at temperatures in the range of 550 – 850 ºC. The total concentration of the precursor solution was equal to 0.15 M. The $[Bi(thd)_3]$ and $[Ti(O^iPr)_2(thd)_2]$ precursors were used for the deposition of the $Bi_4Ti_3O_{12}$ films, for both precursors no oligomerization effect was noticed and normal isothermal behaviour was observed. The temperature of flash evaporator was fixed at 230 ºC and the pressure in the reaction chamber was 26 mbar. The Bi/Ti ratio in the precursor solution was changed from stoichiometric to the 50 % excess of Bi. The substrate carrier was rotated between 550 and 1250 rpm.

The series of deposition temperature was made with 25 % excess of Bi in the precursor solution, since it is known from the literature that Bi is volatile and should be introduced in excess. At high deposition temperatures (800 °C and 850 °C) mainly a Bi poor phase ($Bi_2Ti_4O_{11}$) and poor structural ordering at 850 °C was observed (Fig. 3.4.1). HRXRD analysis shows the existence of characteristic $Bi_2Ti_4O_{11}$ peaks (marked as stars in Fig. 3.4.1) which appear at slightly higher 2θ angles than the $Bi_4Ti_3O_{12}$ peaks (Fig. 3.4.2 a). The amount of $Bi_2Ti_4O_{11}$ was decreasing with the decrease of deposition temperature and at the same time the amount of ferroelectric $Bi_4Ti_3O_{12}$ phase was increasing. A well ordered, pure $Bi_4Ti_3O_{12}$ phase was observed at deposition temperature of 700 ºC. The film was epitaxially grown with (00*l*) orientation on $SrTiO_3$ substrates. The detailed HRXRD analysis of $Bi_4Ti_3O_{12}$ film deposited at 700 °C showed a narrow (006) $Bi_4Ti_3O_{12}$ diffraction peak and thickness oscillations, indicating a rather smooth surface of the film and interface between the film and

substrate (Fig. 3.4.2 b). Further decrease of deposition temperature lead to worse structural ordering (broader peaks), disappearance of the characteristic (00*l*) reflections of $Bi_4Ti_3O_{12}$ and appearance of pyrochlore phase $Bi_2Ti_2O_7$ (characteristic peak at ~ 30° in Fig. 3.4.1, T_d = 600 °C). The films deposited at 550 °C are amorphous.

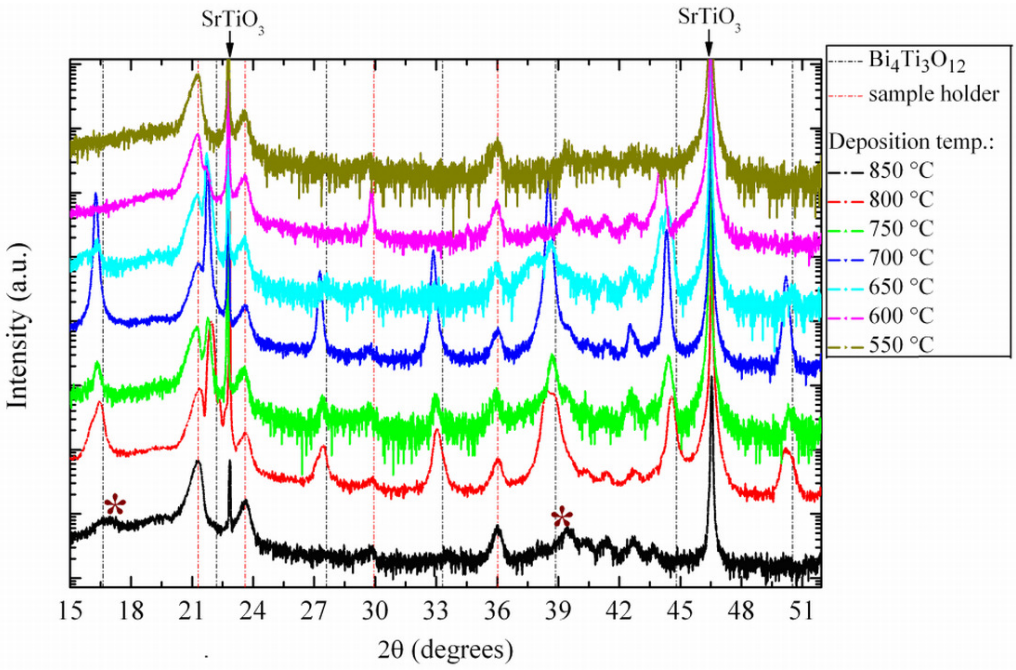

Fig. 3.4.1 HRXRD patterns of the (00*l*) reflection peaks of epitaxial $Bi_4Ti_3O_{12}$ films on $SrTiO_3$ substrates deposited at different temperatures. The vertical lines indicate the position of bulk $Bi_4Ti_3O_{12}$ (00*l*) Bragg reflections and reflections from sample holder. Stars indicate $Bi_2Ti_4O_{11}$ phase.

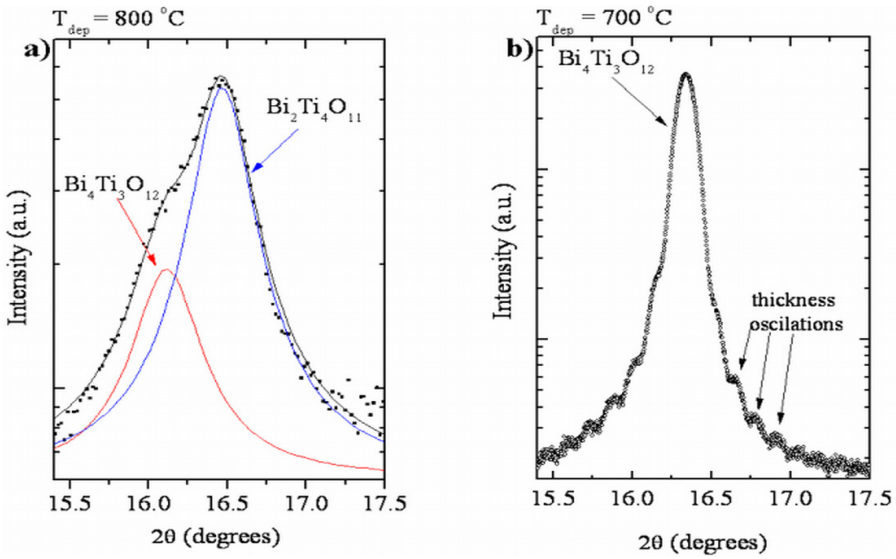

Fig. 3.4.2 a) HRXRD pattern of the (006) reflection peak of $Bi_4Ti_3O_{12}$ and the (-202) reflection peak of $Bi_2Ti_4O_{11}$ deposited at 800 °C and **b)** (006) reflection peak of $Bi_4Ti_3O_{12}$ deposited at 700 °C on $SrTiO_3$.

A significant decrease of surface roughness from 3.1 nm to about 0.6 was observed (Fig. 3.4.3 a) when the temperature was increased form 550 ºC to 700 ºC. The surface morphology of the film deposited at 700 ºC temperature is shown in the inset of Fig. 3.4.3 a. This effect can be correlated with the quality of structural ordering of the films. HRXRD patterns at higher deposition temperatures (T > 700 °C) show that the quality of the films decreases again, because Bi is lost due to its volatility and fragility of Bi-O bond [195]. The loss of bismuth leads to the reduced growth rate for increasing temperature (Fig. 3.4.3 b); similar to what was observed in the case of $SrRuO_3$ films.

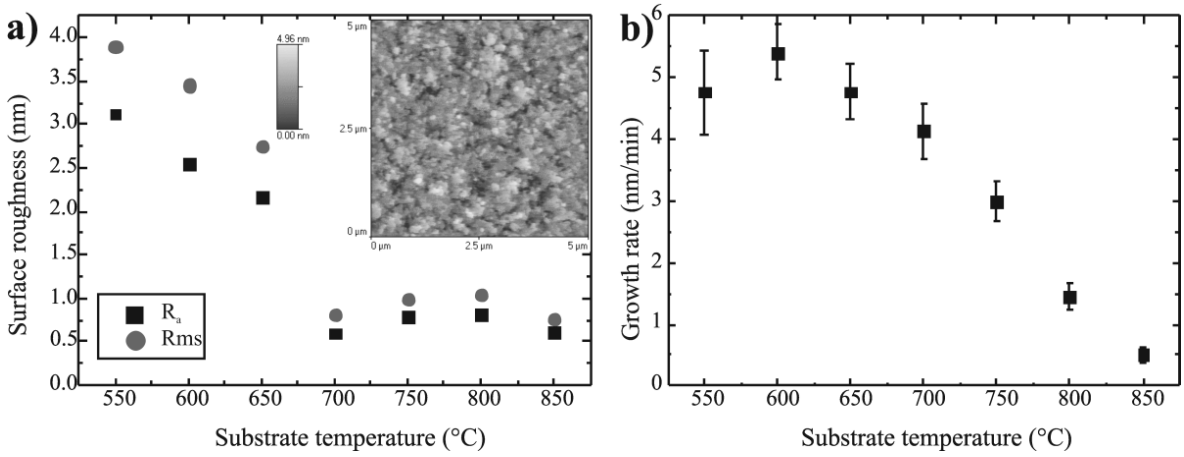

Fig. 3.4.3 a) Surface roughness as a function of growth temperature (R_a – average roughness, RMS – root means square roughness). Inset – AFM image of $Bi_4Ti_3O_{12}$ films deposited at 700 °C; **b)** growth rate versus substrate temperature.

The Bi/Ti ratio in the precursor solution was adjusted for the deposition temperature of 700 °C, since pure and well ordered structure of $Bi_4Ti_3O_{12}$ was observed with a low surface roughness. It was observed that, depending on Bi content in the precursor solution, the films show differences in the phase composition and structural ordering. As can be seen in the HRXRD θ/2θ scans (Fig. 3.4.4), the films deposited by using stoichiometric amount of Bi and Ti in the precursor solution, exhibited a bad ordering, demonstrated by the presence of only few and broad (00*l*) peaks of $Bi_4Ti_3O_{12}$. A detailed HRXRD analysis showed that these broad peaks, consist actually from two contributions, one is related to $Bi_4Ti_3O_{12}$ and other to $Bi_2Ti_4O_{11}$ like it was already observed for the films deposited over 800 °C. It can be concluded that both phases co-exist if the Bi/Ti ratio is stoichiometric. The occurrence of a Bi poorer phase under these deposition conditions can be explained by high volatility of Bi at high temperatures [196,197]. Therefore, an excess of Bi was used in the precursor solution to

improve the phase composition and structural ordering of the films. As it can be seen from Fig. 3.4.4 additional (00*l*) reflection peaks of $Bi_4Ti_3O_{12}$ appear in HRXRD patterns when 25 % and 50 % excess of Bi were employed. In both cases single phase $Bi_4Ti_3O_{12}$ films were obtained. They exhibited improved structural ordering compared with the films which are deposited with stoichiometric Bi/Ti ratio in the precursor solution. No difference was observed in HRXRD patterns between the films deposited with 25 % and 50 % excess. Therefore, in order to get a stoichiometric single phase $Bi_4Ti_3O_{12}$ and to prevent formation of Bi poor phases, Bi excess is required. For this reason in further experiments, 25 % Bi excess in the precursor solution was used.

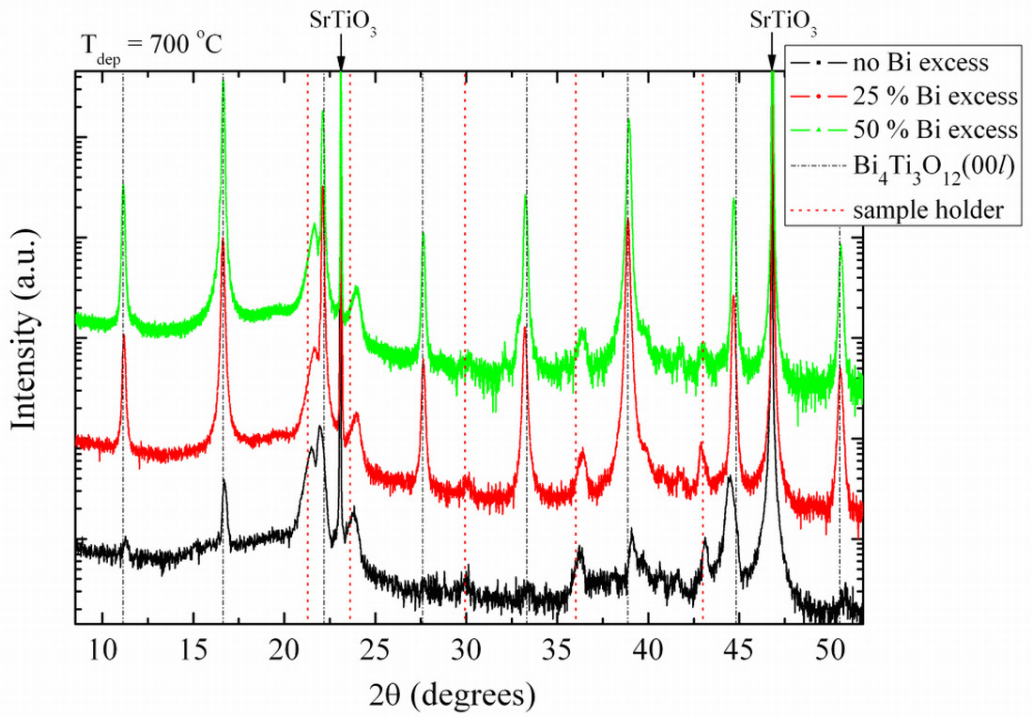

Fig. 3.4.4 HRXRD patterns of the (00*l*) reflection peaks of epitaxial $Bi_4Ti_3O_{12}$ films deposited on $SrTiO_3$ substrates by using different Bi/Ti ratio in the precursor solution. The vertical lines indicate the position of bulk $Bi_4Ti_3O_{12}$ (00*l*) Bragg reflections and reflections of sample holder.

The growth rate of the films was changed by increasing the substrate rotation from 300 to 1250 rpm. Due to that, the boundary layer at the gas – solid interfaces also changed. The growth rate increased significantly from 2.9 nm/min at 300 rpm to 5.6 nm/min at 1250 rpm (Fig. 3.4.5 a) due to the increased mass transport though a thinner boundary layer.

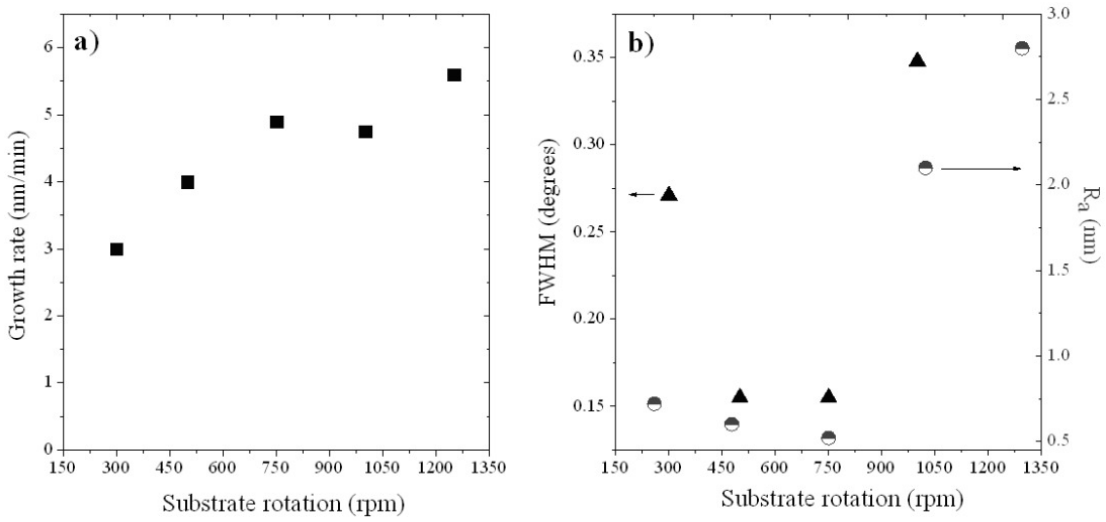

Fig. 3.4.5 a) Growth rate and **b)** FWHM of the (006) reflection peak and average surface roughness dependence on substrate rotation of $Bi_4Ti_3O_{12}$ deposited on $SrTiO_3$ substrate at 700 °C.

HRXRD measurements (Fig. 3.4.6) showed that epitaxial, well ordered $Bi_4Ti_3O_{12}$ layers can be grown if substrate rotations of 500 rpm and 750 rpm are used. Whereas, worse structural ordering, (higher FWHM values of (006) reflections) (Fig. 3.4.5 b), was obtained at lowest rotation of 300 rpm. At high substrate rotations (at 1000 rpm and more), the structural ordering decreases drastically (higher FWHM values) or characteristic peaks of $Bi_4Ti_3O_{12}$ completely disappear (1250 rpm). The smoothest films were observed at 500 and 750 rpm substrate rotations, whereas at highest rotations the average surface roughness increases (Fig. 3.4.5 b), since the species on the surface do not have enough time to diffuse to a suitable places.

With the increase of substrate rotation the boundary layer becomes thinner leading to higher growth rates due to the shorter diffusion time of the precursor particles across the boundary layer. The shorter diffusion time leads to worse ordering of $Bi_4Ti_3O_{12}$ films because of the insufficient time for the atoms to find the correct positions on the substrate surface. In other words, the diffusion across the boundary layer is quicker that the surface diffusion. On the other hand, if the diffusion layer becomes too thick an insufficient amount of Bi reaches the surface, because of the high mass of Bi atoms reducing the diffusion rate of Bi. In conclusion, it can be stated that epitaxially grown well ordered $Bi_4Ti_3O_{12}$ can be obtained for substrate rotations between 500 and 750 rpm if $Bi_4Ti_3O_{12}$ films are deposited at 700 °C with 25 % Bi excess in the precursor solution.

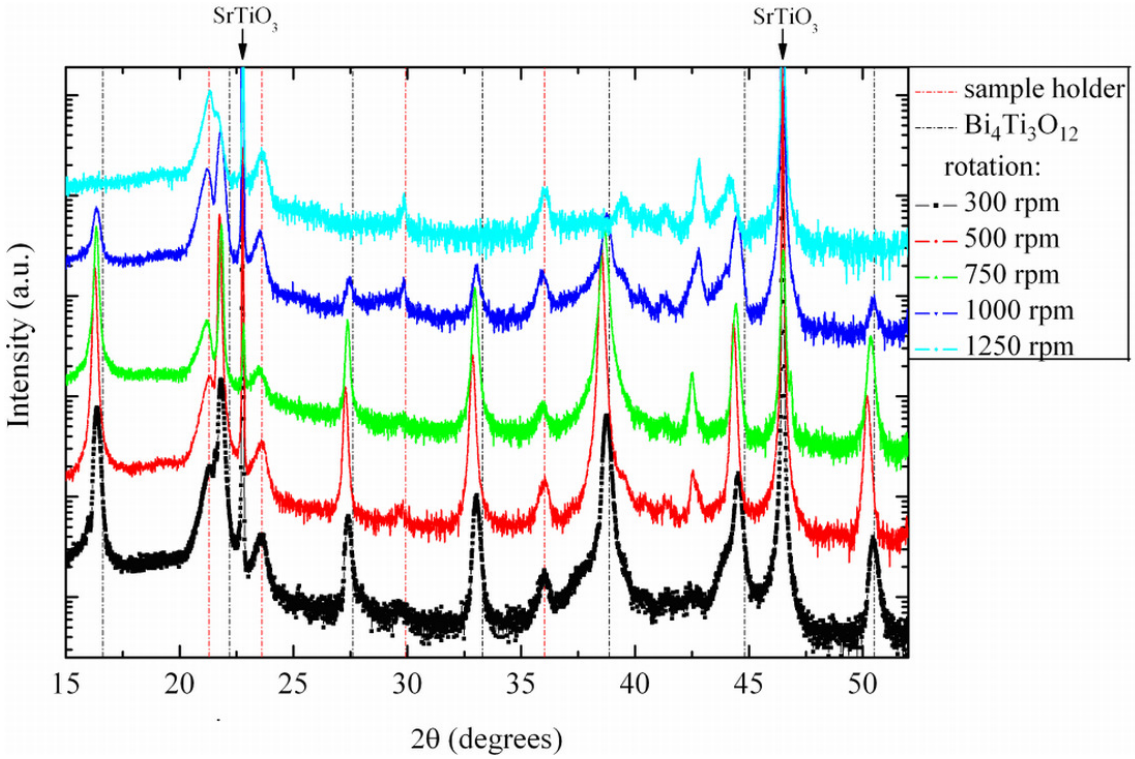

Fig. 3.4.6 HRXRD patterns of the (00*l*) reflection peaks of epitaxial $Bi_4Ti_3O_{12}$ films deposited on $SrTiO_3$ substrates by using different rotations of the substrate. The vertical lines indicate the position of bulk $Bi_4Ti_3O_{12}$ (00*l*) Bragg reflections and reflections of sample holder.

In order to study the influence of the lattice mismatch on the structural properties, thin films of $Bi_4Ti_3O_{12}$ were deposited on three different oxide substrates: $SrTiO_3$(001), $NdGaO_3$(110) and $DyScO_3$(110), which had different lattice constants. HRXRD patterns, in the 2θ range from 5° to 90° (not shown here) confirmed that, well ordered, (00*l*)-oriented $Bi_4Ti_3O_{12}$ films are grown on all three oxide substrates. The (008) reflections of $Bi_4Ti_3O_{12}$ films, deposited on $SrTiO_3$(001), $NdGaO_3$(110) and $DyScO_3$(110) substrates are shown in Fig. 3.4.7.

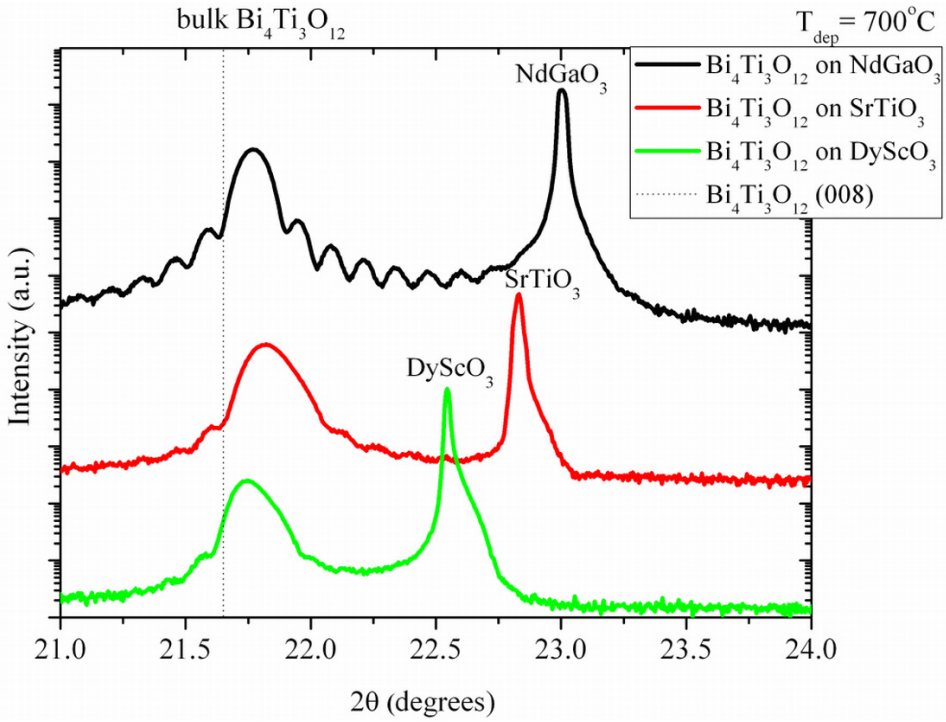

Fig. 3.4.7 HRXRD patterns of the epitaxial $Bi_4Ti_3O_{12}$ films (008) reflection peaks deposited on $SrTiO_3$, $NdGaO_3$ and $DyScO_3$ substrates at 700 °C. The vertical line indicates the position of bulk $Bi_4Ti_3O_{12}$ (008) Bragg reflections.

Additionally, lattice constants of the films in *c*-direction were calculated from a detailed analysis of HRXRD data (Table 3.4.1).

Table 3.4.1 The experimental *c*-lattice parameters of $Bi_4Ti_3O_{12}$ films grown on $SrTiO_3$, $NdGaO_3$, $DyScO_3$. The theoretical mismatch (ε_a) between the film and the substrate is also given.

$Bi_4Ti_3O_{12}$ on:	c-lattice parameter, Å	ε_a, %
$NdGaO_3$(110)	32.628	-0.16
$SrTiO_3$(001)	32.554	-1.27
$DyScO_3$(110)	32.661	-2.19
Relaxed (bulk) $Bi_4Ti_3O_{12}$ [58]	32.830	

The thickness of the films deposited on $SrTiO_3$(001), $NdGaO_3$(110) and $DyScO_3$(110) substrates were 66 nm. It is known that the higher lattice mismatch leads to the lower critical

thickness of the film [24]. For a highly mismatched system like $Bi_4Ti_3O_{12}/DyScO_3$ critical film thickness will be below 66 nm (see for example in [198]), therefore it is expected that $Bi_4Ti_3O_{12}$ films grown on $DyScO_3$ have a high amount of incorporated defects leading to less strained or almost relaxed films with higher out-of-plane lattice parameter compared with the films grown on $SrTiO_3$ and $NdGaO_3$ substrates (Table 3.4.1). Since the matching between the $Bi_4Ti_3O_{12}$ and $NdGaO_3$ is quite good (mismatch value is only -0.16 %), therefore the interface between the film and the substrate is very smooth (clear thickness fringes in Fig. 3.4.7) and only small tensile distortion of the unit cell of $Bi_4Ti_3O_{12}$ is expected. Therefore, it can be assumed that $Bi_4Ti_3O_{12}$ is pseudomorphically grown on $NdGaO_3$ substrate if the thickness of the oxide is about 66 nm. Since the mismatch between $Bi_4Ti_3O_{12}$ and $NdGaO_3$ is low the incorporated strain in the films should be higher compared with the films grown on $DyScO_3$. This is also evident from lower out-of-plane lattice parameter (Table 3.4.1). For $Bi_4Ti_3O_{12}$ films, grown on $SrTiO_3$, lattice mismatch is significantly larger compared with the films grown on $NdGaO_3$, therefore a higher strain in the films is expected (lower out-of-plane lattice parameter). However, the film thickness is equal to 66 nm and is probably larger as the critical film thickness, therefore partial relaxation of strain by the formation of defects has been started. Anyway, the residual strain is higher as for the films grown on $NdGaO_3$ (evident from Fig. 3.4.7 and smaller out-of-plane lattice parameter on $SrTiO_3$).

These results explain only the sequence of the *c*-lattice parameter of $Bi_4Ti_3O_{12}$ on different substrates (in the Table 3.4.1). But the reasons why the relaxed film on $DyScO_3$ does not show the same lattice parameter as bulk $Bi_4Ti_3O_{12}$ it is still not clear yet.

3.5 Na substitution at Bi site in epitaxial $Bi_4Ti_3O_{12}$ films

The influence of the substitution of Bi with aliovalent Na on the structural changes of $Bi_4Ti_3O_{12}$ will be described in this section. So far only very few literature reports on the effect of such substitution on the properties of the oxide compounds are available and mainly concern ceramics [136,199,200]. An important point here is that no reports are available for the films deposited by LD-MOCVD, which makes this particular study even more useful. The biggest challenge in this study was to incorporate Na into the films due to its high volatility. Also, no literature data for MOCVD grown Na containing bismuth titanate films, like $Na_{0.5}Bi_{4.5}Ti_4O_{15}$, with higher number of the perovskite blocks in an Aurivillius structure is available.

Two types of sodium precursors, [Na(thd)] and [$NaN(Si(CH_3)_3)_2$] (NaTMSA), with different concentrations, were used for these investigations. However, depositions with [Na(thd)] precursor were not successful, because they were performed when only one flash evaporator was installed. Chemical reactions with the other precursors (Ti, Bi) prevented the successful deposition of Na containing films. This limitation demanded to the decision to install a second flash evaporator. Furthermore, the tendency of [Na(thd)] to oligomerize (Section 3.2.3.1) limits the application of this precursor. Therefore [$NaN(Si(CH_3)_3)_2$] was successfully applied for the incorporation of Na into the $Bi_4Ti_3O_{12}$ films. This precursor was introduced to the chamber through a separate flash evaporator, whereas the other flash evaporator was used for the Bi/Ti solution. The temperature of both flash evaporators was fixed to 230 °C.

The substitution of $Bi_4Ti_3O_{12}$ with Na was investigated in the temperature interval between 600 - 720 °C. By the systematic increase of Na content (0.01 - 0.03 M) in the precursor solution and subsequently in the gas phase, the change of structure and surface morphology of the substituted $Bi_4Ti_3O_{12}$ were investigated. Different oxide $SrTiO_3$(001), $NdGaO_3$(110), $DyScO_3$(110) substrates were used in order to check the influence of the lattice mismatch on the properties of the films. The pressure in the chamber during deposition was 26 mbar. The substrates were rotated at 500 rpm.

Due to high volatility of Na precursor, depositions were started at relatively low (600 °C) deposition temperature. In previous section, it was shown that well ordered and pure $Bi_4Ti_3O_{12}$ films can be obtained with a minimum temperature of 700 °C. However since the determination of the substrate temperature is performed with a thermocouple nearby the

heating filament, the exact or absolute temperature on the substrate surface may significantly change due to technological changes like; the material and the thickness of the substrate carrier, the distance between carrier and filament, the position of the thermocouple. After the depositions of the $Bi_4Ti_3O_{12}$ films, described in the previous section, some technological improvements had to be implemented in the reactor. Since they directly influenced the thermal conditions in the vicinity of the substrate, it was established that a much lower deposition temperature has to be adjusted to obtain the same structural quality of the films as before.

The effect of Na substitution on the structural properties of $Bi_4Ti_3O_{12}$ was investigated by HRXRD. The corresponding patterns of pure and Na-substituted $Bi_4Ti_3O_{12}$ thin films are shown in Fig. 3.5.1. Pure $Bi_4Ti_3O_{12}$ grows epitaxially on the $SrTiO_3$ substrates with (00*l*) orientation. With the increase of Na content, a second phase appears like a shoulder to the reflections of $Bi_4Ti_3O_{12}$ and are shifted to the higher 2θ angles. From the (00*l*) reflections in HRXRD patterns, the out-of-plane lattice constants were calculated for both phases. The extra phase showed a slightly lower *c*-lattice constant between 32.0 and 32.3 Å compared to the *c*-lattice constant of the pure $Bi_4Ti_3O_{12}$ (32.6 Å, Fig. 3.5.2). The slightly reduced out-of-plane lattice parameter of the second phase suggests that this phase belongs to Aurivillius structure as well and is attributed to a Na-substituted $Bi_4Ti_3O_{12}$ ($(Na, Bi)_4Ti_3O_{12}$) phase.

The observed *c*-lattice parameter of $Bi_4Ti_3O_{12}$ films is slightly lower compared with the bulk value of 32.83 Å [58] indicating slight tensile strain in $Bi_4Ti_3O_{12}$ films grown on $SrTiO_3$ substrates, as it was described in previous section, and which is also confirmed by a reciprocal space mapping.

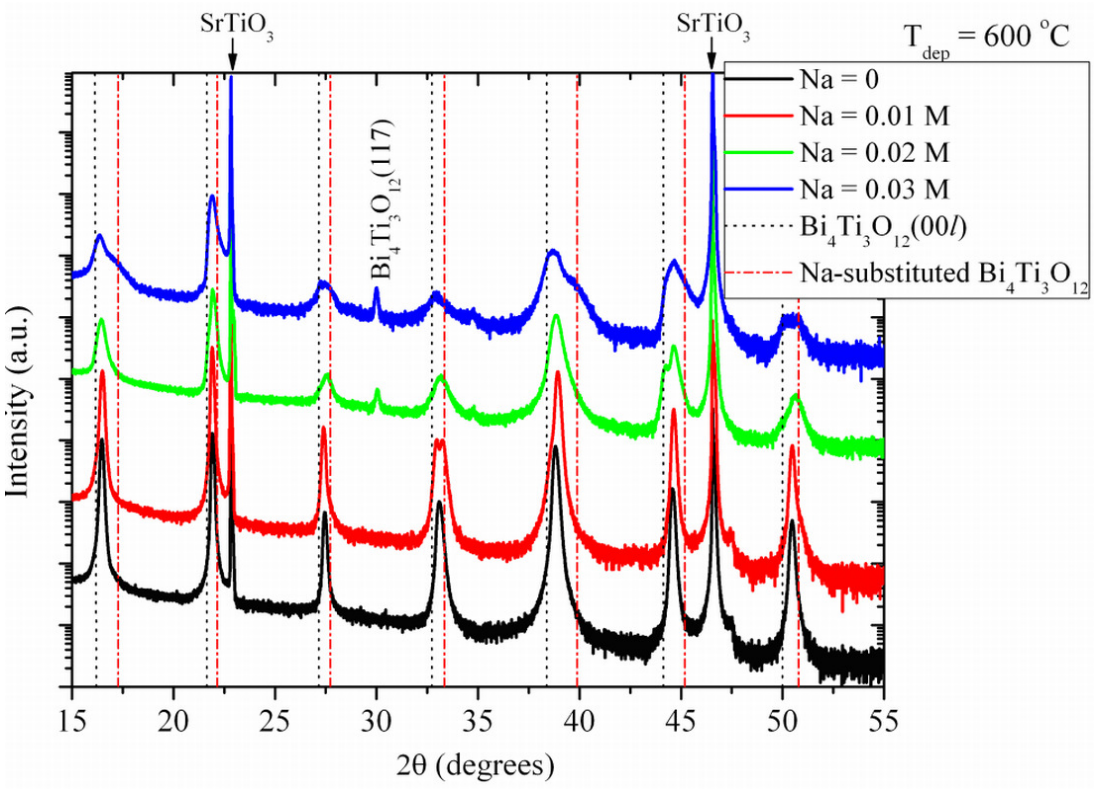

Fig. 3.5.1 HRXRD patterns of $Bi_4Ti_3O_{12}$ films deposited on $SrTiO_3$ at 600 °C by using different amount of Na in the precursor solution. The vertical lines indicate the Bragg reflections of respective films.

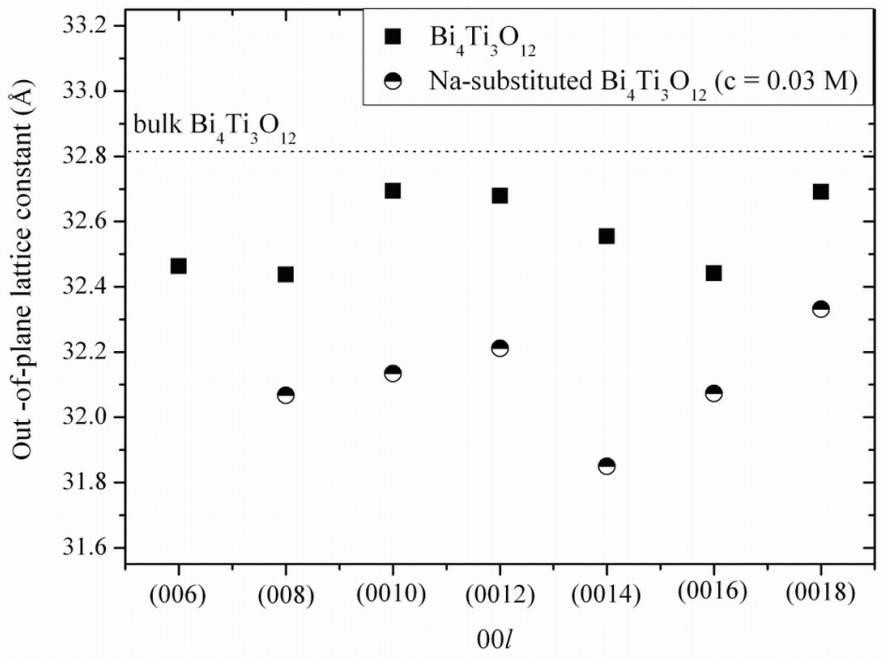

Fig. 3.5.2 The out-of-plane lattice constants of $Bi_4Ti_3O_{12}$ and Na-substituted $Bi_4Ti_3O_{12}$ (c_{Na} = 0.03 M) films, calculated from the 00*l* Bragg reflections.

Additionally, the increase of Na content in the precursor solution and in the films leads to an increase of average roughness of the surface and reduced grain size, as found by AFM measurements (Fig. 3.5.3 and Fig. 3.5.4). The increased intensity of $Bi_4Ti_3O_{12}$(117) reflection peak from HRXRD measurements (Fig. 3.5.1), suggest that with the increase of Na content a worse structural ordering in the films occurs.

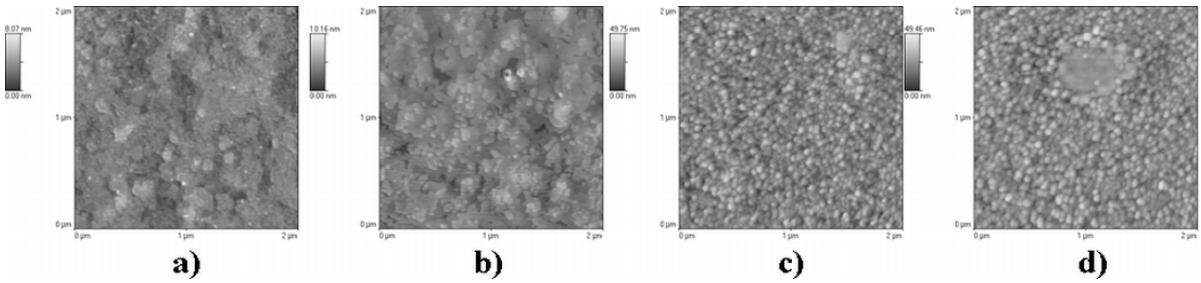

Fig. 3.5.3 AFM images (2 µm × 2 µm) of pure and substituted $Bi_4Ti_3O_{12}$ films deposited on $SrTiO_3$ at 600 °C, where content of Na in the precursor solution was **a)** Na = 0, **b)** Na = 0.01 M, **c)** 0.02 M, **d**) 0.03 M.

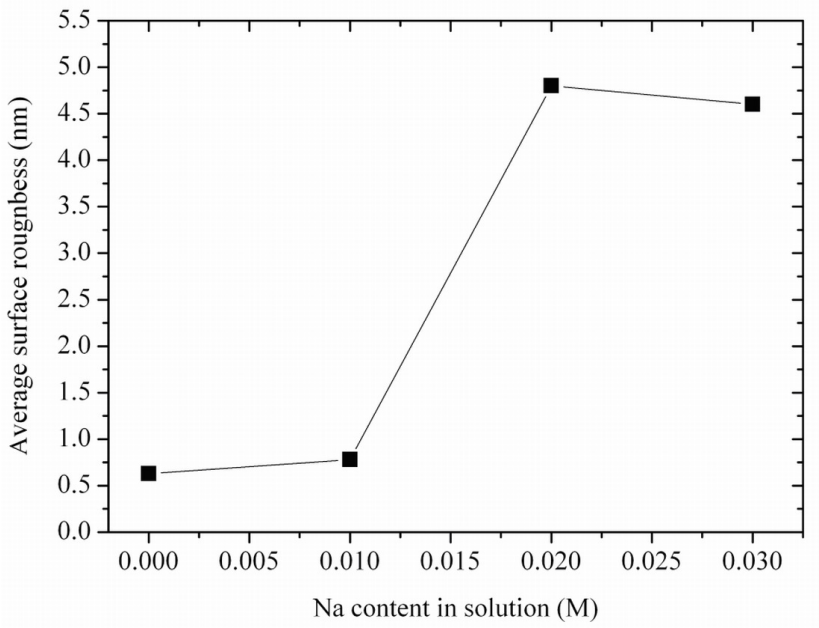

Fig. 3.5.4 The dependence of average surface roughness on the Na content in the precursor solution for the films deposited at 600 °C.

The incorporation of Na into $Bi_4Ti_3O_{12}$ layers was additionally confirmed by XPS and X-ray fluorescence measurements (XRF). According to the XRF data a large amount of Na (~ 10 %) was found on the surface of the pure $Bi_4Ti_3O_{12}$ film, but no Na could be detected in the film. This observation is explained by surface impurities due to handling and storage of

the sample after deposition. For the film deposited from the solution with 0.01 M of Na, a Na concentration of 1-1.5 % was observed over the whole thickness of the film [201]. XPS measurements showed that Na exists on the surface at binding energy of 1070.3 eV for the pure $Bi_4Ti_3O_{12}$ film. Whereas, for the film deposited from the solution with 0.03 M of Na, a shift of the Na 1s peak is observed and assigned to Na bonded to oxygen at binding energy of 1071.6 eV as indicated in Fig. 3.5.5. The XRF and XPS results lead to a conclusion, that Na signal for the pure $Bi_4Ti_3O_{12}$ is caused by "metallic" Na on the surface. The shift of Na 1s core level to higher binding energies, for the Na-substituted $Bi_4Ti_3O_{12}$ film (c_{Na} = 0.03 M), is explained by the incorporation of Na into the lattice and the bonding to oxygen according to literature data [202].

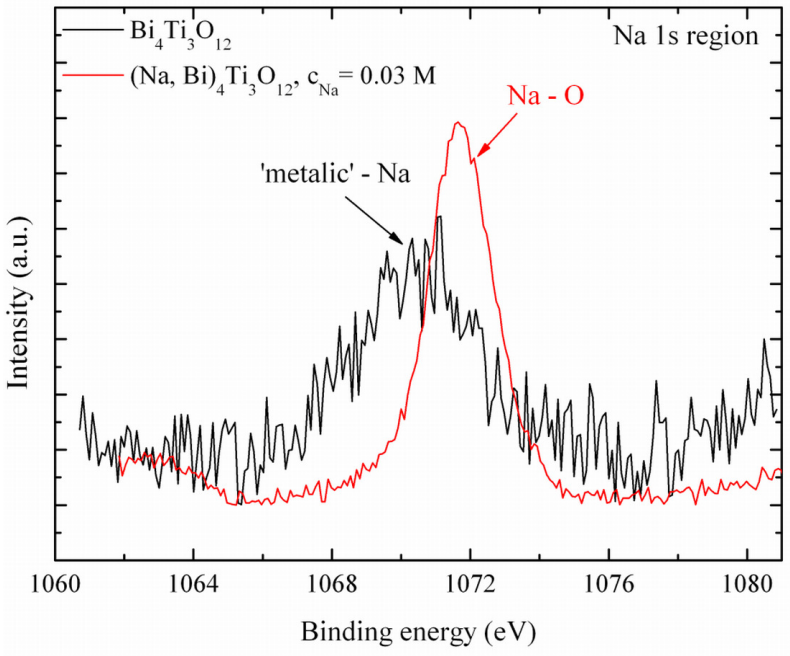

Fig. 3.5.5 Na 1s core level spectra of substituted and pure $Bi_4Ti_3O_{12}$ films deposited at 600 °C on $SrTiO_3$.

The Bi 4f core level spectrum of pure $Bi_4Ti_3O_{12}$ film (Fig. 3.5.6 a) shows that $4f_{5/2}$ (1) core line is located at 164.4 eV and $4f_{7/2}$ (1) located at 159.1 eV, which is in well agreement with literature data [203,204]. Fitting of the Bi 4f core level spectra for the film, which contains Na, was only possible to perform with two duplets. If one duplet was assumed a small deviation between the fitted and experimental curves at higher binding energies remains, indicating the existence of the second component (Fig. 3.5.6 b). The fitting was carried out under the condition that the Bi 4f(1) core level remains the same (position, core level splitting, FWHM) for the samples in Fig. 3.5.6 a) and b). The $4f_{5/2}$ (2) and $4f_{7/2}$ (2) core

levels of the second component are shifted by about 0.5 eV to higher binding energies compared to the $4f_{5/2}$ (1) and $4f_{7/2}$ (1) core levels of the pure $Bi_4Ti_3O_{12}$ film. These contributions can be attributed to Bi^{5+} ions, whose binding energy is specified in the literature to be 0.3-1.0 eV higher than those of Bi^{3+}, depending on the composition of the samples and chemical environment of Bi [203,204,205,206].

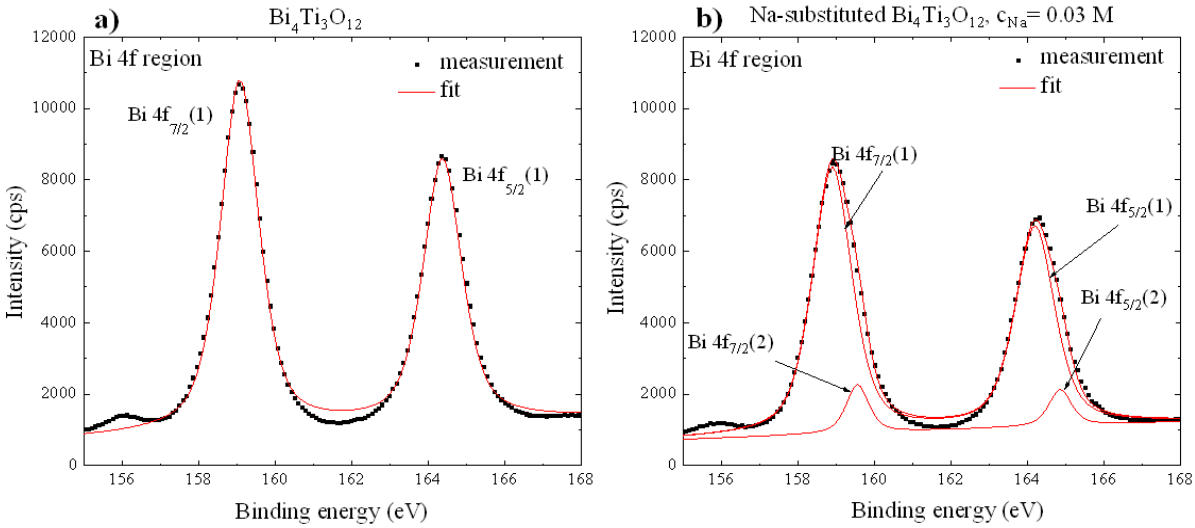

Fig. 3.5.6 Bi 4f core level spectra of **a)** pure $Bi_4Ti_3O_{12}$ and **b)** Na-substituted $Bi_4Ti_3O_{12}$ films deposited at 600 °C on $SrTiO_3$.

Some additional information was gained from the Bi 4d and Ti 2p core level spectra (Fig. 3.5.7).

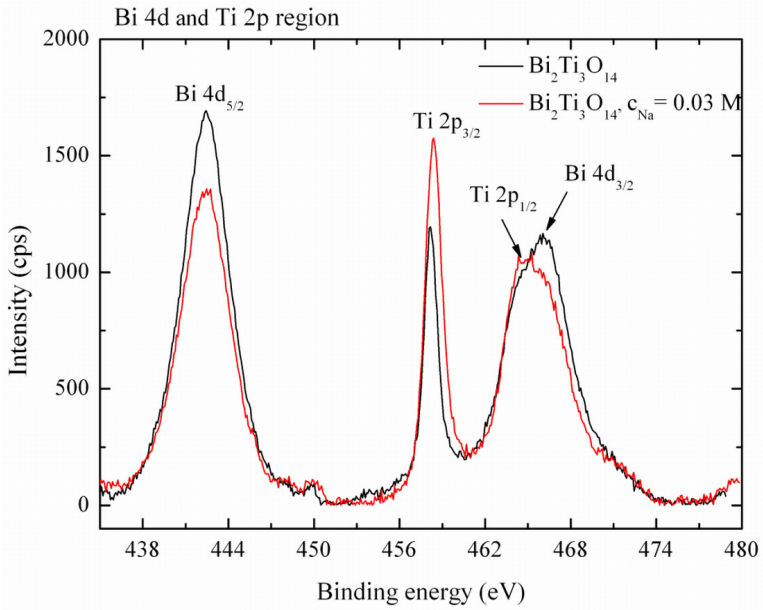

Fig. 3.5.7 Bi 4d and Ti 2p core level spectra of $Bi_4Ti_3O_{12}$ and $(Na, Bi)_4Ti_3O_{12}$ (c_{Na} = 0.03 M) films deposited at 600 °C on $SrTiO_3$.

For a rough estimation the ratios Ti $2p_{3/2}$ / Bi $4d_{5/2}$ of the intensities of the characteristic Ti 2p and Bi 4d core levels in substituted and pure $Bi_4Ti_3O_{12}$ films were calculated. They were equal to 1.19 and to 0.96, respectively. This shows that the amount of Bi cations is reduced in the substituted film compared to the pure film, probably caused by the substitution with aliovalent Na cation or to Bi deficiency.

The XPS data of the O 1s core level of the pure and the Na-substituted $Bi_4Ti_3O_{12}$ film (c_{Na} = 0.03 M) is represented in Fig. 3.5.8. The deconvolution of the O 1s core level spectrum of the pure $Bi_4Ti_3O_{12}$ film reveals two peaks (Fig. 3.5.8 a), where three contributions are necessary to fit the spectrum of the Na-substituted $Bi_4Ti_3O_{12}$ film (Fig. 3.5.8 b). According to literature data [207,208], the feature with the binding energy of 530 eV is attributed to O^{2-} ions, which are bonded to Ti^{4+} (Ti-O contribution), while the second one at 531.5 eV is ascribed to oxygen bonded with Bi^{3+} (Bi^{3+}-O contribution). The third peak at even higher binding energy of 532 eV is assumed to be caused by Bi^{5+}-O contribution, since the electronegativity of Bi^{5+} ions is higher compared to Bi^{3+} ions. More electronegative Bi^{5+} ions are expected to have stronger bonds to oxygen ions.

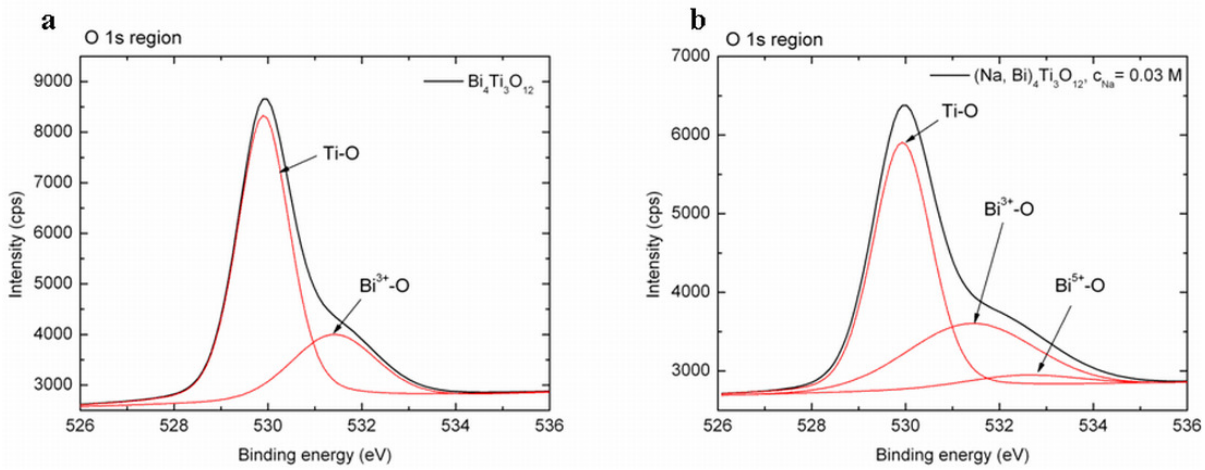

Fig. 3.5.8 O 1s core level spectra of **a)** $Bi_4Ti_3O_{12}$ and **b)** $(Na, Bi)_4Ti_3O_{12}$ (c_{Na} = 0.03 M) films deposited at 600 °C on $SrTiO_3$.

Based on these experimental results, a model describing the incorporation of Na in the $Bi_4Ti_3O_{12}$ structure is proposed. For aliovalent substitution three charge compensation mechanisms are possible [209]: formation of vacancies, generation of interstitials or modification of the valence state of an appropriate number of ions. The formation of oxygen vacancies should be connected to an increased lattice parameter [210], however, it was not

observed in the HRXRD data (see Fig. 3.5.1). The probability of creation of cation interstitials in perovskites is rather low due to their closed packed structure and the large ionic radii of the cations [209]. Therefore, the obtained experimental results are explained by a change of the valence state of the Bi cations. Since Bi in $Bi_4Ti_3O_{12}$ structure has an oxidation state of 3+, the substitution with aliovalent Na^+ would lead to negatively charged structure, therefore, charge has to be compensated in order to achieve charge neutrality in the structure. The ionic radius of Bi^{3+} (r = 103 nm) [130] and Na^+(r = 102 nm) [130] are almost the same; therefore the ionic radius should not cause any structural changes if only the substitution of Bi by Na is concerned. XPS spectra suggests that the oxidation state of some Bi changes from Bi^{3+} to Bi^{5+} during the substitution with Na at Bi-site in the perovskite slabs (Fig. 3.5.6) and in O 1s core levels bonding energy of 532 eV could be attributed to Bi^{5+}-O bonds (Fig. 3.5.8). Since ionic radius of Bi^{5+} is equal to 76 nm [130], the change from lower to higher oxidation state of Bi may lead to a smaller out-of-plane lattice constant, which was observed from HRXRD patterns (Fig. 3.5.1 and Fig. 3.5.2). The occurrence of the additional core level lines, shifted by ~ 0.5 eV to higher binding energies in the Bi 4f core level spectrum (Fig. 3.5.6) of the Na containing film, indicates that Bi^{3+} as well as Bi^{5+} cations are present in the film.

After the successful incorporation of Na into the $Bi_4Ti_3O_{12}$ films at 600 °C, achieved for the first time by LD-MOCVD, the depositions were performed also at higher deposition temperatures (720 °C). HRXRD patterns of the films, deposited at 600 °C and 720°C, are shown in Fig. 3.5.9. As described above, the films, deposited at 600 °C exhibit the co-existence of the Na-substituted $Bi_4Ti_3O_{12}$ ($(Na, Bi)_4Ti_3O_{12}$) phase with smaller out-of-plane lattice constant and $Bi_4Ti_3O_{12}$ phase.

The HRXRD (Fig. 3.5.9) pattern for a layer deposited at 720 °C shows the (00*l*) diffraction peak of a pure $Bi_4Ti_3O_{12}$ phase and additionally some extra peaks (marked by triangles). Different models are proposed to explain the diffraction pattern: a) interpretation of the extra peaks as an extra phase, analysis of the peak positions results in *c* lattice constant of 15.6 Å, together with the incorporated elements is may be attributed to a $Na_2Ti_9O_{19}$ structure, but rather unlikely, due to the preparation conditions normally used for this structure; b) Na is incorporated on nearly all Bi sites in the perovskite, so that the Bi^{5+} ions are arranged in the Bi_2O_2 intermediate layer; however since the lone pair electron is missing for Bi^{5+} it is also not probable; c) regular insertion of an extra perovskite unit every third, fourth or fifth unit cell, so that the film structure contains m = 3 units and some m = 4 units. The results are still under discussion and need some more experiments for a final conclusion.

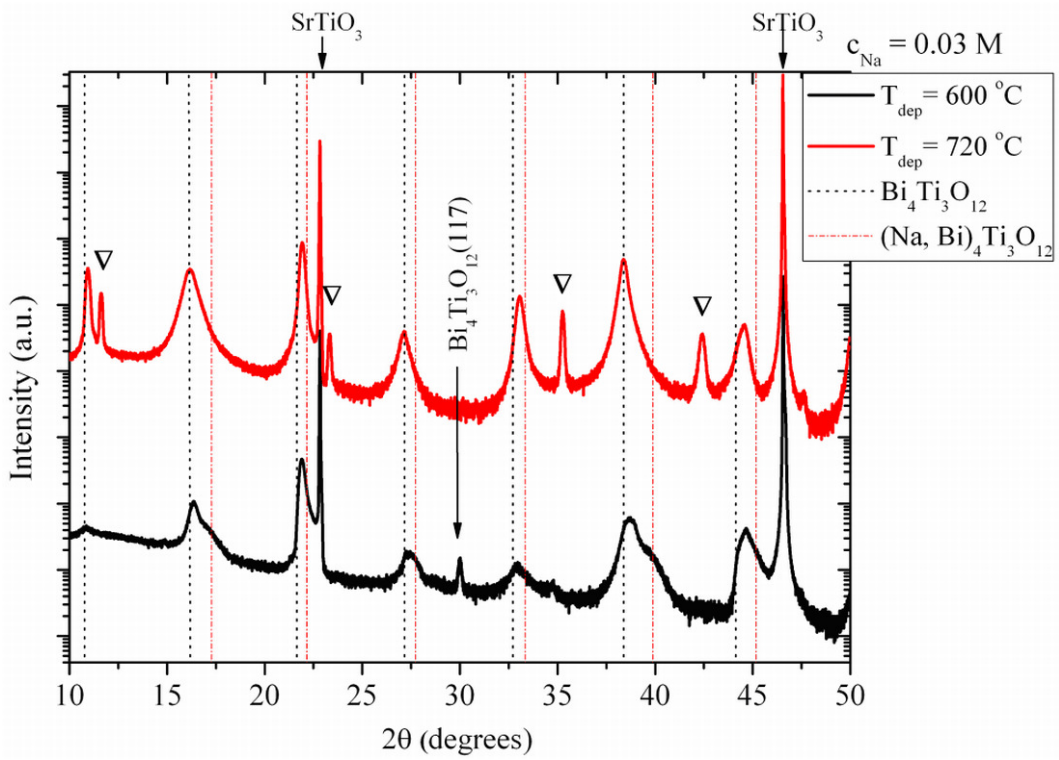

Fig. 3.5.9 HRXRD patterns of the Na-substituted $Bi_4Ti_3O_{12}$ films deposited at different temperatures on $SrTiO_3$, when Na concentration of 0.03 M in the precursor solution was used. The vertical lines indicate the characteristic reflections of $Bi_4Ti_3O_{12}$ and $(Na, Bi)_4Ti_3O_{12}$. Triangles indicate the Bragg reflections of the additional phase.

The conformation about higher structural ordering of the Na-substituted $Bi_4Ti_3O_{12}$ films grown at higher deposition temperatures is gained from HRXRD patterns (Fig. 3.5.9), where narrower (FWHM for (0014) reflection is 0.406°) and more intensive $Bi_4Ti_3O_{12}$ reflections appear in comparison to the films deposited at 600 °C temperature (FWHM = 0.883°). No reflection at 30° degrees for the films deposited at 720 °C appear, which is related to the $Bi_4Ti_3O_{12}$(117) reflection and normally is an indication of films with worse ordering.

Not only the crystal structure, but also the morphology of the films changes with the increase of deposition temperature for the substituted $Bi_4Ti_3O_{12}$ films, corresponding to a Na content in the precursor solution of 0.03 M (Fig. 3.5.10).

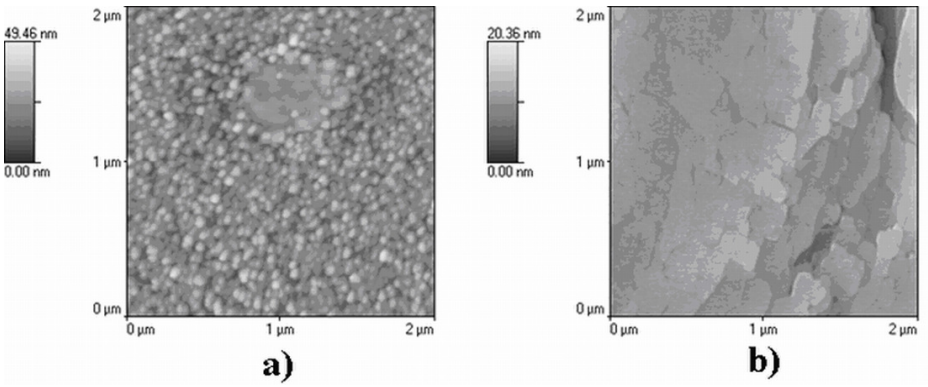

Fig. 3.5.10 AFM images (2 µm × 2 µm) of substituted $Bi_4Ti_3O_{12}$ films deposited on $SrTiO_3$ at different deposition temperatures **a)** 600 °C, **b)** 720 °C**,** where content of Na in the precursor solution was 0.03 M.

The average surface roughness of the films deposited on $SrTiO_3$ at different deposition temperatures decreases, when the temperature increases, and is equal to 4.6 nm and 1.1 nm respectively, for the films deposited at 600 °C and 720 °C. The films deposited at 600 °C contain a larger amount of grain boundaries compared with the film grown at 720 °C, which shows plate-like grains leading to smaller amount of grain boundaries. The higher perfection of the films is achieved at higher deposition temperatures (720 °C), since the the surface mobility is increased. Therefore the diffusing species on the surface can reach growing crystallites, reducing the density of grain boundaries and increasing the grain size, as it was indeed noticed.

The effect of lattice mismatch on the structural properties of Na substituted $Bi_4Ti_3O_{12}$ layers was also investigated by the use of $SrTiO_3$(001), $NdGaO_3$(110) and $DyScO_3$(110) substrates. HRXRD patterns of the substituted (Na, Bi)$_4Ti_3O_{12}$ films (c_{Na} = 0.03 M) deposited at 600 °C on different substrates are shown in Fig. 3.5.11. The characteristic peak of (Na, Bi)$_4Ti_3O_{12}$ phase appear at about 39.9°, which is not visible on $DyScO_3$ substrate. This can be explained by the worse structural ordering of the film on $DyScO_3$ (as a result of a large lattice mismatch), which would cause a broad, low intense contribution in the HRXRD pattern; therefore it is no longer visible and disappear in the background. A clearly pronounced (Na, Bi)$_4Ti_3O_{12}$ peak occurs on $NdGaO_3$ and $SrTiO_3$ substrates. Here, the lattice matching between the film and the substrate is significantly lower compared to the films grown on $DyScO_3$ substrates (see Section 3.4).

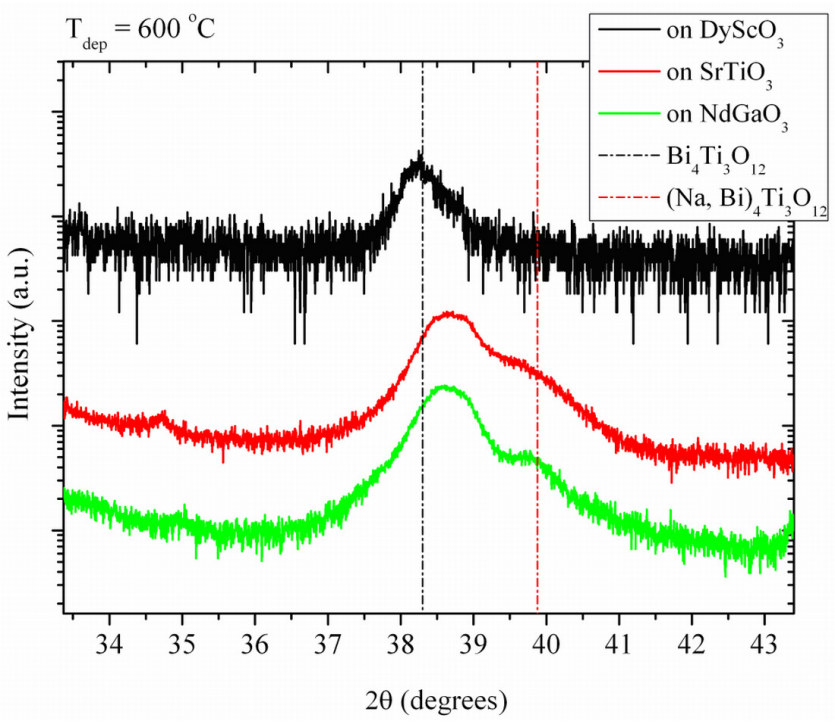

Fig. 3.5.11 HRXRD patterns of Na-substituted $Bi_4Ti_3O_{12}$ films deposited on different substrates at 600 °C, when Na concentration of 0.03 M in the solution was used. The vertical lines indicate the Bragg reflections of respective films.

In conclusion, Na was successfully incorporated for the first time in $Bi_4Ti_3O_{12}$ films deposited by LD-MOCVD. Na-substituted $Bi_4Ti_3O_{12}$ phase preserved the original Aurivillius structure and exhibited a slightly smaller lattice constant than pure $Bi_4Ti_3O_{12}$ phase. However, the characteristic Bragg reflections of Na-substituted phase was not visible in HRXRD pattern for the films deposited on highly mismatched $DyScO_3$ substrate, due to worse structural ordering of the film. The main charge compensation mechanism was proposed for the Na-substituted $Bi_4Ti_3O_{12}$, where some of Bi^{3+} ions were replaced by Na^+ in the perovskite units and the shift of the valance state of Bi^{3+} ions to Bi^{5+} (XPS results) was observed due to incorporation of Na in the films. The increase of deposition temperature could lead to the increased Na incorporation in the films, however these results are still under investigation.

4. Conclusions

Vicinal oxide substrates

- Regularly arranged step-and-terrace structure on 0.1° miscut $SrTiO_3$(001), $NdGaO_3$(110) and $DyScO_3$(110) surfaces were prepared by chemical etching of $SrTiO_3$ and subsequent thermal treatment (T ≥ 1050 °C). For $NdGaO_3$(110) and $DyScO_3$(110) exclusively only thermal annealing was necessary.

- Independently of the gas atmosphere, the surface of $NdGaO_3$ was always terminated by NdO_x. A Ga depletion layer extending up to 4 nm thickness was observed in the sub-surface region obtained under optimized preparation conditions, due to evaporation of Ga (O) at elevated temperatures.

- The surface termination of $DyScO_3$ could be switched between DyO and ScO_x depending on the gas atmosphere and annealing time. A dominant DyO termination was achieved after annealing in oxygen atmosphere for 30 – 60 minutes. On the other hand, annealing of the $DyScO_3$ crystals for 600 minutes in both oxidizing (O_2) or inert (Ar) atmospheres lead to a single ScO_x ($x \leq 2$) surface termination and a depletion layer of Dy and O in the near-surface region. The experimental results are explained by a model where the oxidation of Dy^{3+} to Dy^{4+} and the evaporation of Dy (O) from the bulk takes place, due to the weaker bonding between Dy and O compared with Sc-O bond.

Metal-organic precursors

- The metal-organic precursors were investigated by means of TG-DTA, TG-DSC and EI-MS methods in order to observe the compatibility and stability of different precursor used for the deposition of epitaxial $SrRuO_3$, $Bi_4Ti_3O_{12}$ and $(Na, Bi)_4Ti_3O_{12}$ films. The evaporation temperature intervals, the isothermal behaviour and fragmentation of the precursors showed how compatible these precursors are for the deposition of the desired films. Additionally, from the mass spectrometry data, a tendency of some precursors to oligomerization was observed. As the volatility of the compound is reduced by oligomerization, the concentration of the precursor in solution was increased by adding

more metal-organic precursor. Precursors with tendency to oligomerization ([Na(thd)] and [$Sr(thd)_2$tetraglyme]) were transferred from the different vessels to the reaction chamber via separate delivery lines and/or separated flash evaporators to prevent any pre-reactions.

Epitaxial $SrRuO_3$ films

- The stoichiometric composition of the $SrRuO_3$ films was achieved by the change of Ru/Sr ratio in the precursor solution and ratio between Ar/O_2 gas flows during heating up, deposition process and cooling down. At the deposition temperature of 600 °C the optimal Ru/Sr ratio was 0.5. The Ar/O_2 ratio during the heating up was equal to 50, while during the deposition it has to be in the range of $1 \leq Ar/O_2 \leq 3.3$ and during cooling down equal to 50 in order to get single phase $SrRuO_3$(*l*00) films.

- The deposition parameters like deposition temperature, time and concentration of the precursor solution were varied in order to investigate their influence on the growth mode and structure of $SrRuO_3$ films. Well ordered $SrRuO_3$ were achieved at the deposition temperature of 720 °C, when the growth rate was higher than 0.1 nm/min. The layer-then-island growth was however observed for the $SrRuO_3$ films grown by LD-MOCVD method, probably due to C incorporation during the film growth. The step-flow growth of $SrRuO_3$ films often described by authors using physical deposition methods, like PLD, was not observed here.

- Strained $SrRuO_3$(*l*00) films were grown on single crystalline $SrTiO_3$(001), $DyScO_3$(110), and $NdGaO_3$(110) substrates. By controlling the deposition conditions and the degree of lattice mismatch, the films exhibited compressive or tensile strain at variable levels. The measured T_c decreased with compressive and increased with tensile strain. This effect was explained by an increased (decreased) bending of the Ru-O-Ru bonds in the RuO_6 octahedron for compressively (tensely) strained films on $SrTiO_3$ and $NdGaO_3$ ($DyScO_3$) which determines the electron hopping rate between the Ru sites via the oxygen and ultimately the onset of ferromagnetism.

Epitaxial $Bi_4Ti_3O_{12}$ films

- Single phase epitaxial $Bi_4Ti_3O_{12}$ films were obtained by appropriately tuning the Bi/Ti ratio in the precursor solution, the deposition temperature and the substrate rotation rate. The optimal deposition temperature was determined to be 700 °C. It was also seen that an excess of Bi (≥ 25 %) in the precursor solution has to be used in order to prevent the formation of Bi poor phase. The best ordered $Bi_4Ti_3O_{12}$ films (when using the conditions given above) were observed for the substrate rotations of 500 and 750 rpm.

- The influence of the lattice mismatch on the structural properties of $Bi_4Ti_3O_{12}$ films deposited on $SrTiO_3$(001), $NdGaO_3$(110) and $DyScO_3$(110) was investigated. Considering the lattice mismatch, a tensile strain was expected and observed for the films on all substrates. 66 nm thick films were grown on the different substrates. For the system $Bi_4Ti_3O_{12}/DyScO_3$, the thickness of 66 nm is assumed to be above the critical thickness, therefore, the film is almost relaxed. Whereas for the highly matching $Bi_4Ti_3O_{12}/NdGaO_3$ system the critical thickness is higher than 66 nm, therefore incorporated strain in the film is low, which leads to pseudomorphical growth of $Bi_4Ti_3O_{12}$ films on $NdGaO_3$ substrates. For $Bi_4Ti_3O_{12}$ films, grown on $SrTiO_3$, lattice mismatch is significantly larger compared with the films grown on $NdGaO_3$, therefore a higher strain in the film is observed. However, the film thickness is equal to 66 nm and is larger than the critical film thickness; therefore partial relaxation of strain by the formation of defects has been started. Anyway, the incorporated tensile strain is still higher as for the films grown on $NdGaO_3$.

Na substituted $Bi_4Ti_3O_{12}$ films

- The substitution of $Bi_4Ti_3O_{12}$ with aliovalent Na was achieved by introducing Na in the gas phase via the $[NaN(Si(CH_3)_3)_2]$ precursor at deposition temperature of 600 °C. The Na-substituted films were deposited on $SrTiO_3$ and $NdGaO_3$ substrates. However, the $(Na, Bi)_4Ti_3O_{12}$ phase existed only as secondary phase together with a $Bi_4Ti_3O_{12}$ phase. Lower out-of-plane lattice constant of $(Na, Bi)_4Ti_3O_{12}$ phase in comparison with $Bi_4Ti_3O_{12}$, suggests that a charge compensation mechanism occurs. The valence of Bi^{3+} is increased to Bi^{5+} due to the substitution with monovalent Na^+. This was confirmed by HRXRD and XPS measurements.

- Increase of deposition temperature to 720 °C resulted in phase separation of $Bi_4Ti_3O_{12}$ and another phase which could not be clearly identified. Three different models were proposed and shortly discussed for the explanation of this result.

List of publications

S. Bin Anooz, J. Schwarzkopf, **R. Dirsyte**, E. Agócs, P. Petric, A. Kwasniewski, G. Wagner, R. Fornari, Spectroscopic Ellipsometry studies on the optical constants of $Bi_4Ti_3O_{12}$:xNa thin films grown by MOCVD, Thin Solid Films ((In Press. Corrected Proof. Available online 19 January 2011).

J. Schwarzkopf, **R. Dirsyte**, A. Devi, A. Kwasniewski, M. Schmidbauer, G. Wagner, M. Michling, D. Schmeisser, R. Fornari, Influence of Na on the structure of $Bi_4Ti_3O_{12}$ films deposited by liquid-delivery spin MOCVD, Thin Solid Films (In Press. Corrected Proof. Available online 6 January 2011).

S. Bin Anooz, J. Schwarzkopf, **R. Dirsyte**, G. Wagner, R. Fornari, Effects of post-annealing on physical properties of $SrRuO_3$ thin film grown by MOCVD, Phys. Status Solidi A 207 (2010) 2492-2498.

R. Dirsyte, J. Schwarzkopf, G. Wagner, M. Schmidbauer, K. Irmscher, S. Bin Anooz, R. Fornari, Impact of epitaxial strain on the ferromagnetic transition temperature of $SrRuO_3$ thin films, Thin Solid Films (submitted).

R. Dirsyte, J. Schwarzkopf, G. Wagner, R. Fornari, J. Lienemann, M. Busch, H.Winter, Thermal induced change in surface termination of $DyScO_3$(110), Surf. Sci. 604 (2010) L55-L58.

J. Schwarzkopf, **R. Dirsyte**, A. Devi, M. Schmidbauer, G. Wagner, R. Fornari, Deposition of $SrRuO_3$ thin films on oxide substrates with liquid-delivery spin MOCVD, Thin Solid Films 518 (2010) 4675-4679.

R. Dirsyte, J. Schwarzkopf, G. Wagner, J. Lienemann, M. Busch, H.Winter, R. Fornari, Surface termination of the $NdGaO_3$(110), Appl. Surf. Sci. 255 (2009) 8685-8687.

J. Schwarzkopf, **R. Dirsyte**, M. Rossberg, G. Wagner, R. Fornari, "Deposition of bismuth-titanate films with liquid-delivery spin MO-CVD", Mater. Sci. Eng., B 144 (2007) 132-137.

References

[1] Blanchard, S.; Marcenat, C.; Marcus, J.; Klein, T. and Sulpice, A. (2002): Thermodynamic phase diagram of the cubic (K,Ba)BiO_3 superconductor, Physica C-Superconductivity and Its Applications 369 [1-4], pp. 193-195. URL: <Go to ISI>://WOS:000174200000029

[2] Chao, C.; Wang, Z. H. and Zhu, W. G. (2005): Measurement of longitudinal piezoelectric coefficient of lead zirconate titanate thin/thick films using a novel scanning Mach-Zehnder interferometer, Thin Solid Films 493 [1-2], pp. 313-318. URL: <Go to ISI>://WOS:000233150700050

[3] Fu, D. S.; Taniguchi, H.; Itoh, M.; Koshihara, S.; Yamamoto, N. and Mori, S. (2009): Relaxor $Pb(Mg_{1/3}Nb_{2/3})O_3$: A Ferroelectric with Multiple Inhomogeneities, Physical Review Letters 103 [20]. URL: <Go to ISI>://000271864600049

[4] Jones, G. O.; Kreisel, J.; Jennings, V.; Geday, M. A.; Thomas, P. A. and Glazer, A. M. (2002): Investigation of a peculiar relaxor ferroelectric: $Na_{0.5}Bi_{0.5}TiO_3$, Ferroelectrics 270, pp. 1377-1382. URL: <Go to ISI>://000176862200033

[5] Tan, C. K.; Goh, G. K. L. and Lau, G. K. (2008): Growth and dielectric properties of $BaTiO_3$ thin films prepared by the microwave-hydrothermal method, Thin Solid Films 516 [16], pp. 5545-5550. URL: <Go to ISI>://WOS:000257452200081

[6] Li, L. T.; Zhao, J. C. and Gui, Z. L. (2004): The thermal sensitivity and dielectric properties of $SrTiO_3$-based ceramics, Ceramics International 30 [7], pp. 1073-1078. URL: <Go to ISI>://WOS:000224168300002

[7] Gan, Q.; Rao, R. A.; Eom, C. B.; Garrett, J. L. and Lee, M. (1998): Direct measurement of strain effects on magnetic and electrical properties of epitaxial $SrRuO_3$ thin films, Applied Physics Letters 72 [8], pp. 978-980. URL: <Go to ISI>://WOS:000073218200036

[8] Uchiyama, K.; Shiosaki, T.; Kosaka, T.; Kasamatsu, A. and Echizen, M. (2008): Novel electro-optic properties of epitaxially grown (Pb, La)(Zr, Ti)O_3 (PLZT) thin films derived by advanced sol-gel methods, Ceramics International 34 [4], pp. 979-983. URL: <Go to ISI>://WOS:000256287600064

[9] Pierre, J.; Robaut, F.; Misat, S.; Strobel, P.; Nossov, A.; Ustinov, V. and Vassiliev, V. (1996): Semiconductor-metal transition and magnetoresistance in (La,Ca)MnO_3: Experiments and simple model, Physica B 225 [3-4], pp. 214-224. URL: <Go to ISI>://WOS:A1996VC04500008

[10] Tejuca, L. G.; Bell, A. T. and Corberan, V. C. (1989): TPD and IR spectroscopic studies of CO, CO_2 and H_2 adsorption on $LaCrO_3$, Applied Surface Science 37 [3], pp. 353-366. URL: <Go to ISI>://WOS:A1989AJ12000009

[11] Lufaso, M. W. and Woodward, P. M. (2001): Prediction of the crystal structures of perovskites using the software program SPuDS, Acta Crystallographica Section B-Structural Science 57, pp. 725-738. URL: <Go to ISI>://WOS:000172322300001

[12] Goldschmidt, V.M. (1927): Geochemische Verterlungsgesetze der Elemente, Norske Videnskap, Oslo.

[13] Park, B. H.; Kang, B. S.; Bu, S. D.; Noh, T. W.; Lee, J. and Jo, W. (1999): Lanthanum-substituted bismuth titanate for use in non-volatile memories, Nature 401 [6754], pp. 682-684. URL: <Go to ISI>://WOS:000083207400051

[14] Wang, X. S. and Ishiwara, H. (2003): Polarization enhancement and coercive field reduction in W- and Mo-doped $Bi_{3.35}La_{0.75}Ti_3O_{12}$ thin films, Applied Physics Letters 82 [15], pp. 2479-2481. URL: <Go to ISI>://WOS:000182104900037

[15] Birkholz, M. (2006): Thin Film Analysis by X-ray Scattering, Wiley.

[16] Nix, W. D. (1989): Mechanical properties of thin films, Metallurgical Transactions a-Physical Metallurgy and Materials Science 20 [11], pp. 2217-2245. URL: <Go to ISI>://WOS:A1989CC23300001

[17] Speck, J. S.; Daykin, A. C.; Seifert, A.; Romanov, A. E. and Pompe, W. (1995): Domain configurations due to multiple misfit relaxation mechanisms in epitaxial ferroelectric thin films. 3. Interfacial defects and domain misorientations, Journal of Applied Physics 78 [3], pp. 1696-1706. URL: <Go to ISI>://WOS:A1995RK57600047

[18] Nix, W. D. and Clemens, B. M. (1999): Crystallite coalescence: A mechanism for intrinsic tensile stresses in thin films, Journal of Materials Research 14 [8], pp. 3467-3473. URL: <Go to ISI>://WOS:000082550800043

[19] Bozovic, I.; Logvenov, G.; Belca, I.; Narimbetov, B. and Sveklo, I. (2002): Epitaxial strain and superconductivity in $La_{2-x}Sr_xCuO_4$ thin films, Physical Review Letters 89 [10]. URL: <Go to ISI>://WOS:000177582600041

[20] Wang, J.; Neaton, J. B.; Zheng, H.; Nagarajan, V.; Ogale, S. B.; Liu, B.; Viehland, D.; Vaithyanathan, V.; Schlom, D. G.; Waghmare, U. V.; Spaldin, N. A.; Rabe, K. M.; Wuttig, M. and Ramesh, R. (2003): Epitaxial $BiFeO_3$ multiferroic thin film heterostructures, Science 299 [5613], pp. 1719-1722. URL: <Go to ISI>://WOS:000181519500041

[21] Haeni, J. H.; Irvin, P.; Chang, W.; Uecker, R.; Reiche, P.; Li, Y. L.; Choudhury, S.; Tian, W.; Hawley, M. E.; Craigo, B.; Tagantsev, A. K.; Pan, X. Q.; Streiffer, S. K.; Chen, L. Q.; Kirchoefer, S. W.; Levy, J. and Schlom, D. G. (2004): Room-temperature ferroelectricity in strained $SrTiO_3$, Nature 430 [7001], pp. 758-761. URL: <Go to ISI>://WOS:000223233600035

[22] Biegalski, M. D.; Jia, Y.; Schlom, D. G.; Trolier-McKinstry, S.; Streiffer, S. K.; Sherman, V.; Uecker, R. and Reiche, P. (2006): Relaxor ferroelectricity in strained epitaxial $SrTiO_3$ thin films on $DyScO_3$ substrates, Applied Physics Letters 88. URL: <Go to ISI>://WOS:000237477400072

[23] Kuzel, P.; Kadlec, F.; Petzelt, J.; Schubert, J. and Panaitov, G. (2007): Highly tunable $SrTiO_3/DyScO_3$ heterostructures for applications in the terahertz range, Applied Physics Letters 91 [23]. URL: <Go to ISI>://WOS:000251450600079

[24] Chen, Y. B.; Sun, H. P.; Katz, M. B.; Pan, X. Q.; Choi, K. J.; Jang, H. W. and Eom, C. B. (2007): Interface structure and strain relaxation in $BaTiO_3$ thin films grown on $GdScO_3$ and $DyScO_3$ substrates with buried coherent $SrRuO_3$ layer, Applied Physics Letters 91 [25]. URL: <Go to ISI>://WOS:000251908100063

[25] Liu, W.K and Santos, M.B. (1999): Thin Films: Heteroepitaxial Systems, World Scientific, Singapore.

[26] Bauer, E. and Vandermerwe, J. H. (1986): Structure and growth of crystalline superlattices - from monolayer to superlattice, Physical Review B 33 [6], pp. 3657-3671. URL: <Go to ISI>://WOS:A1986A463700004

[27] Venables, J.A. (2000): Introduction to Surface and Thin Film Processes, Cambridge University Press.

[28] Jiang, Q. D. and Zegenhagen, J. (1995): $SrTiO_3$(001) surfaces and growth of ultra-thin $GdBa_2Cu_3O_{7-X}$ films studied by LEED/AES and UHV-STM, Surface Science 338 [1-3], pp. L882-L888. URL: <Go to ISI>://WOS:A1995RU49200010

[29] Kawasaki, M.; Ohtomo, A.; Arakane, T.; Takahashi, K.; Yoshimoto, M. and Koinuma, H. (1996): Atomic control of $SrTiO_3$ surface for perfect epitaxy of perovskite oxides, Applied Surface Science 107, pp. 102-106. URL: <Go to ISI>://WOS:A1996VV19700019

[30] Koster, G.; Kropman, B. L.; Rijnders, Gjhm; Blank, D. H. A. and Rogalla, H. (1998): Quasi-ideal strontium titanate crystal surfaces through formation of strontium hydroxide, Applied Physics Letters 73 [20], pp. 2920-2922. URL: <Go to ISI>://WOS:000076848700022

[31] Sangwal, K. and Rodriguez-Clemente, R. (1991): Surface Morphology of Crystalline Solids, Trans. Tech Publications, Zürich.

[32] Kohlstedt, H.; Mustafa, Y.; Gerber, A.; Petraru, A.; Fitsilis, M.; Meyer, R.; Bottger, U. and Waser, R. (2005): Current status and challenges of ferroelectric memory devices, Microelectronic Engineering 80, pp. 296-304. URL: <Go to ISI>://WOS:000231517000067

[33] Parkin, S. S. P.; Hayashi, M. and Thomas, L. (2008): Magnetic domain-wall racetrack memory, Science 320 [5873], pp. 190-194. URL: <Go to ISI>://WOS:000254836700032

[34] Eom, C. B.; Cava, R. J.; Fleming, R. M.; Phillips, J. M.; Vandover, R. B.; Marshall, J. H.; Hsu, J. W. P.; Krajewski, J. J. and Peck, W. F. (1992): Single crystal epitaxial thin films of the isotropic metallic oxides $Sr_{1-X}Ca_XRuO_3$ ($0 \leq x \leq 1$), Science 258 [5089], pp. 1766-1769. URL: <Go to ISI>://WOS:A1992KB96400031

[35] Kamo, T.; Nishida, K.; Akiyama, K.; Sakai, J.; Katoda, T. and Funakubo, H. (2007): RF magnetron sputtering growth of epitaxial $SrRuO_3$ films with high conductivity, Japanese Journal of Applied Physics Part 1-Regular Papers Brief Communications & Review Papers 46 [10B], pp. 6987-6990. URL: <Go to ISI>://WOS:000250790200018

[36] Lee, H. N.; Hesse, D.; Zakharov, N. and Gosele, U. (2002): Ferroelectric $Bi_{3.25}La_{0.75}Ti_3O_{12}$ films of uniform a-axis orientation on silicon substrates, Science 296 [5575], pp. 2006-2009. URL: <Go to ISI>://WOS:000176273300046

[37] Lee, H. N.; Senz, S.; Visinoiu, A.; Pignolet, A.; Hesse, D. and Gosele, U. (2000): Epitaxial growth of non-c-oriented ferroelectric $SrBi_2Ta_2O_9$ thin films on Si(100) substrates, Applied Physics a-Materials Science & Processing 71 [1], pp. 101-104. URL: <Go to ISI>://WOS:000088498500019

[38] Wu, T. J. and Tsai, D. S. (2004): Structure and properties of PZT thin films on strontium ruthenate and calcium ruthenate electrodes, Materials Chemistry and Physics 85 [1], pp. 88-95. URL: <Go to ISI>://WOS:000221050900015

[39] Morimoto, T.; Hidaka, O.; Yamakawa, K.; Arisumi, O.; Kanaya, H.; Iwamoto, T.; Kumura, Y.; Kunishima, I. and Tanaka, S. (2000): Ferroelectric properties of Pb(Zi, Ti)O_3 capacitor with thin $SrRuO_3$ films within both electrodes, Japanese Journal of Applied Physics Part 1-Regular Papers Short Notes & Review Papers 39 [4B], pp. 2110-2113. URL: <Go to ISI>://WOS:000088909300032

[40] Eom, C. B.; Vandover, R. B.; Phillips, J. M.; Werder, D. J.; Marshall, J. H.; Chen, C. H.; Cava, R. J.; Fleming, R. M. and Fork, D. K. (1993): Fabrication and properties of epitaxial ferroelectric heterostructures with $SrRuO_3$ isotropic metallic oxide electrodes, Applied Physics Letters 63 [18], pp. 2570-2572. URL: <Go to ISI>://WOS:A1993MD96000040

[41] Cheng, H. F.; Ling, Y. C. and Lin, I. N. (2001): Ferroelectric properties of $(Pb_xLa_{1-x})(Zr_yTi_{1-y})O_3$ thin films prepared by modified pulsed laser deposition process, Japanese Journal of Applied Physics Part 1-Regular Papers Short Notes & Review Papers 40 [1], pp. 234-238. URL: <Go to ISI>://WOS:000167217400049

[42] Callagha.A; Moeller, C. W. and Ward, R. (1966): Magnetic interactions in ternary ruthenium oxides, Inorganic Chemistry 5 [9], pp. 1572-1576. URL: <Go to ISI>://WOS:A19668186800023

[43] Jin, C. Q.; Zhou, J. S.; Goodenough, J. B.; Liu, Q. Q.; Zhao, J. G.; Yang, L. X.; Yu, Y.; Yu, R. C.; Katsura, T.; Shatskiy, A. and Ito, E. (2008): High-pressure synthesis of the cubic perovskite $BaRuO_3$ and evolution of ferromagnetism in $ARuO_{(3)}$ (A = Ca, Sr, Ba) ruthenates, Proceedings of the National Academy of Sciences of the United States of America 105 [20], pp. 7115-7119. URL: <Go to ISI>://WOS:000256162900004

[44] Dabrowski, B.; Chmaissem, O.; Klamut, P. W.; Kolesnik, S.; Maxwell, M.; Mais, J.; Ito, Y.; Armstrong, B. D.; Jorgensen, J. D. and Short, S. (2004): Reduced ferromagnetic transition temperatures in $SrRu_{1-v}O_3$ perovskites from Ru-site vacancies, Physical Review B 70 [1]. URL: <Go to ISI>://WOS:000222996300070

[45] Dabrowski, B.; Avdeev, M.; Chmaissem, O.; Kolesnik, S.; Klamut, P. W.; Maxwell, M. and Jorgensen, J. D. (2005): Freezing of octahedral tilts below the Curie temperature in $SrRu_{1-v}O_3$ perovskites, Physical Review B 71 [10]. URL: <Go to ISI>://WOS:000228065400047

[46] Oh, S. H. and Park, C. G. (2004): Misfit strain relaxation by dislocations in $SrRuO_3/SrTiO_3$ (001) heteroepitaxy, Journal of Applied Physics 95 [9], pp. 4691-4704. URL: <Go to ISI>://WOS:000220875400024

[47] Terai, K.; Ohnishi, T.; Lippmaa, M.; Koinuma, H. and Kawasaki, M. (2004): Magnetic properties of strain-controlled $SrRuO_3$ thin films, Japanese Journal of Applied Physics Part 2-Letters 43 [2A], pp. L227-L229. URL: <Go to ISI>://WOS:000220092900034

[48] Siemons, W.; Koster, G.; Vailionis, A.; Yamamoto, H.; Blank, D. H. A. and Beasley, M. R. (2007): Dependence of the electronic structure of $SrRuO_3$ and its degree of correlation on cation off-stoichiometry, Physical Review B 76. URL: <Go to ISI>://WOS:000249155300063

[49] Imada, M.; Fujimori, A. and Tokura, Y. (1998): Metal-insulator transitions, Reviews of Modern Physics 70 [4], pp. 1039-1263. URL: <Go to ISI>://WOS:000077004600001

[50] Hiratani, M.; Okazaki, C.; Imagawa, K. and Takagi, K. (1996): $SrRuO_3$ thin films grown under reduced oxygen pressure, Japanese Journal of Applied Physics Part 1-Regular Papers Short Notes & Review Papers 35 [12A], pp. 6212-6216. URL: <Go to ISI>://WOS:A1996WF47900056

[51] Shin, J.; Kalinin, S. V.; Lee, H. N.; Christen, H. M.; Moore, R. G.; Plummer, E. W. and Baddorf, A. P. (2005): Surface stability of epitaxial $SrRUO_3$ films, Surface Science 581 [2-3], pp. 118-132. URL: <Go to ISI>://WOS:000228714700004

[52] Sun, J. Z.; Abraham, D. W.; Rao, R. A. and Eom, C. B. (1999): Thickness-dependent magnetotransport in ultrathin manganite films, Applied Physics Letters 74 [20], pp. 3017-3019. URL: <Go to ISI>://WOS:000080352700037

[53] Yamada, H.; Kawasaki, M.; Ogawa, Y. and Tokura, Y. (2002): Perovskite oxide tricolor superlattices with artificially broken inversion symmetry by interface effects, Applied Physics Letters 81 [25], pp. 4793-4795. URL: <Go to ISI>://WOS:000179731000037

[54] Herranz, G.; Martinez, B.; Fontcuberta, J.; Sanchez, F.; Ferrater, C.; Garcia-Cuenca, M. V. and Varela, M. (2003): Enhanced electron-electron correlations in nanometric $SrRuO_3$ epitaxial films, Physical Review B 67 [17]. URL: <Go to ISI>://WOS:000183299400072

[55] Herranz, G.; Martinez, B.; Fontcuberta, J.; Sanchez, F.; Garcia-Cuenca, M. V.; Ferrater, C. and Varela, M. (2003): Impact of microstructure on transport properties of nanometric epitaxial $SrRuO_3$ films, Applied Physics Letters 82 [1], pp. 85-87. URL: <Go to ISI>://WOS:000180134100029

[56] Toyota, D.; Ohkubo, I.; Kumigashira, H.; Oshima, M.; Ohnishi, T.; Lippmaa, M.; Kawasaki, M. and Koinuma, H. (2006): Ferromagnetism stabilization of ultrathin $SrRuO_3$ films: Thickness-dependent physical properties, Journal of Applied Physics 99 [8]. URL: <Go to ISI>://WOS:000237404200606

[57] Chopdekar, R. V.; Takamura, Y. and Suzuki, Y. (2006): Disorder-induced carrier localization in ultrathin strained $SrRuO_3$ epitaxial films, Journal of Applied Physics 99 [8]. URL: <Go to ISI>://WOS:000237404200315

[58] Rae, A. D.; Thompson, J. G.; Withers, R. L. and Willis, A. C. (1990): Structure refinement of commensurately modulated bismuth titanate, $Bi_4Ti_3O_{12}$, Acta Crystallographica Section B-Structural Science 46, pp. 474-487. URL: <Go to ISI>://WOS:A1990DU72300005

[59] Kojima, T.; Watanabe, T.; Funakubo, H.; Saito, K.; Osada, M. and Kakihana, M. (2003): Ferroelectric properties of lanthanide-substituted $Bi_4Ti_3O_{12}$ epitaxial thin films grown by metalorganic chemical vapor deposition, Journal of Applied Physics 93 [3], pp. 1707-1712. URL: <Go to ISI>://WOS:000180630200059

[60] Bae, J. C.; Kim, S. S.; Choi, E. K.; Song, T. K.; Kim, W. J. and Lee, Y. I. (2005): Ferroelectric properties of lanthanum-doped bismuth titanate thin films grown by a sol-gel method, Thin Solid Films 472 [1-2], pp. 90-95. URL: <Go to ISI>://WOS:000225748600016

[61] Arreuin-Zavala, J.; Villafuerte-Castrejon, M. E.; Gonzaleza, F.; Bucio, L.; Novelo-Peralta, O.; Sato-Berru, R. Y. and Ocotlan-Flores, J. (2009): Cation distribution in the $Bi_{4-x}Re_xTi_3O_{12}$ (Re = La, Nd) solid solution and Curie temperature dependence, Materials Characterization 60 [3], pp. 219-224. URL: <Go to ISI>://WOS:000264252800009

[62] Du, C. L.; Zhang, S. T.; Cheng, G. X.; Lu, M. H.; Gu, Z. B.; Wang, J. and Chen, Y. F. (2005): Composition-dependent structures and properties of $Bi_4Ti_{3-x}Zr_xO_{12}$ ceramics, Physica B-Condensed Matter 368 [1-4], pp. 157-162. URL: <Go to ISI>://WOS:000232959400024

[63] Mao, X. Y.; He, J. H.; Zhu, J. and Chen, X. B. (2006): Structural, ferroelectric, and dielectric properties of vanadium-doped $Bi_{4-x/3}Ti_{3-x}V_xO_{12}$, Journal of Applied Physics 100 [4]. URL: <Go to ISI>://WOS:000240236800088

[64] Hou, J. G.; Kumar, R. V.; Qu, Y. F. and Krsmanovic, D. (2009): B-site doping effect on electrical properties of $Bi_4Ti_{3-2x}Nb_xTa_xO_{12}$ ceramics, Scripta Materialia 61 [6], pp. 664-667. URL: <Go to ISI>://WOS:000268371900028

[65] Lee, S. Y. and Park, B. O. (2005): Microstructure and ferroelectric properties of Nb-doped $Bi_4Ti_3O_{12}$ thin films prepared by sol-gel method, Journal of Crystal Growth 283 [1-2], pp. 81-86. URL: <Go to ISI>://WOS:000231869700010

[66] Siriprapa, P.; Watcharapasorn, A. and Jiansirisomboon, S. (2009): Structure properties relation of Co-dope bismuth layer structured $Bi_{3.25}La_{0.75}(Ti_{1-x}W_x)_{(3)}O_{12}$ ceramics, Modern Physics Letters B 23 [31-32], pp. 3793-3799. URL: <Go to ISI>://WOS:000273141400015

[67] Watanabe, T.; Kojima, T.; Sakai, T.; Funakubo, H.; Osada, M.; Noguchi, Y. and Miyayama, M. (2002): Large remanent polarization of $Bi_4Ti_3O_{12}$-based thin films modified by the site engineering technique, Journal of Applied Physics 92 [3], pp. 1518-1521. URL: <Go to ISI>://WOS:000176907700056

[68] Noguchi, Y.; Miyayama, M. and Kudo, T. (2001): Direct evidence of A-site-deficient strontium bismuth tantalate and its enhanced ferroelectric properties, Physical Review B 63 [21]. URL: <Go to ISI>://WOS:000169060700027

[69] Yamamoto, K.; Kitanaka, Y.; Suzuki, M.; Miyayama, M.; Noguchi, Y.; Moriyoshi, C. and Kuroiwa, Y. (2007): High-oxygen-pressure crystal growth of ferroelectric $Bi_4Ti_3O_{12}$ single crystals, Applied Physics Letters 91. URL: <Go to ISI>://WOS:000250295700065

[70] Noguchi, Y.; Matsumoto, T. and Miyayama, M. (2005): Impact of defect control on the polarization properties in $Bi_4Ti_3O_{12}$ ferroelectric single crystals, Japanese Journal of Applied Physics Part 2-Letters & Express Letters 44 [16-19], pp. L570-L572. URL: <Go to ISI>://WOS:000229222000031

[71] Kim, S. J.; Moriyoshi, C.; Kimura, S.; Kuroiwa, Y.; Kato, K.; Takata, M.; Noguchi, Y. and Miyayama, M. (2007): Direct observation of oxygen stabilization in layered ferroelectric $Bi_{3.25}La_{0.75}Ti_3O_{12}$, Applied Physics Letters 91 [6]. URL: <Go to ISI>://WOS:000248661400103

[72] Noguchi, Y. and Miyayama, M. (2001): Large remanent polarization of vanadium-doped $Bi_4Ti_3O_{12}$, Applied Physics Letters 78 [13], pp. 1903-1905. URL: <Go to ISI>://WOS:000167744000034

[73] Chu, M. W.; Ganne, M.; Caldes, M. T. and Brohan, L. (2002): X-ray photoelectron spectroscopy and high resolution electron microscopy studies of Aurivillius compounds: $Bi_{4-x}La_xTi_3O_{12}$(x=0, 0.5, 0.75, 1.0, 1.5, and 2.0), Journal of Applied Physics 91 [5], pp. 3178-3187. URL: <Go to ISI>://WOS:000174182400095

[74] Jeon, M. K.; Kim, Y. I.; Nahm, S. H. and Woo, S. I. (2006): Crystal structure of $Bi_{4-x}Ce_xTi_3O_{12}$(x=0, 0.25, 0.5 and 0.75) studied by Raman spectroscopy and neutron powder diffraction, Journal of Physics D-Applied Physics 39 [23], pp. 5080-5085. URL: <Go to ISI>://WOS:000242650300028

[75] Senateur, J. P.; Dubourdieu, C.; Weiss, F.; Rosina, M. and Abrutis, A. (2000): Pulsed injection MOCVD of functional electronic oxides, Advanced Materials for Optics and Electronics 10 [3-5], pp. 155-161. URL: <Go to ISI>://WOS:000165667200008

[76] Schafer, P. and Waser, R. (2000): MOCVD of perovskite thin films using an aerosol-assisted liquid delivery system, Advanced Materials for Optics and Electronics 10 [3-5], pp. 169-175. URL: <Go to ISI>://WOS:000165667200010

[77] Wright, P. J.; Crosbie, M. J.; Lane, P. A.; Williams, D. J.; Jones, A. C.; Leedham, T. J. and Davies, H. O. (2002): Metal organic chemical vapor deposition (MOCVD) of oxides and ferroelectric materials, Journal of Materials Science-Materials in Electronics 13 [11], pp. 671-678. URL: <Go to ISI>://WOS:000178619300007

[78] Ramesh, R.; Aggarwal, S. and Auciello, O. (2001): Science and technology of ferroelectric films and heterostructures for non-volatile ferroelectric memories, Materials Science & Engineering R-Reports 32 [6], pp. 191-236. URL: <Go to ISI>://WOS:000168966100001

[79] Jones, A.C. and Hitchman, M.L. (2009): Chemical Vapour Deposition. Precursors, Processes and Applications, Royal Society of Chemistry, Cambridge.

[80] Schuster, M. and Herres, N. (2002): Einführungin die Hochauflösungs – Röntgendiffraktometrie, Bruker AXS GmbH.

[81] Settle, F.A. (1997): Handbook of Instrumental Techniques for Analytical Chemistry, New York.

[82] Moulder, J.F.; Sticle, W.F.; Sobol, P.E. and K.D. Bomben (1995): Handbook of X-ray Photoelectron Spectroscopy, USA.

[83] Zhou, W. and Wang, Z.L. (2006): Scanning Microscopy for Nanotechnology, Techniques and Applications, Springer.

[84] Reimer, L. (1985): Scanning Electron Microscopy, Springer-Verlag Berlin.

[85] Kaufmann, E.N. (2003): Characterization of Materials 2, Wiley.

[86] Pauw, L.J. van der (1958): A Method of Measuring Specific Resistivity and Hall Effect of Discs of Arbitrary Shape, Phil. Res. Rep. 13, pp. 1-9.

[87] Pauw, L.J. van der (1958): A Method of Measuring the Resistivity and Hall Coefficient on Lamellae of Arbitrary Shape, Phil. Tech. Rev. 20, pp. 220-224.

[88] Schroder, D.K. (1990): Semiconductor material and device characterization, Wiley.

[89] Volkenshtein, N.V.; Dyakina, V.P. and Startsev, V.E. (1973): Scattering Mechanisms of Conduction Electrons in Transition Metals at Low Temperatures, Phys. Stat. Sol. B 57, pp. 9-42.

[90] Cahn, R.W.; Haassen, P. and Kramer, E.J. (1994): Materials Science and Technology:Characterization of materials 2A, VCH publishers.

[91] Nurgaliev, T.; Donchev, T.; Mateev, E.; Miteva, S.; Mozhaev, P. B. and Mozhaeva, J. E. (2005): Properties of HTS YBCO thin films deposited on tilted $NdGaO_3$ substrates, Physica C-Superconductivity and Its Applications 420 [1-2], pp. 61-67. URL: <Go to ISI>://WOS:000227652900009

[92] Bu, S. D.; Lee, M. K.; Eom, C. B.; Tian, W.; Pan, X. Q.; Streiffer, S. K. and Krajewski, J. J. (2001): Perovskite phase stabilization in epitaxial $Pb(Mg_{1/3}Nb_{2/3})O_3$-$PbTiO_3$ films by deposition onto vicinal (001) $SrTiO_3$ substrates, Applied Physics Letters 79 [21], pp. 3482-3484. URL: <Go to ISI>://WOS:000172204300034

[93] Visinoiu, A.; Scholz, R.; Alexe, M. and Hesse, D. (2005): Morphology dependence of the dielectric properties of epitaxial $BaTiO_3$ films and epitaxial $BaTiO_3$/$SrTiO_3$ multilayers, Applied Physics a-Materials Science & Processing 80 [2], pp. 229-235. URL: <Go to ISI>://WOS:000225864600005

[94] Vonhelmolt, R.; Wecker, J.; Holzapfel, B.; Schultz, L. and Samwer, K. (1993): Giant negative magnetoresistance in perovskite-like $La_{2/3}Ba_{1/3}MnO_X$ ferromagnetic films, Physical Review Letters 71 [14], pp. 2331-2333. URL: <Go to ISI>://WOS:A1993MA02700042

[95] Mozhaev, P. B.; Kotelyanskii, I. M.; Luzanov, V. A.; Mozhaeva, J. E.; Donchev, T.; Mateev, E.; Nurgaliev, T.; Bdikin, I. K. and Narymbetov, B. Z. (2005): Morphology, structure, and electrical properties of $YBa_2Cu_3O_x$, thin films on tilted $NdGaO_3$ substrates, deposited by DC-sputtering, Physica C-Superconductivity and Its Applications 419 [1-2], pp. 53-60. URL: <Go to ISI>://WOS:000227018700008

[96] Tsuchiya, R.; Kawasaki, M.; Kubota, H.; Nishino, J.; Sato, H.; Akoh, H. and Koinuma, H. (1997): $YBa_2Cu_3O_{7-\delta}$ trilayer junction with nm thick $PrGaO_3$ barrier, Applied Physics Letters 71 [11], pp. 1570-1572. URL: <Go to ISI>://WOS:A1997XV72600045

[97] Rijnders, G.; Blank, D. H. A.; Choi, J. and Eom, C. B. (2004): Enhanced surface diffusion through termination conversion during epitaxial $SrRuO_3$ growth, Applied Physics Letters 84 [4], pp. 505-507. URL: <Go to ISI>://WOS:000188316500017

[98] Rao, R. A.; Gan, Q. and Eom, C. B. (1997): Growth mechanisms of epitaxial metallic oxide $SrRuO_3$ thin films studied by scanning tunneling microscopy, Applied Physics Letters 71 [9], pp. 1171-1173. URL: <Go to ISI>://WOS:A1997XU06200012

[99] Haage, T.; Zegenhagen, J.; Li, J. Q.; Habermeier, H. U.; Cardona, M.; Jooss, C.; Warthmann, R.; Forkl, A. and Kronmuller, H. (1997): Transport properties and flux pinning by self-organization in $YBa_2Cu_3O_{7-\delta}$ films on vicinal $SrTiO_3$(001), Physical Review B 56 [13], pp. 8404-8418. URL: <Go to ISI>://WOS:A1997YD86600103

[100] Wang, T. S.; Tian, Y. J.; Peng, W.; Qi, H. H. and Lin, L. (2006): Step-flow-growth YBCO films and BST/YBCO bilayer films on vicinal substrates, Rare Metal Materials and Engineering 35 [4], pp. 542-545. URL: <Go to ISI>://WOS:000237365900008

[101] Huijben, M.; Rijnders, G.; Blank, D. H. A.; Bals, S.; Van Aert, S.; Verbeeck, J.; Van Tendeloo, G.; Brinkman, A. and Hilgenkamp, H. (2006): Electronically coupled complementary interfaces between perovskite band insulators, Nature Materials 5 [7], pp. 556-560. URL: <Go to ISI>://WOS:000238708900021

[102] Salluzzo, M.; Cezar, J. C.; Brookes, N. B.; Bisogni, V.; Luca, G. M.; Richter, C.; Thiel, S.; Mannhart, J.; Huijben, M.; Brinkman, A.; Rijnders, G. and Ghiringhelli, G. (2009): Orbital Reconstruction and the Two-Dimensional Electron Gas at the $LaAlO_3/SrTiO_3$ Interface, Physical Review Letters 102 [16]. URL: <Go to ISI>://WOS:000265479300055

[103] Kawasaki, M.; Takahashi, K.; Maeda, T.; Tsuchiya, R.; Shinohara, M.; Ishiyama, O.; Yonezawa, T.; Yoshimoto, M. and Koinuma, H. (1994): Atomic control of the $SrTiO_3$ crystal surface, Science 266 [5190], pp. 1540-1542. URL: <Go to ISI>://WOS:A1994PV01500037

[104] Lippmaa, M.; Takahashi, K.; Ohtomo, A.; Ohashi, S.; Ohnishi, T.; Nakagawa, N.; Sato, T.; Iwatsuki, M.; Koinuma, H. and Kawasaki, M. (1998): Atom technology for Josephson tunnel junctions: $SrTiO_3$ substrate surface, Materials Science and Engineering B-Solid State Materials for Advanced Technology 56 [2-3], pp. 111-116. URL: <Go to ISI>://WOS:000077655700007

[105] Koster, G.; Rijnders, G.; Blank, D. H. A. and Rogalla, H. (2000): Surface morphology determined by (001) single-crystal $SrTiO_3$ termination, Physica C-Superconductivity and Its Applications 339 [4], pp. 215-230. URL: <Go to ISI>://WOS:000165260800001

[106] Castell, M. R. (2002): Scanning tunneling microscopy of reconstructions on the $SrTiO_3$(001) surface, Surface Science 505 [1-3], pp. 1-13. URL: <Go to ISI>://WOS:000175740200005

[107] Ohnishi, T.; Shibuya, K.; Lippmaa, M.; Kobayashi, D.; Kumigashira, H.; Oshima, M. and Koinuma, H. (2004): Preparation of thermally stable TiO_2-terminated $SrTiO_3$(100) substrate surfaces, Applied Physics Letters 85 [2], pp. 272-274. URL: <Go to ISI>://WOS:000222784300038

[108] Kobayashi, D.; Kumigashira, H.; Oshima, M.; Ohnishi, T.; Lippmaa, M.; Ono, K.; Kawasaki, M. and Koinuma, H. (2004): High-resolution synchrotron-radiation photoemission characterization for atomically-controlled $SrTiO_3$(001) substrate surfaces subjected to various surface treatments, Journal of Applied Physics 96 [12], pp. 7183-7188. URL: <Go to ISI>://WOS:000225482400034

[109] Ohnishi, T.; Takahashi, K.; Nakamura, M.; Kawasaki, M.; Yoshimoto, M. and Koinuma, H. (1999): A-site layer terminated perovskite substrate: $NdGaO_3$, Applied Physics Letters 74 [17], pp. 2531-2533. URL: <Go to ISI>://WOS:000079855900043

[110] Talik, E.; Kruczek, A.; Sakowska, H.; Ujma, Z.; Gala, M. and Neumann, M. (2004): XPS characterisation of neodymium gallate wafers, Journal of Alloys and Compounds 377 [1-2], pp. 259-267. URL: <Go to ISI>://WOS:000223801000048

[111] Leca, V. (2003): Heteroepitaxial Growth of Copper Oxide Superconductors by Pulsed Laser Deposition, University of Twente, The Netherlands.

[112] Dirsyte, R.; Schwarzkopf, J.; Wagner, G.; Lienemann, J.; Busch, M.; Winter, H. and Fornari, R. (2009): Surface termination of the $NdGaO_3$(110), Applied Surface Science 255 [20], pp. 8685-8687. URL: <Go to ISI>://WOS:000268123800064

[113] Gunnarsson, R.; Kalabukhov, A. S. and Winkler, D. (2009): Evaluation of recipes for obtaining single terminated perovskite oxide substrates, Surface Science 603 [1], pp. 151-157. URL: <Go to ISI>://WOS:000262828000026

[114] Kadlec, C.; Kadlec, F.; Nemec, H.; Kuzel, P.; Schubert, J. and Panaitov, G. (2009): High tunability of the soft mode in strained $SrTiO_3$/$DyScO_3$ multilayers, Journal of Physics-Condensed Matter 21 [11]. URL: <Go to ISI>://WOS:000263677300029

[115] Venkatesan, S.; Kooi, B. J.; De Hosson, J. T. M.; Vlooswijk, A. H. G. and Noheda, B. (2007): Substrate influence on the shape of domains in epitaxial $PbTiO_3$ thin films, Journal of Applied Physics 102 [10]. URL: <Go to ISI>://WOS:000251324900067

[116] Nishimura, T.; Ikeda, A.; Namba, H.; Morishita, T. and Kido, Y. (1999): Structure change of TiO_2-terminated $SrTiO_3$(001) surfaces by annealing in O_2 atmosphere and ultrahigh vacuum, Surface Science 421 [3], pp. 273-278. URL: <Go to ISI>://WOS:000078722200008

[117] Davis, L.E.; MacDonald, N.C.; Palmberg, P.W. and Riach, G. (1978): Handbook of Auger Electron Spectroscopy, 2nd. ed., Physical electronics, Minnesota.

[118] Briggs, D. and Seah, M.P. (1990): Practical Surface Analysis: Auger and X-ray Photoelectron Spectroscopy 1, 2. ed., Wiley.

[119] Gryzinacuteski, Michal (1965): Classical Theory of Atomic Collisions. I. Theory of Inelastic Collisions, Physical Review 138 [2A], p. A336. URL: http://link.aps.org/doi/10.1103/PhysRev.138.A336

[120] Lide, D. R. (1994): CRC Handbook of Chemistry and Physics, CRC Press.

[121] Yamaji, K.; Negishi, H.; Horita, T.; Sakai, N. and Yokokawa, H. (2000): Vaporization process of Ga from doped $LaGaO_3$ electrolytes in reducing atmospheres, Solid State Ionics 135 [1-4], pp. 389-396. URL: <Go to ISI>://WOS:000165856800053

[122] Phillips, J. M.; Siegal, M. P.; Vandover, R. B.; Tiefel, T. H.; Marshall, J. H.; Brandle, C. D.; Berkstresser, G.; Strauss, A. J.; Fahey, R. E.; Sengupta, S.; Cassanho, A. and Jenssen, H. P. (1992): Comparison of $Ba_{2Y}Cu_3O_{7-\delta}$ thin films grown on various perovskite substrates by co-evaporation Journal of Materials Research 7 [10], pp. 2650-2657. URL: <Go to ISI>://WOS:A1992JR17000004

[123] Stevenson, J. W.; Armstrong, T. R.; Pederson, L. R.; Li, J.; Lewinsohn, C. A. and Baskaran, S. (1998): Effect of A-site cation nonstoichiometry on the properties of doped lanthanum gallate, Solid State Ionics 113, pp. 571-583. URL: <Go to ISI>://WOS:000077868800081

[124] Rector, J. H.; Koster, P.; Peerdeman, F.; deGroot, D. G. and Dam, B. (1997): Twin-free $YBa_2Cu_3O_{7-\delta}$ films on (001) $NdGaO_3$ showing isotropic electrical behaviour, Journal of Alloys and Compounds 251 [1-2], pp. 114-117. URL: <Go to ISI>://WOS:A1997XM34000027

[125] Young, K. H.; Firpo, G. G.; Smith, E. J. and Magee, C. W. (1992): Substrate interdiffusion in $Tl_2Ba_2CaCu_2O_8$ thin films and its effects on microwave device performance, Applied Surface Science 59 [2], pp. 147-157. URL: <Go to ISI>://WOS:A1992JD98900007

[126] Holleman, A.Fr. and Wiberg, E. (1995): Lehrbuch der Anorganischen Chemie, 101. ed., de Gruyter.

[127] Delugas, P.; Fiorentini, V.; Filippetti, A. and Pourtois, G. (2007): Cation charge anomalies and high-kappa dielectric behavior in $DyScO_3$: Ab initio density-functional and self-interaction-corrected calculations, Physical Review B 75 [11]. URL: <Go to ISI>://WOS:000245329600054

[128] Velickov, B.; Kahlenberg, V.; Bertram, R. and Bernhagen, M. (2007): Crystal chemistry of $GdScO_3$, $DyScO_3$, $SmScO_3$ and $NdScO_3$, Zeitschrift Fur Kristallographie 222, pp. 466-473. URL: <Go to ISI>://WOS:000249792800004

[129] Fromm, K. M. and Gueneau, E. D. (2004): Structures of alkali and alkaline earth metal clusters with oxygen donor ligands, Polyhedron 23 [9], pp. 1479-1504. URL: <Go to ISI>://WOS:000221778800001

[130] Shannon, R. D. (1976): Revised effective ionic radii and systematic studies of interatomic distances in halides and chalcogenides, Acta Crystallographica Section A 32 [SEP1], pp. 751-767. URL: <Go to ISI>://WOS:A1976CD98100001

[131] Herrmann, W. A.; Anwander, R. and Denk, M. (1992): Complexes of the lanthanides. 3. Volatile neodymium and yttrium alkoxides with new bulky chelating ligands, Chemische Berichte-Recueil 125 [11], pp. 2399-2405. URL: <Go to ISI>://WOS:A1992KC74600011

[132] Herrmann, W. A.; Huber, N. W. and Runte, O. (1995): Volatile metal alkoxides according to the concept of donor functionalization, Angewandte Chemie-International Edition in English 34 [20], pp. 2187-2206. URL: <Go to ISI>://WOS:A1995TF24700001

[133] Luten, H. A.; Rees, W. S. and Goedken, V. L. (1996): Preparation and structural characterization of, and chemical vapor deposition studies with, certain yttrium tris(beta-diketonate) compounds, Chemical Vapor Deposition 2 [4], pp. 149-161. URL: <Go to ISI>://WOS:A1996UZ33700004

[134] Tiitta, M.; Leskela, M.; Nykanen, E.; Soininen, P. and Niinisto, L. (1995): Thermoanalytical studies on volatile complexes containing alkali metals, Thermochimica Acta 256 [1], pp. 47-53. URL: <Go to ISI>://WOS:A1995RB42000006

[135] Gorbenko, O. Y.; Kaul, A. R.; Mel'nikov, O. V.; Gan'shina, E. A.; Ganin, A. Y.; Sukhorukov, Y. P.; Loshkareva, N. N. and Mostovshchikova, E. V. (2007): Synthetic routes to colossal magnetoresistance manganites thin films containing unstable or highly volatile metal oxides, Thin Solid Films 515 [16], pp. 6395-6401. URL: <Go to ISI>://WOS:000247045000023

[136] Wang, Z.; Yang, C. H.; Yu, X. Y. and Yu, T. (2005): Synthesis and characteristics of Na-doped $Bi_4Ti_3O_{12}$ thin films on Si substrate, Journal of Crystal Growth 280 [3-4], pp. 557-561. URL: <Go to ISI>://WOS:000230235000033

[137] Shin, W. C.; Choi, K. J.; Seong, N. J.; Choi, E. S.; Kim, B. H. and Yoon, S. G. (2002): Liquid-delivery metal-organic CVD of strontium bismuth tantalate thin films using $SrTa(OC_2H_5)_5(OC_2H_4OCH_3)_2$ and $Bi(C_6H_5)_3$ precursors, Chemical Vapor Deposition 8 [5], pp. 221-225. URL: <Go to ISI>://WOS:000183826800008

[138] Funakubo, H.; Nukaga, N.; Ishikawa, K. and Watanabe, T. (1999): Preparation of $SrBi_2Ta_2O_9$ thin films by metalorganic chemical vapor deposition from two new liquid organometallic sources, Japanese Journal of Applied Physics Part 2-Letters 38 [2B], pp. L199-L201. URL: <Go to ISI>://WOS:000079486800016

[139] Kang, S. W.; Yang, K. J.; Yong, K. J. and Rhee, S. W. (2002): Precursors for deposition of strontium bismuth tantalate films by direct liquid injection-metallorganic chemical vapor deposition, Journal of the Electrochemical Society 149 [1], pp. C44-C49. URL: <Go to ISI>://WOS:000172938900023

[140] Armelao, L.; Bandoli, G.; Casarin, M.; Depaoli, G.; Tondello, E. and Vittadini, A. (1998): Synthesis, X-ray structure and bonding of tris (2,2-6,6-tetramethylheptane-3,5-dionato)bismuth(III), Inorganica Chimica Acta 276 [1-2], pp. 340-348. URL: <Go to ISI>://WOS:000074455100044

[141] Williams, P. A.; Jones, A. C.; Crosbie, M. J.; Wright, P. J.; Bickley, J. F.; Steiner, A.; Davies, H. O.; Leedham, T. J. and Critchlow, G. W. (2001): Crystal structure of $Bi(OCMe_2CH_2OMe)_3$ and its use in the MOCVD of Bi_2O_3, Chemical Vapor Deposition 7 [5], pp. 205-209. URL: <Go to ISI>://WOS:000170921200005

[142] Hintermaier, F.; Hendrix, B.; Desrochers, D.; Roeder, J.; Baum, T.; Van Buskirk, P.; Bolten, D.; Grossmann, M.; Lohse, O.; Schumacher, M.; Waser, R.; Cerva, H.; Dehm, C.; Fritsch, E.; Honlein, W.; Mazure, C.; Nagel, N.; Thwaite, P. and Wendt, H. (1998): Properties of $SrBi_2Ta_2O_9$ thin films grown by MOCVD for high density FeRAM applications, Integrated Ferroelectrics 21 [1-4], pp. 367-379. URL: <Go to ISI>://WOS:000076544100033

[143] Kartavtseva, M. S.; Gorbenko, O. Y.; Kaul, A. R.; Akbashev, A. R.; Murzina, T. V.; Fusil, S.; Barthelemy, A. and Pailloux, F. (2007): $BiFeO_3$ thin films prepared by MOCVD, Surface & Coatings Technology 201 [22-23], pp. 9149-9153. URL: <Go to ISI>://WOS:000249340400066

[144] Ghoshtagore, R.N. (1970): Mechanism of heterogeneous deposition of thin film rutile, Journal of the Electrochemical Society 117 [4], pp. 529-&. URL: <Go to ISI>://A1970F819200028

[145] Bradley, D. C. (1989): Metal alkoxides as precursors for electronic and ceramic materials, Chemical Reviews 89 [6], pp. 1317-1322. URL: <Go to ISI>://WOS:A1989AV59200005

[146] Chandler, C. D.; Roger, C. and Hampdensmith, M. J. (1993): Chemical aspects of solution routes to perovskite phase mixed metal oxides from metalorganic precursors, Chemical Reviews 93 [3], pp. 1205-1241. URL: <Go to ISI>://WOS:A1993LB96000016

[147] Jones, A. C.; Leedham, T. J.; Wright, P. J.; Crosbie, M. J.; Fleeting, K. A.; Otway, D. J.; O'Brien, P. and Pemble, M. E. (1998): Synthesis and characterisation of two novel titanium isopropoxides stabilised with a chelating alkoxide: their use in the liquid injection MOCVD of titanium dioxide thin films, Journal of Materials Chemistry 8 [8], pp. 1773-1777. URL: <Go to ISI>://WOS:000075327100016

[148] Roeder, J. F.; Vaartstra, B. A.; Buskirk, P. C. and Beratan, H. R. (1996): Liquid Delivery MOCVD of Ferroelectric PZT, Mater. Res. Soc. Symp. Proc. 415, p. 123.

[149] Yamazaki, H.; Tsuyama, T.; Kobayashi, I. and Sugimori, Y. (1992): Preparation of $Pb(Zr, Ti)O_3$ thin films using all dipivaloylmethane source materials by metalorganic chemical vapor deposition, Japanese Journal of Applied Physics Part 1-Regular Papers Short Notes & Review Papers 31 [9B], pp. 2995-2997. URL: <Go to ISI>://WOS:A1992JV45500011

[150] Roeder, J. F.; Baum, T. H.; Bilodeau, S. M.; Stauf, G. T.; Ragaglia, C.; Russell, M. W. and Van Buskirk, P. C. (2000): Liquid-delivery MOCVD: Chemical and process perspectives on ferro-electric thin film growth, Advanced Materials for Optics and Electronics 10 [3-5], pp. 145-154. URL: <Go to ISI>://WOS:000165667200007

[151] Cho, Y. S.; Cho, S. I.; Ryu, H. K.; Heo, J. S.; Lee, D. H. and Moon, S. H. (2003): Thermal decomposition mechanism of bis(dipivaloylmethanato)strontium compounds containing glyme adducts, Journal of the Electrochemical Society 150 [2], pp. F11-F19. URL: <Go to ISI>://WOS:000180517000044

[152] Shin, W. C. and Yoon, S. G. (1997): Characterization of RuO_2 thin films prepared by hot-wall metallorganic chemical vapor deposition, Journal of the Electrochemical Society 144 [3], pp. 1055-1060. URL: <Go to ISI>://WOS:A1997WR23700048

[153] Aoyama, T. and Eguchi, K. (1999): Ruthenium films prepared by liquid source chemical vapor deposition using bis-(ethylcyclopentadienyl)ruthenium, Japanese Journal of Applied Physics Part 2-Letters 38 [10A], pp. L1134-L1136. URL: <Go to ISI>://WOS:000083277500018

[154] UhlenBrock, S. and Vaarstra, B.A. (1999):

[155] Boyd, E. P.; Ketchum, D. R.; Deng, H. B. and Shore, S. G. (1997): Chemical vapor deposition of metallic thin films using homonuclear and heteronuclear metal carbonyls, Chemistry of Materials 9 [5], pp. 1154-1158. URL: <Go to ISI>://WOS:A1997WZ30000017

[156] Green, M. L.; Gross, M. E.; Papa, L. E.; Schnoes, K. J. and Brasen, D. (1985): Chemical vapor deposition of ruthenium and ruthenium dioxide films, Journal of the Electrochemical Society 132 [11], pp. 2677-2685. URL: <Go to ISI>://WOS:A1985ATZ4700032

[157] Frohlich, F.; Machajdik, D.; Cambel, V.; Fedor, J.; Pisch, A. and Lindner, J. (2001): Growth of Ru and RuO_2 films by metal-organic chemical vapour deposition, Journal De Physique Iv 11 [PR3], pp. 325-332. URL: <Go to ISI>://WOS:000171140300042

[158] Hones, P.; Levy, F.; Gerfin, T. and Gratzel, M. (2000): MOCVD of thin ruthenium oxide films: Properties and growth kinetics, Chemical Vapor Deposition 6 [4], pp. 193-198. URL: <Go to ISI>://WOS:000088725200006

[159] Vetrone, J.; Foster, C. M.; Bai, G. R.; Wang, A.; Patel, J. and Wu, X. (1998): Growth, microstructure, and resistivity of RuO_2 thin films grown by metal-organic chemical vapor deposition, Journal of Materials Research 13 [8], pp. 2281-2290. URL: <Go to ISI>://WOS:000074989200035

[160] Kadoshima, M.; Nabatame, T.; Hiratani, M.; Nakamura, Y.; Asano, I. and Suzuki, T. (2002): Ruthenium films prepared by liquid source metalorganic chemical vapor deposition using $Ru(dpm)_3$ dissolved with tetrahydrofuran solvent, Japanese Journal of Applied Physics Part 2-Letters 41 [3B], pp. L347-L350. URL: <Go to ISI>://WOS:000176444200017

[161] Lee, D. J.; Kang, S. W. and Rhee, S. W. (2002): Chemical vapor deposition of ruthenium oxide thin films from $Ru(tmhd)_3$ using direct liquid injection, Thin Solid Films 413 [1-2], pp. 237-242. URL: <Go to ISI>://WOS:000177272700034

[162] Aaltonen, T.; Ritala, M.; Arstila, K.; Keinonen, J. and Leskela, M. (2004): Atomic layer deposition of ruthenium thin films from $Ru(thd)_3$ and oxygen, Chemical Vapor Deposition 10 [4], pp. 215-219. URL: <Go to ISI>://WOS:000224473500006

[163] Meda, L.; Breitkopf, R.C.; Haas, T.E. and Kirss, R.U. (1998), Mater. Res. Soc. Symp. Proc. 495.

[164] Barreca, D.; Buchberger, A.; Daolio, S.; Depero, L. E.; Fabrizio, M.; Morandini, F.; Rizzi, G. A.; Sangaletti, L. and Tondello, E. (1999): A Ru(II) eta_3-allylic complex as a novel precursor for the CVD of Ru- and RuO_2-nanostructured thin films, Langmuir 15 [13], pp. 4537-4543. URL: <Go to ISI>://WOS:000081119900038

[165] Niskanen, A.; Hatanpaa, T.; Ritala, M. and Leskela, M. (2001): Thermogravimetric study of volatile precursors for chemical thin film deposition. Estimation of vapor pressures and source temperatures, Journal of Thermal Analysis and Calorimetry 64 [3], pp. 955-964. URL: <Go to ISI>://WOS:000169215300012

[166] Bedoya, C.; Condorelli, G. G.; Finocchiaro, S. T.; Di Mauro, A.; Fragala, I. L.; Cattaneo, L. and Carella, S. (2005): Comparison of thermal and mass-transport properties of $Bi(tmhd)_3$, $Bi(p\text{-}tol)_3$, and $Bi(o\text{-}tol)_3$ MOCVD precursors, Chemical Vapor Deposition 11 [5], pp. 261-268. URL: <Go to ISI>://WOS:000229767100006

[167] Turgambaeva, A. E.; Krisyuk, V. V.; Sysoev, S. V. and Igumenov, I. K. (2001): Thermal behavior of $Ti(dpm)_2((OPr)\text{-}Pr\text{-}l)_2$ vapors, Chemical Vapor Deposition 7 [3], pp. 121-124. URL: <Go to ISI>://WOS:000168630300006

[168] Lashdaf, M.; HatanpSs, T. and Tiitta, M. (2001): Volatile beta-diketonato complexes of ruthenium, palladium and platinum. Preparation and thermal characterization, Journal of Thermal Analysis and Calorimetry 64 [3], pp. 1171-1182. URL: <Go to ISI>://WOS:000169215300038

[169] Sumi, A.; Takahashi, K.; Yokoyama, S.; Morioka, H.; Funakubo, H. and Yoshimoto, M. (2005): Metalorganic chemical vapor deposition of atomically flat $SrRuO_3$ films on stepped $SrTiO_3$ substrates, Applied Physics Letters 87 [5]. URL: <Go to ISI>://WOS:000230886100042

[170] Choi, J.; Eom, C. B.; Rijnders, G.; Rogalla, H. and Blank, D. H. A. (2001): Growth mode transition from layer by layer to step flow during the growth of heteroepitaxial $SrRuO_3$ on (001) $SrTiO_3$, Applied Physics Letters 79 [10], pp. 1447-1449. URL: <Go to ISI>://WOS:000170647200013

[171] Lee, H. N.; Christen, H. M.; Chisholm, M. F.; Rouleau, C. M. and Lowndes, D. H. (2004): Thermal stability of epitaxial $SrRuO_3$ films as a function of oxygen pressure, Applied Physics Letters 84 [20], pp. 4107-4109. URL: <Go to ISI>://WOS:000221269800051

[172] Iliev, M. N.; Litvinchuk, A. P.; Lee, H. G.; Chen, C. L.; Dezaneti, M. L.; Chu, C. W.; Ivanov, V. G.; Abrashev, M. V. and Popov, V. N. (1999): Raman spectroscopy of $SrRuO_3$ near the paramagnetic-to-ferromagnetic phase transition, Physical Review B 59 [1], pp. 364-368. URL: <Go to ISI>://WOS:000077943800075

[173] Herranz, G.; Sanchez, F.; Fontcuberta, J.; Garcia-Cuenca, M. V.; Ferrater, C.; Varela, M.; Angelova, T.; Cros, A. and Cantarero, A. (2005): Domain structure of epitaxial $SrRuO_3$ thin films, Physical Review B 71 [17]. URL: <Go to ISI>://WOS:000229935000059

[174] Suzuki, T.; Nishi, Y. and Fujimoto, M. (2000): Defect structure in homoepitaxial non-stoichiometric strontium titanate thin films, Philosophical Magazine a-Physics of Condensed Matter Structure Defects and Mechanical Properties 80 [3], pp. 621-637. URL: <Go to ISI>://WOS:000085873500008

[175] Oh, S. H. and Park, C. G. (2003): Microstructural accommodation of excess Ru in epitaxial $SrRuO_3$ films, Philosophical Magazine 83 [11], pp. 1307-1327. URL: <Go to ISI>://WOS:000181850800002

[176] Bin Anooz, S.; Schwarzkopf, J.; Dirsyte, R.; Wagner, G. and Fornari, R. (2010): Effects of post-growth annealing on physical properties of $SrRuO_3$ thin film grown by MOCVD, Physica Status Solidi a-Applications and Materials Science 207 [11], pp. 2492-2498. URL: <Go to ISI>://WOS:000284055700013

[177] Szot, K.; Pawelczyk, M.; Herion, J.; Freiburg, C.; Albers, J.; Waser, R.; Hulliger, J.; Kwapulinski, J. and Dec, J. (1996): Nature of the surface layer in ABO_3-type Perovskites at elevated temperatures, Applied Physics a-Materials Science & Processing 62 [4], pp. 335-343. URL: <Go to ISI>://WOS:A1996UD73400006

[178] Hartmann, A. J.; Neilson, M.; Lamb, R. N.; Watanabe, K. and Scott, J. F. (2000): Ruthenium oxide and strontium ruthenate electrodes for ferroelectric thin-films capacitors, Applied Physics a-Materials Science & Processing 70 [2], pp. 239-242. URL: <Go to ISI>://WOS:000085952800019

[179] Choe, H. C.; Kang, T. S.; Je, J. H.; Moon, J. H.; Lee, B. T. and Kim, S. S. (2005): Early stage heteroepitaxial growth of $SrRuO_3$ films on $SrTiO_3$(001) depending on the growth temperature during pulsed laser deposition, Thin Solid Films 474 [1-2], pp. 44-49. URL: <Go to ISI>://WOS:000226886900008

[180] Kim, H. C.; Kim, Y. S.; Kim, Y. B. and Choi, D. K. (2004): Characterization of (Ba, Sr)RuO_3 films deposited by metal organic chemical vapor deposition, Journal of Non-Crystalline Solids 336 [2], pp. 107-112. URL: <Go to ISI>://WOS:000220762000005

[181] Triyoso, D. H.; Ramon, M.; Hegde, R. I.; Roan, D.; Garcia, R.; Baker, J.; Wang, X. D.; Fejes, P.; White, B. E. and Tobin, P. J. (2005): Physical and electrical characteristics of HfO_2 gate dielectrics deposited by ALD and MOCVD, Journal of the Electrochemical Society 152 [3], pp. G203-G209. URL: <Go to ISI>://WOS:000227607300064

[182] Sun, H. J.; Kim, Y. S.; Park, S. E.; Hong, K.; Roh, J. S. and Sohn, H. C. (2004): Fabrication of highly dense Ru thin films by high-temperature metal-organic chemical vapor deposition with NH_3 gas as Ru oxidation suppressing agent, Japanese Journal of Applied Physics Part 1-Regular Papers Short Notes & Review Papers 43 [8A], pp. 5482-5486. URL: <Go to ISI>://WOS:000224841400077

[183] Holme, T. P. and Prinz, F. B. (2007): Atomic layer deposition and chemical vapor deposition precursor selection method application to strontium and barium precursors, Journal of Physical Chemistry A 111 [33], pp. 8147-8151. URL: <Go to ISI>://WOS:000248758800014

[184] Schwarzkopf, J.; Dirsyte, R.; Devi, A.; Schmidbauer, M.; Wagner, G. and Fornari, R. (2010): Depositions of $SrRuO_3$ thin films on oxide substrates with liquid-delivery spin MOCVD, Thin Solid Films 518 [16], pp. 4675-4679. URL: <Go to ISI>://WOS:000279377600046

[185] Uecker, R.; Velickov, B.; Klimm, D.; Bertram, R.; Bernhagen, M.; Rabe, M.; Albrecht, M.; Fornari, R. and Schlom, D. G. (2008): Properties of rare-earth scandate single crystals (Re = Nd-Dy), Journal of Crystal Growth 310 [10], pp. 2649-2658. URL: <Go to ISI>://WOS:000256237400037

[186] Marti, W.; Fischer, P.; Altorfer, F.; Scheel, H. J. and Tadin, M. (1994): Crystal structures and phase transitions of orthorhombic and rhombohedral $RGaO_3$ (R = La, Pr, Nd) investigated by neutron powder diffraction, Journal of Physics-Condensed Matter 6 [1], pp. 127-135. URL: <Go to ISI>://WOS:A1994MQ33000014

[187] Cao, G.; Alexander, C. S.; McCall, S.; Crow, J. E. and Guertin, R. P. (1999): From antiferromagnetic insulator to ferromagnetic metal: a brief review of the layered ruthenates, Materials Science and Engineering B-Solid State Materials for Advanced Technology 63 [1-2], pp. 76-82. URL: <Go to ISI>://WOS:000081887800014

[188] Cao, G.; McCall, S.; Shepard, M.; Crow, J. E. and Guertin, R. P. (1997): Thermal, magnetic, and transport properties of single-crystal $Sr_{1-x}CaxRuO_3$ ($0 \leq x \leq 1.0$), Physical Review B 56 [1], pp. 321-329. URL: <Go to ISI>://WOS:A1997XJ27200058

[189] Bouchard, R. J. and Gillson, J. L. (1972): Electrical properties of $CaRuO_3$ and $SrRuO_3$ single crystals, Materials Research Bulletin 7 [9], pp. 873-&. URL: <Go to ISI>://WOS:A1972N159100002

[190] Son, J. Y.; Kim, B. G. and Cho, J. H. (2007): Thin film growth of epitaxial, polycrystalline and amorphous $SrRuO_3$, Thin Solid Films 515 [18], pp. 7086-7090. URL: <Go to ISI>://WOS:000247897900007

[191] Orgiani, P.; Aruta, C.; Balestrino, G.; Lavanga, S.; Medaglia, P. G. and Tebano, A. (2002): Strain effect on transport properties of $SrRuO_3$ films grown by laser MBE, European Physical Journal B 26 [1], pp. 23-28. URL: <Go to ISI>://WOS:000175092900004

[192] Zayak, A. T.; Huang, X.; Neaton, J. B. and Rabe, K. M. (2008): Manipulating magnetic properties of $SrRuO_3$ and $CaRuO_3$ with epitaxial and uniaxial strains, Physical Review B 77 [21]. URL: <Go to ISI>://WOS:000257288900054

[193] Yuan, Q. S. (2004): Comment on "Strain effect and the phase diagram of $La_{1-x}Ba_xMnO_3$ thin films", Physical Review B 70. URL: <Go to ISI>://WOS:000223716300086

[194] Zhang, J.; Tanaka, H.; Kanki, T.; Choi, J. H. and Kawai, T. (2001): Strain effect and the phase diagram of $La_{1-x}Ba_xMnO_3$ thin films, Physical Review B 64 [18]. URL: <Go to ISI>://WOS:000172239400058

[195] Wu, D.; Li, A. D.; Zhu, T.; Liu, Z. G. and Ming, N. B. (2000): Ferroelectric properties of $Bi_{3.25}La_{0.75}Ti_3O_{12}$ thin films prepared by chemical solution deposition, Journal of Applied Physics 88 [10], pp. 5941-5945. URL: <Go to ISI>://WOS:000165068700068

[196] Wills, L. A.; Feil, W. A.; Wessels, B. W.; Tonge, L. M. and Marks, T. J. (1991): Growth studies of ferroelectric oxide layers prepared by organometallic chemical vapor deposition, Journal of Crystal Growth 107 [1-4], pp. 712-715. URL: <Go to ISI>://WOS:A1991EY07200121

[197] Lee, H. N.; Zakharov, D. N.; Senz, S.; Pignolet, A. and Hesse, D. (2001): Epitaxial growth of ferroelectric $SrBi_2Ta_2O_9$ thin films of mixed (100) and (116) orientation on $SrLaGaO_4$(110), Applied Physics Letters 79 [18], pp. 2961-2963. URL: <Go to ISI>://WOS:000171726300033

[198] Hollmann, E.; Schubert, J.; Kutzner, R. and Wordenweber, R. (2009): Stress generated modifications of epitaxial ferroelectric $SrTiO_3$ films on sapphire, Journal of Applied Physics 105 [11]. URL: <Go to ISI>://WOS:000267053200113

[199] Jiang, A. Q.; Li, G. H. and Zhang, L. D. (1998): Dielectric properties of $Bi_{3.97}Na_{0.1}Ti_3O_{12}$, Ferroelectrics 215 [1-4], pp. 103-111. URL: <Go to ISI>://WOS:000084101900010

[200] Jiang, A. Q. and Zhang, L. D. (1999): Asymmetric polarization of defect dipoles in $Bi_4Ti_3O_{12}$ and $Bi_2Ti_4O_{11}$ ceramics with Na^+ and La^{3+} modifications, Physical Review B 60 [13], pp. 9204-9207. URL: <Go to ISI>://WOS:000083079200005

[201] Beckhoff, B. (2010), Berlin

[202] Barrie, A. and Street, F. J. (1975): Auger and X-ray photoelectron spectroscopic study of sodium metal and sodium oxide Journal of Electron Spectroscopy and Related Phenomena 7 [1], pp. 1-31. URL: <Go to ISI>://WOS:A1975AK55300001

[203] Morgan, W. E.; Stec, W. J. and Vanwazer, J. R. (1973): Inner orbital binding energy shifts of antimony and bismuth compounds, Inorganic Chemistry 12 [4], pp. 953-955. URL: <Go to ISI>://WOS:A1973P217600054

[204] Debies, T. P. and Rabalais, J. W. (1977): X-ray photoelectron spectra and electronic structure of Bi_2X_3 (X = O,S,Se,Te), Chemical Physics 20 [2], pp. 277-283. URL: <Go to ISI>://WOS:A1977CY38400013

[205] Shimizugawa, Y.; Sugimoto, N. and Hirao, K. (1997): X-ray absorption fine structure glasses containing Bi_2O_3 with third-order non-linearities, Journal of Non-Crystalline Solids 221 [2-3], pp. 208-212. URL: <Go to ISI>://WOS:000071297700012

[206] Barreca, D.; Morazzoni, F.; Rizzi, G. A.; Scotti, R. and Tondello, E. (2001): Molecular oxygen interaction with Bi_2O_3: a spectroscopic and spectromagnetic investigation, Physical Chemistry Chemical Physics 3 [9], pp. 1743-1749. URL: <Go to ISI>://WOS:000168035300029

[207] Jovalekic, C.; Pavlovic, M.; Osmokrovic, P. and Atanasoska, L. (1998): X-ray-photoelectron spectroscopy study of $Bi_4Ti_3O_{12}$ ferroelectric ceramics, Applied Physics Letters 72 [9], pp. 1051-1053. URL: <Go to ISI>://WOS:000072290400018

[208] Fan, H. Y.; Wang, G. N. and Hu, L. L. (2009): Infrared, Raman and XPS spectroscopic studies of Bi_2O_3-B_2O_3-Ga_2O_3 glasses, Solid State Sciences 11 [12], pp. 2065-2070. URL: <Go to ISI>://WOS:000273067400007

[209] West, A. R. (2006): Inorganic functional materials: Optimization of properties by structural and compositional control, Chemical Record 6 [4], pp. 206-216. URL: <Go to ISI>://WOS:000240207500004

[210] Zhao, T.; Chen, F.; Lu, H. B.; Yang, G. Z. and Chen, Z. H. (2000): Thickness and oxygen pressure dependent structural characteristics of $BaTiO_3$ thin films grown by laser molecular beam epitaxy, Journal of Applied Physics 87 [10], pp. 7442-7447. URL: <Go to ISI>://WOS:000086730000048